Quantum dynamics of the diffusion of adsorbates

Oussama Bindech

Université de Strasbourg

UNIVERSITÉ DE STRASBOURG

EDSC École Doctorale des Sciences Chimiques

ÉCOLE DOCTORALE DES SCIENCES CHIMIQUES

Institut de Chimie UMR 7177

THÈSE présentée par :

Oussama BINDECH

soutenue le : **8 décembre 2023**

pour obtenir le grade de : **Docteur de l'université de Strasbourg**

Discipline/ Spécialité : Chimie / Chimie Théorique

Quantum dynamics of the diffusion of adsorbates

THÈSE dirigée par :

M. Roberto MARQUARDT	Professeur, Université de Strasbourg, France

RAPPORTEURS :

Mme Shirin FARAJI	Professeure, University of Groningen, The Netherlands
M. Marius LEWERENZ	Professeur, Université Gustave Eiffel, France

---

EXAMINATEURS :

M. Peter FOUQUET	Scientifique principal, Institut Laue-Langevin, Grenoble, France
Mme Christine GOYHENEX	Chargée de Recherches, Université de Strasbourg, France
Mme Alexandra VIEL	Directrice de Recherches, Université de Rennes, France

"If you want to find the secrets of the universe, think in terms of energy, frequency and vibration."

Nikola Tesla

.

Remerciements

C'est avec plaisir et passion que ce travail de recherche aboutit. Ces années de thèse ont été sans aucun doute les plus formatrices de mon parcours académique. Le temps passé avec soi-même, pour surmonter divers défis et obstacles méthodologiques, a été enrichissant d'un point de vue scientifique mais également personnel. Cette expérience inoubliable n'aurait pas été possible sans toutes les personnes qui ont contribué à la réalisation de ce projet, et que je souhaite remercier ici.

Je tiens tout d'abord à remercier mon directeur de thèse le Professeur Roberto Marquardt pour son engagement indéfectible durant ces années de thèse. Ses conseils et sa disponibilité ont été indispensables pour mener à bien ce projet. Je lui suis extrêmement reconnaissant pour la confiance, l'autonomie et la liberté dans le travail dont j'ai bénéficié. Cela m'a permis de m'approprier profondément mon sujet de thèse et de surmonter les obstacles techniques et intellectuels auxquels j'ai pu faire face tout au long de ce travail.

Je tiens également à exprimer ma profonde gratitude envers les membres du jury qui ont bien voulu examiner ma thèse: Shirin Faraji, Professeure à l'université de Groningen, Marius Lewerenz, Professeur à l'université Gustave Eiffel, Peter Fouquet, scientifique principal à l'institut Laue-Langevin, Christine Goyhenex, Chargée de Recherches à l'institut de physique et de chimie des matériaux de Strasbourg et Alexandra Viel, Directrice de recherches à l'institut de physique de Rennes. Je leur suis reconnaissant de leur engagement et de la rigueur avec laquelle ils ont examiné chaque aspect de ma thèse.

Je souhaite ensuite remercier tous les membres du projet ANR dont cette thèse fait partie: le Professeur Roberto Marquardt, le Directeur de recherches Fabien Gatti,

le Professeur Jean Christophe Tremblay et les Docteurs Souvik Mandal et Lei Shi, pour le partage de leur expertise et pour toutes les discussions enrichissantes que nous avons pu avoir ces dernières années.

Je voudrais aussi remercier le Professeur Hans Dieter Meyer pour son aide et sa disponibilité pour résoudre les problèmes techniques rencontrés sur le programme MCTDH.

Une pensée spéciale à mes collègues de laboratoire de Chimie Quantique de Strasbourg. Un grand merci au Professeur Vincent Robert d'avoir partagé sa passion pour la science et tous les échanges stimulants que nous avons pu avoir. Je le remercie également pour sa bienveillance, son soutien aux doctorants et ses grandes qualités humaines. Merci au Professeur Emmanuel Fromager pour toutes les discussions sur son domaine de recherche que nous avons eu et leurs résonnances avec mes propres travaux, approfondir un domaine complémentaire à mon sujet de recherche a été très enrichissant. Merci au Docteur Saad Yallouz pour son implication tant dans le domaine scientifique que dans la vie commune du laboratoire. Merci aux doctorants et docteurs fraichement diplômés du LCQS: Filip, Pablo, Lucie, Sajan et Wafa d'avoir rendu la vie quotidienne au laboratoire si épanouissante. Merci à Paola Sager pour sa réactivité et sa disponibilité durant ces dernières années. Je voudrais enfin remercier la Directirce de Recherches Chantal Daniel, les Docteurs Christophe Gourlaouen et Etienne Gindensperger, notre ingénieur informatique Guillaume Rouaut et tous les membres du LCQS pour les efforts et les contributions qu'ils apportent à ce laboratoire.

Je souhaite enfin exprimer ma gratitude envers mes proches, particulièrement à Lauren pour son soutien constant pendant cette période exigeante. Elle s'est investie à mes côtés au point, d'une certaine façon, de soutenir une seconde thèse à mes côtés. Merci à mes amis pour leurs encouragements et leur compréhension lors des derniers mois de la thèse qui ont été particulièrement chargés. Enfin je souhaite remercier ma mère, mon père et mon frère pour leur inconditionnel soutien et la passion de l'apprentissage qu'ils m'ont transmis.

Je n'oublie pas de remercier toutes les personnes qui ont à leur façon participer à cette recherche, par quelques conseils, de brefs échanges, un mot lors des derniers

instants. Tout cela a contribué à ce long processus qu'est le travail de recherche et fut essentiel à son aboutissement.

Je vous remercie tous très sincèrement d'avoir fait de ce voyage académique et humain une expérience inoubliable.

Contents

List of Figures

List of Tables

List of acronyms

BS Bulirsch-Stoer

CMF Constant Mean Field

DAV Davidson

DFT Density Functional Theory

DOF Degree Of Freedom

DSF Dynamical Structure Factor

DVR Discrete Variable Representation

FBR Finite Basis Representation

HREELS High-Resolution Electron Energy Loss Spectroscopy

IAA InterAtomic Axis

ISF Intermediate Scattering Function

IVR Intramolecular Vibrational Redistribution

IWF Initial Wave Function

MAF MonoAtomic Function

MCTDH Multi-Configuration Time-Dependent Hartree

PES Potential Energy Surface

POTFIT POTential FIT

QDDA Quantum Dynamics of the Diffusion of Adsorbates

RK8 Range Kutta order 8

RFFs Reactive Force Fields

RPD Reduced Probability density(ies)

SIL Short Iterative Lanczos

SPF Single-Particle Function

SPP Single-Particle Potential

STM Scanning Tunneling Microscopy

TDH Time-Dependent Hartree

VMF Variable Mean Field

ZPE Zero-Point Energy

^{3}**HeSE** Helium-3 Spin-Echo

Résumé (French summary)

La dynamique quantique des surfaces est une branche fascinante de la recherche scientifique qui permet d'étudier le comportement complexe des atomes et des molécules à l'échelle nanoscopique de la surface des matériaux selon les principes de la mécanique qui correspond à cette échelle : la mécanique quantique. Cette étude relie les principes de la mécanique quantique, qui expliquent les mouvements des particules à l'échelle atomique et subatomique, à la science des surfaces, qui examine les propriétés et les interactions des atomes et des molécules à la surface des solides et des liquides. Les chercheurs dans ce domaine utilisent, d'une part, des techniques expérimentales avancées, telles que la microscopie à effet tunnel (*scanning tunneling microscope*, STM) [1], la spectroscopie de perte d'énergie des électrons à haute résolution (*high resolution electron energy loss spectroscopy*, HREELS) [2], la diffusion de neutrons ou d'atomes d'hélium [3], et d'autre part, la modélisation numérique, y compris les simulations classiques de dynamique moléculaire pour dévoiler les principes fondamentaux régissant les processus de surface [3]. Les simulations basées sur des approches entièrement quantiques à partir de calculs de premier principe sont toutefois moins courantes.

L'objectif de cette thèse est d'étudier la dynamique quantique des atomes d'hydrogène après leur adsorption sur une surface métallique formée d'atomes de palladium (Pd). Elle s'inscrit dans un domaine de recherche passionnant au sein de la vaste discipline de la dynamique quantique des surfaces. Cette étude se concentre sur la compréhension des interactions à l'échelle quantique entre les atomes d'hydrogène, les entités les plus simples, et la surface de palladium. Ce type de substrat est particulièrement intéressant dans ce contexte en raison de ses propriétés uniques qui en font un excellent catalyseur pour diverses réactions chimiques. Comprendre

la dynamique quantique des atomes d'hydrogène sur la surface du palladium est également d'une importance cruciale pour des applications telles que le stockage de l'hydrogène [4]. En comprenant les processus quantiques impliqués, les scientifiques visent à améliorer l'efficacité et la performance des applications liées à l'hydrogène, contribuant ainsi à l'avancement des solutions énergétiques durables.

Nous nous intéressons particulièrement aux situations où un ou deux atomes d'hydrogène sont adsorbés sur la surface de Pd(111); les deux systèmes seront désignés dans cette thèse par H/Pd(111) et H_2/Pd(111) respectivement. Les propriétés dynamiques de ces systèmes dépendent principalement du type d'interactions interatomiques entre l'adsorbat et les atomes du substrat. Lorsque ces interactions impliquent des couplages de nature quantique, la dynamique des adsorbats peut être fortement influencée par les phénomènes quantiques induits par ces couplages, tels que l'effet tunnel, mais non exclusivement. Les atomes d'hydrogène, compte tenu de leur masse, sont fortement soumis à ce type d'interaction. Dans ce cas, leur mouvement sur la surface du métal est principalement soumis aux lois de la mécanique quantique. Une compréhension complète de leur dynamique nécessite une approche entièrement quantique; on parle alors de dynamique quantique des adsorbats.

Dans cette thèse, une étude basée sur une telle approche a été réalisée, par laquelle des effets non-classiques susceptibles d'impacter le comportement des atomes d'hydrogène adsorbés à la surface du palladium ont été dévoilés. Le système est alors défini par sa fonction d'onde, et son évolution temporelle se fait par la résolution de l'équation de Schrödinger dépendante du temps. Les potentiels interatomiques possèdent généralement des formulation mathématiques complexes, ce qui rend impossible une résolution analytique exacte de cette équation. Les méthodes numériques sont les principaux outils permettant d'obtenir des solutions susceptibles de décrire le système de manière réaliste.

La dissipation en général, et le frottement en particulier, résultent de l'interaction de la particule, dans ce cas l'atome d'hydrogène, avec toute la pléthore de particules qui l'entourent, parmi lesquelles nous pouvons compter d'autres atomes d'hydrogène sur le substrat, mais aussi les atomes du substrat en mouvement ou les électrons environnants. En raison de la taille de l'espace linéaire contenant tous les états

du milieu environnant, le traitement théorique direct par l'obtention d'une solution de la fonction d'onde à plusieurs corps à partir de l'équation de Schrödinger est pratiquement impossible. Ce fait nous oblige à developper des modèles qui nous permettent de décrire de façon approximative ces interactions avec l'environement.

Cette thèse fait partie du projet de recherche "Dynamique Quantique de la Diffusion des Adsorbats (QDDA)", financé par l'Agence Nationale de la Recherche (ANR). Un des aspects de ce projet est le développement de méthodes pratiques pour traiter l'effet de dissipation, ce qui a donné lieu à deux publications en relation avec le présent travail [5, 6]. Ces méthodes sont actuellement en cours d'applicationaux systèmes étudiés dans cette thèse. Cependant, aucun résultat n'a été au moment de la rédaction de cette thèse et nous nous abstenons donc de présenter ici cette partie du projet QDDA. Les effets de la dissipation et de la friction ne sont pas pris en compte dans le cœur de cette thèse, qui se concentre uniquement sur les aspects quantiques du mouvement des atomes d'hydrogène.

Une grande partie de ce travail est liée à l'étude des états stationnaires et des énergies des atomes d'hydrogène, lorsqu'ils sont adsorbés sur la surface du palladium. Cette étude est cruciale pour la compréhension de leur mouvement. Le dihydrogène s'adsorbe sur le palladium de manière dissociative. Dans le cadre des approximations susmentionnées, les états stationnaires sont les états vibrationnels des adsorbats dans la surface d'énergie potentielle (SEP) multidimensionnelle, ce qui inclut les translations frustrées et les rotations entravées des espèces diatomiques. Les états vibrationnels sont associés aux mouvements vibratoires quantifiés des atomes au sein d'une molécule ou d'un réseau cristallin. Les états propres vibrationnels révèlent plusieurs effets importants de la dynamique quantique, notamment l'effet tunnel, l'intrication quantique, l'énergie du point zéro et en particulier les propriétés thermodynamiques des systèmes quantiques. Leur nature quantifiée et leurs interactions avec d'autres états quantiques les rendent fondamentaux pour comprendre et prédire le comportement des atomes d'hydrogène adsorbés à l'échelle quantique. Nous avons pu notamment montrer dans cette étude la présence d'un effet tunnel et d'un couplage par résonance de Fermi [7] entre certains modes vibrationnels localisés du système. Plusieurs simulations dynamiques dépendantes du temps ont ensuite été réalisées, mettant en évidence l'impact majeur de ces effets sur le mouvement

des atomes d'hydrogène adsorbés à cette surface.

La diffusion de surface, quant à elle, est un domaine d'étude qui se concentre sur la manière dont les particules, en particulier les atomes et les molécules, interagissent et diffusent à la surface des matériaux. Cette discipline est cruciale pour notre compréhension des processus qui se produisent à la surface des matériaux, ce qui a des implications significatives dans des domaines tels que la catalyse, la croissance des couches minces, la chimie des surfaces, les nanotechnologies et bien d'autres. À l'échelle atomique, les particules doivent surmonter des barrières énergétiques pour se déplacer le long de la surface. Ces barrières résultent des interactions entre les particules adsorbées et les atomes de la surface. Alors qu'en mécanique classique, la diffusion est le résultat d'un comportement collectif de nombreuses particules décrites par leurs trajectoires aléatoires individuelles dans l'espace de configuration, en mécanique quantique, les particules sont décrites par leurs fonctions d'onde, dont la distribution dans l'espace de configuration est généralement délocalisée à un degré élevé et dont l'interprétation physique contient des éléments fondamentaux de stochasticité. Par conséquent, l'image quantique d'une particule se déplaçant dans l'espace de configuration reflète intrinsèquement une diffusion d'un type différent, peut-être, de la diffusion dans la compréhension classique du terme, et ceci indépendamment de son interaction éventuelle avec les particules composant son environement. Ces dernières pourraient être déduites de la fonction d'onde à plusieurs corps de particules interagissant de manière aléatoire et nous pourrions conjecturer que ces effets s'ajouteraient simplement aux effets déjà causés par la nature ondulatoire de l'état d'une seule particule. Or, les échelles de temps où ces interactions à plusieurs corps deviennent importantes sont typiquement bien plus longues que les échelles de temps du mouvement vibratoire des adsorbats, ce qui rend notre approximation plausible dans l'échelle de temps de celui-ci: la sub-picoseconde ($\sim 10^{-15}$ à 10^{-12} s).

Pour étudier la diffusion en surface, les scientifiques utilisent des techniques expérimentales telles que les expériences d'écho de spin de l'hélium 3 [3] pour extraire les coefficients de diffusion. Cependant, pour extraire ces coefficients des données mesurées, et même pour en déduire la topographie de la SEP des surfaces catalytiques, de nombreuses étapes de modélisation intermédiaires doivent être réalisées. Les résultats expérimentaux des expériences d'écho de spin de l'hélium 3 reposent

sur l'évaluation du facteur de structure dynamique (FSD), introduit pour la première fois par van Hove [8], et de sa transformée de Fourier, la fonction de diffusion intermédiaire (FDI). Plutôt que de déterminer directement le coefficient de diffusion, la recherche se concentre désormais sur l'évaluation et l'interprétation du FSD et de la FDI directement observables, comme cela est clairement décrit dans la réf. [3].

L'importance de la nature quantique de la dynamique sous-jacente au mouvement de diffusion a été soulignée à plusieurs reprises et également dans des travaux publiés [9, 10, 11, 12, 13]. Une évaluation détaillée de l'approche purement quantique pour calculer les observables n'a pas été faite avant que les résultats sur le FSD ne soient obtenus à partir de calculs de premier principe [10]. Cependant, plusieurs questions sont restées ouvertes depuis lors, parmi lesquelles une question majeure émerge : comment évaluer théoriquement la FDI directement observée à partir d'un calcul de dynamique purement quantique ? Une nouvelle méthode de calcul de cette fonction fait partie intégrante de la proposition de projet QDDA [14] dont est issu le présent projet de thèse. Elle repose sur une formulation entièrement quantique basée sur une approche stochastique. Cette méthode a été testée pour la première fois dans les présents travaux.

Dans ce qui suit, nous présentons quelques aspects généraux des études qui ont été couvertes dans cette thèse.

Théorie & méthodes

Les systèmes étudiés étant représentés par leurs fonctions d'onde, la dynamique est réalisée par le biais de l'équation de Schrödinger dépendante du temps. La solution analytique exacte de cette équation n'est pas possible pour les systèmes étudiés. Nous avons donc utilisé des méthodes basées sur une approche numérique pour sa résolution.

La méthode *Multi-Configuration Time-dependent Hartree* (MCTDH) [15, 16] a été utilisée pour la résolution numérique de l'équation de Schrödinger dépendante du temps. Le programme permet de traiter un large éventail de problèmes de dynamique moléculaire quantique, y compris ceux de grande dimension. La puis-

sance de cette méthode provient du traitement compact multi-configurationnel de la fonction d'onde à l'aide d'un ensemble de fonctions dépendantes du temps appelé *single particle functions* (SPF). Pour un problème avec f degrés de liberté (DL), la décomposition de la fonction d'onde du système dans cette base s'écrit

$$\Psi(Q_1,..,Q_f,t) = \sum_{i_1}^{n_1}...\sum_{i_f}^{n_f} A_{i_1,...,i_f}(t)\prod_{\kappa=1}^{f}\varphi_{i_\kappa}^{(\kappa)}(Q_\kappa,t) \tag{1}$$

Avec $\kappa = \{1,..,f\}$, $\varphi_{i_\kappa}^{(\kappa)}(Q_\kappa,t)$ est la i_κ-ième SPF utilisée pour décrire le DL Q_κ, n_κ est le nombre de SPF utilisées pour chaque DL et $A_{i_1,...,i_f}(t)$ représente les coefficients d'expansion de la fonction d'onde en fonction du temps dans la base SPF.

Une décomposition similaire à celle utilisée pour la fonction d'onde est nécessaire pour l'ensemble des opérateurs utilisés dans les calculs MCTDH, en particulier l'Hamiltonien du système. L'opérateur d'énergie cinétique convient généralement à cette forme. Pour les potentiels interatomiques, cependant, les opérateurs associés ne permettent pas une décomposition analytique de cette forme dans la plupart des cas. MCTDH comprend un module appelé *potfit* qui permet de représenter numériquement le potentiel avec la forme requise pour MCTDH.

Pour propager la fonction d'onde d'un système initialement préparé dans un état Ψ_0, une base SPF et un vecteur $\boldsymbol{A}$ sont initialement construits de manière à reproduire Ψ_0 sous la forme adaptée à MCTDH. Comme la base SPF et le vecteur $\boldsymbol{A}$ dépendent du temps, ils sont tous les deux propagés dans le temps selon le principe variationnel de Dirac-Frenkel [17, 18]. Le calcul variationnel conduit aux équations de mouvement de MCTDH données par :

$$\mathrm{i}\dot{A}_I = \sum_{I'} \langle\varphi_I|\hat{H}|\varphi_{I'}\rangle\, A_{I'} \tag{2}$$

$$\mathrm{i}\dot{\boldsymbol{\varphi}}^{(\kappa)} = (\hat{1}-\hat{P}^{(\kappa)})(\boldsymbol{\rho}^{(\kappa)})^{-1}\,\langle\boldsymbol{H}\rangle^{(\kappa)}\,\boldsymbol{\varphi}^{(\kappa)} \tag{3}$$

$\boldsymbol{\varphi}^{(\kappa)}$ est un vecteur composé des n_κ SPF utilisées pour le DL Q_κ. L'opérateur $(1-\hat{P}^{(\kappa)})$ garantit que la dérivée temporelle de la SPF est orthogonale à l'espace généré par ces fonctions. $\boldsymbol{\rho}^{(\kappa)}$ et $\boldsymbol{H}^{(\kappa)}$ représentent respectivement la matrice de densité d'une seule particule et la matrice du champ moyen [15].

Pour résoudre l'équation de Schrödinger indépendante du temps, nous avons utilisé la méthode de relaxation améliorée par blocs implémentée dans MCTDH [19, 20, 21].

Cette approche est basée sur l'idée que si nous propageons un état avec un Hamiltonien en temps imaginaire négatif, il convergera vers l'état propre de plus basse énergie du système étudié. La version en bloc de cette méthode permet de relaxer simultanément plusieurs états vers les états propres du système. Cette méthode est non seulement plus rapide en termes de temps de calcul que la relaxation d'un seul état, mais elle est également cruciale pour traiter les problèmes avec des états propres dégénérés, comme c'est le cas dans cette étude.

Le choix d'utiliser l'approche MCTDH est fondé sur sa capacité à traiter des systèmes nécessitant des bases de fonctions mathématiques relativement importantes pour leur description. Bien que les systèmes étudiés dans cette thèse ne possèdent pas de dimensionnalité très élevée, le calcul des états propres vibrationnels et de la dynamique quantique effectué dans cette étude a représenté un véritable défi pour le calcul numérique. En effet, les interactions interatomiques entre les atomes d'hydrogène et les atomes du substrat sont d'une nature très complexe. La dualité entre la forte corrélation impliquant les degrés de liberté internes et externes de chaque atome d'hydrogène rend le calcul numériques très coûteux. Le choix de "bons" vecteurs de base avec des combinaisons de modes adaptées à ce type d'interaction était essentiel pour la réalisation des calculs. D'autre part, les interactions à longue portée entre les atomes d'hydrogène signifient que de grandes cellules de calcul périodiques sont nécessaires pour modéliser correctement le système, ce qui nécessite de très grandes bases primitives. Ceci rend également l'étude de la dynamique de ces systèmes à l'échelle de temps de la picoseconde extrêmement coûteuse numériquement pour garantir des calculs précis. L'utilisation de MCTDH nous a permis de réduire cet effort numérique tout en conservant une description correcte du système.

Analyse des surfaces d'énergie potentielle

Nous effectuons nos calculs dans l'approximation de Born-Oppenheimer dans laquelle les mouvements des électrons et ceux des noyaux sont découplés adiabatiquement, les noyaux évoluent alors dans une SEP représentant les interactions entre les composants du système. La SEP utilisée dans ce travail a été développée par

W.Dong et al. [22] pour une surface de palladium normale à la direction cristalline ⟨111⟩. Elle a été construite dans l'état électronique fondamental du système. Les auteurs ont fourni une formulation analytique du potentiel en utilisant des modèles d'ajustement [23]. Dans cette étude, les atomes de palladium sont considérés comme fixes dans leur position d'équilibre, et les seuls DLs de la SEP sont ceux des atomes d'hydrogène. La SEP est donc définie par une fonction tri-dimensionnelle dans le cas de H/Pd(111) et une fonction six-dimensionnelle dans le cas de H_2/Pd(111).

Présentation de la cellule élémentaire

Afin de simuler une surface infinie dans nos calculs, une approche périodique a été adoptée qui comprend une cellule élémentaire donnée par un bloc de cinq couches de Pd où chacune contient 3×3 atomes de Pd. L'espace vide correspond à cinq couches de Pd(111). La cellule élémentaire utilisée dans nos calculs est la même que celle utilisée par les auteurs pour développer la SEP. La figure 1 présente un schéma de cette grille montrant uniquement le plan de surface (ligne continue) et le premier plan inférieur (ligne pointillée).

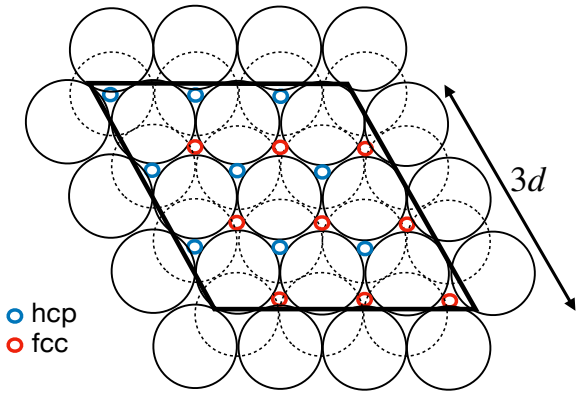

Figure 1: Cellule 3×3 utilisée pour les calculs périodiques.

Cette grille contient 9 sites hcp équivalents et 9 sites fcc équivalents. Ces derniers correspondent aux sites d'adsorption les plus stables au niveau de la surface. La périodicité spatiale est appliquée suivant les vecteurs $\boldsymbol{x_t}$ et $\boldsymbol{y_t}$ formant un angle $\alpha = (\widehat{\boldsymbol{x_t}, \boldsymbol{y_t}}) = 120°$ comme le montre la figure 2.

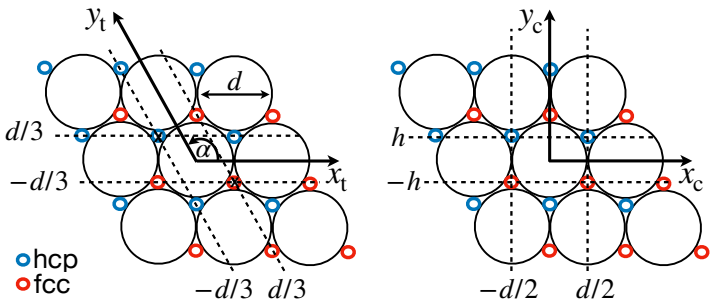

Figure 2: Representation des bases "*twisted*" et cartésienne dans la cellule élémentaire 3×3. $d \approx 2.75$Å.

Nous définissons un repère non orthogonale dit "*twisted*" ($\boldsymbol{x_t}$, $\boldsymbol{y_t}$, $\boldsymbol{z_t}$) où l'origine est située au centre de l'atome de Pd situé au milieu de la couche extérieure de la cellule élémentaire. La transformation entre les deux systèmes de coordonnées est donnée par :

$$\begin{cases} x_t = x_c + \dfrac{1}{\sqrt{3}} y_c \\ y_t = \dfrac{2}{\sqrt{3}} y_c \\ z_t = z_c \end{cases} \tag{4}$$

Les deux systèmes de coordonnées sont utilisés dans ce travail en fonction de la nature de la tâche effectuée. Dans ce qui suit, nous ferons référence aux coordonnées cartésiennes en tant que (x, y, z).

SEP de H/Pd(111)

La figure 3 montre une section bidimensionnelle de la SEP dans les coordonnées cartésiennes du système H/Pd(111). Elle illustre la structure du potentiel perçu par l'atome d'hydrogène lorsqu'il se déplace dans un plan parallèle au substrat. Cela permet de visualiser la structure des différents puits de potentiel situés au niveau de ce plan.

Des lignes d'énergie équipotentielle allant de 0 à 300 meV sont représentées sur la figure. On constate que tous les puits de potentiel sont situés sur les sites fcc et hcp de la grille. Ils possèdent une forme trianglaire soulignant la symétrie locale du type $\boldsymbol{C}_{3v}$ du potentiel. Le minimum global du potentiel est pris comme énergie

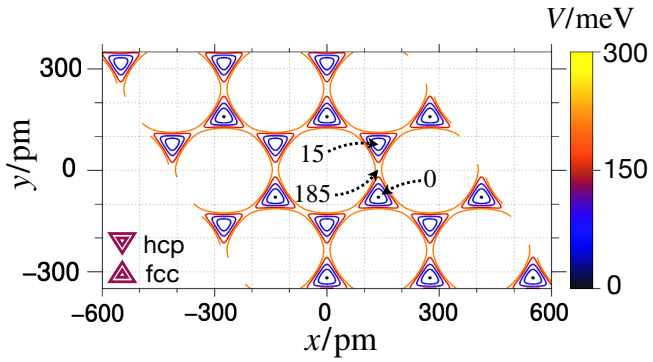

Figure 3: Coupe bidimentionnelle de la SEP de H/Pd(111) dans les coordonnées cartésiennes avec $z = 90$ pm.

de référence, il est atteint lorsque l'atome d'hydrogène est situé sur un des sites fcc. L'énergie du système lorsque l'atome d'hydrogène est situé dans un site hcp est d'environ 15 meV pour z=90 pm. Les puits de potentiel situés sur les sites hcp correspondent donc aux minima locaux du potentiel. La cellule périodique contient alors au niveau de la surface 18 puits de potentiel dont 9 équivalents de chaque type. Les barrières de potentiel qui séparent les puits de potentiel à $z = 90$ pm sont toutes équivalentes et de taille finie avec une hauteur de 185 meV.

SEP de H_2/Pd(111)

Les minima du SEP H_2/Pd(111) sont atteints lorsque les deux atomes d'hydrogène occupent des sites fcc ou hcp. Dans ce qui suit, nous symbolisons le site fcc par la lettre majuscule A et le site hcp par la lettre majuscule B. Nous pouvons ainsi distinguer trois situations :

- Les deux atomes d'hydrogène sont situés sur des sites fcc (AA).
- Les deux atomes d'hydrogène sont situés sur des sites hcp (BB).
- Un atome d'hydrogène est situé sur un site fcc et l'autre sur un site hcp (AB).

Le tableau 1 donne les énergies de toutes les différentes configurations possibles avec la dégénérescence "classique" associée. Les indices "I" et "II" sont utilisés pour désigner les situations dans lesquelles les deux atomes occupent respectivement les sites des premiers et de seconds voisins. L'indice "NN" (Nearest Neighbors) utilisé dans la configuration (AB) correspond à la situation où les deux atomes occupent

les sites fcc et hcp les plus proches. Cette configuration n'est pas incluse dans cette étude pour cause de son énergie déjà assez elevée.

Configuration	$d_{\text{H-H}}/d$	E/meV	Dégénérescence
$(\text{AA})_{\text{I}}$	1	0	54
$(\text{BB})_{\text{I}}$	1	17	54
$(\text{AB})_{\text{I}}$	$2/\sqrt{3}$	38	54
$(\text{AA})_{\text{II}}$	$\sqrt{3}$	67	18
$(\text{AB})_{\text{II}}$	$\sqrt{7/3}$	71	54
$(\text{BB})_{\text{II}}$	$\sqrt{3}$	99	18
$(\text{AB})_{\text{NN}}$	$1/\sqrt{3}$	357	54

Table 1: Énergies et dégénérescence classique de tous les types de configurations possibles du système H_2 dissociatif sur la surface de Pd. $d \approx 275$ pm est la distance entre deux atomes de Pd voisins et $d_{\text{H}-\text{H}}$ représente la distance entre les deux atomes H dans chaque configuration.

La figure 4 montre une représentation bidimensionnelle de la SEP du système lorsqu'un atome d'hydrogène est fixé à un site fcc (figure 4a) ou à un site hcp (figure 4b), tandis que le second se déplace dans un plan parallèle au substrat. Cette représentation illustre les différents types de configuration donnés dans le tableau 1.

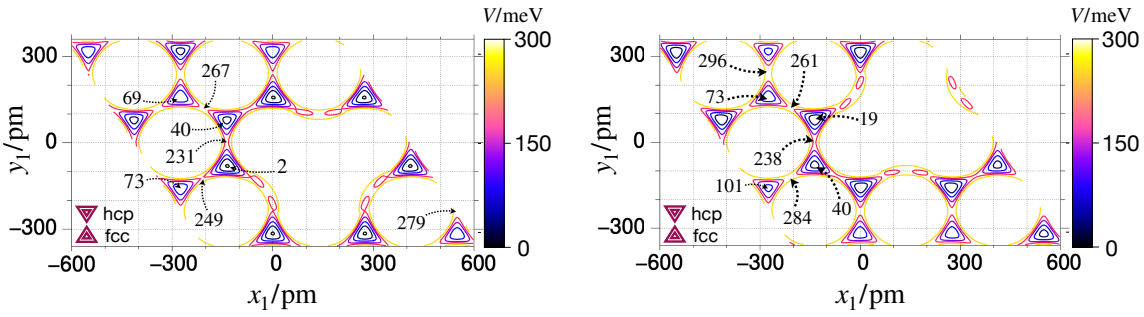

(a) (b)

Figure 4: Coupes bidimensionnelles de la SEP de H_2/Pd(111) lorsque l'un des deux atomes d'hydrogène est fixé sur un site fcc (4a) ou hcp (4b), tandis que le second se déplace dans un plan parallèle au substrat donné par $z_1 = 87$ pm. Les lignes équipotentielles allant de 0 à 300 meV sont représentées sur la figure.

Résultats & discussions

L'étude théorique de la spectroscopie vibrationnelle réalisée dans cette thèse a fourni un moyen puissant de comprendre, d'une part, la structure des états propres vibrationnels d'un et de deux atomes d'hydrogène adsorbés sur la surface de palladium Pd(111). D'autre part, cette compréhension nous permet de rationaliser le comportement dynamique complexe de ces atomes sur la surface. Les points suivants résument les résultats clés et les implications de cette recherche :

- L'étude théorique de la spectroscopie vibrationnelle d'un seul atome d'hydrogène adsorbé sur la surface du palladium a révélé la présence d'un effet tunnel affectant tous les états vibrationnels excités. Ce dernier s'est manifesté de diverses manières à travers différentes barrières de potentiel, conduisant à de multiples éclatements de plusieurs niveaux d'énergie en sous-niveaux avec des écarts relatifs allant de 1 meV à 8 meV.

  L'étude a également montré l'existence d'une résonance de Fermi entre les états purs possédant un seul quantum d'excitation vibrationnelle perpendiculaire au substrat et ceux possédant deux quanta d'excitation vibrationnelle parallèle au substrat. L'interaction entre ces deux états vibrationnels entraîne la formation de paires de Fermi d'états stationnaires possédant simultanément des excitations vibrationnelles perpendiculaires et parallèles au substrat.

- L'étude théorique de la spectroscopie vibrationnelle de H_2/Pd(111) a montré que dans les situations où les deux atomes d'hydrogène occupent des sites d'adsorption voisins de même type, l'excitation du système se manifeste systématiquement sur les deux atomes. Ces derniers adoptent alors des modes de vibration concertés en phase et en opposition de phase, démontrant ainsi la présence d'une forte corrélation entre les deux atomes. Dans les cas où ces derniers occupent des sites de types différents, les excitations vibrationnelles sont localisées séparément sur les deux atomes, indiquant une corrélation plus faible dans ce type de configuration.

  Dans les deux cas, la présence d'un second atome d'hydrogène dans le voisinage modifie significativement le spectre du système. En particulier, nous

avons constaté que les barrières de potentiel séparant les différents sites sont importantes, conduisant à un effet tunnel beaucoup moins prononcé que celui observé sur l'atome d'hydrogène isolé.

La résonance de Fermi, telle qu'observée sur un atome d'hydrogène isolé, reste localement présente sur chaque atome de la diatomique malgré les fortes interactions entre eux lorsqu'ils occupent des sites voisins de même type. Ceci montre également la persistance de l'intensité des interactions locales entre les modes vibrationnels internes de chaque atome d'hydrogène.

- L'intégration de la dynamique quantique dans cette étude nous a permis de mieux comprendre les processus quantiques qui sous-tendent la structure des états propres vibrationnels des systèmes. Nous avons examiné plusieurs simulations numériques mettant en évidence la manifestation de l'effet tunnel et de la résonance de Fermi dans le comportement dynamique des atomes d'hydrogène à la surface du palladium. Ces études ont permis de dégager trois grandes conclusions :

  – La dynamique des atomes d'hydrogène suite à une excitation dans un mode parallèle au substrat est principalement gouvernée par l'effet tunnel à travers les barrières de potentiel. Ceci est beaucoup plus important dans le cas d'un atome d'hydrogène isolé.

  – La résonance de Fermi telle que prédite dans cette étude, couple les mouvements de vibration perpendiculaire et parallèle au plan de surface dans une échelle de temps d'environ 200 fs. Lorsqu'un atome d'hydrogène est excité dans un mode perpendiculaire au substrat, l'excitation vibrationnelle alterne dans le temps entre les modes parallèles et perpendiculaires. La quasi-périodicité de nature quantique observée entre ces vibrations est directement liée à l'écart énergétique entre les états formant les paires de Fermi au sein du système.

  – L'excitation d'un atome d'hydrogène conduit à un transfert systématique d'énergie vers l'atome d'hydrogène voisin à l'échelle de temps de quelques centièmes de femtosecondes, si ce dernier occupe un site voisin du même type. Le temps de transfert de cette énergie est directement lié aux

énergies des états vibrationnels correspondant au même type d'excitation.

- La méthode de calcul de la fonction de diffusion intermédiaire utilisée dans cette thèse permet de relier directement les observations expérimentales dans les expériences d'écho de spin à l'approche quantique de la diffusion. L'étude préliminaire que nous avons réalisé dans ce projet a permis d'extraire des premières données pouvant être comparées directement aux résultats expérimentaux, tout en décrivant précisément l'ensemble des mécanismes se déroulant à l'échelle de la femtoseconde.. Elle représente un premier pas vers l'exctraction des coefficients de diffusion directement de ces simulations numériques à partir de calculs de premiers principes.

Perspectives

Les connaissances acquises dans le cadre de cette thèse ouvrent de nouvelles perspectives de recherches futures. Pour n'en citer que quelques-unes :

- l'évaluation de l'impact de la dissipation et de la friction ; trois sources principales peuvent être ciblées, à cet égard, à savoir l'interaction entre plus de deux atomes d'hydrogène adsorbés, l'interaction avec les atomes de palladium en mouvement (couplages de phonons), et les interactions avec les électrons environnants hors de l'approximation de Born-Oppenheimer (couplages avec les paires électron-trou).

- une évaluation théorique précise du spectre HREELS de l'hydrogène sur le palladium ; des idées ont été explorées dans cette thèse, les résultats sont prometteurs mais absents de ce manuscrit, car ils nécessitent des recherches plus approfondies;

- l'étude des modifications para et ortho de H_2 adsorbé, et le mécanisme subtil de leur interconversion lors de l'adsorption via l'inclusion du couplage hyperfin faible ; à cette fin, cependant, la précision numérique devra être augmentée d'au moins deux ordres de grandeur.

En fin de compte, cette recherche met en évidence la profonde interconnexion entre la spectroscopie vibrationnelle et la dynamique quantique, deux domaines

qui s'enrichissent mutuellement pour fournir une compréhension plus profonde des phénomènes moléculaires à l'interface entre les matériaux solides et leur environnement.

Summary

Quantum surface dynamics is a fascinating branch of scientific research that investigates the complex quantum mechanical behavior of atoms and molecules on the quantum scale at the surface of materials. This discipline interconnects the principles of quantum mechanics, which studies particles on the atomic and subatomic scales, with surface science, which examines the properties and interactions of atoms and molecules on the surfaces of solids and liquids. Researchers in this field employ, on the one hand, advanced experimental techniques, such as Scanning Tunneling Microscopy (STM) [1], High-Resolution Electron Energy Loss Spectroscopy (HREELS) [2], neutron or helium atom scattering [3], on the other hand, numerical modeling, including classical molecular dynamics simulations to unveil the fundamental principles governing surface processes [3]. Fully quantum mechanical simulations from first principle calculations are less common, however.

The aim of this thesis is to study the quantum dynamics of hydrogen atoms following adsorption onto a metal surface formed by palladium atoms. It is part of an exciting area of research within the broad discipline of quantum surface dynamics. This study focuses on understanding the quantum-scale interactions between hydrogen atoms, the simplest entities, and the palladium surface. The latter is of particular interest in this context due to its unique properties that make it an excellent catalyst for various chemical reactions. Understanding the quantum dynamics of hydrogen atoms on the palladium surface is of crucial importance also for applications such as hydrogen storage [4]. By understanding the quantum processes involved, scientists aim to improve the efficiency and performance of hydrogen-related applications, thereby contributing to the advancement of sustainable energy solutions.

We are particularly interested in situations where one or two hydrogen atoms are

adsorbed onto the Pd(111) surface; the two systems will be denoted in this thesis by H/Pd(111) and H_2/Pd(111), respectively. The dynamical properties of these systems depend mainly on the type of interatomic interactions between the adsorbate and the substrate atoms. When the interactions involve couplings of quantum mechanical nature, the dynamics of the adsorbates can be strongly impacted by quantum phenomena induced by these couplings, such as the tunneling effect [24]. Hydrogen atoms, given their mass, are strongly subject to this type of interaction. When this is the case, their motion on the metal surface is mainly subject to the laws of quantum mechanics. A complete understanding of their dynamics requires a fully quantum approach; we then speak of adsorbate quantum dynamics.

In this thesis, a study based on such an approach was carried out, by which non-classical effects likely to impact on the behavior of hydrogen atoms adsorbed on the palladium surface were unveiled. The system is then defined by its wave functions, and its temporal evolution is achieved by solving the time dependent Schrödinger equation. Interatomic potentials generally have complicated forms, making an exact analytical resolution of this equation unfeasible. Numerical methods are the main tools to obtain solutions that might describe the system realistically.

Dissipation in general, and friction in particular, result from the interaction of the particle, in this case the hydrogen atom, with the whole plethora of particles surrounding it, among which we may count other hydrogen atoms on the substrate, but also the moving substrate atoms or the surrounding electrons. Due to the size of the linear space containing all the states of the surrounding environment, the direct theoretical treatment by obtaining a solution for the many body wave function from the Schrödinger equation is practically impossible. This thesis is part of the research project "Quantum Dynamics of the Diffusion of Adsorbates (QDDA)", financed by the Agence National de la Recherche (ANR). One aspect of that project is the development of practical methods to tackle the effect of dissipation, out of which two publications emerged in connection with the present work [5, 6]. Currently these methods are being implemented. Yet, no results have been obtained so far and we therefore refrain to report on this part of the QDDA project here. The effects of dissipation and friction are not considered in the core of this study, the main focus of which are the quantum mechanical aspects of the motion of the hydrogen atoms.

A large part of this work is related to the study of the stationary states and energies of the hydrogen atoms, when they are adsorbed on the palladium surface. This study is crucial to the project. Dyhydrogen adsorbs on palladium dissociativelly. Within the aforementioned approximations, stationary states are the vibrational states of the adsorbates on the multi-dimensional potential energy surface (PES), which includes frustrated translations and hindered rotations of the diatomic species. Vibrational states are associated with the quantized vibrational motions of atoms within a molecule or in a crystal lattice. Vibrational eigenstates reveal several significant effects of the quantum dynamics, including tunneling, quantum entanglement, zero-point energy (ZPE) and particularly thermodynamic properties of quantum systems. Their quantized nature and interactions with other quantum states make them fundamental to understand and to predict the behavior of adsorbed hydrogen atoms at the quantum scale. In particular, we were able to show in this study the presence of tunneling between and Fermi resonance coupling [7] of localized vibrational modes of the system. Several time dependent dynamical simulations have subsequently been carried out, highlighting the major impact of these effects on the dynamics of hydrogen atoms at this surface.

Surface diffusion, on the other hand, is a field of study that focuses on how particles, in particular atoms and molecules, interact and diffuse at the surface of materials. This discipline is crucial for our understanding of the processes that occur at the surface of materials, which has significant implications in fields such as catalysis, thin film growth, surface chemistry, nanotechnology and many others. At the atomistic scale, particles must overcome energy barriers to move along the surface. These barriers are the result of the interactions between the adsorbed particles and the surface atoms, i.e. the topography of the PES. While in classical mechanics diffusion is the result of a collective behaviour of many particles described by their individual random trajectories in configuration space, in quantum mechanics particles are described by their wave functions, the distribution of which in configuration space is generally delocalized to a high degree and the physical interpretation of which contains fundamental elements of stochasticity. Consequently the quantum picture of a particle moving independently of other particles in configuration space inherently reflects diffusion of a different type, perhaps, than diffusion in classical mechanical

understanding of the term. The latter could be inferred from the many-body wave function of randomly interacting particles and we might conjecture that these effects would just be added to the effects already caused by the wave function of a single particle on time scales when many-body interactions become important.

To study surface diffusion, scientists use experimental techniques such as helium-3 spin-echo experiments [3] to extract diffusion coefficients. However, to extract these coefficients from these measured data, and even to deduce from them on the topography of the PES of catalytic surfaces, many intermediate modeling steps have to be carried out. The experimental results from the helium-3 spin-echo experiments rely on the evaluation of the dynamical structure factor (DSF), first introduced by van Hove [8], and its Fourier-transform, the intermediate scattering function (ISF). Rather than determining the diffusion coefficient directly, research is now concentrated on the evaluation and interpretation of the directly observable DSF and ISF, as clearly described in ref. [3].

The importance of the quantum nature of the dynamics underlying the diffusion motion was underlined many times and also in published work [9, 10, 11, 12, 13].. A detailed assessment of the pure quantum approach to calculate the observables was not made before results on the DSF were obtained from first principle calculations [10]. However, several questions have remained open since then, among which one major questions emerge: How do we evaluate theoretically the directly observed intermediate scattering function (ISF) from a pure quantum dynamical calculation? A new method to calculate the ISF is an integral part of the QDDA project proposal [14] out of which resulted the present thesis project. It relies on a fully quantum formulation based on a stochastic approach.

In the following, we present some general aspects of the studies that have been covered in this thesis.

Theory & methods

The systems studied being represented by their wave functions, the dynamics are carried out by means of the time-dependent Schrödinger equation. The exact an-

alytical solution of this equation is not possible for the studied systems. We have therefore used methods based on a numerical approach to solve this equation.

The Multi-Configuration Time-dependent Hartree (MCTDH) [15, 16] method was used for the numerical resolution of the time-dependent Schrödinger equation. The program allows to one treat a wide range of problems in quantum molecular dynamics including those with large dimension. The power of this method comes from the multi-configuration compact treatment of the wave function using a set of a time-dependent vectors called single particle function (SPF). For a problem with f degrees of freedom (DOF), the decomposition of the system's wave function in this basis is as follows

$$\Psi(Q_1,..,Q_f,t) = \sum_{i_1}^{n_1}...\sum_{i_f}^{n_f} A_{i_1,...,i_f}(t) \prod_{\kappa=1}^{f} \varphi_{i_\kappa}^{(\kappa)}(Q_\kappa,t) \tag{5}$$

With $\kappa = \{1,..,f\}$, $\varphi_{i_\kappa}^{(\kappa)}(Q_\kappa,t)$ is the i_κ-th SPF used to describe the DOF Q_κ, n_κ are the number of SPF used for each DOF and $A_{i_1,...,i_f}(t)$ represent the time-dependent expansion coefficients of the wave function in the SPF basis.

A similar decomposition to that used for the wave function is required for the set of operators used in MCTDH calculations, in particular the system Hamiltonian. The kinetic energy operator is generally suitable for this form. For interatomic potentials, however, the associated operators do not allow analytical decomposition of this form in most cases. MCTDH includes a module called potfit which allows to represent the potential numerically with the required form for MCTDH.

To propagate the wave function of a system initially prepared in a state Ψ_0, an SPF basis and an A-vector are initially constructed so as to reproduce Ψ_0 in the form suited to MCTDH. As the SPF and the A-vector are time-dependent, they are both propagated in time following the Dirac-Frenkel variational principle [17, 18]. The variational calculation leads to the MCTDH equations of motion given by :

$$\mathrm{i}\dot{A}_I = \sum_{I'} \langle\varphi_I|\hat{H}|\varphi_{I'}\rangle\, A_{I'} \tag{6}$$

$$\mathrm{i}\dot{\boldsymbol{\varphi}}^{(\kappa)} = (\hat{1} - \hat{P}^{(\kappa)})(\boldsymbol{\rho}^{(\kappa)})^{-1} \langle \boldsymbol{H} \rangle^{(\kappa)} \boldsymbol{\varphi}^{(\kappa)} \tag{7}$$

$\boldsymbol{\varphi}^{(\kappa)}$ is a vector composed of the n_κ SPF used for the DOF Q_κ. The operator $(1 - \hat{P}^{(\kappa)})$ ensures that the time derivative of the SPF is orthogonal to the space

spanned by the functions. $\boldsymbol{\rho}^{(\kappa)}$ and $\boldsymbol{H}^{(\kappa)}$ represent the single-particle density matrix and mean-field matrix respectively [15].

For solving the time-independent Schrödinger equation, we used the block improved-relaxation method which is implemented in MCTDH [19, 20, 21]. This approach is based on the idea that if we propagate a state with a Hamiltonian in negative imaginary time, then it will converge to the lowest-energy eigenstate of the Hamiltonian used. The block version of this method allows to relax simultaneously several states to eigenstates of the system. This method is not only faster in terms of computational time than single-state relaxation, it is also crucial for dealing with problems with degenerate eigenstates, as is the case in this study.

The choice of using the MCTDH approach is based on its ability to handle systems requiring relatively large bases of mathematical functions for their descriptions. Although the systems studied in this thesis do not possess very high dimensionality, the calculations of the vibrational eigenstates and quantum dynamics carried out in this study presented a real challenge for numerical computation, indeed. The interatomic interactions between hydrogen atoms and the substrate atoms are of a very complex nature. The duality between the strong correlation involving the internal and external degrees of freedom of each hydrogen atom renders the calculation of the time dependent and time independent dynamics very costly. The choice of 'good' basis vectors with mode combinations suitable for this type of interaction was essential for accomplishment of the calculations. The long-range interactions between the hydrogen atoms mean that large periodic calculation cells are required to model the system correctly, necessitating very large primitive bases. This makes the study of the dynamics of these systems on the picosecond time scale extremely costly numerically, given the time step needed to guarantee accurate calculations. The use of MCTDH enabled us to reduce the numerical effort while maintaining a physically sound description of the system.

Potential energy surfaces analysis

We perform our calculations within the Born-Oppenheimer approximation in which the DOFs of electrons and those of nuclei are decoupled, the nuclei evolve then in a

PES representing the interactions between the components of the system. The PES used in this work was developed by W.Dong et al. [22]. It was constructed within the the ground electronic state of the system. The authors have provided an analytical formulation of the potential using a some fit models [23]. In this study, the palladium atoms are considered to be fixed in their equilibrium position, and the only DOFs of the PES are those of the hydrogen atoms. The PES is therefore defined by a three-dimensional function in the case of H/Pd(111) and a six-dimensional function in the case of H_2/Pd(111).

Presentation of the elementary cell

In order to simulate an infinite surface in our calculations, a periodic approach was adopted which includes an elementary cell given by a slab of five Pd layers where each one contains 3×3 Pd atoms. The vacuum space corresponds to five Pd(111) layers. We will refer to this as "(3×3)-grid". The elementary cell used in our calculations is the same as the one used by the authors to develop the PES. Figure 5 shows a scheme of this grid showing only the surface plane (solid line) and the one below (dashed line).

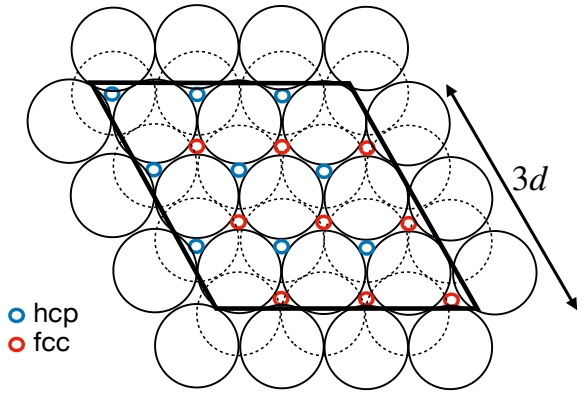

Figure 5: (3×3)-grid used for periodic calculations.

This grid contains 9 equivalent fcc sites and 9 equivalent hcp sites. The latter correspond to the most stable adsorption sites at the surface level. The spatial periodicity is applied following the twisted vectors $\boldsymbol{x_t}$ and $\boldsymbol{y_t}$ with $\alpha = (\widehat{\boldsymbol{x_t}, \boldsymbol{y_t}}) = 120°$ as shown in figure 6.

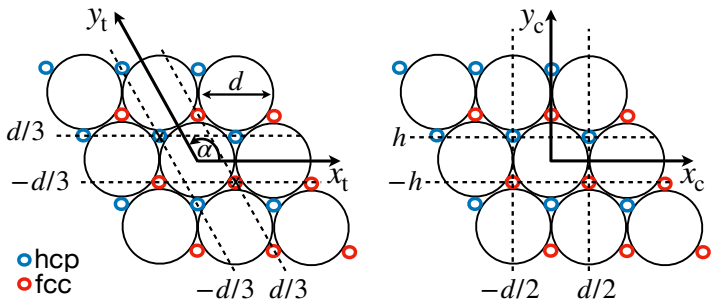

Figure 6: Twisted and Cartesian coordinates used for the (3×3)-grid. $d = 2.75$Å.

We define therefore a non-orthogonal basis set $(\boldsymbol{x_t},\boldsymbol{y_t},\boldsymbol{z_t})$ where the origin is located in the center of the Pd atom located in the middle of the topmost layer of the elementary cell. The transformation between the two systems coordinate is given by :

$$\begin{cases} x_t = x_c + \dfrac{1}{\sqrt{3}} y_c \\ y_t = \dfrac{2}{\sqrt{3}} y_c \\ z_t = z_c \end{cases} \tag{8}$$

Both coordinate systems are used in this work depending on the nature of the performed task. In the following, we will refer to Cartesian coordinates as (x,y,z).

H/Pd(111) PES

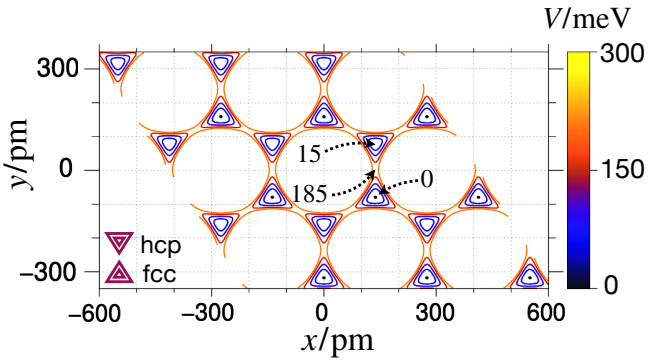

Figure 7: Two-dimensional section of the PES in the Cartesian coordinates (x, y) with $z = 90$ pm.

A two-dimensional section of the PES in the Cartesian coordinates of the H/Pd(111) system is shown in figure 7. It illustrates the structure of the potential perceived by

the hydrogen atom as it moves in a plane parallel to the substrate. This allows to visualize the structure of the various potential wells located at this plane level.

Equipotential energy lines ranging from 0 to 300 meV are shown in the figure. One sees that all potential wells are located at the fcc and hcp sites of the grid. They have the shape of up-pointing or down-pointing triangles for the fcc and hcp sites respectively, which gives the potential a local $\boldsymbol{C}_{3v}$ symmetry. The global minima are shifted to the zero reference energy value, they are reached when the hydrogen atom is located at fcc sites. The energy of the system when the hydrogen atom is located in an hcp site is around 15 meV for z=90 pm. The potential wells located at the hcp sites corresponds then to the local minima of the potential. The (3×3)-grid then contains 18 potential wells including 9 equivalents of each type. Potential barriers that separate the potential wells at $z = 90$ pm are all equivalent and of finite size with a height of 185 meV.

H_2/Pd(111) PES

The minima of the H_2/Pd(111) PES are reached when both hydrogen atoms occupy the fcc or hcp sites. In the following we symbolize the fcc site with the capital letter A and the hcp site with the capital letter B. We can then distinguish between three situations:

- Both hydrogen atoms are located on fcc sites (AA).
- Both hydrogen atoms are located on hcp sites (BB).
- One hydrogen atom is located on a fcc site and the other on a hcp site (AB).

Table 2 gives the energies of all the different possible configurations with the associated "classical" degeneracy. "I" and "II" indices are used to refer to situations where the two atoms occupy first and second neighbor sites respectively. "NN" index (Nearest Neighbors) used in configuration (AB) corresponds to the situation where both atoms occupy the closest fcc and hcp sites. This configuration is not included in this study.

Configuration	$d_{\text{H-H}}/d$	E/meV	Degeneracy
$(\text{AA})_{\text{I}}$	1	2	54
$(\text{BB})_{\text{I}}$	1	19	54
$(\text{AB})_{\text{I}}$	$2/\sqrt{3}$	40	54
$(\text{AA})_{\text{II}}$	$\sqrt{3}$	69	18
$(\text{AB})_{\text{II}}$	$\sqrt{7/3}$	73	54
$(\text{BB})_{\text{II}}$	$\sqrt{3}$	101	18
$(\text{AB})_{\text{NN}}$	$1/\sqrt{3}$	359	54

Table 2: Energies and classical degeneracy of all possible types of configurations of the dissociative H_2 system on the Pd surface. $d \approx 275$ pm is the distance between two neighboring Pd atoms and $d_{\text{H}-\text{H}}$ represent the distance between the two H atoms in each configuration. $z_1 = z_2 = 87$ pm for all these configurations[a].

[a]The overall PES minimum is reached when the two hydrogen atoms are out of the crystallographic position $(\text{AA})_{\text{I}}$.

Figure 8 shows a two-dimensional representation of the system's PES when one hydrogen atom is fixed to a fcc site (figure 8a) or to a hcp site (figure 8b), while the second moves in a plane parallel to the substrate. This representation illustrates the different types of configuration given in table (ref).

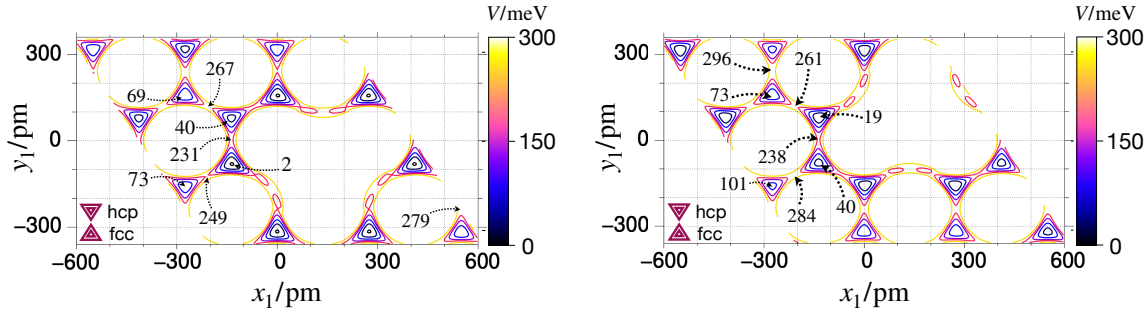

(a) (b)

Figure 8: Two dimensional sections of the potential energy surface when one of the two hydrogen atoms is fixed to an fcc site (8a) or hcp site (8b), while the second one moves in a plane parallel to the substrate given by $z_1 = 87$ pm. The equipotential lines ranging from 0 to 300 meV are represented in the figure.

Results & discussions

The theoretical study of the vibrational spectroscopy carried out in this thesis has provided a powerful means to understand on one hand, the structure of the vibrational eigenstates of one and two hydrogen atoms adsorbed on the palladium Pd(111) surface, on the other hand, this understanding allows us to rationalize the intricate quantum dynamical behaviour of these atoms on the surface. the following points summarize the key findings and implications of this research:

- The theoretical study of the vibrational spectroscopy of a single hydrogen atom adsorbed on the palladium surface revealed the presence of tunneling affecting all excited vibrational states. The latter manifested itself in a variety of ways across different potential barriers, leading to multiple splittings of several energy levels into sub-levels with relative gaps ranging from 1 meV to 8 meV.

  The study also confirmed the existence of Fermi resonance between local vibrational mode of single hydrogen atoms where a state with a single quantum of vibrational excitation perpendicular to the substrate strongly couples with a state carrying two quanta of vibrational excitation parallel to the substrate. The interaction between these two vibrational states results in the formation of Fermi pairs of stationary states possessing vibrational excitations perpendicular and parallel to the substrate simultaneously.

- The theoretical study of the vibrational spectroscopy of H_2/Pd(111) has shown that in situations where the two hydrogen atoms occupy neighboring adsorption sites of the same type, excitation of the system systematically manifests itself on both atoms. The latter then adopt concerted modes of vibration in phase and out-of-phase, thus demonstrating the presence of a strong correlation between the two atoms. In cases where the latter occupy sites of different types, the vibrational excitations were observed only on one of the two atoms, indicating a weaker correlation in this type of configuration.

  In both cases, the presence of a second hydrogen atom in the vicinity significantly changes the spectrum of the system. In particular, we found that

the potential barriers separating the different sites are significant, leading to a much less pronounced tunneling effect than that observed on the isolated hydrogen atom.

The Fermi resonance, as observed on an isolated hydrogen atom remains locally present on each atom despite the strong interactions between them when they occupy neighboring sites of the same type. This also shows the persistence of the intensity of local interactions between the internal vibrational modes of each hydrogen atom.

- The integration of quantum dynamics in this study has enabled us to gain a deeper understanding of the quantum processes underlying the vibrational eigenstate structure of the systems. We considered several numerical simulations highlighting the manifestation of tunneling and Fermi resonance in the dynamical behavior of hydrogen atoms on the palladium surface. Three major findings emerged from these studies:
  - The dynamics of hydrogen atoms involving a translational motion parallel to the substrate toward other adsorption sites on the surface following excitation is governed mainly by tunneling through potential barriers. This is much more important in the case of an isolated hydrogen atom.
  - Fermi resonance as predicted in this study, couples the perpendicular and in-plane breathing motion. When a hydrogen atom is excited in a mode perpendicular to the substrate, the vibrational excitation alternates in time between parallel and perpendicular modes. The quasi-periodicity of a quantum nature observed between theses two vibrations is directly related to the energy gap between the Fermi pair states within the system.
  - The excitation of a hydrogen atom leads to a systematic transfer of energy to the neighboring hydrogen atom on the time scale of a few hundredths of femtoseconds, if the latter occupies a neighboring site of the same type. The transfer time of this energy is directly related to the energies of the vibrational states corresponding to the same type of excitation.
- The method for the calculation of the intermediate scattering function (ISF)

used in this thesis enables to directly link experimental observations in spin-echo experiments to the quantum mechanical view of diffusion. The preliminary study we have carried out in this project represents a first step towards understanding these mechanisms. Further work is planned to extract scattering coefficients from numerical simulations, while accurately describing all the mechanisms taking place on the femtosecond scale.

Outlook

The knowledge gained from this thesis opens up new opportunities for future research. To name but a few:

- the evaluation of the impact of dissipation and friction; three main sources can be targeted, in this respect, namely the interaction between more than two adsorbed hydrogen atoms, the interaction with moving palladium atoms (phonon-couplings), and the interactions with the surrounding electrons from the break-down of the Born-Oppenheimer approximation (couplings to electron-hole pairs);
- a precise theoretical assessment of the complicated HREELS spectrum of hydrogen on palladium; ideas have been explored in this thesis, results are promising but absent in this manuscript, as they need further investigation;
- the study of the para and ortho modifications of adsorbed H_2, and the subtle mechanism of their interconversion upon adsorption via inclusion of the weak hyperfine coupling; to this end, however, the numerical accuracy will need to be increased by at least two orders.

Ultimately, this research highlights the profound interconnection between vibrational spectroscopy and quantum dynamics, two fields that mutually enrich each other to provide a deeper understanding of molecular phenomena at the interface between solid materials and their environment.

Chapter 1

Introduction

Quantum surface dynamics is a fascinating branch of scientific research that investigates the complex quantum mechanical behavior of atoms and molecules on the quantum scale at the surface of materials. This discipline interconnects the principles of quantum mechanics, which studies particles on the atomic and subatomic scales, with surface science, which examines the properties and interactions of atoms and molecules on the surfaces of solids and liquids. Researchers in this field employ, on the one hand, advanced experimental techniques, such as Scanning Tunneling Microscopy (STM) [1], High-Resolution Electron Energy Loss Spectroscopy (HREELS) [2], neutron or helium atom scattering [3], on the other hand, numerical modeling, including classical molecular dynamics simulations to unveil the fundamental principles governing surface processes [3]. Fully quantum mechanical simulations from first principle calculations are less common, however.

The aim of this thesis is to study the quantum dynamics of hydrogen atoms following adsorption onto a metal surface formed by palladium atoms. It is part of an exciting area of research within the broad discipline of quantum surface dynamics. This study focuses on understanding the quantum-scale interactions between hydrogen atoms, the simplest entities, and the palladium surface. The latter is of particular interest in this context due to its unique properties that make it an excellent catalyst for various chemical reactions. Understanding the quantum dynamics of hydrogen atoms on the palladium surface is of crucial importance also for applications such as hydrogen storage [4]. The latter application is in particular relevant for the devel-

opment of clean energy technologies such as hydrogen fuel cells. By understanding the quantum processes involved, scientists aim to improve the efficiency and performance of hydrogen-related applications, thereby contributing to the advancement of sustainable energy solutions.

We are particularly interested in situations where one or two hydrogen atoms are adsorbed onto the Pd(111) surface; the two systems will be denoted in this thesis by H/Pd(111) and H_2/Pd(111) respectively. The dynamical properties of these systems depend mainly on the type of interatomic interactions between the adsorbate and the substrate atoms. When the interactions involve couplings of quantum mechanical nature, the dynamics of the adsorbates can be strongly impacted by quantum phenomena induced by these couplings, such as the tunneling effect [24]. Hydrogen atoms, given their small mass, are strongly subject to this type of interaction. When this is the case, their motion on the metal surface is mainly subject to the laws of quantum mechanics. A complete understanding of their dynamics requires a fully quantum approach; we then speak of adsorbate quantum dynamics.

In this thesis, a study based on such an approach was carried out, by which non-classical effects likely to impact the behavior of hydrogen atoms adsorbed on the palladium surface were unveiled. The system is then defined by its wave functions, and its temporal evolution is achieved by solving the time dependent Schrödinger equation. Interatomic potentials generally have complicated forms, making an exact analytical resolution of this equation unfeasible. Numerical methods are the main tools to obtain solutions that might describe the system realistically.

Researchers use advanced theoretical models and numerical simulations to predict and explain the behaviour of adsorbates at surface level. These models help to elucidate the quantum-scale processes involved in the interactions. The results obtained in this thesis are based mainly on numerical simulations. These were carried out using the Multi Configurational Time-Dependant Hartree (MCTDH) method [16]. The choice of using this method is based on its ability to handle systems requiring relatively large bases of mathematical functions for their descriptions. Although the systems studied here do not possess very high dimensionality, the long-range interactions found to exist between hydrogen atoms mean that a sufficiently large

surface area is required to describe the system's dynamics correctly, resulting in an extended surface treatment and higher numerical cost. MCTDH enables us to reduce the numerical effort while maintaining a physically sound description of the system.

This work is based on the Born-Oppenheimer approximation. The interactions between the system's components are represented via a potential energy surface (PES) elaborated by W. Dong *et al* [22, 23] for the H_2/Pd(111) system. Several tests have already been carried out on this surface by these authors, demonstrating its reliability and accuracy. The palladium atoms are considered to be fixed on their crystallographic equilibrium positions. The PES is then three-dimensional in the case of H/Pd(111) and six-dimensional in the case of H_2/Pd(111). It depends on the three spatial coordinates of each hydrogen atom.

Dissipation in general, and friction in particular, result from the interaction of the particle, in this case the hydrogen atom, with the whole plethora of particles surrounding it, among which we may count other hydrogen atoms on the substrate, but also the moving substrate atoms or the surrounding electrons. Due to the size of the linear space containing all the states of the surrounding environment, the direct theoretical treatment by obtaining a solution for the many body wave function from the Schrödinger equation is practically impossible. This thesis is part of the research project "Quantum Dynamics of the Diffusion of Adsorbates (QDDA)", financed by the Agence National de la Recherche (ANR). One aspect of that project is the development of practical methods to tackle the effect of dissipation, out of which two publications emerged in connection with the present work [5, 6]. Currently these methods are being implemented. Yet, no results have been obtained so far and we therefore refrain to report on this part of the QDDA project here. The effects of dissipation and friction are not considered in the core of this study, the main focus of which are the quantum mechanical aspects of the motion of the hydrogen atoms.

A large part of this work is related to the study of the stationary states and energies of the hydrogen atoms, when they are adsorbed on the palladium surface. This study is crucial to the project. Dihydrogen adsorbs on palladium dissociative. Within the aforementioned approximations, stationary states are the vibrational states of the

adsorbates on the multi-dimensional PES, which includes frustrated translations and hindered rotations of the diatomic species. Vibrational states are associated with the quantized vibrational motions of atoms within a molecule or in a crystal lattice. Vibrational eigenstates reveal several significant effects of the quantum dynamics, including tunneling, quantum entanglement, zero-point energy (ZPE) and particularly thermodynamic properties of quantum systems. Their quantized nature and interactions with other quantum states make them fundamental to understand and to predict the behavior of adsorbed hydrogen atoms on the quantum scale. In particular, we were able to show in this study the presence of tunneling between and Fermi resonance coupling [7] of localized vibrational modes of the system. Several time dependent dynamical simulations have subsequently been carried out, highlighting the major impact of these effects on the dynamics of hydrogen atoms at this surface.

Surface diffusion, on the other hand, is a field of study that focuses on how particles, in particular atoms and molecules, interact and diffuse at the surface of materials. This discipline is crucial for our understanding of the processes that occur at the surface of materials, which has significant implications in fields such as catalysis, thin film growth, surface chemistry, nanotechnology and many others. At the atomistic scale, particles must overcome energy barriers to move along the surface. These barriers are the result of the interactions between the adsorbed particles and the surface atoms, i.e. the topography of the PES. While in classical mechanics diffusion is the result of a collective behaviour of many particles described by their individual random trajectories in configuration space, in quantum mechanics particles are described by their wave functions, the distribution of which in configuration space is generally delocalized to a high degree and the physical interpretation of which contains fundamental elements of stochasticity. Consequently the quantum picture of a particle moving independently of other particles in configuration space inherently reflects diffusion of a different type, perhaps, than diffusion in classical mechanical understanding of the term. The latter could be inferred from the many-body wave function of randomly interacting particles and we might conjecture that these effects would just be added to the effects already caused by the wave function of a single particle on time scales when many-body interactions become important.

To study surface diffusion, scientists use experimental techniques such as helium-3 spin-echo experiments [3] to extract diffusion coefficients. However, to extract diffusion coefficients from these measured data, and even to deduce from them on the topography of the PES of catalytic surfaces, many intermediate modeling steps have to be carried out. The experimental results from the helium-3 spin-echo experiments rely on the evaluation of the dynamical structure factor (DSF), first introduced by van Hove [8], and its Fourier-transform, the intermediate scattering function (ISF). Rather than determining the diffusion coefficient directly, research is now concentrated on the evaluation and interpretation of the directly observable DSF and ISF, as clearly described in ref. [3].

The importance of the quantum nature of the dynamics underlying the diffusion motion was underlined many times and also in published work [10, 13, 11, 12, 9]. A detailed assessment of the pure quantum approach to calculate the observables was not made before results on the DSF were obtained from first principle calculations [10]. However, several questions have remained open since then, among which one major question emerges: How do we evaluate theoretically the directly observed intermediate scattering function (ISF) from a pure quantum dynamical calculation? A new method to calculate the ISF is an integral part of the QDDA project proposal [14] out of which resulted the present thesis project. It relies on a fully quantum formulation based on a stochastic approach. This approach will be presented and discussed in this thesis report and preliminary results will be addressed in comparison with results from spin echo experiments.

In a previous thesis work was achieved on this system [25], problems were noted in the treatment of the H_2/Pd(111) system, which arose from the construction of the PES representation of the system. The current work is based on a new PES more suited to our study, built by the same authors. This thesis is to some extent a continuation of that project.

This manuscript is organized as follows: In Chapter 2, a general presentation of the theoretical framework used in this project will be given. Some aspects of quantum molecular dynamics will be discussed, in particular the approximations made in this work for solving the Schrödinger equation. We will also discuss the numerical

methods used to solve it, from the standard methods to the MCTDH method. In Chapter 3, the analysis of the PES of the H/Pd(111) and H_2/Pd(111) systems will be given. We will first recall the geometric parameters of the substrate's crystallographic structure, then show some important aspects of the structure of the PES for the two systems, particularly around the potential wells and barriers. In chapter 4, the results of the study of the vibrational stationary states of these two systems will be presented. A detailed description of the latter will be given, together with a discussion of the quantum effects observed at the level of eigenstates. In chapter 5, we will present several simulations of wave function propagation of the prepared system in various states; in particular, we will highlight the consequences of certain quantum effects on the dynamics of the hydrogen atoms. In Chapter 6, we discuss the method proposed in this project to calculate the ISF, followed by a preliminary study of this function on the H/Pd(111) system. Chapter 7 concludes this work.

Chapter 2

Theory & methods

A theoretical study has been carried out in this work on the dynamics of adsorbates on metallic surfaces based on a fully quantum approach. The systems studied being represented by their wave functions, the dynamics are carried out by means of the time-dependent Schrödinger equation. The exact analytical solution of this equation is not possible for the studied systems. We have therefore used methods based on a numerical approach to solve this equation. The numerical tools commonly used in quantum molecular dynamics are based on several theoretical approximations. In this chapter, we highlight some general aspects of the methods we have used, in particular those to which we will often refer in this work.

2.1 Molecular Hamiltonian Operator

2.1.1 General aspects

In this thesis project, a time-dependent and time-independent study was carried out mainly on the H/Pd(111) and H_2/Pd(111) systems. These two systems do not interact with an external electromagnetic field in the framework of this study, we therefore treat them as an isolated collection of interacting nuclei and electrons. The time-independent molecular Hamiltonian of such systems can be defined by the (non-relativistic) effective Coulomb Hamiltonian given by the following formula [20]:

$$\hat{H}^{mol}(\boldsymbol{r}, \boldsymbol{R}) = \hat{V}^{e-e}(\boldsymbol{r}) + \hat{V}^{n-n}(\boldsymbol{R}) + \hat{V}^{n-e}(\boldsymbol{r}, \boldsymbol{R}) + \hat{T}^{n}(\boldsymbol{R}) + \hat{T}^{e}(\boldsymbol{r}) \tag{2.1}$$

Where $\boldsymbol{R} = \{\boldsymbol{R}_\alpha\}_{1\leq\alpha\leq N}$ and $\boldsymbol{r} = \{\boldsymbol{r}_i\}_{1\leq i\leq n}$ define the set of nuclei and electrons position vectors respectively. The different terms appearing in the Hamiltonian correspond to :

- $\hat{V}^{e-e}(\boldsymbol{r})$ is the electrostatic repulsion potential operator between the electrons in the system, with e the electron charge. In the SI, it is given by:

$$\hat{V}^{e-e}(\boldsymbol{r}) = \sum_{i<j}^{n} \frac{e^2}{4\pi\epsilon_0 ||\boldsymbol{r}_i - \boldsymbol{r}_j||} \tag{2.2}$$

  ϵ_0 is the dielectric constant, i and j are electron indices and e is the elementary charge.

- $\hat{V}^{n-n}(\boldsymbol{R})$ is the electrostatic repulsion potential operator between the system's nuclei. It is given by the formula :

$$\hat{V}^{n-n}(\boldsymbol{r}) = \sum_{\alpha<\beta}^{N} \frac{Z_\alpha Z_\beta e^2}{4\pi\epsilon_0 ||\boldsymbol{R}_\alpha - \boldsymbol{R}_\beta||} \tag{2.3}$$

  Z_α and Z_β are the atomic numbers of the nuclei α and β respectively.

- $\hat{V}^{n-e}(\boldsymbol{r})$: is the electrostatic attraction potential operator between nuclei and electrons. It is defined analogously to the previous formulas by :

$$\hat{V}^{n-e}(\boldsymbol{r}, \boldsymbol{R}) = -\sum_{\alpha}^{N}\sum_{i}^{n} \frac{Z_\alpha e^2}{4\pi\epsilon_0 ||\boldsymbol{R}_\alpha - \boldsymbol{r}_i||} \tag{2.4}$$

- $\hat{T}^n(\boldsymbol{R})$ represents the kinetic energy operator of nuclei. It is given by :

$$\hat{T}^n(\boldsymbol{R}) = -\sum_{\alpha}^{N} \frac{\hbar^2}{2M_\alpha} \left(\frac{\partial^2}{\partial X_\alpha^2} + \frac{\partial^2}{\partial Y_\alpha^2} + \frac{\partial^2}{\partial Z_\alpha^2} \right) \tag{2.5}$$

  $\hbar = h/2\pi$ is the reduced Planck constant, M_α and $(X_\alpha, Y_\alpha, Z_\alpha)$ are the mass and the Cartesian coordinates of the nucleus α.

- Finally $\hat{T}^e(\boldsymbol{R})$ represents the electron kinetic energy operator. It is given by :

$$\hat{T}^e(\boldsymbol{r}) = -\sum_{i}^{n} \frac{\hbar^2}{2m_\mathrm{e}} \left(\frac{\partial^2}{\partial x_i^2} + \frac{\partial^2}{\partial y_i^2} + \frac{\partial^2}{\partial z_i^2} \right) \tag{2.6}$$

  With m_e and (x_i, y_i, z_i) the electron mass and the coordinates of the electron i respectively.

This molecular Hamiltonian includes the electrostatic interactions between the various components of the system, but does not consider the magnetic forces, since we are working in a non-relativistic regime i.e. the magnetic field created by charge displacement remains negligible. Under this approach, the time-dependent and time-independent Schrödinger equations can be written as follows:

$$\hat{H}^{mol}(\boldsymbol{r},\boldsymbol{R})\Psi^{mol}(\boldsymbol{r},\boldsymbol{R},t) = \mathrm{i}\hbar\frac{\partial\Psi^{mol}(\boldsymbol{r},\boldsymbol{R},t)}{\partial t} \tag{2.7}$$

$$\hat{H}^{mol}(\boldsymbol{r},\boldsymbol{R})\Psi_l^{mol}(\boldsymbol{r},\boldsymbol{R}) = E_l\Psi_l^{mol}(\boldsymbol{r},\boldsymbol{R}) \tag{2.8}$$

$\Psi^{mol}(\boldsymbol{r},\boldsymbol{R},t)$ represents the system's time-dependent molecular wave function, E_l and $\Psi_l^{mol}(\boldsymbol{r},\boldsymbol{R})$ represent the eigenenergies and the associated eigenfunctions of $\hat{H}^{mol}(\boldsymbol{r},\boldsymbol{R})$. The resolution of these equations in the current state is extremely complex and several approximations are generally needed to make it possible. In the remainder of this section, we will give the various approximations that were assumed and used in this work.

2.1.2 Approximations

The aim of the approximations that will be presented in this section is to decouple the motion of the nuclei from that of the electrons, in order to obtain a factorized form of the wave function that is more computationally manageable.
The first step is to separate the molecular Hamiltonian (2.1) into two terms:

$$\hat{H}^{mol}(\boldsymbol{r},\boldsymbol{R}) = \hat{T}^{n}(\boldsymbol{R}) + \hat{H}^{el}(\boldsymbol{r};\boldsymbol{R}) \tag{2.9}$$

With $\hat{H}^{el}(\boldsymbol{r};\boldsymbol{R})$ the electronic Hamiltonian defined by:

$$\hat{H}^{el}(\boldsymbol{r};\boldsymbol{R}) = \hat{V}^{e-e}(\boldsymbol{r}) + \hat{V}^{n-n}(\boldsymbol{R}) + \hat{V}^{n-e}(\boldsymbol{r},\boldsymbol{R}) + \hat{T}^{e}(\boldsymbol{r}) \tag{2.10}$$

This Hamiltonian depends parametrically on the position of the nuclei, since the nuclear kinetic energy term $\hat{T}^{n}(\boldsymbol{R})$ has been discarded. This separation takes on a physical meaning when the motion of nuclei is considered very slow compared to that of electrons, given the mass difference between these two systems. Although this picture is based on a "classical" description of electrons and nuclei, it nonetheless serves to illustrate the origin of the will of separating the two motions.

Let's now consider two orthonormal basis sets composed of nuclear functions $\{\Phi^n_\lambda(\boldsymbol{R})\}$ and electronic functions $\{\Phi^e_m(\boldsymbol{r};\boldsymbol{R})\}$. The molecular wave function can be decomposed in this basis into the following sum of product form:

$$\Psi^{mol}(\boldsymbol{r},\boldsymbol{R},t) = \sum_m \sum_\lambda c_{m\lambda}(t)\Phi^n_\lambda(\boldsymbol{R})\Phi^e_m(\boldsymbol{r};\boldsymbol{R}) \tag{2.11}$$

With $c_{m\lambda}(t)$ the time-dependent components of this wave function in this basis. The electronic basis functions depend explicitly on the electron positions and parametrically on the nuclear positions.

If we consider :

$$\Psi_m(\boldsymbol{R},t) = \sum_\lambda c_{m\lambda}(t)\Phi^n_\lambda(\boldsymbol{R}) \tag{2.12}$$

The previous formula simplifies to :

$$\Psi^{mol}(\boldsymbol{r},\boldsymbol{R},t) = \sum_m \Psi_m(\boldsymbol{R},t)\Phi^e_m(\boldsymbol{r};\boldsymbol{R}) \tag{2.13}$$

The time dependence of the molecular wave function is now given through the nuclear wave functions $\Psi_m(\boldsymbol{R},t)$ associated with the electronic basis function $\Phi^e_m(\boldsymbol{r};\boldsymbol{R})$. Projecting the time-dependent Schrödinger equation into the electronic basis gives the following system of coupled differential equations:

$$\sum_m \left(\hat{T}^{nucl}_{nm}(\boldsymbol{R}) + \hat{H}^e_{nm}(\boldsymbol{R})\right)\Psi_m(\boldsymbol{R},t) = i\hbar\frac{\partial\Psi_n(\boldsymbol{R},t)}{\partial t} \tag{2.14}$$

With :

$$\hat{T}^{nucl}_{nm}(\boldsymbol{R}) = \langle\Phi^e_n;\boldsymbol{R}|\hat{T}^{nuc}(\boldsymbol{R})|\Phi^e_m;\boldsymbol{R}\rangle_{\boldsymbol{r}} \tag{2.15}$$

$$\hat{H}^e_{nm}(\boldsymbol{R}) = \langle\Phi^e_n;\boldsymbol{R}|\hat{H}^e(\boldsymbol{R})|\Phi^e_m;\boldsymbol{R}\rangle_{\boldsymbol{r}} \tag{2.16}$$

The differential equation (2.14) introduces coupling terms $T^{nucl}_{nm}(\boldsymbol{R})$ and $H^e_{nm}(\boldsymbol{R})$ between the system's electronic functions[1]. The couplings induced by the electronic Hamiltonian $H^e_{nm}(\boldsymbol{R})$ can be reduced if we work in an eigenbasis of the electronic states and which therefore verify the relation :

$$\hat{H}^e(\boldsymbol{r};\boldsymbol{R})\Phi^e_m(\boldsymbol{r};\boldsymbol{R}) = E^e_m(\boldsymbol{R})\Phi^e_m(\boldsymbol{r};\boldsymbol{R}) \tag{2.17}$$

[1]Dirac's notation $\langle|\rangle_{\boldsymbol{r}}$ indicates integration over electronic coordinates only.

The eigenstates of the electronic Hamiltonian are called adiabatic electronic states. In the following, we will denote them by $\Phi_m^{e,ad}(\boldsymbol{r};\boldsymbol{R})$. They form an orthonormal basis set which allows us to eliminate all off-diagonal terms of $\hat{H}^e(\boldsymbol{R})$ in this basis. Equations (2.16) and (2.14) then become :

$$\hat{H}^e_{nm}(\boldsymbol{R}) = \langle \Phi^e_n;\boldsymbol{R}|\hat{H}^e(\boldsymbol{R})|\Phi^e_m;\boldsymbol{R}\rangle_{\boldsymbol{r}} \equiv \delta_{nm}E^e_m(\boldsymbol{R}) \tag{2.18}$$

$$\sum_m \left(\hat{T}^{nucl}_{nm}(\boldsymbol{R}) + E^e_m(\boldsymbol{R})\right)\Psi_m(\boldsymbol{R},t) = i\hbar\frac{\partial\Psi_n(\boldsymbol{R},t)}{\partial t} \tag{2.19}$$

Here, the electronic energy $E^e_m(\boldsymbol{R})$ is a function of the nuclear coordinates only, and thus appears as a potential energy surface (PES) with respect to nuclei motion [26]. At this stage we have not yet used any approximations. The use of the adiabatic electron basis eliminates all coupling terms in the second term of differential equation (2.14). However, these equations are still coupled through the kinetic energy term of the nuclei. The coupling terms $\hat{T}^{nucl}_{nm}(\boldsymbol{R})$ can be decoupled under special conditions within the Born-Oppenheimer approximation. This approximation is based on the fact that, as mentioned above, the large mass difference between nuclei and electrons means that the motion of nuclei can be considered stationary compared to that of electrons, while electrons adapt almost instantaneously to the motion of nuclei. This results into neglecting the action of the kinetic energy operator of the nuclei $\hat{T}^{nuc}(\boldsymbol{R})$ on the electron basis function $\Phi^e_m(\boldsymbol{r};\boldsymbol{R})$. Equation (2.15) becomes :

$$\hat{T}^{nucl}_{nm}(\boldsymbol{R}) = \langle \Phi^e_n;\boldsymbol{R}|\hat{T}^{nuc}(\boldsymbol{R})|\Phi^e_m;\boldsymbol{R}\rangle_{\boldsymbol{r}} \approx \delta_{nm}\hat{T}^{nuc}(\boldsymbol{R}) \tag{2.20}$$

This allows us to write the system of equations (2.19) of each nuclear wave function $\Psi_m(\boldsymbol{R},t)$ with completely decoupled terms:

$$\left(\hat{T}^{nucl}(\boldsymbol{R}) + E^e_m(\boldsymbol{R})\right)\Psi_m(\boldsymbol{R},t) = i\hbar\frac{\partial\Psi_m(\boldsymbol{R},t)}{\partial t} \tag{2.21}$$

This equation ultimately reflects the fact that each nuclear wave function $\Psi_m(\boldsymbol{R},t)$ will evolve separately on an associated PES given by E^e_m. When the energies of the adiabatic electronic states of a system are very close $E^e_m(\boldsymbol{R}) \approx E^e_n(\boldsymbol{R})$, this approximation is no longer correct and one has to follow a different approach for representing the system's wave function [20].

To conclude this section, the Born-Oppenheimer approximation allows to neglect the electronic couplings within the nuclei kinetic energy operator when describing the total molecular wave function. When used in an adiabatic electronic basis set, it allows us a formulation of the Schrödinger equation with uncoupled terms[2], which makes the calculation much more manageable for the considered systems. This approximation will be assumed in the following.

2.2 Nuclear quantum dynamics

Nuclear dynamics are given by the time evolution of the nuclear wave function within PES corresponding to the different electronic adiabatic states of the system. The PES of H/Pd(111) and H_2/Pd(111) systems that are studied in this work was elaborated within the lowest adiabatic electronic state E_0^e [22, 23]. The Pd atoms are considered to be fixed at their equilibrium positions, only the degrees of freedom (DOFs) of the hydrogen atoms are taken into account in our calculations, a more detailed description is given in chapter 3. The problem is thus three-dimensional in the case of a single hydrogen atom, and six-dimensional in the case of two hydrogen atoms. The time-dependent Schrödinger equation reads :

$$\left(\hat{T}^{nucl}(x_i, y_i, z_i) + E_0^e(x_i, y_i, z_i)\right) \Psi_0(x_i, y_i, z_i, t) = i\hbar \frac{\partial \Psi_0(x_i, y_i, z_i, t)}{\partial t} \tag{2.22}$$

(x_i, y_i, z_i) represent the Cartesian coordinates of hydrogen $i = \{1; 2\}$. $\Psi_0(x_i, y_i, z_i, t)$ represent the wave function evolving in the lowest PES of the system. In the following, $\hat{T}^{nucl}$ is denoted by $\hat{T}$, E_0^e by E^e and Ψ_0 by Ψ. The kinetic energy operator in Cartesian coordinates takes the simple form given by :

$$\hat{T} = \sum_{i=1}^{N_H} \frac{1}{2m_p} \left(\frac{\partial^2}{\partial x_i^2} + \frac{\partial^2}{\partial y_i^2} + \frac{\partial^2}{\partial z_i^2} \right) \tag{2.23}$$

m_p is the proton mass and $N_H = \{1; 2\}$.

In this study, we worked in the twisted coordinate system (x_t, y_t, z_t) where $\boldsymbol{z}_t \equiv \boldsymbol{z}$ and $(\widehat{\boldsymbol{x}_t, \boldsymbol{y}_t}) = 120°$[3] (see equation 3.1). This is a non-Euclidean basis adapted

[2]The Born-Oppenheimer approximation applies also to the time-independent Schrödinger equation[20].

[3]The symbol $(\hat{.},\hat{.})$ represents the angle measure between two vectors.

to the periodicity of the potential. A more detailed description of this coordinate systems is given in section 3.1.2. The expression of the kinetic energy operator in those coordinate systems becomes :

$$\hat{T} = \sum_{i=1}^{N_H} \frac{2}{3m_p} \left(\frac{\partial^2}{\partial x_i^2} + \frac{\partial^2}{\partial y_i^2} + \frac{\partial}{\partial x_i} \frac{\partial}{\partial y_i} \right) - \sum_{i=1}^{N_H} \frac{1}{2m_p} \frac{\partial^2}{\partial z_i^2} \tag{2.24}$$

Determining the action of the kinetic energy operator on a given state is not difficult in the general case. The complexity of equation 2.22 therefore depends mainly on the type of the potential used. In the simplest cases, the resolution of the time-independent Schrödinger equation can be done analytically and allows to compute the eigenstates of the system. We can then build a complete eigenstates basis set in which the time evolution of the wave function simplifies to:

$$|\Psi(t)\rangle = \sum_k c_k(0) e^{-iE_k t/\hbar} |\varphi_k\rangle \tag{2.25}$$

The bra-ket notation was used to simplify notations. E_k and $|\varphi_k\rangle$ represent the eigenenergies and the associated eigenstates of the system. $c_k(0)$ are the coefficients of the initial wave function in this basis. In the general case, the potential term makes solving Schrödinger equations analytically infeasible. Numerical resolution becomes the only alternative for approaching the theoretically exact wavefunction solution. In the following, we will give a general introduction to the numerical approach, and then present the methods we have particularly used in this work.

2.3 Numerical methods

In this section, we present an introduction to the numerical methods used to solve the time-(in)dependent Schrödinger equation. A more detailed and complete description can be found in [27, 20]. we will start by introducing the general standard method.

2.3.1 Standard method

The wave function of a given system is defined by a quantum state that lives in an infinite-dimensional Hilbert space [28]. Numerical implementation of such a state is only possible if we consider a truncated basis of finite size. This basis should be large enough to cover all the quantum states that the system can reach during

simulation, and small enough to make numerical simulations feasible. The very first step is therefore to choose a suitable basis set for the calculations we wish to carry out. For simplicity's sake, let us assume that we are dealing with a three-dimensional system that depends on Cartesian coordinates (x, y, z).

$$\Psi(\boldsymbol{r}, t) = \Psi(x, y, z, t) \tag{2.26}$$

We can assign to each DOF an orthonormal basis set given by $\mathcal{B}_x = \{\phi_{i_x}^{(x)}\}_{1 \leq i_x \leq N_x}$, $\mathcal{B}_y = \{\phi_{i_y}^{(y)}\}_{1 \leq i_y \leq N_y}$ and $\mathcal{B}_z = \{\phi_{i_z}^{(z)}\}_{1 \leq i_z \leq N_z}$ with N_x, N_y and N_z the associated dimensions. The total basis called the primitive basis, is given by the tensor product $\mathcal{B} = \mathcal{B}_x \otimes \mathcal{B}_y \otimes \mathcal{B}_z$. The total wave function can therefore be decomposed as :

$$\Psi(x, y, z, t) = \sum_{i_x=1}^{N_x} \sum_{i_y=1}^{N_y} \sum_{i_z=1}^{N_z} A_{i_x, i_y, i_z}(t) \phi_{i_x}^{(x)}(x) \phi_{i_y}^{(y)}(y) \phi_{i_z}^{(z)}(z) \tag{2.27}$$

$A_{i_x, i_y, i_z}(t)$ represent the time-dependent expansion coefficients of the wave function in this basis. In the standard method, the basis vectors are not time-dependent, the time dependence of the wave function is therefore defined through its coefficients.

Numerical basis set

The choice of primitive basis should facilitate the evaluation of the matrix elements of the Hamiltonien. Commonly used primitive basis vectors are Disctrete Variable representation (DVR) and Finite Basis Representation (FBR) [29, 30]. Both of them are numerically complete if the number of vectors chosen is large enough for the problem under study. The choice of these functions depends on the nature of the DOFs they represent. We will give an example of two types of FBR function we have used in this project.

- Exponential FBR

$$\phi_{i_\kappa}^{(\kappa)}(\kappa) = 1/\sqrt{L_\kappa} \exp\left(\mathrm{j} 2\pi i_x \frac{\kappa - \kappa_0}{L_\kappa}\right) \tag{2.28}$$

- Sine FBR

$$\phi_{i_\kappa}^{(\kappa)}(\kappa) = \begin{cases} \sqrt{2/L_\kappa} \sin\left(i_\kappa \dfrac{(\kappa - \kappa_0)}{L_\kappa} \pi\right) & \text{for } \kappa_0 \leq \kappa \leq \kappa_0 + L_\kappa \\ 0 & \text{elsewhere} \end{cases} \tag{2.29}$$

$\kappa = \{x, y, z\}$, L_κ the grid length, j is the imaginary unit, N_κ is the total number of FBR functions used in the DOF κ and $-\frac{N_\kappa - 1}{2} \leq i_\kappa \leq \frac{N_\kappa - 1}{2}$ for exponential FBR (N_κ should be odd in this case) and $1 \leq i_\kappa \leq N_\kappa$ for sine FBR.

Exponential FBRs are adapted by construction to periodic DOFs, while sine FBRs represent the eigenfunctions of a particle in a box. They are therefore well suited to bounded DOF that cancel outside the grid. For example, we used sine-type FBR functions to describe the z coordinates of hydrogen atoms, since they are adsorbed at the surface and their z coordinates remain confined in space. Then exponential-type functions to describe the DOFs x and y which represent the lateral motion of these atoms at the surface and which require periodicity to simulate an infinite surface. FBR functions are analytical and continuous in space. They are generally stable by derivative and can therefore be seen as eigenstates of derivative operators such as kinetic energy. This makes the matrix representation of $\hat{T}$ diagonal and very easy to evaluate in this basis. But unlike the DVR basis, these functions have no particular advantage for evaluating the matrix elements of the potential operator.

One way of constructing DVR functions is to diagonalize the position operator in an FBR basis. The two bases are then related by a unitary transformation. Let's suppose we're working with N_κ FBR function to describe a κ mode defined on an interval $I_\kappa = [\kappa_{min}; \kappa_{\max}]$. By unitary transformation, we then obtain N_κ DVR to describe the same mode. Unlike FBR functions, DVR functions are discrete and highly localized around some points κ_{i_κ} uniformly spaced across I_κ with a distance $\Delta_\kappa = \frac{\kappa_{\max} - \kappa_{\min}}{N_\kappa + 1}$ such that $\kappa_{i_\kappa + 1} - \kappa_{i_\kappa} = \Delta_\kappa$, they are called grid points. Considering the example of sine DVR, one can obtain in this particular case the analytical formula of these functions from the sine FBR [20]. Using the same notations as in the previous example, and this time denoting the basis functions by $\{\chi_\kappa\}$, we obtain the analytical formulation of sine-DVR :

$$\chi_{i_\kappa}^{(\kappa)}(\kappa) = \frac{1}{2\sqrt{L_\kappa(N_\kappa + 1)}} \left\{ \frac{\sin\left((2N_\kappa + 1)\frac{\pi}{2}\frac{\kappa - \kappa_{i_\kappa}}{L_\kappa}\right)}{\sin\left(\frac{\pi}{2}\frac{\kappa - \kappa_{i_\kappa}}{L_\kappa}\right)} - \frac{\sin\left((2N_\kappa + 1)\frac{\pi}{2}\frac{\kappa + \kappa_{i_\kappa}}{L_\kappa}\right)}{\sin\left(\frac{\pi}{2}\frac{\kappa + \kappa_{i_\kappa}}{L_\kappa}\right)} \right\} \quad (2.30)$$

The local spatial nature of DVRs makes the action of the potential operator on these vectors simply equivalent to the value taken by the potential at the grid point around which the DVR is located. The potential will therefore have a diagonal

representation in this basis, which drastically simplifies the evaluation of these matrix elements. On the other hand, because of their discrete nature, the evaluation of derivative operators becomes more complicated and extrapolation methods are required to evaluate the action of a derivative on this function.

In general, both basis sets are used in the standard method to evaluate the matrix elements of the Hamiltonian. The kinetic term is evaluated in the FBR basis and the potential term in the DVR basis. The unitary transformation between the two bases allows us to evaluate the matrix representation of the Hamiltonian in any one of these two basis.

Time (in)dependent numerical study

In the case of a time-independent study, the Schrödinger equation can be solved by diagonalization of the Hamltonian matrix, for example. This gives access to the system's eigenenergies and associated eigenstates. In the case of a time-dependent study, given that the primitive functions are time-independent, the aim is to determine only the time-dependent expansion coefficients of the wave function $A_{i_x,i_y,i_z}(t)$. One frequently used method is the Dirac-Frenkel variational principle [17, 18]:

$$\langle \delta\Psi | \hat{H} - i\hbar \frac{\partial}{\partial t} | \Psi \rangle = 0 \tag{2.31}$$

Where $\langle \delta\Psi |$ in the bra-ket notation represents an infinitesimal variation of the wave function by a varying its parameters. In this case, the parameters correspond to the expansion coefficients $A_{i_x,i_y,i_z}(t)$.

$$\delta\Psi = \sum_{i_x,i_y,i_z} \frac{\partial \Psi}{\partial A_{i_x,i_y,i_z}} \delta A_{i_x,i_y,i_z} \tag{2.32}$$

By replacing equation 2.32 in equation 2.31 and after some simplifications, we arrive at the following equation:

$$\mathrm{i}\hbar \dot{A}_I = \sum_{I'} \langle \phi_I | \hat{H} | \phi_{I'} \rangle \, A_{I'} \tag{2.33}$$

Here we have used the super indices $I = (i_x, i_y, i_z)$ and $\phi_I = \phi_{i_x,i_y,i_z} = \phi^{(x)}_{i_x} \phi^{(y)}_{i_y} \phi^{(z)}_{i_z}$ to simplify notations. This brings us to simple first-order differential equations having as a formal solution for time-independent Hamiltonian :

$$\boldsymbol{A}(t) = e^{-\frac{i}{\hbar}\hat{H}t} \boldsymbol{A(0)} \tag{2.34}$$

This approach finally allows us to determine the expansion coefficients that give the most accurate possible representation of the wave function over time in a given basis. In principle, this approach preserves the norm and the energy of the system if the numerical integrators used are well chosen. The choice of a good representative basis for the system is also very important for reducing numerical errors.

Despite that this method gives access to an almost exact representation of the system's wave function, It is highly limited by the dimensionality of the problem. Indeed, if we take the previous three-dimensional example, equation 2.33 contains $N_x \times N_y \times N_z$ coupled differential equations. In the general case, the number of equations to solve scales exponentially with the size of the problem and quickly becomes impractical when dealing with systems having several DOFs.

2.3.2 Multi-Configuration Time-Dependent Hartree method

The Multi-Configuration Time-dependent Hartree (MCTDH) is a very efficient method used for numerical resolution of the time-dependent Schrödinger equation. The program allows to treat a wide range of problems in quantum molecular dynamics including those with large dimension. In the following, we will highlight some general aspects of the method to which we will refer in the remaining chapters of this thesis. A more complete description of the Heidelberg package of MCTDH can be found in [16, 15].

MCTDH is based on the Time-Dependent Hartree (TDH) approach [31] in which the basis vectors are time-dependent and given by a single function for each DOF called single-particle function (SFP). The total wave function is then given by a single product of the SFP of each DOF called Hartree product. Considering the example of a three-dimensional system in the previous section, the wave function in this case can be written as :

$$\Psi(x, y, z, t) = a(t)\varphi_x(x, t)\varphi_y(y, t)\varphi_z(z, t) \tag{2.35}$$

Where $\varphi_x(x, t)$, $\varphi_y(y, t)$ and $\varphi_z(z, t)$ represent the SPF associated with the DOF x, y and z respectively. a(t) represents the time-dependent coefficient of the wave function in this basis. Each SPF admits a decomposition in the primitive basis

associated with the same DOF. If we consider the DVR basis set, the decomposition reads

$$\varphi_\kappa(\kappa,t) = \sum_{i_\kappa}^{N_\kappa} c_{i_\kappa}^{(\kappa)}(t)\chi_{i_\kappa}^{(\kappa)}(\kappa) \tag{2.36}$$

Where $\kappa = \{x, y, z\}$ and $c_{i_\kappa}^{(\kappa)}(t)$ are the expansion coefficients of the SPF φ_κ in the DVR basis associated to the same DOF.

Only three SPF are needed in this case to describe the problem. Each SPF evolves in time, so as to guarantee a good description of the wave function during propagation. While this approach considerably reduces the number of effectively needed representation functions compared to the standard method, it remains effective only for a certain type of problems which do not require the use of multiple configurations. This problem has been overcome in MCTDH by expanding the wave function in a sum of product of one-dimensional basis vectors as in the standard method, but considering the basis set to be time-dependent as in the (TDH) method. These vectors are also called SPF. The idea of making basis vectors time-dependent is the key behind this effective reduction of dimensionality. Indeed, when we consider a "frozen" basis set in time, the latter must describe the wave function initially and after each time step throughout propagation, many vectors are then needed to guarantee a suitable description of the system within time, contrary to the case of time-dependent vectors that evolve in time according to the evolution of the wave function at each time step which requires less basis vectors to give a representation with the same quality as in the previous one. This finally allows the wave function to be expressed in a similar way as in the standard method but using a smaller number of vectors for each DOF. The decomposition of the three dimensional wave function in the SPF basis used in MCTDH is given by :

$$\Psi(x,y,z,t) = \sum_{i_x}^{n_x}\sum_{i_y}^{n_y}\sum_{i_z}^{n_z} A_{i_x,i_y,i_z}(t)\varphi_{i_x}^{(x)}(x,t)\varphi_{i_y}^{(y)}(y,t)\varphi_{i_z}^{(z)}(z,t) \tag{2.37}$$

With $1 \leq n_\kappa \leq N_\kappa$, $\kappa = \{x, y, z\}$. $A_{i_x,i_y,i_z}(t)$ represent the time-dependent expansion coefficients of the wave function in the SPF basis. If we use the super-index $I = (i_x, i_y, i_z)$, each coefficient A_I of the set $\{A_I\}_{1\leq I\leq n_x n_y n_z}$ can be seen as the element of a vector $\boldsymbol{A}$ of length $n_x \times n_y \times n_z$ which groups all the expansion coefficients of the wave function called A-Vector in MCTDH. The number of SPF used for each DOF

is generally a fraction of the number of associated primitive basis functions, which considerably reduces the dimensionality of the problem. One can use the standard method by taking $n_\kappa = N_\kappa$, the calculation is then said to be exact. If $n_\kappa = 1$ $(\forall\kappa)$, this is equivalent to using the TDH approach.

It is also possible to generate multi-dimensional SPF that combine two or more DOFs. This technique is known as mode combination. If, for example, we choose to combine the x and y within a a single mode $Q \equiv (x, y)$ called the logical coordinate. The expansion of the wave function in the new basis will take the following form :

$$\Psi(Q, z, t) = \sum_{i_Q}^{n_Q} \sum_{i_z}^{n_z} A_{i_Q, i_z}(t) \varphi_{i_Q}^{(Q)}(Q, t) \varphi_{i_z}^{(z)}(z, t) \tag{2.38}$$

This technique is useful when two or more DOFs are strongly coupled which allows to include the correlations within the same SPF. At the same time, it considerably reduces the size of the A-vector. The disadvantage is that it could make the propagation of the SPF (now multi-dimensional) slower. The user must therefore make a choice (often intuitive) on the way to combine modes to make the calculations more optimal.

Now, to propagate the wave function of a system initially prepared in a state Ψ_0, an SPF basis and an A-vector are initially constructed so as to reproduce Ψ_0 in the form suited to MCTDH. As the SPF and the A-vector are time-dependent, they are both propagated in time following the Dirac-Frenkel variational principle as explained in the previous section, but this time taking the A-vector and the SPF as parameters to optimize. The variational calculation leads to the MCTDH equations of motion given by :

$$\mathrm{i}\dot{A}_I = \sum_{I'} \langle \varphi_I | \hat{H} | \varphi_{I'} \rangle \, A_{I'} \tag{2.39}$$

$$\mathrm{i}\dot{\boldsymbol{\varphi}}^{(\kappa)} = (\hat{1} - \hat{P}^{(\kappa)})(\boldsymbol{\rho}^{(\kappa)})^{-1} \langle \boldsymbol{H} \rangle^{(\kappa)} \boldsymbol{\varphi}^{(\kappa)} \tag{2.40}$$

$\boldsymbol{\varphi}^{(\kappa)}$ is a vector composed of the n_κ SPF used for the DOF $\kappa = \{x, y, z\}$. The operator $(1 - \hat{P}^{(\kappa)})$ ensures that the time derivative of the SPF is orthogonal to the space spanned by the functions. $\boldsymbol{\rho}^{(\kappa)}$ and $\boldsymbol{H}^{(\kappa)}$ represent the single-particle density matrix and mean-field matrix respectively. The derivation of these calculations can be found in [15].

To solve equations 2.39 and 2.40, there is a wide range of integrators available in MCTDH. Each of these integrators has its own specificity, depending on the problem and the precision required. Even if the calculation scheme used in MCTDH preserves the norm and energy of the system during propagation, this is only possible if the integrator parameters are well chosen, such as integration step size and error tolerance. Chapter 9 of [21] gives a detailed description of the integrators and diagonalizers available in MCTDH.

The use of a small SPF basis can lead to errors in the wave function propagation, and therefore in the mean values of observables. It is therefore necessary to check the convergence of the SPF basis during each calculation. MCTDH indirectly evaluates the populations of SPF called natural populations by diagonalizing the density matrices $\boldsymbol{\rho}^{(\kappa)}$. These populations represent the weights of the SPF and thus the degree of importance that each SPF adds to the description of the total wave function of the system during propagation. The natural populations are ordered in ascending order. If the weight of the last SPF in the used basis is small enough, we can conclude that the dimension of the basis used is sufficient for the calculation we're performing . If this is not the case, we increase the number of SPF and repeat the same operation until convergence is achieved. Tolerance errors vary according to the type of information we wish to extract from the wave function. In general, the basis is well suited if the weight of the last SPF of each DOF (or combined mode) is of the order of 10^{-3}.

It is also important to check the convergence of the primitive basis. If the dimension of the latter is not large enough, the SPF basis will be "poor" by construction. Checking the quality of the primitive basis is slightly different from that of SPF. We generally use DVR or FBR functions as primitive functions. In the first case, the population of the first and last grid points must be small. This would mean that the grid is sufficiently wide that the wave function does not reach its edges during propagation. An exception is made when working under periodic conditions. In this case, the first and last grid points of each DOF concerned by periodicity may be populated during propagation. However, it will be necessary to check that the symmetries of the weights are preserved in certain cases. In the case of an FBR basis, the weight of the last function must be checked in the same way as for the

natural population of SPF.

To conclude this section, the use of MCTDH, with a judicious choice of the basis set and integrators, allows us to obtain accurate results with relatively short computational time. The power of this method comes from the multi-configuration compact treatment of the wave function using a set of a time-dependent vectors. However, the sum of product form used for the expansion of the wave function is also required for the system Hamiltonian. The user is therefore constrained to rewrite the Hamiltonian as a sum of product of operators acting on each mode. The kinetic energy operator is generally suited to this form while the potential term depends on the complexity of the studied problem. When it is not possible to rewrite it analytically, one can make use of a program implemented in MCTDH called potential fit (potfit), which rewrites the potential in the required form using numerical approach similar to MCTDH. In section 2.3.4, we present the general aspects of this method. But before that, we will discuss in the next section the numerical methods used to solve the time-independent Schrödinger equation.

2.3.3 Time-independent study : a discussion about the block improved relaxation method

There are several numerical methods for solving the time-independent Schrödinger equation. The most direct one is the diagonalization of the Hamiltonian matrix in a given basis. The size of the basis to work with depends on the number of DOFs and on the number of eigenstates we wish to calculate. The diagonalization of large matrices is time consuming and sometimes not feasible. This makes the method non optimal for multi-dimensional systems. There are several approaches in the literature for calculating the eigenvalues and eigenvectors of large matrices, such as iterative schemes like the Davidson and Lanczos methods [32, 33]. In this project, we used an approach implemented in MCTDH called Improved-Relaxation that combines these techniques with the relaxation method. In the following, we will briefly introduce the general relaxation method and then discuss some improvements made by MCTDH on the latter.

Relaxation Method

The relaxation method was developed by R. Kosloff et al. [34]. It solves the time-independent Schrödinger equation with a time-dependent scheme. The approach is based on the idea that if we propagate a state with a Hamiltonian in negative imaginary time, then it will converge to the lowest-energy eigenstate of the Hamiltonian used. This idea can be illustrated very simply by looking at the time evolution of any state in the eigenstates basis. If we consider $t = -i\tau$ in equation 2.25 (with $\tau \in \mathbb{R}^+$), we get :

$$|\Psi(\tau)\rangle = \sum_k c_k(0) e^{-E_k \tau/\hbar} |\varphi_k\rangle \tag{2.41}$$

In contrast to equation 2.25, here the wave function components in the eigenstates basis $c_k(t) = c_k(0)e^{-E_k\tau/\hbar}$ do no longer oscillate in time, each component decreases exponentially with a rate proportional to its energy E_k. This means that those associated to the high-energy eigenvectors will decay over time at a much faster rate than those associated with the less energetic states. If we propagate over a sufficiently long interval, only the lowest state remains present in equation 2.41 after renormalization. The system is then relaxed to its ground state. To calculate the excited states, we project the Hamiltonian onto a Hilbert space not containing the previously calculated state, and relax the system back to its lowest state, which this time represents the system's first excited state, and so on. The choice of initial wave function can be very important in achieving convergence. Indeed, the calculation will always lead us to the lowest-energy state included in the initial wave function we use. It's important to choose an initial state that covers the part of the spectrum one wants to determine.

Improved relaxation Method

MCTDH as its name suggests, is designed to treat the time-dependent Schrödinger equation. It also allows the calculation of stationary states within the improved relaxation program since the relaxation method is based on the time-dependent Schrödinger equation. The program improves this method by adding diagonalization steps during the relaxation process. In particular, when propagating the A-vector, the program then adds a few partial diagonalization steps using Davidson's

algorithm to speed up the convergence of the calculations. These intermediate steps also enhance the initial wave function, allowing the determination of eigenstates not initially included in the wave packet. A block version called block improved relaxation has also been developed and implemented in MCTDH. It allows to relax simultaneously several states to eigenstates of the system. When we need to calculate multiple eigenstates of the system, this method is not only faster in terms of computational time than single-state relaxation, it is also crucial for dealing with problems with degenerate eigenstates, as we will see in chapter 4. A more detailed description of the (block)improved method can be found in [19, 20, 21].

2.3.4 Potential representation with potfit

The use of MCTDH requires a structure of the Hamiltonian given by a sum of products of operators acting on one DOF. Although the kinetic operator can in most cases be written in this form, the potential term in multi-dimensional problems often involves non-separable terms, making this decomposition analytically unfeasible. MCTDH proposes a program called potential fit (potfit) which, using a numerical procedure, rewrites the potential in the required form. In this section, we will briefly outline some of the key elements of the potfit approach, which we will refer to in the remainder of this manuscript. The reader is invited to read [35, 36, 15] for a more detailed description of the method.

As mentioned above, the evaluation of potential matrix elements is carried out at the DVR basis defined on the grid points. DVR functions are highly localized in space, the potential can then be defined only by the values taken on these points. we will use the notations used in the previous three dimensional example in the Cartesian coordinates of section 2.3.2. We recall that each DOF $\kappa = \{x, y, z\}$ is defined on an interval $I_\kappa = [\kappa^{\min}, \kappa^{\max}]$. If we consider N_κ DVR function for the κth DOF, then the latter will be defined on grid points $\{\kappa_{i_\kappa}\}_{1 \leq i_\kappa \leq N_\kappa}$ spaced by $\Delta_\kappa = \dfrac{\kappa^{\max} + \kappa^{\min}}{N_\kappa + 1}$ and evenly distributed over I_κ. since the potential is defined only at these points, we can write

$$V(x_{i_x}, y_{i_y}, z_{i_z}) \equiv V_{i_x, i_y, i_z} \tag{2.42}$$

As in the treatment of the wave function, the use of the full DVR basis gives very ac-

curate results, but at a very high numerical cost for multi-dimensional systems. The idea, therefore, is to build a basis with a smaller size than the primitive one, which can approximate the potential correctly. In the same approach used to build the SPF basis, potfit generates a compact basis called Single-Particle Potential (SPP). The vectors of this basis are constructed by diagonalizing the potential density matrix associated with each DOF. The provided eigenvalues and eigenvertors are called the natural potential populations $\{\lambda^{(\kappa)}_{j_\kappa}\}_{1\leq j_\kappa\leq m_\kappa}$ and the natural potential $\{v^{(\kappa)}_{j_\kappa}(\kappa_{i_\kappa})\}_{1\leq j_\kappa\leq m_\kappa}$ respectively, with $m_\kappa \leq N_\kappa$ the number of SPP used for each DOF κ. It generally represents a fraction of the total number N_κ of primitive functions. Given that these vectors are defined only on grid points i_κ, we will in the following simply denote them by $v^{(\kappa)}_{j_\kappa}(\kappa_{i_\kappa}) \equiv v^{(\kappa)}_{i_\kappa j_\kappa}$. The general decomposition of the approximate potential V^{app} on the SPP basis is then given by:

$$V^{\text{app}}_{i_x,i_y,i_z} = \sum_{j_x}^{m_x}\sum_{j_y}^{m_y}\sum_{j_z}^{m_z} C_{j_xj_yj_z} v^{(y)}_{i_xj_x} v^{(y)}_{i_yj_y} v^{(z)}_{i_zj_z} \tag{2.43}$$

The expansion coefficients $C_{j_xj_yj_z}$ are obtained by minimizing the error on the fit given by:

$$\Delta^2 = \sum_{i_x}^{N_x}\sum_{i_y}^{N_y}\sum_{i_z}^{N_z}(V_{i_x,i_y,i_z} - V^{\text{app}}_{i_x,i_y,i_z})^2 \tag{2.44}$$

This gives:

$$C_{j_xj_yj_z} = \sum_{i_x}^{N_x}\sum_{i_y}^{N_y}\sum_{i_z}^{N_z} V_{i_x,i_y,i_z} v^{(y)}_{i_xj_x} v^{(y)}_{i_yj_y} v^{(z)}_{i_zj_z} \tag{2.45}$$

Potfit allows to combine modes in a similar way to MCTDH discussed in section 2.3.2 and also to contract over one or more DOFs. Contraction over a DOF is achieved by summing the expansion coefficients of the latter over the entire associated grid. If we consider an example where we contract on x :

$$D_{j_yj_z} = \sum_{j_x}^{N_x} C_{j_xj_yj_z} v^{(x)}_{i_xj_x} \tag{2.46}$$

Equation 2.43 becomes :

$$V^{\text{app}}_{i_x,i_y,i_z} = \sum_{j_y}^{m_y}\sum_{j_z}^{m_z} D_{j_yj_z} v^{(y)}_{i_yj_y} v^{(z)}_{i_zj_z} \tag{2.47}$$

Note that in equation 2.47 the sum has been taken over the entire grid of size N_x, which improves the quality of the contraction.

Evaluating the error of the potential approximation is important for assessing the quality of the fit. Equation 2.44 gives the overall error on the grid. To evaluate the average error, we calculate the root-mean square (rms) error defined by $\Delta_{\text{rms}} = \sqrt{\Delta^2/N_{\text{tot}}}$ with N_{tot} the total number of primitive functions. When we use a number of SPP equal to the number of primitive functions ($m_\kappa = N_\kappa$), then the rms error is zero. The calculation is then said to be exact. In the opposite case ($m_\kappa < N_\kappa$), the rms error can be estimated from the natural potential populations $\{\lambda_{j_\kappa}^{(\kappa)}\}_{m_\kappa \leq j_\kappa \leq N_\kappa}$ of the neglected SPP. Let's assume, for example, that we only truncate on one DOF κ, in which case the rms error is given by:

$$\Delta_{\text{rms}} = \sqrt{\sum_{j_\kappa=m_\kappa+1}^{N_\kappa} \lambda_{j_\kappa}^{(\kappa)}/N_\kappa} \tag{2.48}$$

If we truncate over several DOFs, this quantity becomes an upper bound on the error:

$$\Delta_{\text{rms}} \leq \sqrt{\sum_{\kappa} \sum_{j_\kappa=m_\kappa+1}^{N_\kappa} \lambda_{j_\kappa}^{(\kappa)}/N_\kappa} \tag{2.49}$$

The populations of natural potentials are ordered in ascending order, and Δ_{rms} then represents the importance of the SPP that were neglected. This is a very useful tool for evaluating the quality of the SPP basis set used.

It is also possible to optimize the fit at certain energy intervals, potfit allows weights $\{w_{i_\kappa}^{(\kappa)}\}$ to be added to the potential to optimize the fit only in those relevant regions of space corresponding to the selected energy interval. The rms error is then evaluated by replacing N_{tot} by $\sum_{i_\kappa} \prod_{i_\kappa} w_{i_\kappa}^{(\kappa)}$. This is referred to as the weighed rms error Δ_{rms}^{w}. Minimizing the error on all grid points is numerically very costly and often of no use when working in a finite energy domain, since it is assumed that the wave function will not explore high-energy regions during the simulation. It is therefore more important to reduce errors as much as possible in the regions where most of the dynamics take place. Often, these regions represent only a part of the total grid, so at the same time the error is distributed over a smaller set of points, making the representation of the potential more optimal for the calculations.

The use of potfit in MCTDH was designed to optimize the writing of the potential, making the determination of the matrix elements much faster than with the primitive

basis, which considerably reduces the computation time required for the propagation of a given state. The PES used in this project are multi-dimensional functions with highly correlated DOFs. Although these PES have been defined analytically by the authors [23], the presence of non-separable multidimensional terms makes the separation of this potential into one-dimensional functions unfeasible. The use of potfit was necessary to adapt the potential to MCTDH calculations. In section 3.2.3, we will give all the technical details about the parameters used to represent the PES used in this work.

Chapter 3

Potential energy surfaces analysis for H/Pd(111) and H_2/Pd(111)

In this work, we have carried out a time-dependent and time-independent study based on a fully quantum approach of the H and H_2 systems adsorbed on a Pd(111) surface which are H/Pd(111) and H_2/Pd(111) respectively. One of the aims of this study is to determine the stationary vibrational states of these systems and to investigate some aspects of their quantum dynamics at the surface level. The time-(in)dependent study is carried out by solving the time-(in)dependent Schrödinger equation. We perform our calculations within the Born-Oppenheimer approximation in which the DOFs of electrons and those of nuclei are decoupled (section 2.1.2), the nuclei evolve then on a PES representing the interactions between the components of the system.

The PES used in this work was developed by W.Dong et al. [22]. It was constructed within the ground electronic state of the system. As we shall see later in this chapter, the authors have provided an analytical formulation of the potential using a some fit models [23]. In this study, the palladium atoms are considered to be fixed in their equilibrium position, and the only DOFs of the PES are those of the hydrogen atoms. The PES will therefore be defined by a three-dimensional function in the case of H/Pd(111) and a six-dimensional function in the case of H_2/Pd(111).

In the following, we will start by presenting the geometrical aspect of the crystallo-

graphic structure of the system. Then the remainder is dedicated to the analysis of the PES features of the two studied systems.

3.1 Lattice geometry analysis

We will focus in the following on the crystallographic structure of the fixed Pd atoms at bulk and surface level since hydrogen atoms can move freely on the surface.

3.1.1 General presentation of the palladium crystal structure

Palladium is a metal that crystallizes in the fcc (face-centred cubic) structure. The fcc unit cell is characterized by the presence of an atom on each face and vertex of the cube called a node. The length of the cube edge is given by $a = 389$ and called the lattice parameter. Figure 3.1 illustrates the unit cell of the fcc structure.

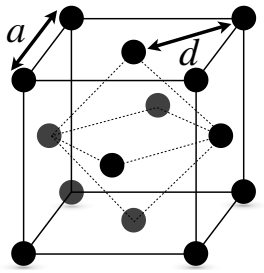

Figure 3.1: Face-centered cubic unit cell of the Pd crystal structure. $a = 389$ pm represents the lattice parameter and $d = \frac{a}{\sqrt{2}} = 275.114$ pm is the nearest neighbour distance.

As this crystal is anisotropic, the study of hydrogen adsoption on the palladium surface depends on the direction that we consider. In each direction, we can define the system as a stack of reticular planes (or atomic planes in our case) where each plane is defined by 3 nodes. These planes vary in density and configuration according to the chosen direction. To identify the different directions in the crystal, we use Miller indices. They are given by a set of three numbers (h, k, l), corresponding to the inverses of the intersections of the reticular plane with the edges of the unit cell called lattice vectors [37]. For example, if we take the (111) direction, the first reticular plane in this direction will be defined by the three nodes numbered 1, 3

and 6 and the second reticular plane by nodes 7, 9 and 12 as shown in figure 3.2. The bulk structure of Pd(111) is therefore given by a stacking of these planes along

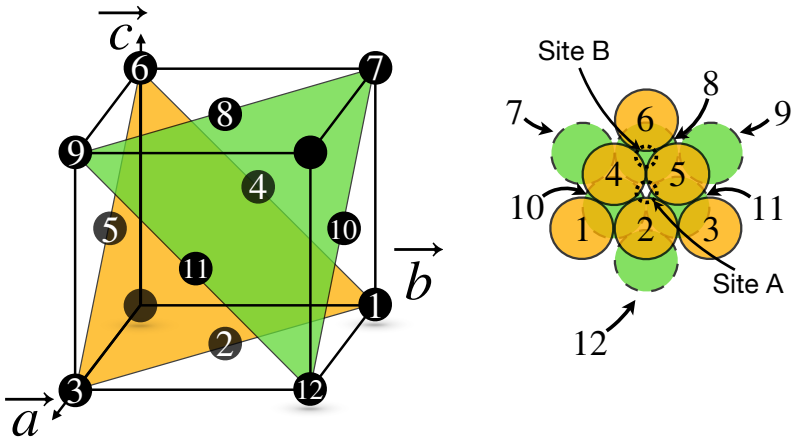

(a) Overview.

(b) Perpendicular view to the Pd(111) plane.

Figure 3.2: Reticular planes contained in the unit cell of the fcc structure along the (111) direction.

the (111) direction. They are all spaced by $\frac{a}{\sqrt{3}}$ (see [25] for more details).

We will now consider that the plane at the surface level is the one that includes atoms {1..6} and the one that contains atoms {7..12} lies just below. Figure 3.2b shows these planes from a view with perpendicular direction to the surface. We will see later in the PES analysis (section 3.2) that for a hydrogen atom moving at the surface level, the minima of the potential are located around some geometrical points such as site A and B shown on figure 3.2b. They represent the most stable adsoption sites for hydrogen on the Pd(111) surface. Each of these sites are located between three Pd atoms. The arrangement of Pd atoms in the reticular planes varies from one plane to another. We can see from fig 3.2 that there is a Pd atom located directly below site B, unlike site A (a Pd atom will be located below site A only at the 2^{nd} plane below the surface). Therefor, the different configuration of Pd atoms on each reticular plane differentiates A-type sites from B-type sites. They are called fcc site (face-centred cubic) and hcp site (hexagonal closed-packed) for A and B respectively. We will see later that there's a significant energy difference between these two situations.

3.1.2 Grid presentation

In order to simulate an infinite surface in our calculations, a periodic approach was adopted which includes an elementary cell given by a slab of five Pd layers where each one contains 3×3 Pd atoms. The vacuum space corresponds to five Pd(111) layers. We will refer to this as "(3×3)-grid". A more detailed description of this grid will be given in section 3.2.3. The elementary cell used in our calculations is the same as the one used by the authors to develop the PES. Figure 3.3 shows a scheme of this grid showing only the surface plane (solid line) and the one below (dashed line). As can be seen directly from the figure, this grid contains 9 equivalent fcc sites and 9

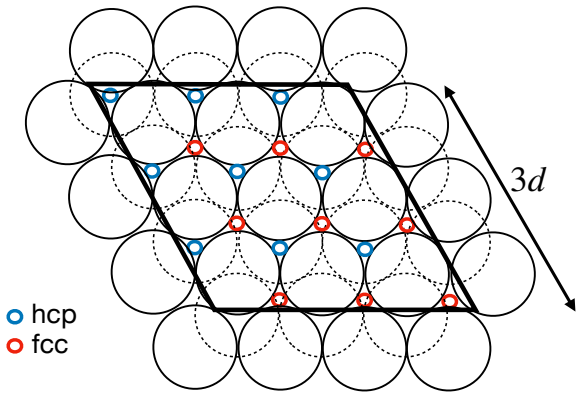

Figure 3.3: (3×3)-grid used for periodic calculations.

equivalent hcp sites. The spatial periodicity is applied following the twisted vectors $\boldsymbol{x_t}$ and $\boldsymbol{y_t}$ with $\alpha = (\widehat{\boldsymbol{x_t}, \boldsymbol{y_t}}) = 120°$ as shown in figure 3.4. We define therefore a non-orthogonal basis set ($\boldsymbol{x_t}$,$\boldsymbol{y_t}$,$\boldsymbol{z_t}$) where the origin is located in the center of the Pd atom located in the middle of the topmost layer of the elementary cell. A set of twisted coordinates (x_t,y_t,z_t) will be used in the following. The transformation

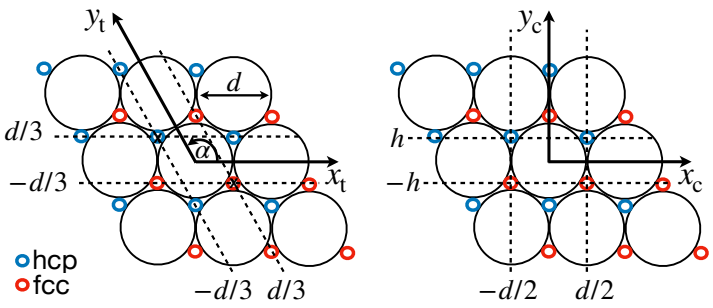

Figure 3.4: Twisted and Cartesian coordinates used for the (3×3)-grid.

between the twocoordinate systems is given by :

$$\begin{cases} x_t = x_c + \frac{1}{\sqrt{3}} y_c \\ y_t = \frac{2}{\sqrt{3}} y_c \\ z_t = z_c \end{cases} \tag{3.1}$$

Figure 3.4 shows the coordinates of one fcc and one hcp site surrounding the central Pd of the grid. The set of coordinates of all possible fcc and hcp sites contained in the (3×3)-grid are given in table 3.1. A detailed calculation of these coordinates is given in [25].

	Twisted coordinates		Cartesian coordinates	
	x_t	y_t	x_c	y_c
fcc	$d/3 \pm d$	$-d/3 \pm d$	$d/2 \pm d$	$-h \pm 3h$
hcp	$-d/3 \pm d$	$d/3 \pm d$	$-d/2 \pm d$	$h \pm 3h$

Table 3.1: Twisted and Cartesian coordinates parallel to the surface for all fcc and hcp sites of the (3×3)-grid.

In table 3.1, we have only considered coordinates parallel to the surface. The fcc and hcp sites are actually located at the minima of the PES which are reached a few tens of pm above the surface level. They will be given in the next section treating the PES analysis. Both coordinate systems will be used in this work depending on the nature of the performed task. In the following, we will refer to Cartesian coordinates as (x,y,z).

3.2 Potential energy surfaces analysis

The periodic cell used in our calculations contains two H atoms and 45 Pd atoms (5(planes)×9(Pd)). The dimension of the PES is extremely high if we consider the DOFs of all its components. The energy range in which we performed our calculations does not include situations where the hydrogen atoms are highly excited. Their presence at the surface level has therefore a very low impact on the motion of Pd nuclei given the large mass difference between the two elements. Pd atoms will remain very close to their equilibrium positions. Consequently, we consider in all

our calculations that the Pd atoms remain fixed in their equilibrium positions over time. The PES will be defined by a six-dimensional hypersurface that depends on the six space coordinates of the hydrogen atoms only. This assumption allows us to considerably reduce the dimensionality of the problem without losing any significant precision in the calculations we have carried out. The construction of the PES allows also transferability to the three-dimensional case of a single H atom adsorbed on a Pd(111) surface. It was implemented numerically in a program written with FORTRAN 90. The program allows to choose the number of hydrogen atoms (1 or 2) to study either H/Pd(111) or H_2/Pd(111) systems.

The construction of this PES was done in two steps : First, the generation of the database which consists in calculating the system energy along several well-chosen pathways of the dissociative adsorption of H_2 on Pd(111) by using the density functional theory (DFT). Then fitting the obtained database on an adequate interatomic potential. The type of interatomic potential they have chosen is based on the Reactive Force Fields (RFFs) approach developed by Brenner [38], which confers to the potential a fully analytical formula. The technical details concerning the development and configuration of this surface are given in Appendix A.

The PES as presented in the author's papers [22, 23] was originally developed on a periodic cell containing 10×10 Pd atoms at each layer. The size of this cell is relatively large and does not allow us to perform calculations optimally by exploiting the full periodicity of the grid. Similar work has been carried out in the past [25] and showed erroneous results when using this PES on a smaller grids. A new PES based on the (3×3)-grid was constructed and shared by the authors. Several tests have been carried out on the latter and have shown it to be highly reliable. In the following we will present the analysis of this PES used for the H/Pd(111) and H_2/Pd(111) systems. Aspects that are directly related to the calculations that was carried out in this work will be particularly highlighted.

3.2.1 H/Pd(111) PES

In this section, the analysis of the three-dimensional PES for the H/Pd(111) system will be presented. We will be particularly interested in the various potential wells

present at the surface level and the potential barriers that separate them. For subsurface interactions, I refer the reader to the analysis by Saalfrank and Tremblay [39]. Subsurface interactions are outside the scope of this thesis. The analysis of these elements provides crucial information for studying the stationary states of the system and for understanding the dynamical behaviour of hydrogen atoms on the palladium surface.

The PES analysis shows that all global minima are located at around 90 pm from the surface. A two-dimensional section of the PES in the Cartesian coordinates is shown in figure 3.5. It allows to visualize the structure of the various potential wells located at this plane level.

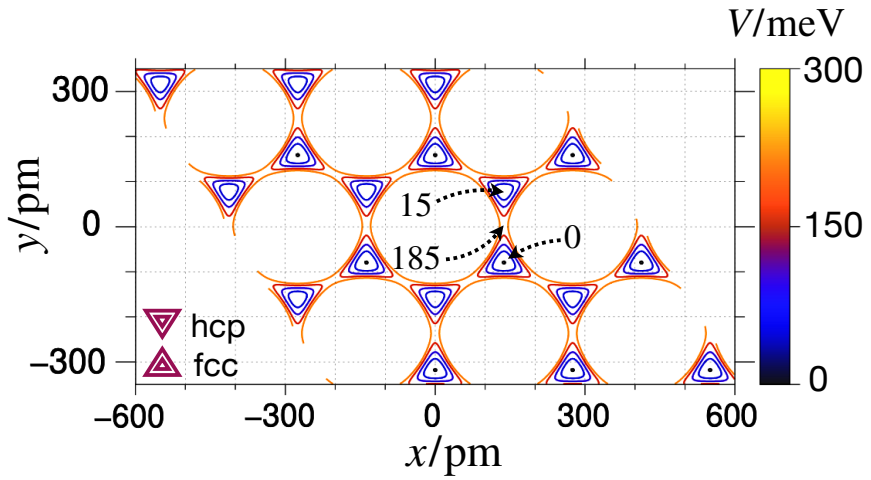

Figure 3.5: Two-dimensional section of the H/Pd(111) PES in the Cartesian coordinates (x, y) with $z = 90$ pm.

Equipotential lines ranging from 0 to 300 meV are shown in the figure. One sees that all potential wells are located at the fcc and hcp sites of the grid. They have the shape of up-pointing or down-pointing triangles for the fcc and hcp sites respectively, which gives the potential a local $\boldsymbol{C}_{3v}$ symmetry. The global minima are shifted to the zero reference energy value, they are reached when the hydrogen atom is located at fcc sites. The energy of the system when the hydrogen atom is located in an hcp site is around 15 meV for z=90 pm. The potential wells located at the hcp sites corresponds then to the local minima of the potential. The analysis of the PES shows that actually the minimum value of the energy in the hcp site is about 14

meV, this energy is reached when the hydrogen atom is located at z=91.6 pm above the surface. The atomic environment for a hydrogen atom located on these sites is different due to the presence of a Pd atom in the subsurface plane in the case of the hcp site, which slightly increases the energy at that site. The (3×3)-grid then contains 18 potential wells including 9 equivalents of each type.

Figure 3.5 shows that all potential barriers that separate the potential wells[1] at $z = 90$ pm are equivalent and of finite size with a height of 185 meV. Figure 3.6 shows the shape of the potential barrier in a plane perpendicular to the surface.

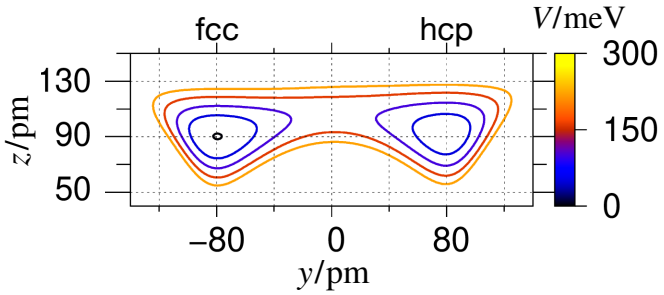

Figure 3.6: Two-dimensional section of the PES in the Cartesian coordinates (y, z) with $-d/2 \leq y \leq d/2$, 40 pm $\leq z \leq$ 150 pm and $x = d/2$.

The equipotential lines show that the barrier decreases when the hydrogen atom goes away from the surface. To better visualize this barrier variation, figure 3.7 shows one-dimensional cuts along the line joining an fcc and an hcp site for z fixed at z=90 pm (solid line) then for z relaxed (dashed line). The latter was done by minimizing the energy along the z coordinate on each point of the line joining the fcc and hcp sites. One sees that the potential barrier drops to 120 meV at z=106 pm, which represents almost 35%. This would mean that the hydrogen atom will always tend to move slightly away from the surface as it moves from one site to another.

[1]Here we consider only the lateral potential barriers separating the different sites at the surface level. The barrier in the z direction which prevents the H atom to penetrate the Pd bulk is about 937 meV at the fcc site. This value is above the energy range of our calculations and of no particular interest in our studies.

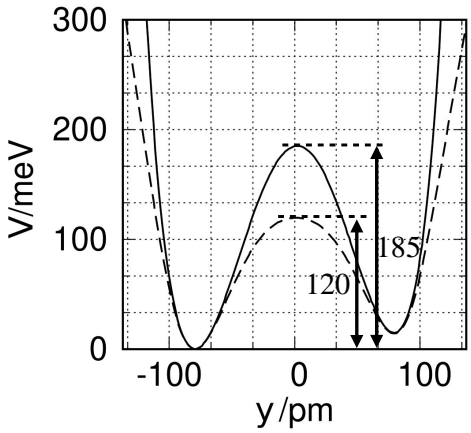

Figure 3.7: One-dimensional sections of the H/Pd(111) PES along the line joining fcc and hcp site with z fixed at 90 pm (solid lines) and z relaxed (dashed lines).

The regions with the lowest energies are mainly concentrated around the various potential wells located around 90 pm from the surface. Most of the dynamics of interest in this thesis will therefore take place in these regions. Analysis of these different geometrical aspects of the PES provides some preliminary information of the system dynamics. We will conclude this section by citing some of the direct consequences we can draw from the preceding analysis.

- Given that there are 9 equivalent potential wells located on the fcc sites and 9 other equivalent wells located on the hcp sites, several vibrational stationary states will be degenerate (or quasi-degenerate) with a degeneracy factor of at least 9.

- Figure 3.6 shows that the potential is much more "contracted" in the direction perpendicular to the surface than in the parallel direction. This can be seen directly by observing the density of the equipotential lines in the z direction or by looking directly at the curvature of the potential. A direct consequence of this property of the potential is that vibrational excited states in the perpendicular direction to the surface will have much higher energies than the parallel ones.

- The finite potential barrier may allow hydrogen to tunnel from one site to another, even in relatively low energy domains. Analysis of the height and width of the potential barrier gives an idea of the importance that tunneling

may have on the dynamics of the system.

3.2.2 H_2/Pd(111) PES

In this section, following a similar approach to the previous one, we present some important aspects of the PES of the H_2/Pd(111) system. In particular, the analysis of the different potential wells and the different potential barriers separating them as well as the resulting equilibrium configurations and their degeneracy.

The minima of the PES correspond to the most favorable situations for the adsorption of H_2 on the Pd(111) surface. These minima are reached when both hydrogen atoms occupy one of the fcc or hcp sites of the grid. In order to facilitate the naming of the different possible situations, we will in the following symbolize the fcc site with the capital letter A and the hcp site with the capital letter B. We can then distinguish between three situations:

- Both hydrogen atoms are located on fcc sites (AA).
- Both hydrogen atoms are located on hcp sites (BB).
- One hydrogen atom is located on a fcc site and the other on a hcp site (AB).

Given that the grid we used in our periodic calculations contains 9 fcc sites and 9 hcp sites, then there are $2 \times \binom{9}{2} = 72$ different combinations of placing the two hydrogen on fcc sites, $2 \times \binom{9}{2} = 72$ combination of placing the two hydrogen on hcp sites and $2 \times \binom{9}{1} \times \binom{9}{1} = 162$ combination of placing one hydrogen on a fcc site and the other on a hcp site. The energy of the system is different between these three configurations, given that the potential wells at the fcc and hcp sites are different.

The PES analysis also showed that, within each configuration, several energetically different subconfigurations are possible. Figure 3.8 shows some examples. For the (AA) and (BB) configuration types, we distinguish between two different situations: the two atoms occupy two neighboring sites (figure (a) and (c)) which we will call $(AA)_I$ and $(BB)_I$, then the situation where they occupy non-neighboring sites (figures (b) and (d)) which we will call $(AA)_{II}$ and $(BB)_{II}$. Then for the configuration of type (AB), there are three cases with different energies. We will only consider situations (e) and (f), because the last configuration $(AB)_{NN}$ (Near Neighbors) is very

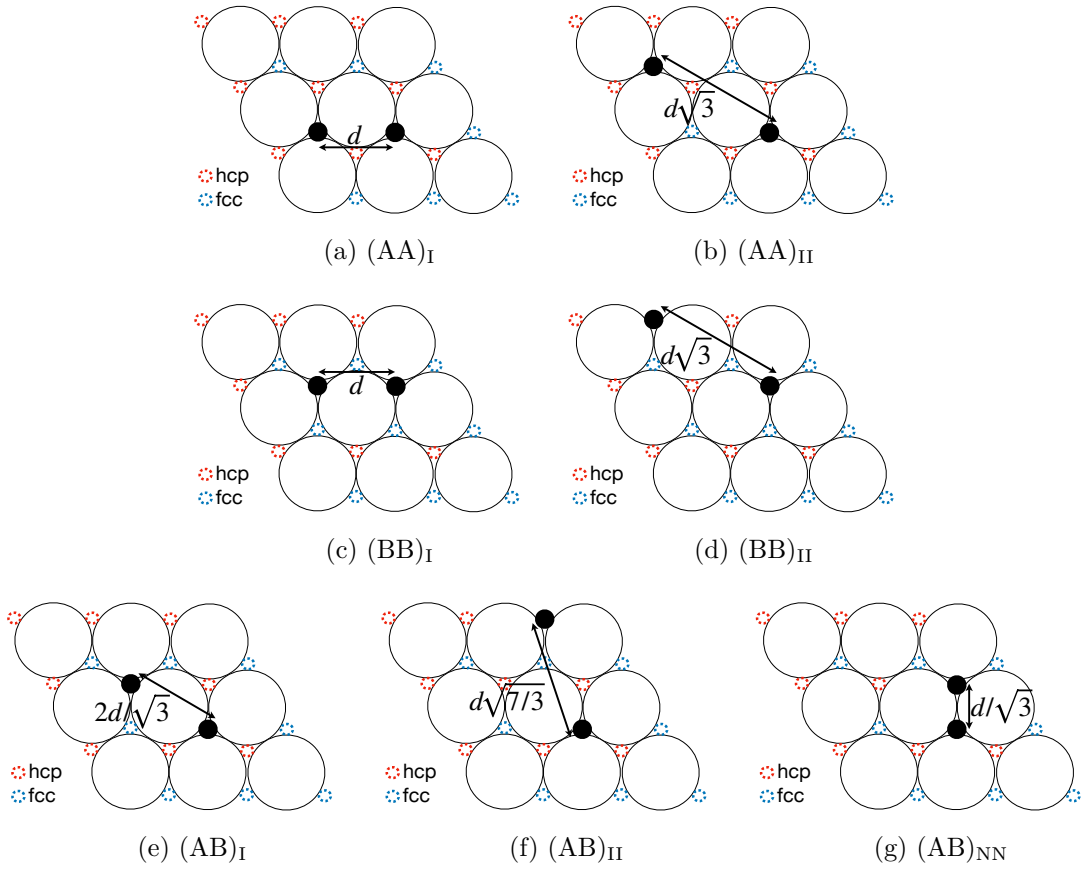

Figure 3.8: Examples of each possible type of configuration for placing the two H atoms on fcc and hcp sites.

energetic ($\approx$ 359 meV) given that the two H atoms are close and repel each other. As a result, this configuration will be very sparsely populated within the dynamical calculations we wish to perform in this work. It is therefore of little interest for the following. We will represent the remaining configurations by $(AB)_I$ and $(AB)_{II}$ as shown in the figure. Some situations in 3.8 seem to be energetically equivalent. If we take the example of the two configurations $(AA)_I$ and $(AA)_{II}$, despite the fact that the hydrogen atoms in these two configurations have the same atomic environment if we restrict ourselves only to the first neighbors, these situations present a significant energy difference as shown in table 3.2. This is due to the fact that the development of this PES takes into account the three-body interactions between the system's components. W.Dong has calculated additional three-body terms between the hydrogen and palladium atoms and incorporated them into his

calculations[2] (see appendix A). Table 3.2 gives the energies of all the different possible configurations with the associated "classical"[3] degeneracy.

Configuration	$d_{\text{H-H}}/d$	E/meV	Degeneracy
$(\text{AA})_{\text{I}}$	1	2	54
$(\text{BB})_{\text{I}}$	1	19	54
$(\text{AB})_{\text{I}}$	$2/\sqrt{3}$	40	54
$(\text{AA})_{\text{II}}$	$\sqrt{3}$	69	18
$(\text{AB})_{\text{II}}$	$\sqrt{7/3}$	73	54
$(\text{BB})_{\text{II}}$	$\sqrt{3}$	101	18
$(\text{AB})_{\text{NN}}$	$1/\sqrt{3}$	359	54

Table 3.2: Energies and classical degeneracy of all possible types of configurations of the dissociative H_2 system on the Pd surface. $d \approx 275$ pm is the distance between two neighboring Pd atoms and $d_{\text{H}-\text{H}}$ represent the distance between the two H atoms in each configuration. $z_1 = z_2 = 87$ pm for all these configurations[a].

[a]The overall PES minimum is reached when the two hydrogen atoms are out of the crystallographic position $(\text{AA})_{\text{I}}$ (see table 3.3).

The degeneracy given in the previous table simply lists the number of equivalent configurations on the (3×3)-grid that we use in our calculations. If we consider the situation $(\text{AA})_{\text{I}}$ as an example, by placing one hydrogen atom on an fcc site, the second hydrogen has 6 possibilities to occupy a neighboring fcc site. Given that there are 9 fcc sites in this grid, this makes a total of 9×6=54 different configurations. A similar procedure can be used to find all the other[4] values in table 3.2.

[2]One of these terms is $d_{\text{H}-\text{H}-\text{Pd}}$, which represents the situation where two H atoms and one Pd atom interact. This term, is considered only when these three atoms are close to each other for example in the configuration $(\text{AA})_{\text{I}}$ and equal to zero in the configuration $(\text{AA})_{\text{II}}$.

[3]This degeneracy is considered to be classical because if we consider the tunneling through the system's potential barriers may induce an energy splitting and partially lift the degeneracy on these states. We will see this later in the section of the stationary states calculation of this system.

[4]The periodic conditions of the grid must also be taken into account to obtain the complete degeneracy.

Actually, the minima of the potential do not coincide exactly with the christalographic coordinates of the fcc and hcp sites. By relaxing the hydrogen atoms around their equilibrium positions on the fcc and hcp sites, we reach slightly lower energies. Table 3.3 gives an example of the energies reached after after relaxation of the hydrogen atom coordinates around the positions of the configurations shown in figure 3.8.

	First hydrogen			Second hydrogen			
Relaxed configurations	x_1/pm	y_1/pm	z_1/pm	x_2/pm	y_2/pm	z_2/pm	E/meV
$(AA)_I$	135.2	-80.4	87.8	-135.2	-80.4	87.8	0.0
$(BB)_I$	135.2	80.4	87.5	-135.2	80.4	87.5	17.1
$(AB)_I$	136.7	-78.8	86.9	-136.7	78.8	86.9	39.3
$(AA)_{II}$	137.2	-79.7	89.0	-274.9	159.3	89.0	67.1
$(AB)_{II}$	137.9	-79.1	89.7	-00.4	317.3	89.7	70.0
$(BB)_{II}$	137.4	78.9	90.3	-274.8	318.0	90.3	95.8

Table 3.3: Energies of the configurations shown in 3.8 after relaxation. The optimal value is $d_{H-H} = 270.4$ pm.

The neighboring potential wells are separated by finite potential barriers. In the case of a single hydrogen atom, the potential barriers "seen" by the hydrogen atom are time-independent, since the Pd atoms are all fixed at their equilibrium positions. But if a second hydrogen atom is present at the surface, these barriers will no longer be constant and depend on the position of the second hydrogen atom. So it is not possible to give exact potential barrier values. We can, however, study the cases where one of the two hydrogen atoms is fixed to an fcc or hcp site of the surface. This will enable us to extract information on the potential barriers "perceived" by the two hydrogen atoms when they are near to their equilibrium positions.

We have therefore considered the situation where the first hydrogen atom is fixed to an fcc site and the second one is free to move in a plane parallel to the surface. the second situation is similar to the first one but with a hydrogen fixed to an hcp site. The PES corresponding to these two situations are therefore two-dimensional

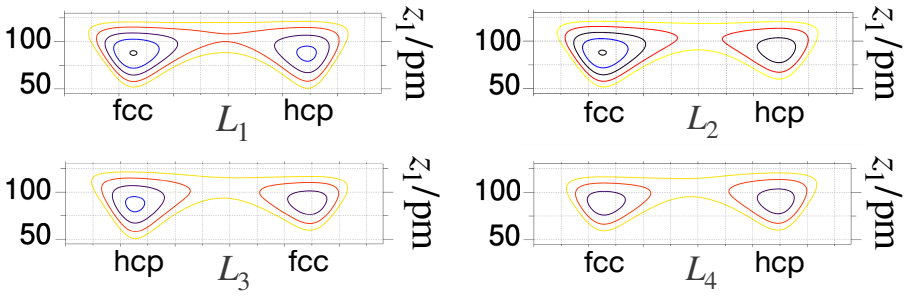

(a) Two dimensional section of the PES along (L_k, z_1).

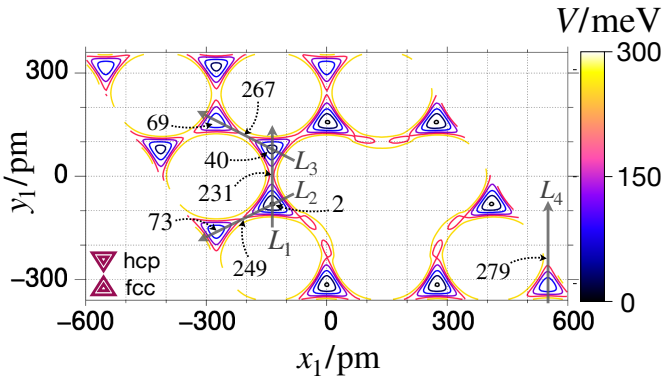

(b) Two dimensional section of the PES along (x_1, y_1) with $z_1 = z_2 = 87$ pm.

Figure 3.9: Two dimensional sections of the H_2/Pd(111) PES when one of the two hydrogen atoms is fixed to an fcc site. The equipotential lines ranging from 0 to 300 meV are represented in the figure.

functions, covering all the possible configurations given in table 3.2. Figures 3.9 and 3.10 show two-dimensional sections of these reduced PES that we will call PES-A and PES-B referring to a fixed hydrogen to an fcc or hcp site respectively.

The global minimum of the PES has been shifted to 0.0 meV, corresponding to the situation where the two hydrogen atoms occupy neighboring fcc sites but are slightly displaced from these positions, as shown in the table 3.3. The energies given in figures 3.9b and 3.10b (the same as in table 3.2) are therefore slightly above these values, given that in PES-A and PES-B one of the two hydrogen atoms is fixed exactly on the crystallographic coordinates of the fcc or the hcp site. This figure explicitly illustrates some examples of the configurations given in figure 3.8. For instance, it shows that when the second H is located on a non-neighboring fcc site,

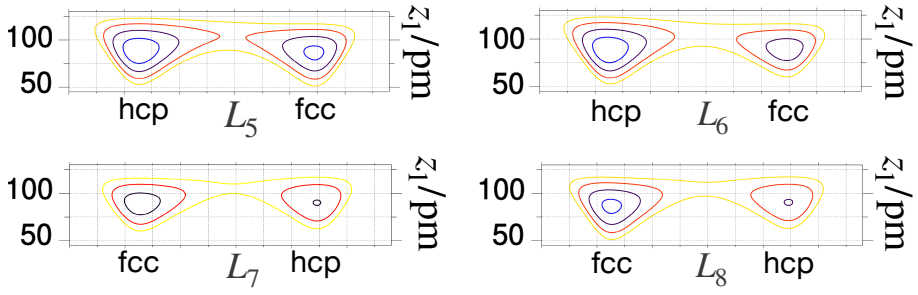

(a) Two dimensional section of the PES along (L_k, z_1).

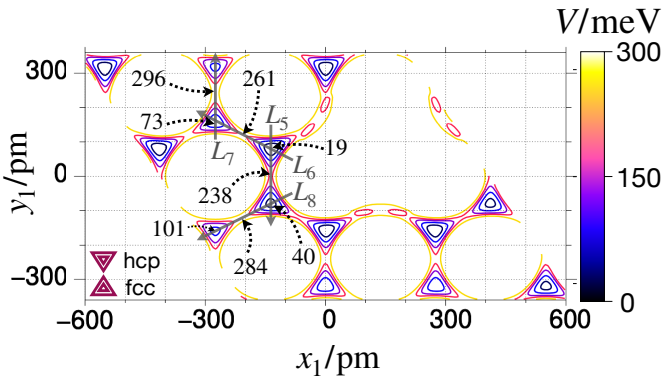

(b) Two dimensional section of the PES along (x_1, y_1) with $z_1 = z_2 = 87$ pm.

Figure 3.10: Two dimensional sections of the H_2/Pd(111) PES when one of the two hydrogen atoms is fixed to an hcp site. The equipotential lines ranging from 0 to 300 meV are represented in the figure.

its energy is 69 meV, whereas it is 2 meV in the opposite case[5]. The figure also shows the values of the potential barriers in these two situations. The barriers are all higher than that of a single hydrogen atom. To better visualize these barriers, figures 3.9a and 3.10a show two-dimensional sections perpendicular to the surface along the lines joining the different sites. These barriers give us information about the dynamical behavior of H_2 system on the Pd(111) surface. For example, if both hydrogen atoms are located on fcc sites, it is more favorable for one hydrogen to pass through the barrier L_1 to the neighboring hcp site compared to the others. The same reasoning could be applied to other sites on the grid. This allows us to identify

[5]The energy of the system increases when a hydrogen atom approaches the nearest site where the other one is fixed. In figures (3.9,3.10), the PES section has been limited to 300 meV. No potential lines therefore appear around this site.

the most "favorable" diffusion channels for a given configuration.

To conclude this section, analysis of the PES structure of H_2/Pd(111) has enabled us to identify the various possible minima of the potential. Each minimum corresponds to several energetically equivalent situations. The direct consequence of this finding is that our system will be highly degenerate, and this degeneracy will evidently emerge in the calculations of stationary states. In addition, analysis of the PES has shown an important difference between the potential barriers surrounding the different potential wells of the surface. This will have a significant impact on the dynamics of the system and also on the "intensity" of the tunneling that can occur. All these elements are necessary to understand correctly the behaviour of the adsorbed hydrogen atoms on the palladium surface.

3.2.3 Product form of the potential using potfit

The analytical formula of the potential as defined by Dong [23] contains non-separable multidimensional terms, making its decomposition into the sum of products of one-dimensional terms required for MCTDH calculations infeasible. We therefore used the potfit program presented in section 2.3.4 to approximate the PES of H/Pd(111) and H_2/Pd(111) systems with a representation of the desired form. In this section, we give some technical details of the different parameters used for the representation of the potentials with potfit.

As mentioned in the previous section, we use a periodic approach to simulate an infinite surface. Given that periodicity is defined at the level of the twisted basis, we define the Hamiltonian modes by the twisted coordinates of the hydrogen atoms. The formulation of the kinetic energy operator in this basis was given in equation 2.24. The PES were already formulated using those coordinates by the authors. The very first step is to define the grid in which we wish to perform our calculations. Since we wish to study the dynamics of hydrogen atoms adsorbed at the Pd surface in an energy range from 0 to 500 meV, the wave functions of these systems will mainly occupy regions of space close to the surface where the potential is relatively low. We saw in the previous section that the minima of the potential are located around $z_t = 90$ pm from the surface. The grid should contain all these minima as

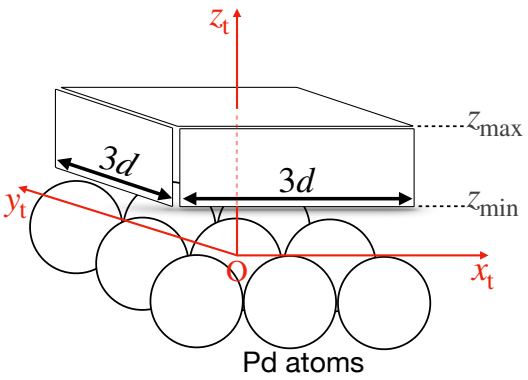

Figure 3.11: Schematic representation of the grid used for periodic calculation.

well as all the more energetic regions located below and above this plane that the wave function can reach during simulation. We therefore considered a grid height $z_t \in [z_t^{min}, z_t^{max}]$ with $z_t^{min} = 20$ pm and $z_t^{max} = 170$ pm. This region of space largely encompasses the energy domain of our study, to ensure that the system wavefunction vanishes systematically at the grid edge in the z_t coordinate. The coordinates x_t and y_t were naturally chosen to occupy the entire periodic cell used in the PES[6]. They are therefore given by $x_t \in [-3d/2, 3d/2]$ and $y_t \in [-3d/2, 3d/2]$ where the center of the reference frame coincides with the center of the Pd atom located in the middle of the grid as shown in figure 3.11.

The next step is to define the number and type of primitive basis functions to be used. As mentioned in section 2.3.1, exponential-type primitive functions are well suited to periodic DOFs, while sine-type primitive functions are well suited to DOFs describing the motion of a particle confined to a segment of space. For each hydrogen atom, we have therefore chosen exponential DVR functions for the x_t and y_t modes, and sine DVR functions for the z_t mode. The number of primitive functions should be chosen to match the variation in potential. The grid we use contains 18 potential wells located at the fcc and hcp sites separated by potential barriers. The grid points where the DVRs are located are homogeneously distributed, and the distribution of these points should be dense enough to correctly describe the system's potential wells and potential barriers, and small enough to avoid very long calculation times. The dimensions of the H/Pd(111) and H_2/Pd(111) systems are different, so we have

[6]It is possible to construct a periodic grid smaller than the one used, but this can lead to situations where hydrogen atoms interact with their 'images' giving non-physical results.

chosen a parameterization for the potential representation adapted to each situation. In the following, we will describe the potfit parameters used for these two systems.

Potfit for H/Pd(111)

In the case of a single hydrogen atom, the PES is a three-dimensional function, which does not represent a major difficulty for numerical calculations. We have therefore chosen a primitive basis that is amply sufficient to represent the potential. The grid length of x_t and y_t is greater than that used for z_t. We considered fewer primitive functions for the latter and we chose a basis containing 61×61×31 DVRs as shown in table 3.4.

coordinate (κ)	x_t	y_t	z_t
DVR	EXP	EXP	SIN
N_κ	61	61	31
m_κ	30	30	contr

Table 3.4: Primitive functions used for potential representation of H/Pd(111). EXP and SIN denote exponential and sine DVRs respectively. N_κ and m_κ represent the number of DVR and SPP functions used for each DOF κ.

Once the primitive grid has been defined, we proceed to build an SPP basis set which will be used to directly represent the potential. The use of potfit requires a contraction on one of the modes used. We have chosen to contract over the z_t mode and work with 30 SPP for the x_t and y_t modes. There is no direct way of estimating the number of SPP required for the system's DOFs, the only way to assess the quality of the basis is to look at the natural potential populations $\lambda^{(\kappa)}$ which represent the weights of the SPP (see section 2.3.4). These are ordered in ascending order, the sum over the weights of the neglected SPP gives an idea of the total contribution of these vectors to the representation of the potential. When this quantity becomes small, we truncate the primitive basis with the number of SPP selected. In the case of the basis we have used, this quantity is : $\sum_{m_x=31}^{N_x} \lambda_{m_x}^{(x)} \approx \sum_{m_y=31}^{N_y} \lambda_{m_y}^{(y)} \approx 10^{-10}$ which is completely negligible for our calculations. The rms error Δ_{rms} on the fit can then be evaluated on all grid points by comparing the values of the original potential and those obtained with the program. We saw in section 2.3.4 that weights can be added

to the SPP in order to reduce the error mainly in relevant regions, in which case we speak of weighted rms-error $\Delta^{\mathrm{w}}_{\mathrm{rms}}$. These weights can be introduced separately for each DOF or in a correlated way. In the latter case, a condition is imposed directly on the energy interval on which we want to optimize the potential called relevent regions. The weights are then set to 1 within relevant region and are 0 otherwise. To illustrate this, we carried out a calculation without the use of weights and another with the addition of a constraint on the optimization of regions defined by $V \leq 500$ meV. Figure 3.12 shows the difference in absolute values between the representation of the potential with the program and the exact values taken on the grid point belonging to the plane of equation $z_{\mathrm{t}} = 90$ pm in both calculations.

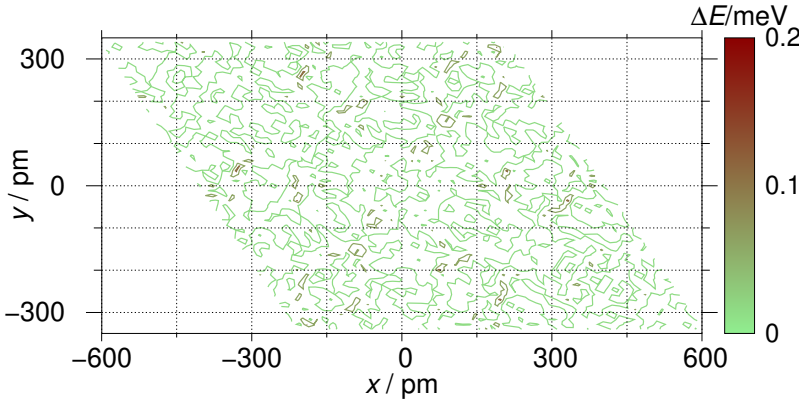

(a) Without using weights.

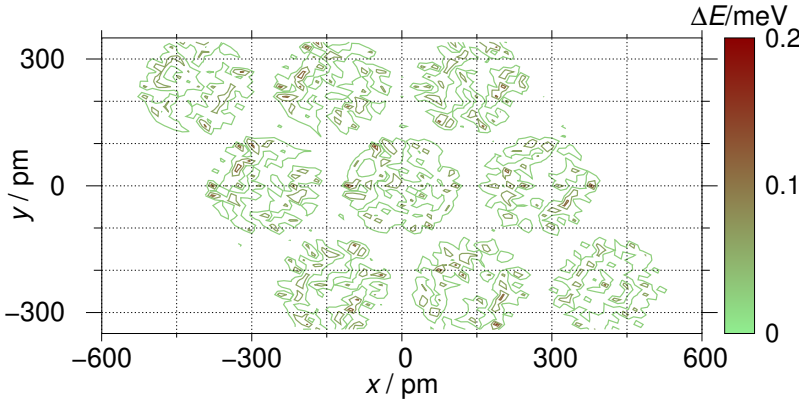

(b) With correlated weights for $V \leq 500$ meV.

Figure 3.12: Two-dimensional representation giving $|V - V^{\mathrm{app}}|$ at each grid point located at z_{t}=90 pm. V and V^{app} represent the original potential and that obtained with potfit.

In the first case (figure 3.12a), the error is distributed almost homogeneously over the grid, while in the second it is mainly concentrated in regions of high potential values. Here we have only considered a single plane of the total grid, but that's enough to illustrate the impact of weights on the approximation. The total number of grid points where $V \leq 500$ meV represents around 31% of the total grid. The potential error is then considerably reduced in restricted regions that are frequently occupied by the wavefunction during propagation. In this example, however, even if $\Delta^{\mathrm{w}}_{\mathrm{rms}} \leq \Delta_{\mathrm{rms}}$, we can see that the error in both examples is already very small, on the order of a few hundredths of a meV in both cases. The use of correlated weights becomes indispensable for systems with a very large primitive basis, as we shall see later in the potential representation of the H_2/Pd(111) system. In the present case, the potfit calculation was very fast (less than a minute) and the results sufficiently precise without the use of weights and with an SPP basis of dimension 30×30 only. One should recall that subsequent propagation or relaxation calculations with MCTDH become substantially faster, if the SPP basis is small.

Potfit for H_2/Pd(111)

The PES of the H_2/Pd(111) system is a six-dimensional function that depends on the three twisted coordinates of each hydrogen atom. The grid used to describe each DOF should be minimized as much as possible to avoid a large total grid dimension. In this case, we chose to work with 41 exponential DVRs for the x_t and y_t modes and 15 sine DVRs for the z_t modes of each H. Table 3.5 summarizes the parameters for the H_2/Pd(111) potfit.

The total dimension of the grid is given by $(41\times41\times15)^2$, which represents hundreds of millions of primitive basis functions. Reducing the basis size is therefore essential to make numerical calculations feasible. As a first step, we proceeded to combine the system's DOFs. This means using multidimensional SPP that treat several DOFs as a single mode. In this situation, we have six DOFs, so there are several possible combinations. In principle, all combinations are feasible, but one needs to choose the one that is adapted to the correlations between the system's DOFs. We considered two types of combination in the course of this project: firstly, a combination based on the idea that individuel modes of the two hydrogens are strongly correlated. In

	First hydrogen			Second hydrogen		
coordinate (κ)	x_t	y_t	z_t	x_t	y_t	z_t
DVR	EXP	EXP	SIN	EXP	EXP	SIN
N_κ	41	41	15	41	41	15
mode combination	(x_t,y_t,z_t)			(x_t,y_t,z_t)		
m_κ	5000			contr		

Table 3.5: Primitive functions used for potential representation of H_2/Pd(111). EXP and SIN denote exponential and sine DVRs respectively. N_κ and m_κ represent the number of DVR and SPP functions used for each DOF κ. The DOFs of each hydrogen atom have been combined into a single mode.

this case, we combined the DOFs with the same coordinate for both hydrogens, resulting in three modes of the type $Q_1 = (x_1, x_2)$, $Q_2 = (y_1, y_2)$ and $Q_3 = (z_1, z_2)$, where the index relates to the twisted coordinate of hydrogen atom 1 or 2. In the second configuration, we consider that there are more correlations between the DOFs of the same hydrogen atom than between the others. We then combined the three DOFs of each atom separately, giving $Q_1 = (x_1, y_1, z_1)$ and $Q_2 = (x_2, y_2, z_2)$. Both representations of the potential were made, but it turned out during the eigenstate calculations that the second type of combination is much more suitable for the potential we're using. We will discuss this point later in the time-(in)dependent studies. This type of combination allows us to drastically reduce the number of expansion coefficients given in equation 2.43, the disadvantage being that the SPP are now multidimensional and defined on a grid of size (41×41×15), which can slow down their construction. We then selected m_1=5000 SPP to represent the Q_1 mode and contracted over the Q_2 mode. The number of SPP is chosen so as to reduce the rms error, which is exactly equal to the sum of the natural populations of the SPP that we neglect, given that the contracted mode is not counted. The number of mode 1 SPP we used represents around 5000/(41×41×15)≈25% of the associated primitive basis. The sum of the natural potential population of the remaining 75% is around 70 meV, which represents a non-negligible amount. To reduce this error, we have optimized only those regions of the grid where the potential is less than 500 meV, representing only 1.9% of the total grid points. Potfit allows to add several

iterations after the end of the calculation to re-optimize the SPP and to better represent the potential in these regions. This finally enabled us to reduce the $\Delta^{\mathrm{w}}_{\mathrm{rms}}$ error to less than 1 meV which is still very reasonable given the size of the grid.

The representation of the potential in the sum of product form required for MCTDH calculations was done finally with a very reasonable number of basis vectors. The calculation took around 75 h. However, The dimension of the SPP are relatively large and this combination mode should be identical to that used in MCTDH calculations. The SPF will therefore have the same dimensionality, which could slow down their propagation. When the dimensionality of the SPF is large, MCTDH suggest a Multi Layer version (ML-MCTDH) where the SPF are themselves propagated with MCTDH. But in our case, the computation time was generally reasonable and we finally refrained from using the Multi Layer version.

Chapter 4

Study of vibrational stationary states of H/Pd(111) and H_2/Pd(111)

The eigenstates of the hydrogen atoms adsorbed on the palladium Pd(111) surface will be discussed and analyzed in this chapter. As mentioned previously, a periodic approach is used with an elementary cell containing 9 fcc sites and 9 hcp sites. The latter represent the regions where the potential wells are located. They therefore correspond to the most stable adsorption sites at the surface, around which the atoms may move. Such a motion is of vibrational nature and therefore stationary states are naturally referred to as being vibrational. The study we have carried out concerns the case of a single or two hydrogen atoms contained in this periodic cell. These two systems correspond to a substrate coverage of around 5.55 % and 11.1 % respectively if we consider that the coverage is given by the number of the occupied adsorption sites by hydrogen atoms. This study has also revealed the presence of an important tunneling impact on most of vibrational states, as well as a strong Fermi resonance [7] between some system modes. In the following, we'll start by discussing some of the technical tips we've used to realise the calculations we've carried out, then we'll present the obtained results for the calculations of the vibrational stationary states of these systems.

4.1 Methods and calculation details

4.1.1 About the initial wave function

The calculation of eigenstates of a system using the relaxation method is performed by propagating a given state in negative imaginary time $t = -\mathrm{i}\tau$ with $\tau \in \mathbb{R}^+$ (section 2.3.3). Its use therefore requires the construction of an initial wave function (IWF) as in a propagation calculation. The latter should be adapted to the eigenstate to be determined. Let us denote the eigenenergies and eigenvectors of a given Hamiltonian $\hat{H}$ by $\{E_k\}$ and $\{|\varphi_k\rangle\}$ respectively. The evolution in imaginary time of a state initially prepared in $|\Psi(0)\rangle$ in the eigenbasis is given by :

$$|\Psi(\tau)\rangle = \sum_k c_k(0) e^{-E_k\tau/\hbar} |\varphi_k\rangle \tag{4.1}$$

Such that $c_k(0) = \langle\varphi_k|\Psi(0)\rangle$. Relaxation will therefore lead the system to evolve towards the lowest-energy eigenstate of those initially contained in $|\Psi(0)\rangle$, i.e. $\langle\varphi_k|\Psi(0)\rangle \neq 0$. We must therefore systematically ensure that the overlap between the IWF and the target eigenstate we wish to calculate does not vanish[1]. In the case of the H/Pd(111) and H_2/Pd(111) systems, the various potential wells are located around the fcc and hcp sites. The low lying eigenstates of these two systems are thus mainly located around these sites. The nature of the IWF should then be delocalized to cover all these regions at the surface level. In its simples use, MCTDH requires the IWF to be given as a Hartree product of one dimensional functions for individual DOF. The program offers a choice of analytically predefined functions, such as Gaussian functions or harmonic oscillators [21]. It is also possible to construct the initial state numerically, such as in equation 2.36 as a superposition of primitive basis functions, giving the value c_{i_κ} of the wave function at each grid point we use. For each DOF κ a function $f^{(\kappa)}(\kappa)$ may then be defined on the associated grid such that :

$$f^{(\kappa)}(\kappa) = \sum_{i_\kappa}^{N_\kappa} c_{i_\kappa} \chi_{i_\kappa}^{(\kappa)}(\kappa) \tag{4.2}$$

With N_κ the number of primitive functions used for the κ-th degree of freedom and $\{\chi_{i_\kappa}^{(\kappa)}\}_{1\leq i_\kappa \leq N_\kappa}$ the associated DVR-type primitive basis. As this function is

[1] Otherwise the system may converge to another eigenstate.

defined only on grid points, it can be represented by a vector with N_κ components $\{c_{i_\kappa} = f^{(\kappa)}(\kappa_{i_\kappa})|\ i_\kappa = 1, \ldots, N_\kappa\}$ taken at each grid point i_κ. The total IWF is given by the product of these functions:

$$\Psi(\{\kappa\}, 0) = \prod_\kappa f^{(\kappa)}(\kappa) \tag{4.3}$$

We therefore followed this numerical approach to construct the IWF since it allows greater flexibility in its construction. A trivial choice of functions $f^{(\kappa)}(\kappa)$ are the constant (normalized) functions defined homogeneously on all grid points, giving the total wave function a flat shape that systematically ensures the occupancy of the entire surface.

$$f^{(\kappa)}(\kappa) = \frac{1}{\sqrt{N_\kappa}} \sum_{i_\kappa}^{N_\kappa} \chi_{i_\kappa}^{(\kappa)}(\kappa) \tag{4.4}$$

Although such a state fulfills the condition of spatial delocalization, the latter may still be orthogonal to some of the system's eigenstates[2]. Therefore, its decomposition in the system's eigenbasis may not cover some of the eigenstates we wish to calculate, leading to biased results. One way to fix this is to add random phases to each component of $f^{(\kappa)}(\kappa)$ in the primitive basis. To do this, we define a normalized complex random number $e^{i\theta_{i_\kappa}^{(\kappa)}}$ constructed by drawing a random angle $\theta_{i_\kappa}^{(\kappa)} \in [0, 2\pi]$ associated with each grid point. The functions $f^{(\kappa)}(\kappa)$ are now defined by:

$$f^{(\kappa)}(\kappa) = \frac{1}{\sqrt{N_\kappa}} \sum_{i_\kappa}^{N_\kappa} e^{i\theta_{i_\kappa}^{(\kappa)}} \chi_{i_\kappa}^{(\kappa)}(\kappa) \tag{4.5}$$

This allows us to "destroy" the spatial homogeneity of this state without modifying its norm. Figure 4.1 shows a two-dimensional representation of such a state. In this example, we have considered 61 grid points for each DOF (x and y), where each point is defined by a different random phase, giving this disordered and delocalized aspect to the wave function.

The use of this type of random states to define IWFs in the relaxation calculation has enabled us to determine a part of the spectrum of the H/Pd(111) system, with the correct degeneracy of each level. However, these states are initially very energetic

[2]Because this state has a constant sign and the overlap with eigenstates that change sign on the grid can vanish in some cases.

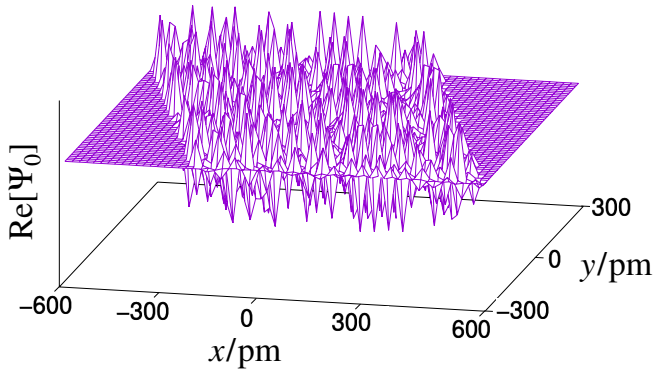

Figure 4.1: Two-dimensional representation in the xy-plane of the real part of an initial state defined with random coefficients in the primitive basis. 61 grid points were considered for each DOF.

(on average 15 eV), firstly because they are extended over the entire grid, including regions of high potential, and secondly because of the abrupt variation in the wave function, which tends to increase the kinetic energy of this state, too. The relaxation process therefore takes a long time to lower the system's energy towards stationary states, making this approach less practical, especially for the higher-dimensional system H_2/Pd(111).

A new model of the IWF more suited for our calculations was constructed where the latter have large amplitudes only around potential wells such as to cover only relevant regions. The construction of a wave function with amplitudes on both fcc and hcp potential wells cannot be written in the form of a single Hartree product required for MCTDH calculations, as the different potential wells are not aligned along a single direction including a single DOF of the system. However, it is possible to construct a Hartree product wave function having large amplitudes only around the potential barriers located at the middle of the segments connecting the fcc and hcp sites. The thus chosen $f^{(\kappa)}(\kappa)$ functions used for each hydrogen atom are given by:

$$\begin{cases} f^{(x)}(x) = C_x \sum_{k=1}^{3} e^{-1/4((x-x_k)/\Delta x)^2} \\ f^{(y)}(y) = C_y \sum_{k=1}^{4} e^{-1/4((y-y_k)/\Delta y)^2} \\ f^{(z)}(z) = \quad C_z e^{-1/4((z-z_0)/\Delta z)^2} \end{cases} \tag{4.6}$$

$f^{(\kappa)}(\kappa)$ are Gaussian functions defined in the twisted coordinates $(x, y, z) \equiv (x_t, y_t, z_t)$

with x_k=-d+$(k-1)d$, y_k=$-3d/2$+$(k-1)d$ and z_0=90 pm. C_κ and Δ_κ represent normalization constants and Gaussian widths respectively. The Δ_κ widths have been chosen to be sufficiently large ($\Delta_x = \Delta_y = d/6$ and $\Delta_z = 50$ pm) to simultaneously cover a part of the two potential wells around each barrier. This ensures the IWF to overlap with all stationary states of the system. Figure 4.2 shows a two-dimensional section in the xy-plane of the IWF used for the H/Pd(111) system. The energy of this state is around 0.9 eV and 2.7 meV for a single hydrogen atom and two hydrogen atoms respectively, which is much smaller than the energy of the previous model.

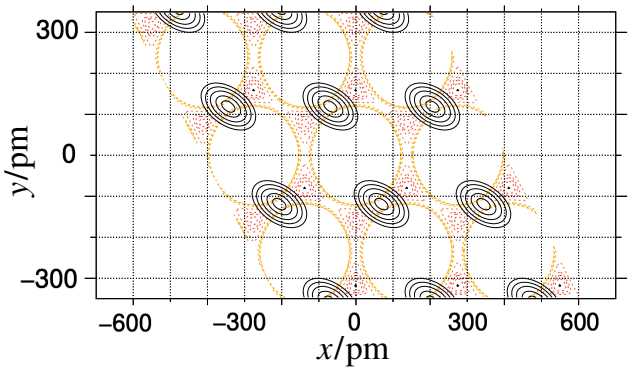

Figure 4.2: Two-dimensional representation of the initial wave function used in relaxation calculations. The latter is defined by the superposition of Gaussian functions constructed in the twisted coordinates with maxima localized at the level of each potential barrier. The functions used to construct the IWF are given in equation 4.6.

The improved relaxation method in its block form used in this project has the advantage of enriching the configuration space generated by the IWF. But despite this, the use of predefined functions in MCTDH such as Gaussian functions or harmonic oscillators like IWF led to incomplete results. The good choice of the IWF was crucial to cover systematically all the desired eigenstates with complete degeneracy of each level.

4.1.2 About the use of the block improved relaxation method

The block improved relaxation method allows to propagate simultaneously a set of initial vectors collectively called vector block to the system's eigenstates. The IWF

can indeed be seen as a 'super wave function', a vector valued wave function, where each individual component function is treated as the projection of the super wave function on an electronic state [19]. The numerical resources required to propagate such a state are far greater than those required to propagate a single state with improved relaxation. But when we want to determine a large number of eigenstates of a system, the block form turns out to be much faster and more efficient. In this section, we discuss some technical tricks used to ensure and improve the convergence of the calculation with this program.

Vector block

Let's consider for a given system L_k spectral levels with energy E_k; g_k is the associated degeneracy or near-degeneracy, as illustrated in the figure 4.3. In the case of the H/Pd(111) and H_2/Pd(111) systems, the degeneracy of each level can be estimated by counting the different energetically equivalent configurations that result from the grid symmetry as given in table 3.2[3].

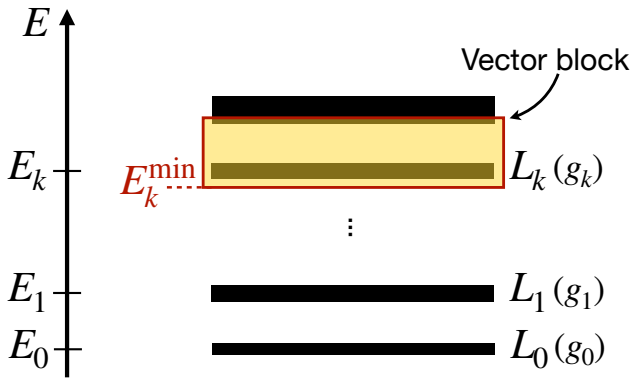

Figure 4.3: Schematic diagram showing the procedure used in the block improved relaxation method for the determination of the various degenerate levels of vibrational states.

The eigenstates of the system are computed starting from the lowest level. There is no particular constraint on the number of states to be used in a block improved relaxation and it is in principle possible to calculate hundreds of states at once.

[3]Although this approach is based on classical picture and does not take into account quantum effects, it allows us to estimate preliminary values for the g_k.

However, the SPF used in such a calculation are optimized such as to represent all the eigenstates we wish to calculate. These states may have very different structures, which may require a large number of SPF to represent them correctly. We have therefore taken a local approach, dividing the total number of eigenstates we wish to determine into several blocks targeting one or more levels of the spectrum. We start by calculating the states belonging to the L_0 level, by relaxing a block of size N^{states} which includes all the states of the target level such that $g_0 < N^{\text{states}}$. The program ensures orthogonality between these states, allowing us to determine all linearly independent eigenstates of the L_0 level.

To compute higher energy states, the program allows us to fix an energy value $E_k^{\min}$ as the minimum energy of the eigenstates one wishes to calculate. This makes it possible to target a given energy interval and filter out all states with energies below $E_k^{\min}$. To evaluate the energy $E_1^{\min}$ for the first level, we use a vector block with a size strictly larger than the degeneracy g_0 in the previous calculation. Any additional states calculated will belong to the next level, and their energy will serve as a lower bound for the next calculation. Then the same procedure is repeated for the calculation of subsequent levels. Figure 4.3 illustrates this procedure schematically. When the level degeneracy is not large, several levels can be computed together using a single vector block.

SPF basis set

The size of the SPF basis set, as mentioned in section 2.3.2, should be chosen to be large enough to correctly describe the system's wave function and small enough to avoid slowing down numerical simulations. In a dynamics calculation, the system's wavefunction must be correctly represented throughout the propagation in order to correctly reproduce the time evolution of the system's dynamic properties. In a relaxation calculation, the only property of interest is the system's final energy. The optimal representation of the wave function at the beginning of relaxation is not necessary, and only the final structure of the eigenstates is important in determining the system's eigenenergies. We followed an approach based on this idea to optimize the structure of the SPF basis as much as possible in our calculations. We subdivide each relaxation calculation into several parts. We start by relaxing the initial system

for a certain time with a small SPF basis, then we resume the relaxation with a larger SPF basis and using as IWF the final state of the previous calculation, then we repeat this scheme until convergence is reached. During the first relaxation calculation, the energies of the various states used decrease and start to oscillate after a certain time. The oscillatory behavior is in fact specific to the use of small SPF and disappears as the size of the basis increases. At the end of the last relaxation calculation, the energies of the vector block stabilize and converge towards those of the system's eigenstates. A number of tests have been carried out to verify the efficiency of this approach, using as a reference example a single block relaxation with the same basis as that used for the last relaxation calculation run of the convergence series. Both calculations give the same results, except that in the case of a single shot relaxation, the simulation time is almost three times longer. We finally followed this approach to progressively determine the spectra of the H/Pd(111) and H_2/Pd(111) systems. In addition to the block size used, SPF basis sizes vary depending on the system and also on the calculated level energies. Describing the system's excited eigenstates generally requires more SPF. Table 4.1 summarizes information on the SPF used for each system.

SPF $[n_\kappa^{\min}, n_\kappa^{\max}]$				
H/Pd(111)			H_2/Pd(111)	
n_x	n_y	n_z	$n_{x_1y_1z_1}$	$n_{x_2y_2z_2}$
$[30, 40]$	$[30, 40]$	$[4, 8]$	$[30, 100]$	$[30, 100]$

Table 4.1: Number of SPF used to describe the different system modes during relaxation calculations. The average minimum and maximum wall time required for each relaxation calculation ranges from 3h to 31h.

The eigenstate calculation of the two studied systems was focused mainly on the ground and the first exited levels. This represents 10 energy levels containing around 140 vibrational states for the H/Pd(111) system and 24 energy levels containing around 1500 eigenstates for the H_2/Pd(111) (including the degeneracy). For the first system, two vector blocks of 75 states were used. The maximum dimension of the SPF basis used represents around 11% of the total primitive basis (table 4.1). The natural population of the weakest populated SPF generated in each final

relaxation calculation is less than 10^{-3}, which is considered by the developers of the MCTDH program to be a very accurate description of the system's stationary states.

When calculating the eigenstates of the H_2/Pd(111) system, we used the same type of mode combination used to represent the potential with the potfit program. The DOFs of each hydrogen atom have been combined into a single mode. The second type of combination cited in section 2.3.4, i.e. the $Q_1 = (x_1, x_2)$, $Q_2 = (y_1, y_2)$ and $Q_3 = (z_1, z_2)$ combination, allowed us to merely determine the ground states, as convergence was not reached when calculating excited states even with very large SPF basis. As we'll see in the next section, the DOFs of each hydrogen atom are highly correlated within the same atom. It makes sense to integrate them within the same mode in order to reduce the correlated terms and the dimension of the A-vector. Because the number of eigenstates we calculated is relatively large, we subdivided the relaxation into several parts. In each calculation, a block of 160 states was used. We found that a smaller block size does not lead to convergence, especially when calculating excited states. One gets oscillatory behaviour of eigenenergies even for large SFPs basis. We are currently unable to explain this behavior. The relatively large block size allowed to stabilize the results. We used a sufficiently large number of SPF to ensure an accurate description of all block states. The natural population of the weakest populated SPF generated in each last relaxation calculation is less than 10^{-3}. The maximum size of the SPF basis used in the relaxation calculations is about $10^{-3}\%$ of the total primitive basis, which extremely reduces the numerical dimension of the problem.

Integrators

Both the SPF and the A-vector are propagated in time during relaxation according to the equations of motion given in 2.40. The Hamiltonian matrix elements, as well as the density matrix and mean field in the equations of motion of the A-vector and SPF are recalculated either after each iteration in time or kept constant for some time and then recalculated after a certain number of time steps. These two schemes are called Variable Mean-Field (VMF) and Constant Mean-Field (CMF),

respectively [15]. Both schemes have advantages depending on the situation, but in the case of a relaxation calculation, the CMF scheme is required in MCTDH. The user can choose the number of time steps in which the above-mentioned quantities are kept constant and inspect the calculations manually to check the efficiency of the scheme. Alternatively, one can choose a variable number of steps in time and define a constraint directly on the desired accuracy. The latter should normally be evaluated from errors coming from the A-vector and the SPF, but in the case of relaxation the A-vector varies discontinuously and only the variation in the SPF is taken into account in the evaluation of the number of tolerated steps. This scheme is generally the one recommended by the developers of the program, so we used it in all our relaxation calculations, defining an initial step of 0.5 fs and an accuracy of 10^{-8}, which corresponds to the recommendation given for the use of the program [21].

Integrators (CMF)	
SPF	A-vector
RK8 { accuracy $=10^{-8}$; initial stepsize$= 0.1$	rrDAV { maximal order$\leq$ dim({SPF}); accuracy $= 10^{-9}$

Table 4.2: Integrator parameters used to propagate SPF and A-vector within the block improved relaxation.

The SPF and the A-vector are propagated separately in the CMF scheme. There are several types of integrators proposed in MCTDH [15, 21]. For the calculation of a block relaxation, the most suitable integrators are the Range Kutta method of order 8 (RK8) for SPF and the Davidson method for A-vector diagonalization (rrDAV). The latter is used for real and Hermitian matrices, which corresponds to the Hamiltonian used in our calculations. Both routines take parameters like those of the CMF. The maximum order used in the Davidson routine represents the number of iterations required for convergence in each time step. This number is always smaller than the size of the SPF basis by definition, and it must be large enough to prevent diagonalization processes from failing during the iterations. As a general rule, we take it almost equal to the basis size to avoid this kind of numerical problems.

The use of the block-improved relaxation program showed a very high performance for calculating the stationary states of the two studied systems. However, the correct parameterization of the program and the use of the tricks mentioned in this section, such as the choice of the IWF and the type of mode combinations, were necessary to ensure convergence and the smooth running of the calculation.

4.2 Vibrational stationary states of H/Pd(111)

A detailed analysis of the energies of the vibrational stationary states of the hydrogen atom adsorbed on the Palladium Pd(111) surface and the structure of the corresponding wave functions will be presented in this section. The focus is on the ground (non-excited) level and other levels of the system, which can be identified as having a single quantum of vibrational motion along one of the modes. We call these levels singly excited. Some doubly excited levels will also be discussed. To support this analysis, we considered to study two model systems. Details of these studies are given in the appendices B and C, respectively, and ensuing results will be addressed in due course in this section.

The vibrational states of the hydrogen atom on the palladium surface can be separated, in zeroth order, into those with vibrational excitation parallel or perpendicular to the substrate. Perpendicular vibration coincides with the z mode, while parallel vibration includes both x and y modes. To label these states, we adopt a nomenclature of the form $N^v_{\{\mathrm{A/B}\}}$, $N \in \{0;1;2\}$ where 1 and 2 refer to vibrational states perpendicular and parallel to the surface, respectively, and 0 stands for non-excited states. The integer v gives the vibrational quantum excitation number of the state under consideration. The indices A and B stand for fcc and hcp, see section 3.1, and refer to the location of the state in the fcc and hcp sites, respectively.

This labeling of states is motivated by the local $\boldsymbol{C}_{3\mathrm{v}}$ symmetry of the potential which holds approximately in either the fcc or hcp sites (see figure 3.5). The perpendicular mode is of A_1 type, while the parallel mode is two-fold degenerate of type E. Following [40], the A_1 mode is attributed the mode number 1, the E mode is mode 2.

For example, 2^1_B refers to a state located on an hcp potential well having a single vibrational quantum excitation parallel to the substrate. When a given eigenstate has a probability density occupying both the fcc and hcp wells, the labels used for each type of site are added together. For example, $2^1_B + 2^1_A$ represents a state similar to the previous one, but delocalized on both potential wells. The same notation applies to a state with several different types of excitation. For instance $2^2_A + 1^1_A$ represents a state localized on a fcc site while mixing two zeroth order states, one with two quanta of vibrational excitation parallel and the other with one quantum of vibration perpendicular to the substrate. The sum notation actually indicates that zeroth order vibration modes cannot be separated[4], rather the parallel and perpendicular modes of the system are strongly correlated, as we shall see later, and the resulting vibrational probability density represented by such a state is given by a strong mixing of the two zeroth order vibrational modes. This mixing of zeroth order states reflect a strong coupling between the latter and is a purely quantum mechanical effect. The example $2^1_A + 2^1_B$ reflects the state of a particle tunneling under the barrier separating the sites A and B, while the particle has one quantum of vibration in mode 2 in either site; the example $2^2_A + 1^1_A$ reflects a so-called Fermi resonance [7], as will be explained below.

We recall in this context that vibrational states of type 2^2 split into two different types, A_1 and E [41]. To distinguish between these states, we shall denote them by $2^2(A_1)$ and $2^2(E)$. The combination of these different terms finally allows us to label the set of all vibrational eigenstates of the system computed in this study. Table 4.3 gives the vibrational eigenenergies of the system obtained with the block improved relaxation routine of the MCTDH program.

[4]Separable modes would have been denoted in this case by $2^2_A 1^1_A$.

Level	Sub-level	State number	Label	E_n/meV	g
1	-	1 ... 9	0_A	**0.0**	9
2	-	10 ... 18	0_B	**6.1**	9
3	3.a	19 ... 28	2^1_A+2^1_B	**73.9**	10
	3.b	29 ... 34	2^1_A+2^1_B	74.5	6
	3.c	35 ... 36	2^1_A	74.9	2
4	4.c	37 ... 38	2^1_B	78.0	2
	4.b	39 ... 44	2^1_B+2^1_A	78.6	6
	4.a	45 ... 54	2^1_B+2^1_A	**79.7**	10
5	5.a	55	$\{2^2_A(A_1)$+$1^1_A\}$+$\{2^2_B(A_1) + 1^1_B\}$	**99.5**	1
	5.b	56 ... 61	$\{2^2_A(A_1)$+$1^1_A\}$+$\{2^2_B(A_1) + 1^1_B\}$	102.1	6
	5.c	62 ... 63	$2^2_A(A_1) + 1^1_A$	105.4	2
6	6.c	64 ... 65	$2^2_B(A_1) + 1^1_B$	106.5	2
	6.b	66 ... 71	$\{2^2_B(A_1)$+$1^1_B\}$+$\{2^2_A(A_1) + 1^1_A\}$	110.2	6
	6.a	72	$\{2^2_B(A_1)$+$1^1_B\}$+$\{2^2_A(A_1) + 1^1_A\}$	**114.1**	1
7	7.a	73 ... 82	$2^2_A(E) + 2^2_B(E)$	**125.5**	10
	7.b	83 ... 88	$\{2^2_A(E) + 2^2_B(E)\}^{a)}$	127.8	6
	7.c	89 ... 90	$2^2_A(E)^{a)}$	129.3	2
8	8.c	91 ... 92	$\{2^2_A(A) + 1^1_A\}^{b)}$	130.2	2
	8.b	93 ... 98	$\{2^2_A(A_1) + 1^1_A\} + \{2^2_B(A_1) + 1^1_B\}$	130.9	6
	8.a	99	$\{2^2_A(A_1) + 1^1_A\} + \{2^2_B(A_1) + 1^1_B\}$	**131.4**	1
9	9.a	100	$\{2^2_B(A_1) + 1^1_B\} + \{2^2_A(A_1) + 1^1_A\}$	**149.1**	1
	9.b	101 ... 106	$\{2^2_B(A_1) + 1^1_B\} + \{2^2_A(A_1) + 1^1_A\}$	150.6	6
	9.c	107 ... 108	$\{2^2_B(A_1) + 1^1_B\}^{b)}$	152.4	2
10	10.c	109 ... 110	$2^2_B(E)^{a)}$	153.3	2
	10.b	111 ... 116	$2^2_B(E) + 2^2_A(E)$	155.0	6
	10.a	117 ... 126	$2^2_B(E) + 2^2_A(E)$	**156.3**	10

Table 4.3: Vibrational eigenenergies of H/Pd(111) in the (3×3)-grid. The last column of the table gives the near-degeneracy associated with each level. Footnotes: *a*) states contain some mixing of states of the A_1 type located on the opposite site; *b*) states contain some mixing of states of the E type located on the opposite site.

The elementary cell we used for our periodic calculations (see figures 3.5 and 3.11) contains 18 potential wells, 9 of which are located around fcc sites and 9 around hcp sites. The potential wells located around the same type of sites are all equivalent. This induces a configurational degeneracy for each individual level in the table given by multiples of 9, which was already addressed from a 'classical' analysis in section 3.2.1. Strictly, this degeneracy holds only approximately for low energy stationary states; it tends to break apart when level energies approach or exceed the tunneling barriers. To obtain a reference for the energy of a given level, we conducted additional calculations using a reduced elementary cell which contains both an fcc and an hcp site, a single one of each type. In the discussion following below, we shall refer to these calculations as the "1×1"-calculations. Parameters for these calculations are given as in section 3.2.3, with the difference that $x_t \in [-d/2, d/2]$ and $y_t \in [-d/2, d/2]$. In a 1×1-calculation, configurational degeneracy is reduced to 1.

The origin of remaining degeneracy g of sub-levels indicated in table 4.3 will be addressed below. We estimate the numerical error of the sub-level energies given in the table to of the order of ± 0.2 meV. This error results essentially from the block improved relaxation method with the chosen parameters, in particular the sizes of the PBF and SPF bases. Individual state energies do actually vary within this error interval, and in this sense we rather speak of an "essential", "quasi-" or "near" degeneracy, as any potentially additional splitting of the level is not resolved within the present calculations.

The quantum effects present in the system tend to mix the localized vibrational modes in addition to lifting the degeneracy of certain levels. These quantum effects also become manifest within the structure of the corresponding wave functions. The label attribution proposed in table 4.3 relies on the inspection of the spatial distribution of the probability densities.

MCTDH allows us to calculate the reduced probability density (RPD) P of the wave function of a given system. The latter is obtained by integrating the total probability density over one or more DOFs of the system to obtain a two-dimensional representation. For example, the reduced probability density of an eigenstate $|\varphi_k\rangle$

in the xy-plane is given by $P_k(x,y) = \int_{z_{\min}}^{z_{\max}} |\varphi_k(x,y,z)|^2 \mathrm{d}z$. By calculating the RPDs at the various DOFs of the system, we can visualize the shape of the total probability density of a given vibrational state, in particular its nodal structure, which potentially tells us about the type of vibrational excitation of this state. The nodal structure of densities generally has the same characteristics as the wave function, except detailed phase relationships. Figures 4.4 to 4.10 show two-dimensional representations in the Cartesian coordinates (x,y) and (x,z) of the RPDs of selected vibrational eigenstates given in table 4.3. In the following, we analyze the data contained in this table while referring line by line to the individual figures.

4.2.1 Levels 1 and 2

The vibrational states of the levels labeled 0_A and 0_B are degenerate within the numerical accuracy with a degeneracy factor $g = 9$ for both. This degeneracy is in agreement with the 'classical' analysis given in section 3.2.1, from which we deduced that the energy of the hydrogen atom is the same in any of the 9 sites of the same type. Energies given in bold face indicate that the same energy value is obtained, within the numerical errors mentioned above, from the 1×1-calculation inferred above. Bold faced energies are thus the reference energies for the given level.

The zero point energy at the lowest fcc site is around 160 meV. The 0_B level is 6.1 meV higher than the 0_A level. This energy difference is smaller that the 15 meV between the two potential well minima (see figures 3.5 and 3.7). This is due to the difference in the local curvature of the fcc and hcp potential wells. As the potential is less contracted along z at the hcp well level (figure 3.6), the wavefunction broadens and lowers its energy, thus reducing the initial energy gap between the two wells.

The RPD of two selected states, one of each in levels 1 and 2, respectively, are shown in figure 4.4. The wave function of these states is normally completely delocalized over all wells of the same type, as they correspond to Bloch waves [42]. Being essentially degenerate, any linear combination of these states is also, to an excellent approximation, an eigenstate of the system. This can result in states with distributions of the probability density that are more localized on some potential

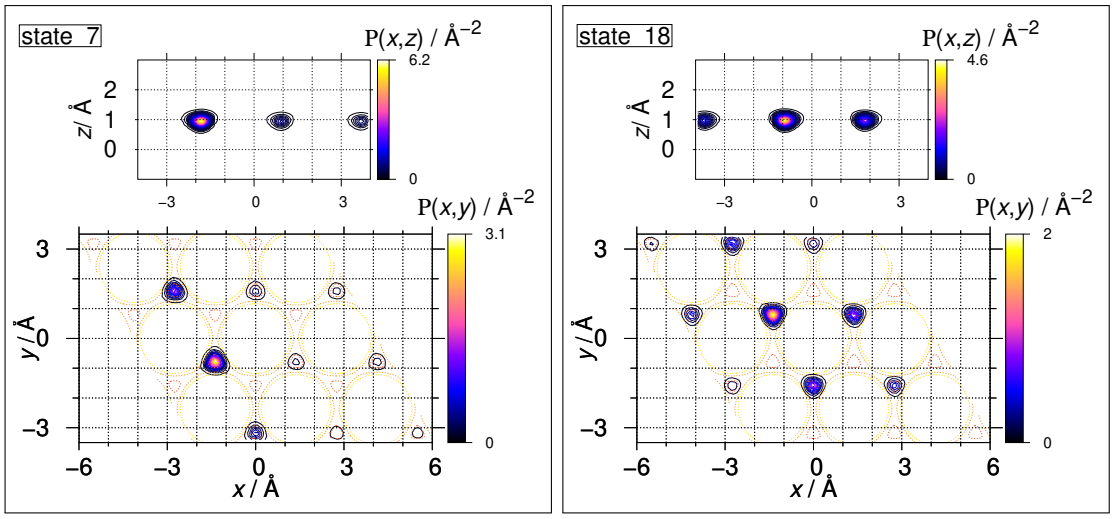

Figure 4.4: Two-dimensional representation of the reduced probability densities (RPD) of two selected eigenstates in levels 1 (state 7, left hand side) and 2 (state 18, right hand side). RPD are superimposed on equipotentials represented by dashed yellow lines corresponding to those shown in figure 3.5.

wells than in others.[5] Other states in these levels have differently distributed, yet always somewhat localized probability densities. The selection shown in figure 4.4 is just exemplary. We conclude from this figure, that levels 1 and 2 contain ground states with node-less probability densities that are localized on either the fcc or the hcp sites, which justifies the given labels.

4.2.2 Levels 3 and 4

Level 3 is a cluster of 18 close lying states gathered in groups of 10, 6 and 2 states. Individually, these sub-levels, termed 3.a, 3.b and 3.c are essentially degenerate, where 'essential' has the same meaning as discussed above. Sub-level 3.a has the same energy as in the 1×1-calculation and is consequently the reference of level 3. Sub-level 3.c has the highest energy in the cluster and is separated from 3.a by about 1 meV. This energy difference is the width of the energy band pertaining to a continuum of Bloch waves that would be obtained when the grid was enlarged

[5] In general, we can observe that for levels having a smaller degeneracy, the stationary state calculated by the program is 'forced' to delocalize over all equivalent potential wells (states 36 and 38 for example, discussed in figure 4.7).

from the 1×1 elementary cell to the infinitely large grid. The band width can be readily obtained from a calculation using a 2×2 elementary cell, but also from the calculation on the basis of the 3×3 elementary cell. For energy levels lying below the barrier separating stable sites in neighboring 1×1 elementary cells, the band width is a direct manifestation of the tunneling through that barrier.

Level 4 is, similarly to level 3, a cluster of 18 close lying states grouped in sub-levels 4.c, 4.b and 4.a of 2, 6 and 10 essentially degenerate states. The ordering of sub-levels of level 4 is given in the table as rightly opposed to that of level 3, with the highest energy in sub-level 4.a being the reference energy (bold-faced). Indeed, inspection of the RPD unveils the sub-level correspondence suggested by the ordering in table 4.3.

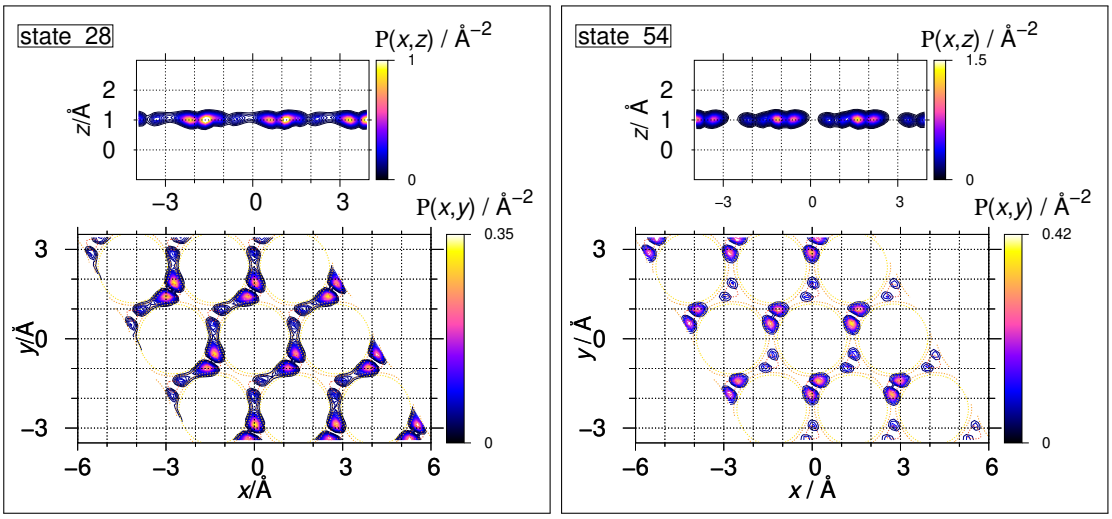

Figure 4.5: Two-dimensional representation of the RPD of eigenstates 26 (left hand side) and 54 (right hand side), lying in sub-levels 3.a and 4.a, respectively. See also the caption of figure 4.4.

Figure 4.5 shows the RPD of stationary states 26 and 54 as two typical members of sub-levels 3.a and 4.a. Both show the presence of a single node at the equilibrium sites in the $xy-$plane parallel to the substrate, while the z-axis remains node-less. Closer inspection shows that state 26 has non-zero probability density at the saddle points linking the fcc and hcp stable sites, while state 54 has additional nodes at these points. Finally, state 26, of lower energy, has predominant probability density on fcc sites and some minor probability density on hcp sites, while the higher energetic state 54 has the exactly opposite distribution.

The RPD from the 1×1-calculation correspond to the reference states of levels 3 and 4, respectively. They present essentially the same features as in figure 4.5. Plots are not shown here, for simplicity. In a 1×1 elementary cell, the hydrogen atom may occupy a single fcc (A) or a single hcp (B) site, or tunnel between both sites. From the 1×1-calculation we can clearly infer that the lower energy state, corresponding to state 26 in figure 4.5, is a lower component of a tunneling doublet, while the higher energy state, corresponding to state 54, is the upper component. We may therefore speak of an "AB"-tunneling doublet while referring to a state in sub-level 3.a and a second state in level 4.a. Because the two sites do not have the same energy, some preponderance for the occupation of a given site remains in the tunneling states. The clear attribution of state 26 as being the corresponding tunneling partner state of state 54 is blurred by the fact that sub-levels are themselves essentially degenerate, so that any linear combination of states in a given sub-level is also a stationary state. The RPD shown in figure 4.5 reflect numerically this ambiguity, which could in principle be removed by an appropriate orthogonal transformation in the respective vector spaces. The question is, what causes the remaining degeneracy.

The local $\boldsymbol{C}_{3v}$ symmetry around the potential wells at the stable sites suggests that the stationary states depicted in figure 4.5 are locally of E type. If the $\boldsymbol{C}_{3v}$ symmetry were exactly extendable over the entire 3×3-grid, each E type state would be doubly degenerate, giving rise to 18 states per type of stable adsorption site. These levels split under the symmetry group of the lattice underlying the calculation, however. This splitting gives rise to the sub-levels of degeneracy 2, 6 and 10. No further attempt was made here to determine either the actual lattice symmetry group used for the calculation, or the reduction of its representation in the space of vibrational states of the adsorbate. It is possible that irreducible representations may even lead to an additional lifting of the degeneracy that is not resolved within the accuracy of the present calculations.

Figure 4.6 shows the RPD of stationary states 32 and 43 as two typical members of sub-levels 3.b and 4.b. While we cannot obtain corresponding states from a 1×1-calculation, the shape of the functions depicted in this figure allows us to draw similar conclusions as we did from figure 4.5, with a a more pronounced preponderance of the density on the original sites: state 32 is more strongly occupying fcc sites than state

26 and, reciprocally, state 43 is more important on hcp sites than the states of sub-level 4.a. We may nevertheless still state that state 32 is a typical lower component of an AB-tunneling doublet, whereas state 43 is a typical upper component thereof.

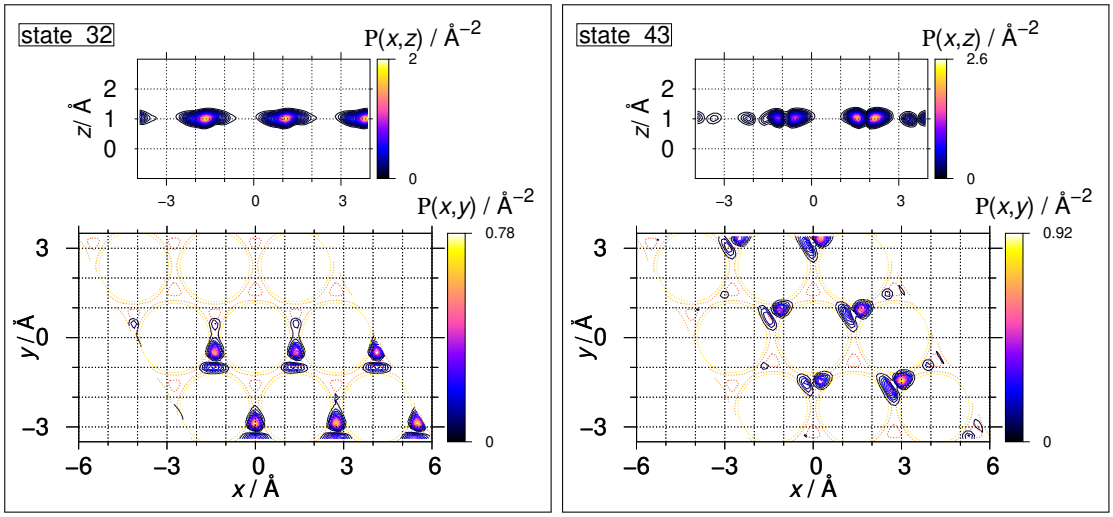

Figure 4.6: Two-dimensional representation of the RPD of eigenstates 32 (left hand side) and 43 (right hand side), lying in sub-levels 3.b and 4.b, respectively. See also the caption of figure 4.4.

Figure 4.7 shows the RPD of stationary states 36 and 38 as two typical members of sub-levels 3.c and 4.c. Again, there are no corresponding states obtainable from a 1×1-calculation. Yet, the shape of the functions depicted in this figure allows us to draw very similar conclusions as we did from figures 4.5 and 4.6, with the main differences being that the densities seem to be fully delocalized, occupying either fcc (A) or hcp (B) sites, but not both of them simultaneously.

States 36 and 38, as well as states 35 and 37 (not shown here), at first sight apparently lack any mixing of A and B sites. Naively, they could therefore be considered as uncoupled zeroth order states with respect to AB-tunneling. Uncoupled states would more likely be localized on single well of a given type, however, instead of being fully delocalized as in figure 4.7. And if they were zeroth order states, there should be 9 of each type on a 3×3 grid. Rather, the extreme delocalization shown in the figure suggests that these states result from a strong tunneling between all fcc sites, in the case of state 36 (and 35), or tunneling between all hcp sites, in the case of state 38 (and 37). Because a tunneling from one fcc to its nearest fcc neighbor

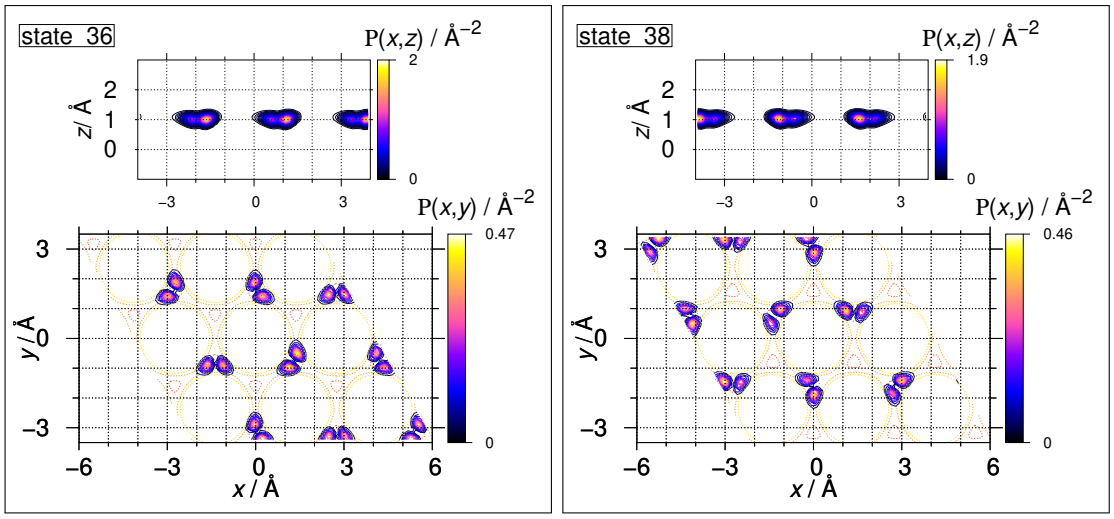

Figure 4.7: Two-dimensional representation of the RPD of eigenstates 36 (left hand side) and 38 (right hand side), lying in sub-levels 3.c and 4.c, respectively. See also the caption of figure 4.4.

site across the high energy regions at the position of the palladium atoms is quite improbable, the tunneling is more likely taking place via an intermediate site of the opposite type, i.e. a hydrogen atom might tunnel from an A to an A site via a B site, and inversely. We may thus speak of an "ABA" or a "BAB" tunneling.

All states in level 3 may be viewed as being tunneling states of the ABA type, with increasing preponderance of the A over the B site from sub-level 3.a to 3.c. Level 3, seen as a band of Bloch waves, is therefore likely generated via tunneling between the A sites, where tunneling paths are multiple and involve intermediate B sites. Reciprocally, all states in level 4 may be viewed as being tunneling states of the BAB type, with increasing preponderance of the B over the A site from sub-level 4.a to 4.c; level 4, seen as a band of Bloch waves, is similarly generated via tunneling between the B sites with multiple tunneling paths involving intermediate A sites.

States 35 and 36 in level 3.c have the largest energy separation from the states in the reference sub-level 3.a. Similarly, states 37 and 38 are furthest away from the reference level 4.a. It is interesting to note that the level 3 band is formed towards higher energies with respect to the reference energy, while the level 4 band is formed just in the opposite direction, towards lower energies with respect to the reference level. The same behavior can be seen in some higher energy level bands, but not in

all cases, as discussed below.

In summary, states in levels 3 and 4 are characterized by nodal structures at the equilibrium sites in the xy-plane, which we relate to the presence of one quantum of vibrational motion parallel to the surface, and for which the notation 2^1 applies in local $\boldsymbol{C}_{3v}$ symmetry; states of level 3 are preponderantly located on the fcc (A) site, those of level 4 on the hcp (B) site, each with some mixing of probability density in the other site due to tunneling under the barrier separating the sites of different type, dubbed AB-tunneling; each level itself spreads in energy due to tunneling under a barrier separating sites of the same type, which takes very likely place via the site of the opposite type and therefore dubbed ABA or BAB-tunneling; the spreading of a level occurs in clusters of degenerate sub-levels of finite size, when elementary cells of finite size are considered ,1×1 and 3×3 cells in this study, and evolves into the formation of continuous bands of Bloch waves for infinitely large periodic lattices. The labeling proposed in table 4.3 grasps this summary.

4.2.3 Levels 5, 6, 8 and 9

We will now proceed with the analysis of levels 5 and 6 which, as we shall see, are strongly related to levels 8 and 9. All four levels contain each 9 states which cluster in three sub-levels of different energies with degeneracies 1, 2 and 6. The sub-levels with a sub-label "a" contain a single state; they are reference levels, as they are obtained also from the 1×1-calculation. These are the states 55, 72, 99 and 100. Figure 4.8 shows the RPD of each one of these states.

All four states are characterized by the complete delocalization of the RPD over the entire grid. Furthermore, the RPD in the zx-plane are indicative of a nodal structure along the z-axis, which leads us to conclude that these states involve states with one quantum of vibration perpendicular to the substrate. In local $\boldsymbol{C}_{3v}$ symmetry, this motion transforms as an irreductible representation of type A_1 and has the mode number 1. However, the RPD also spreads in a highly symmetric way at each individual equilibrium site in the xy-plane which indicates the involvement of vibrations in parallel direction. Indeed, the second excited vibrational state of mode

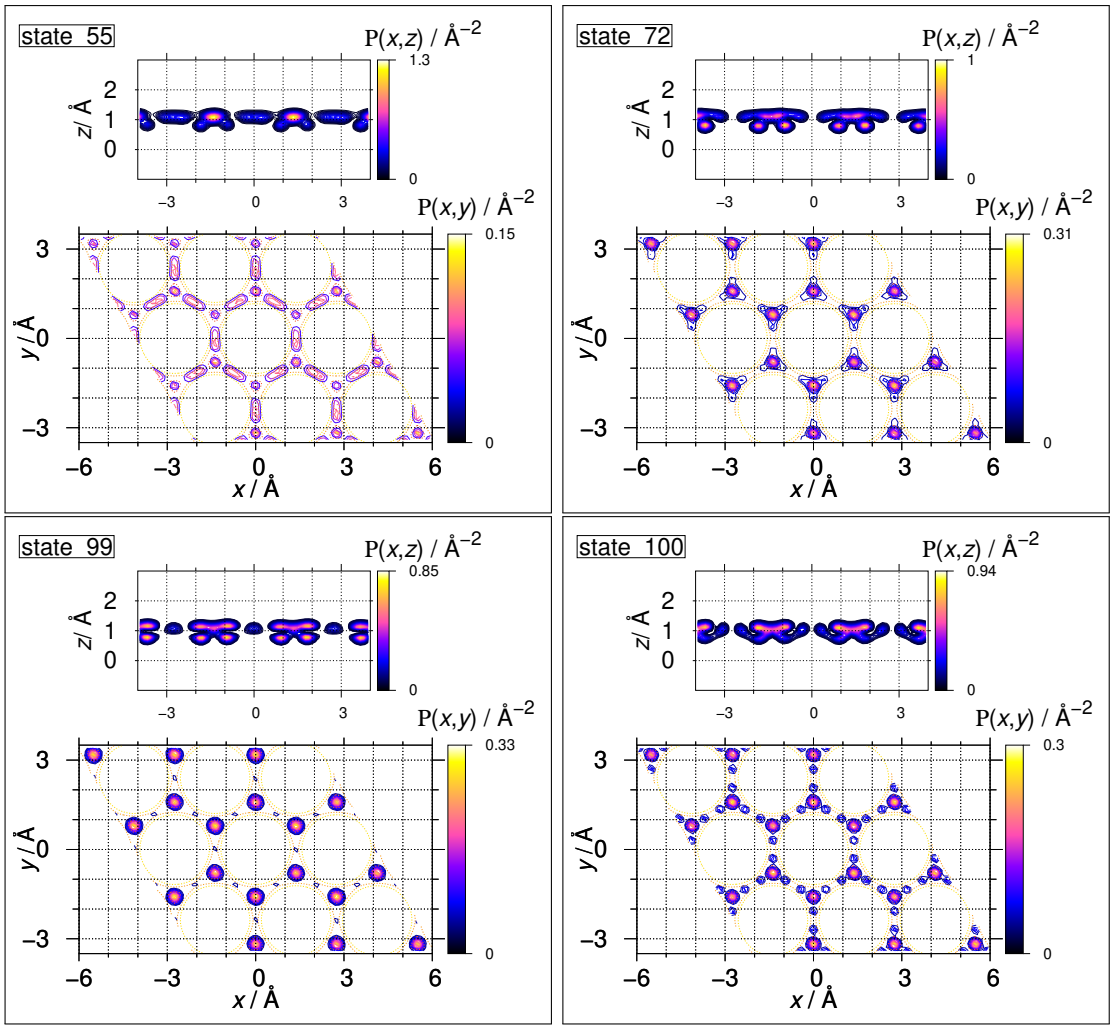

Figure 4.8: Two-dimensional representation of the RPD of eigenstates 55 and 99 (left hand side), as well as 72 and 100 (right hand side). These are the states composing levels L.a, with $L = 5, 6, 8$ and 9. See also the caption of figure 4.4.

2, in local $\boldsymbol{C}_{3v}$ symmetry, reduces to one state of type A_1 and one doubly degenerate level of type E. The $2^2(A_1)$ state may couple with state 1^1 and form a mixed state. This quantum phenomenon is known as Fermi resonance [7]. The doublet of states formed may be called a Fermi pair.

These states are thus characterized by both a global and a local spreading of the RPD. While the former can be related to tunneling between the different equilibrium adsorption sites, the latter is due to a Fermi resonance between vibrations perpendicular and parallel to the substrate. The states are related one to each other, but the detailed relationship does not become evident from inspection of the figure. The Fermi resonance is a local property and therefore one should gain more information

on its effect on the spectrum from the investigation of a local model potential mimicking the essence of the potential hypersurface in the vicinity of the equilibrium sites. Such a model is proposed in the study of appendix C.

That study shows the formation of a Fermi pair between two vibrational states with energies of 102.7 meV and 129.6 meV. We may hence conclude firmly that state 55 is the lower component of the Fermi resonance doublet, while state 99 is its upper component. Simultaneously, states 72 and 100 are the lower and upper energy components of a second Fermi resonance pair. From the energies, states 55 and 99 are more likely related to the fcc (A) site, while states 72 and 100 might be attributed to the hcp (B) site. RPD are delocalized over both sites, however. Closer inspection of figure 4.8 allows us to notice that states 55 and 99 have non-vanishing probability densities at the saddle points between the fcc and hcp sites, whereas states 72 and 100 have a nodal structure at these sites, from which we may conclude that state 99 is simultaneously the upper energy Fermi resonance partner of state 55 and the lower energy tunneling partner of state 100, while state 72 is simultaneously the lower energy Fermi resonance partner of state 100 and the upper energy tunneling partner of state 55.

Figure 4.9 shows RPD of typical states in the levels 5.b, 6.b, 8.b and 9.b. As these levels are essentially degenerate, some ambiguity remains from the numerical evaluation and an exact attribution and labeling is awkward. We may nevertheless deduce by comparison with the attributions drawn for levels 5.a, 6.a, 8.a and 9.a, that levels 5.b with 8.b on one hand, and 6.b with 9.b on the other hand contain respectively lower and upper energy components of a Fermi pair, while 5.b with 6.b on one hand, and 8.b with 9.b on the other hand contain respectively lower and upper energy components of tunneling doublets.

Similar conclusions can be drawn for the states in levels 5.c, 6.c, 8.c and 9.c. A full set of plots of all RPD up to level 10 is given in the appendix, and we refer to it for further details. We should mention that, in addition to the ambiguity caused by the numerical evaluation of eigenstates in (near) degenerate levels, with increasing energy the local $\boldsymbol{C}_{3v}$ symmetry no longer holds, and hence some mixing of E and A_1 type states become apparent in the densities.

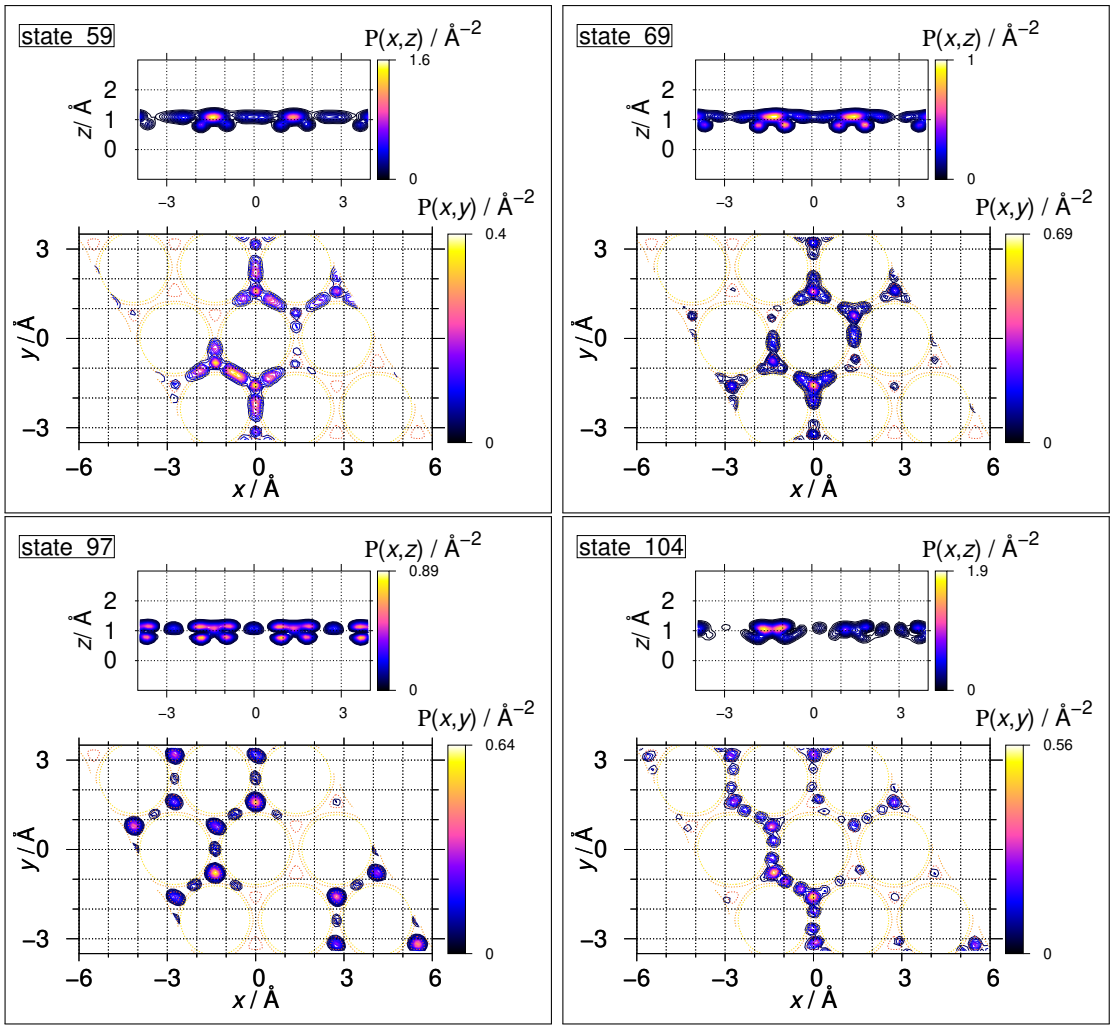

Figure 4.9: Two-dimensional representation of the RPD of eigenstates 59 and 97 (left hand side), as well as 69 and 104 (right hand side), as typical states composing levels L.b, with L as in figure 4.8. See also the caption of figure 4.4.

From the calculations we cannot extract sufficient information to actually define the zeroth order states, and hence we cannot deduce a value for the Fermi resonance coupling strength. In appendix B we discuss simple analytical models that allow us to extract such pieces of information from the model potentials. In particular, the interplay between Fermi resonance and tunneling coupling is investigated there. As shown in that study, tunneling can reduce or enhance the effective Fermi resonance coupling strength, and vice-versa. Indeed, while the states in levels 5 and 8 may be considered to be nearly equal weight mixtures of 1^1 and 2^2 zeroth order states, the states in level 6 seem to have a slight preponderance of 1^1 states, and states in level 9 of 2^2 states. Because level 6 also has some preponderance of zeroth order states

localized on the fcc site, and level 9 of states localized on the hcp site, one might say that the Fermi resonance coupling between zeroth order states located in the hcp site is slightly weaker than at the fcc site.

The lifting of configurational degeneracy in all four levels can be surely related to ABA or BAB tunneling. A detailed rationale for the remaining quasi degeneracies might be deduced from group theoretical investigations, as already pointed out in the discussion of levels 3 and 4. Interestingly, the reference sub-levels in levels 8 and 9 are close to each other, while in levels 3 and 4, or 5 and 6 they have the largest energy separation. In the $\{8, 9\}$ pair of levels, ABA or BAB tunneling bands are thus formed in the opposite direction compared to the pairs $\{4, 5\}$ and $\{5, 6\}$.

To summarize: level 5 is an ABA, level 8 is a BAB tunneling level; they respectively collect lower and upper energy components of Fermi resonance pairs of zeroth order vibrational states containing one quantum of perpendicular and two quanta of parallel vibration; levels 6 and 9 are related one to the other similarly. Simultaneously, levels 5 and 6 on one hand, and levels 8 and 9 on the other hand are pairs of AB-tunneling levels.

4.2.4 Levels 7 and 10

The remaining two levels to be discussed in table 4.3 can be attributed to states essentially composed of the E-type of zeroth order states with two vibrational quanta in parallel direction, and tunneling mixtures thereof. Figure 4.10 shows the RPD of typical members of the reference sub-levels 7.a and 10.a. States in the other sub-levels are less well delocalized and also contain some ad-mixture of zeroth order vibrational states of the A_1 type, which become possible, as already discussed above, due to the gradual breakdown of the $\boldsymbol{C}_{3v}$ symmetry with increasing energy. General trends can still be recognized, however.

Level 7 collects lower energy components of AB tunneling pairs of zeroth order vibrational states containing two quanta of parallel vibration, while level 10 contains the corresponding upper energy components. The relation between these levels is similar to that between levels 3 and 4, but both their average energy gap as well

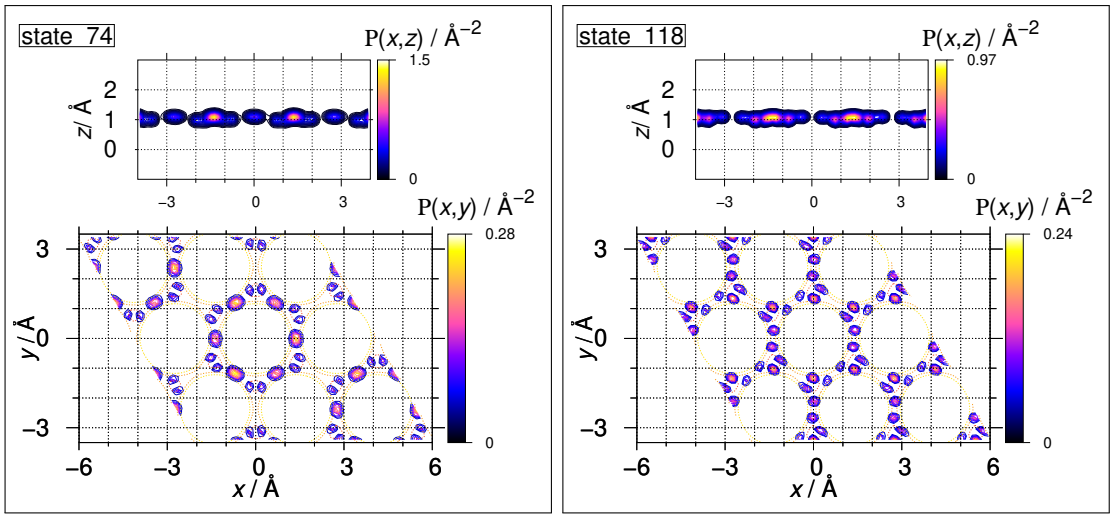

Figure 4.10: Two-dimensional representation of the RPD of eigenstates 74 (left hand side) and 118 (right hand side), lying in sub-levels 7.a and 10.a, respectively. See also the caption of figure 4.4.

as their internal ABA or BAB tunneling band spread are larger than in the case of the lower energy levels. The average energy of level 7 is of the same order than the barrier of $\sim$ 120 meV to AB-tunneling on the electronic potential from figure 3.7, that of level 10 is even beyond. This does not mean that the hydrogen atoms move more freely over the barrier, as there will still be a zero point energy from the motion orthogonal to the tunneling path that is added to the electronic barrier, by which the effective barrier is increased. In multidimensional systems, tunneling can indeed occur "over the barrier" [43, 24], and can even be inhibited far above the barrier [44].

4.3 Comparison with other work and assessment of the experimental spectrum

Calculated levels may be compared with results from previous work [45, 39], in particular with results obtained in Firmino's thesis [46]. In [45, 46], contrary to the study carried out in the present work, vibrational eigenstates were calculated using a variant of the PES from [23] that was parameterized on the basis of periodic grid DFT calculations relying on cells containing 10×10 Pd atoms, see also section

2.2. In the following, we shall refer to that PES parameterization as being the "10x10-PES", while the parameterization used in the present work, see also sections 3.2.1 and 3.2.2, will be called "3x3-PES", for brevity. The analytical form and the parameters of the 3x3-PES are given in appendix A

Quite generally, we note here that the eigenvalues reported by Firmino [46] and Firmino *et al* [45] were systematically calculated by multiplying the raw MCTDH data with the factor $2/\sqrt{3}$. This factor corresponds to the Jacobian of the coordinate transformation from the Cartesian to the twisted coordinates defined in section 3.1.2. It was argued there, that this factor had to be considered in the calculation of matrix elements ensuing the MCTDH calculations. Indeed, the Jacobian needs to be considered in the evaluation of probability densities, but not in the calculation of matrix elements.

This misinterpretation of the MCTDH working equations led to incorrect eigenvalues in [45, 46]. For instance, the eigenvalues for the lowest excited vibrational level reported in table 7 of Firmino's thesis for the H/Pd(111) system is 743.6 $hc\,\mathrm{cm}^{-1}$, corresponding to 92.2 meV. This value must be corrected to $(92.2 \times \sqrt{3}/2)\,\mathrm{meV} = 79.8\,\mathrm{meV}$. The tunneling band with for this level given in column “grid 3” of that table given as 0.06 meV, should rather be 0.05 meV. The corresponding values from the evaluation of the 3x3-PES in table 4.3 are about 74.5 and 1 meV, respectively. Similarly, the average energy in level 5 is about 102 meV, for the 3x3-PES, the corresponding band width is 5 meV, while these values are 112.5 and 1.3 meV for the 10x10-PES. Even by considering the correction factor of $\sqrt{3}/2$ for all levels reported in the work of Firmino *et al*, we find that the vibrational eigenvalues obtained from the evaluation of the 10x10-PES are larger, the tunneling splittings smaller than the corresponding values for the 3x3-PES. This comparison, as well as the comparison of the barrier energies and curvatures of the potential energy surfaces show that the 10x10-PES is clearly "stiffer” than the 3x3-PES.

The PES derived in [47] used by Saalfrank and Tremblay in [39] leads to even larger vibrational eigenvalues. These authors obtain from calculations on a 1×1-grid roughly 89 and 114 meV for the corresponding levels 3 and 5 in table 4.3. As reported by Tremblay [48], the wave function structure of the higher energetic

vibrational eigenvalues also reveal the typical form a Fermi resonance between zeroth order modes of the type 1^1 and 2^2.

The accuracy of the calculated eigenvalues, and consequently the underlying PES as well as the complete quantum dynamics, is ultimately to be validated by comparison with experimental data. Experimental data is available from measurements using the High Resolution Electron Energy Loss Spectroscopy (HREELS) method. These measurements were carried out by Conrad *et al.* [2] and enabled the extraction of two peaks at 96 meV and 124 meV to be associated to states with parallel and perpendicular excitation, respectively. Several aspects hamper the direct comparison between these experimental and the theoretical data investigated in this work.

First, a detailed theory for the intensity distribution of the HREELS spectrum as a function of the loss energy is at least highly complicated, if ever existant [49, 50]. In particular, selection rules are not clear or difficult to be assessed. Secondly, the experimental approach followed to extract this information does not allow us to know whether these energies correspond to that of an essentially isolated hydrogen atom located on a fcc or hcp site, or whether the latter is surrounded by other hydrogen atoms adsorbed in the surface. The HREELS spectrum of H_2/Pd(111) cannot be treated completely in this report. The theory for its calculation is based on the DSF discussed in chapter 6, but detailed calculations are still in work. Preliminary results indicate that it clearly differs from that of the H/Pd(111) system, but confirm the quality of the underlying PES.

4.4 Vibrational stationary states of H_2/Pd(111)

The presence of two adsorbed hydrogen atoms in close proximity on the palladium surface affects the spectrum of the stationary states. The interaction between these two atoms remains important even after adsoption on the surface, and correlations between them can take place leading this system to adopt a different behavior compared to the situation of an isolated hydrogen atom. We have specifically investigated the stationary states of two hydrogen atoms adsorbed on the periodic (3×3)-grid. In this section, we present the results obtained for this study.

The wave function of the total system is now represented by a six-dimensional func-

tion depending on the three DOF (x_i, y_i, z_i) of each hydrogen atom $i \in \{1; 2\}$. We saw in section 3.2.2 that this system possesses multitudes of energetically equivalent configurations to place the two hydrogen atoms on the fcc and hcp sites at the surface, leading to an important configurational degeneracy, see table 3.2. As in the case of a single adsorbed hydrogen atom, stationary states inherit this degeneracy. Non-excited, singly and doubly excited stationary states corresponding to the configurations $(\mathrm{AA})_{\mathrm{I}}$, $(\mathrm{BB})_{\mathrm{I}}$, $(\mathrm{AB})_{\mathrm{I}}$, $(\mathrm{AA})_{\mathrm{II}}$ and $(\mathrm{BB})_{\mathrm{II}}$ given in table 3.2 were calculated. This nomenclature was introduced in section 4.2. For excited states, we are mainly interested in configurations where the two hydrogen atoms occupy neighboring sites. This represents 22 levels with distinct energies.

Table 4.4 gives the eigenenergies of these levels. The first and second column of the table give the numbers of the level and the lowest state in that level. The third column gives the label used for each level. The fourth column gives a literal description of the typical motion of the two atoms in relation to the corresponding motion in the gas phase. The fifth column gives the eigenenergies of the lowest state in each level. The two remaining columns give the width and the number of states g associated to each level. The width is the energy difference between the highest and the lowest energy in each level. It is of the order of the numerical error reported in section 4.2 and, in the spirit of the discussion carried out there, we may term g a "quasi-"degeneracy factor.

Labels are assigned by looking at the structure of the reduced probability densities (RPD) of the states of each level. A two-dimensional representation of the latter is obtained by integrating the total probability density of the system over the other four unrepresented DOFs. For example,

$$P(x_1, y_1) = \int_{z_1} \int_{x_2} \int_{y_2} \int_{z_2} P(x_1, y_1, z_1, x_2, y_2, z_2)\, \mathrm{d}z_1 \mathrm{d}x_2 \mathrm{d}y_2 \mathrm{d}z_2 \tag{4.7}$$

This makes it possible to determine the spatial location of the two hydrogen atoms separately, and thus the type of configuration of the vibrational states at each level.

The labels listed in table 4.4 conform to the nomenclature used in table 3.2 to label the possible stable "classical" configurations of hydrogen atoms adsorbed on the palladium substrate. In general, the label $(\phi_{\mathrm{X}}\phi_{\mathrm{Y}})_K$ refers to linear combinations of Hartree products of monoatomic functions (MAF) $\phi_{\mathrm{X}}(i)$ and $\phi_{\mathrm{Y}}(i)$, located at the

sites X and Y, where X and Y can both take the values A and B. The index K can take the values I, II, III, etc and gives the possible classical configurations referred to in table 3.2. The monoatomic functions $\phi(i) \equiv \phi(x_i, y_i, z_i)$ are evaluated at the coordinates of particle i, where $i = 1, 2$.

The order of the MAF appearing in the symbol is irrelevant. The label $\phi_X\phi_Y$ may indeed refer to a diatomic wave function of the type

$$\Phi(1,2) \;=\; \cos(\alpha)\,\phi_X(1)\phi_Y(2) \;+\; \sin(\alpha)\,\phi_X(2)\phi_Y(1) \tag{4.8}$$

It may thus specifically also refer to wave functions of the dihydrogen system that are symmetrical ($\alpha = \pi/4$) or anti-symmetrical ($\alpha = -\pi/4$) under permutation of the nuclei, corresponding to para- and ortho-dihydrogen.

More specifically the label symbol ϕ for a MAF stands for another symbol of the type N^v, which was used to describe the H/Pd(111) system in section 4.2. It denotes the nature of an underlying local zeroth order vibrational wave function, where $N \in 0, 1, 2$ and $v = 0, 1, 2, \ldots$. Labels convey hence information on properties of preponderant zeroth order functions. A possible label may for instance be $(1^1_A\, 2^2_B)_I$, which indicates that the states are mainly composed of states with one quantum in local mode 1 at site A and states with two quanta of mode 2 at site B, where sites A and B are in the $(AB)_I$ configuration. Mode numbers 1 and 2 refer to the local $\boldsymbol{C}_{3v}$ symmetry group inferred for the H/Pd(111) system. A monoatomic function can also contain a mode combination, e.g. the label $([1^1 + 2^2]_A\, 2^2_B)_{II}$ indicates that the states it describes are mainly composed of Fermi resonance states with one quantum in local mode 1 and two quanta in local mode 2 at site A and states with two quanta of mode 2 at site B, where sites A and B are in the $(AB)_{II}$ configuration. In the latter example, it is understood that the $2^2(A_1)$ component of the 2^2 overtone state of local mode 2 is mixed with the 1^1 fundamental state of local mode 1.

Level	$n_{\min}$	label	description	$E_{n_{\min}}$/meV	ΔE/meV	g
1	1	$(0_A\ 0_A)_I$		0.00	≤ 0.1	54
2	55	$(0_B\ 0_B)_I$		5.88	≤ 0.1	54
3	109	$(0_A\ 0_B)_I$		28.20	≤ 0.1	54
4	163	$(0_A\ 0_B)_{II}$		51.34	≤ 0.1	54
5	217	$(0_A\ 0_A)_{II}$		56.34	≤ 0.1	18
6	235	$(0_B\ 0_B)_{II}$		71.64	≤ 0.1	18
7	253	$(0_A\ 2^1_A)^{\parallel +}_I$	tra h $\parallel$ AA	79.98	0.15	54
8	307	$(0_A\ 2^1_A)^{\perp -}_I$	helicopter AA	84.07	0.26	54
9	361	$(0_B\ 2^1_B)^{\parallel +}_I$	tra h $\parallel$ BB	85.01	0.31	54
10	415	$(0_A\ 2^1_A)^{\perp +}_I$	tra h $\perp$ AA	85.43	0.24	54
11	469	$(0_B\ 2^1_B)^{\perp -}_I$	helicopter BB	88.13	0.14	54
12	523	$(0_B\ 2^1_B)^{\perp +}_I$	tra h $\perp$ BB	88.79	0.16	54
13	577	$(0_A\ 2^1_A)^{\parallel -}_I$	stretch AA	91.09	0.22	54
14	631	$(0_B\ 2^1_B)^{\parallel -}_I$	stretch BB	96.32	0.33	54
15	685	$(0_A\ 2^1_B)^{\perp}_I$	tra h $\perp$ B	104.45	0.19	54
16	739	$(2^1_A\ 0_B)^{\perp}_I$	tra h $\perp$ A	106.11	0.38	54
17	793	$(0_A\ 2^1_B)^{\parallel}_I$	tra h $\parallel$ B	108.60	0.23	54
18	847	$(2^1_A\ 0_B)^{\parallel}_I$	tra h $\parallel$ A	112.54	0.24	54
19	901	$(0_A\ [1^1+2^2]_A)^{+}_I$	tra v AA	116.43	0.53	54
20	955	$(0_A\ [1^1+2^2]_A)^{-}_I$	cartwheel AA	117.19	0.37	54
21	1009	$(0_B\ [1^1+2^2]_B)^{+}_I$	tra v BB	117.98	0.49	54
22	1063	$(0_B\ [1^1+2^2]_B)^{-}_I$	cartwheel BB	118.79	0.63	54

Table 4.4: Vibrational eigenenergies of H_2/Pd(111) in the (3×3)-grid. The number of the state with the lowest energy in a level is given by $n_{\min}$, the difference between the highest and lowest energies is given by ΔE; it is also referred to as the width of the level. The last column of the table gives the near-degeneracy associated with each level. Atomic motions of adsorbed atoms can be associated to corresponding motions of desorbed atoms (either A or B) or molecules (either AA or BB) in the gas phase as follows: translational motion ("tra"), horizontal ("h"), i.e. parallel to the substrate - and here along ("$\parallel$") or at a certain angle ("$\perp$") with the interatomic axis, or vertical ("v"), i.e. perpendicular to the substrate; rotational motion either parallel ("helicopter") or perpendicular ("cartwheel") to the substrate; vibrational motion of the diatomic ("stretching").

This choice of labeling bears the caveat that MAF are supposed to be localized at a single site. Tunneling states of the AB, ABA or BAB type are delocalized states. They are prominent in the H/Pd(111) system. At first sight one could think that such states cannot be represented by the labels given here. As a matter of fact, inspection of the RPD, which is the basis of the label attribution, often does not provide us with sufficient information regarding the delocalized nature of the MAF. Consequently, despite the formally local nature of the MAF used in the labeling of the levels, simple labels remain ambiguous on the actual localization or delocalization of the monoatomic functions composing the total wave functions of the diatomic system, although a diatomic wave function such as given in equation 4.8 is delocalized[6]. In other cases, however, some RPD allow us to clearly state on the delocalization of states. This occurs, in particular, when the motion of two hydrogen atoms becomes strongly correlated and the use of MAF is no longer suitable to label the label. In such a case, additional superscript indices of the type "+" and "-" are added to the label. Other superscript indices of the type $\perp$ and $\parallel$ will also be used to differentiate directions of vibrations along the substrate.

The various levels formed have a large number of states, given the degeneracy of the system. Nevertheless, the states of each level have common characteristics. In the following, we present for each level the RPD of a typical state in that level, the analysis of which will be used to rationalize the label attributions.

We start by analyzing the non-excited states. They all lie in the six first levels $\{L_1 ... L_6\}$.

4.4.1 Analysis of non-excited states

Figure 4.11 shows two-dimensional reduced probability densities $P(x_i, y_i)$ and $P(x_i, z_i)$ for $i = 1$ (left hand side panel (a)) and $i = 2$ (right hand side panel (b)), representative of a typical vibrational state of the first level. Figure 4.11a shows presence probabilities mainly at one fcc site, with small amplitudes at other neighboring fcc

[6] A diatomic wave function such as given in equation 4.8 is composed of MAF, yet it is delocalized.

sites[7]. Figure 4.11b shows also non-zero probabilities of finding of the second hydrogen atom only on fcc sites. The latter are mainly attributed to fcc sites neighboring the ones in which the RPD are maximal for the first atom.

Level 1

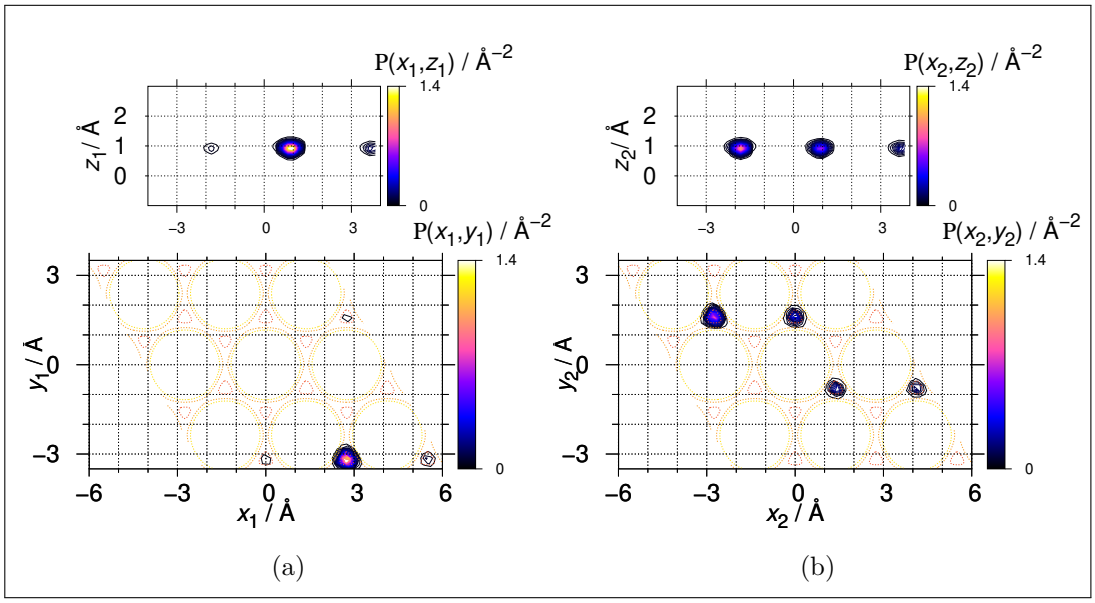

Figure 4.11: Two-dimensional representation of the reduced probability densities (RPD) of state 1 as a typical eigenstate in level 1. The dotted yellow lines show the regions of the adsoption sites on the surface. Left hand panel (a): atom 1; right hand panel (b): atom 2.

In the following, the terms "neighbor" and "non-neighbor" have a special meaning introduced in section 3.2.2. Neighboring atoms are in the configurations labeled by the capitalized roman I index, see figure 3.8. The "next-neighbor" configuration labeled by the capitalized NN index in figure 2.8e is highly energetic and will not be investigated further here.

Both representations are node-less, indicating that both hydrogen atoms are in a non-excited state. According to the label definitions outlined above we label this level by $(0_A\ 0_A)_I$ indicating that the two hydrogen atoms occupy neighboring fcc

[7]Delocalized vibrational states are given by the linear combination of localized states, and vice versa. Since these states all have essentially the same energy within the numerical accuracy, the MCTDH program renders wave functions with various degrees of delocalization within the same level.

sites and are non-excited. The energy of the first state of this level is 332.25 meV above the minimum of the PES. This energy is the global zero-point energy of the H_2/Pd(111) system and will hereafter be taken as the energy reference for all reported energies. The L_1 level has a degeneracy factor of 54, which corresponds to the configurational degeneracy resulting from placing the two hydrogen atoms in two neighboring fcc sites (see table 3.2).

Level 2

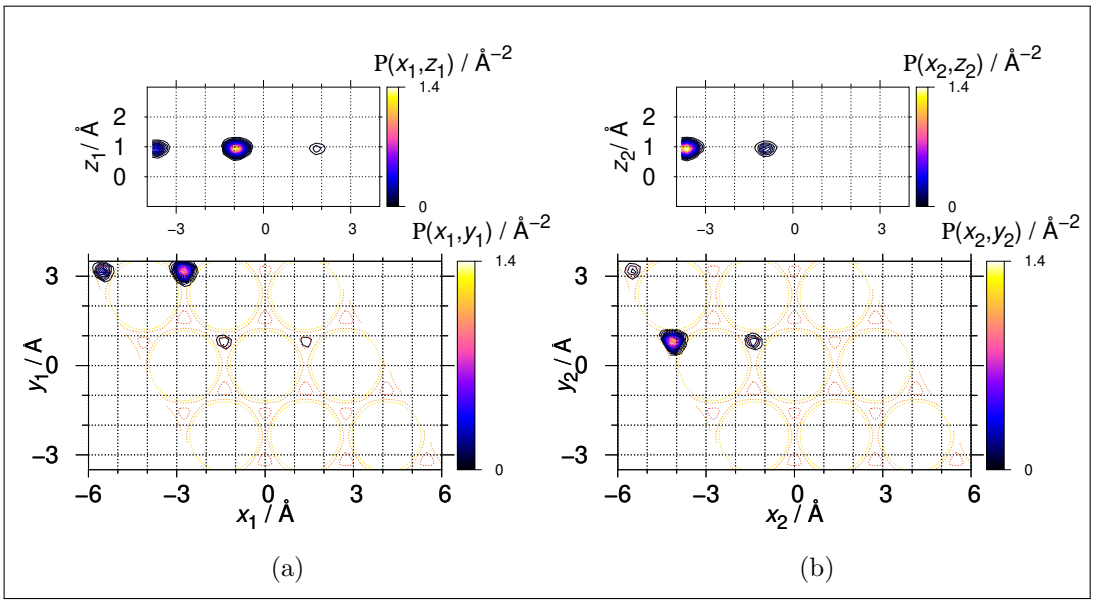

Figure 4.12: Two-dimensional representation of the RPD of eigenstate 55 in level 2. See also the caption of figure 4.11.

The RPD of a typical state in level 2 have the same characteristics as those of the previous one, except that now only the hcp sites have non-zero amplitudes. We have labeled this level by $(0_B\ 0_B)_I$ indicating configurations where two non-excited hydrogen atoms are located on neighboring hcp sites. The energy of the states of this level is about 5.9 meV higher than that of the states of level $(0_A\ 0_A)_I$ located on the fcc sites.

The difference in energy between the minima of the potentials in the $(AA)_I$ and $(BB)_I$ configurations is around 17 meV (table 3.2). The decrease of the gap between the energies of the states in these two configurations is related to the local shape of the PES at the respective sites, as revealed by figure 3.9: the relaxed local PES is

somewhat shallower at the hcp than at the fcc site, which results in wave functions for vibrational states localized at hcp sites that are broadened with respect to those localized on the fcc sites. The consequence is that the effective one-particle zero point energy at the hcp site is smaller that that at the fcc site.

Level 3

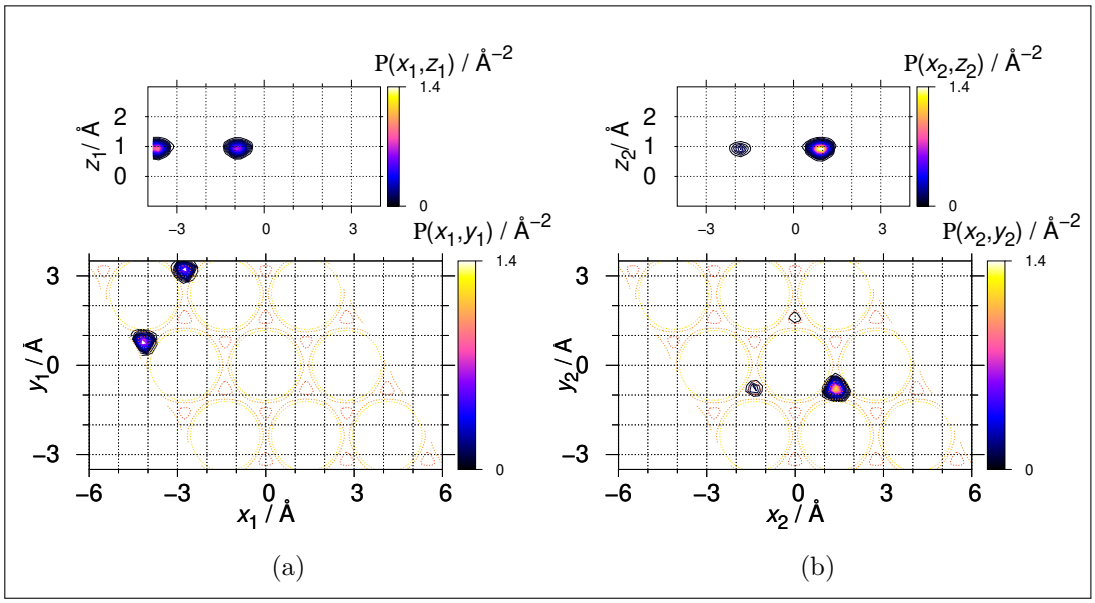

Figure 4.13: Two-dimensional representation of the RPD of eigenstate 111 in level 3. See also the caption of figure 4.11.

Figure 4.13 shows the RPD of a typical state of the third level. Figure 4.13a shows that the first hydrogen atom is likely to be found only on fcc sites, while the second hydrogen atom (figure 4.13b) is probably found only on hcp sites. This indicates a configuration in which the two hydrogen atoms occupy sites of different types. Reduced probability density analysis does not always tell us whether the two atoms are located on neighboring sites or not. But given the significant difference in energy between the two configurations $(AB)_I$ and $(AB)_{II}$ (table 3.2), we can safely assign this level to neighboring $(AB)_I$ configurations and label it $(0_A\ 0_B)_I$.

Level 4

Figure 4.14 shows the RPD of a typical state of the fourth level. The probability density of the first hydrogen atom (figure 4.14a) appears only at hcp sites, while that

of the second atom (figure 4.14b) is present only at fcc sites. This suggests that this is another (AB) type configuration. The energy of this state is about 23 meV higher than that of the previous level. This indicates that these are the higher-energy configuration states where the two atoms are further apart in a non-neighboring configuration. We have labelled this level by $(0_A\ 0_B)_{II}$ indicating the two hydrogen atoms are non-excited and occupy non-neighboring fcc and hcp sites.

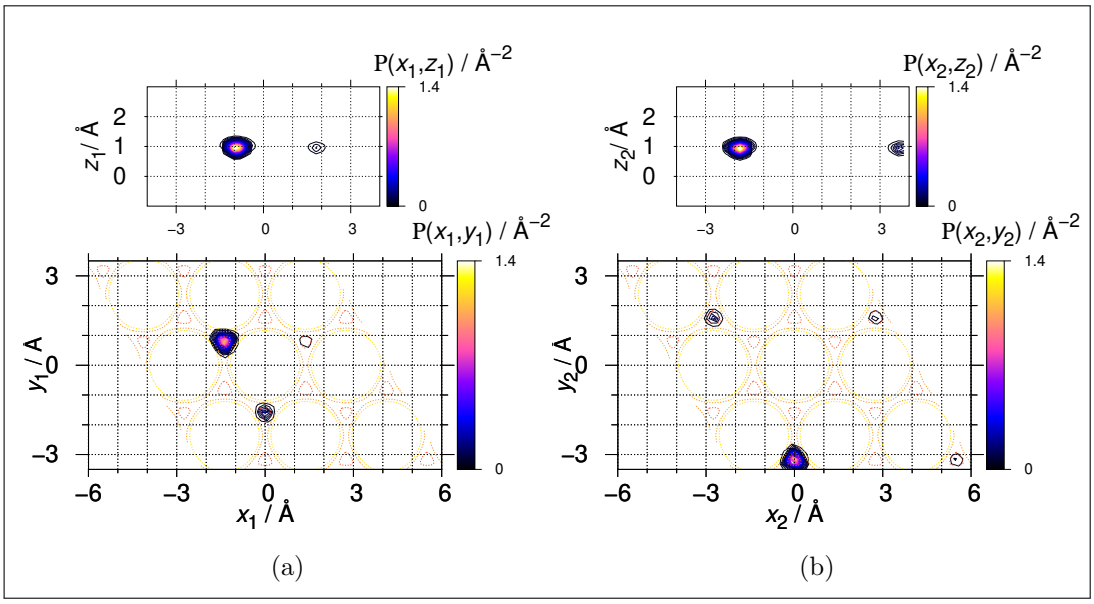

Figure 4.14: Two-dimensional representation of the RPD of eigenstate 180 in level 4. See also the caption of figure 4.11.

Level 5

The RPD of this state, shown in figure 4.15, indicate that the two hydrogen atoms are probable only at the fcc sites. The structure of this state is highly localized. Clearly, the two hydrogen atoms occupy non-neighboring fcc sites. We thus label this level $(0_A\ 0_A)_{II}$. The energies of the states of this level are about 5 meV higher than those of the $(0_A\ 0_B)_{II}$ level. Classically, this configuration is 3 meV higher than the $(AA)_{II}$ configuration (table 3.3). Similarly to the situation discussed above for level 2, this is due to the shape of the local potential in each one of these two configurations. The two-dimensional cuts of the potential given in figure 3.9b (section along line 4) show that the potential is slightly more contracted in the $(AA)_{II}$ configuration than in the $(AB)_{II}$ configuration (this can be seen by looking at the gap between the equipotential energy lines around the potential wells). This tends to increase the

effective one-particle vibrational energies in these (AA)-type configurations relative to those in the (AB)-type configurations.

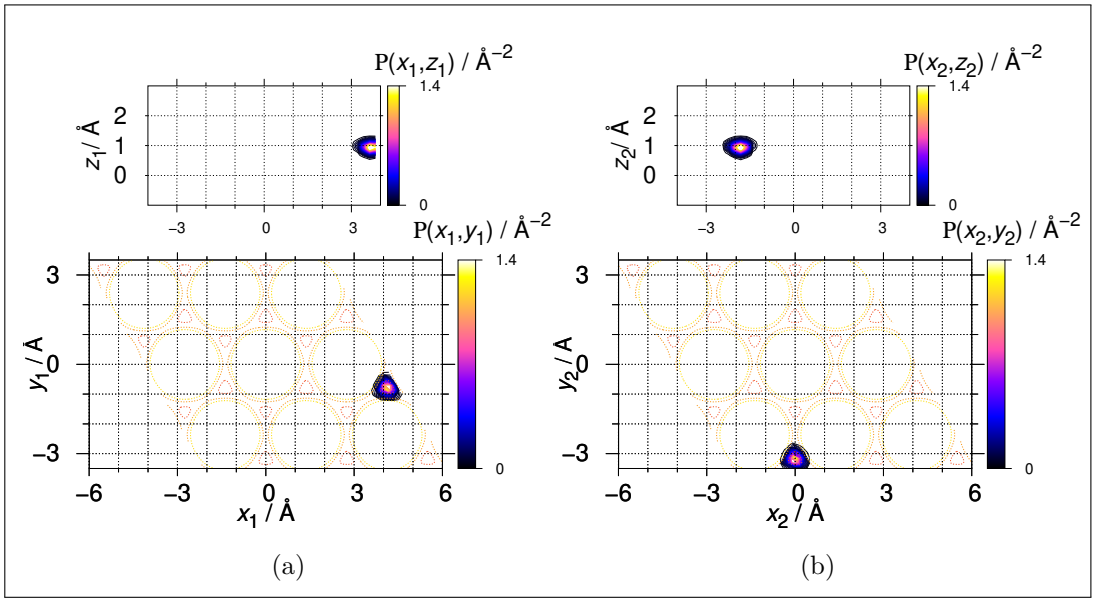

Figure 4.15: Two-dimensional representation of the RPD of eigenstate 229 in level 5. See also the caption of figure 4.11.

Level 6

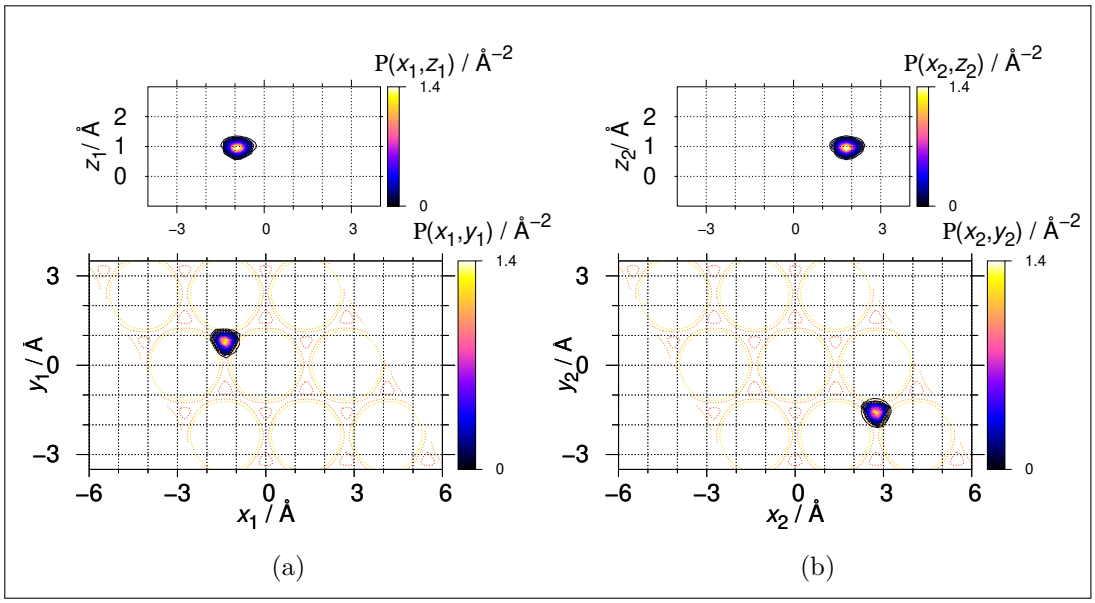

Figure 4.16: Two-dimensional representation of the RPD of eigenstate 236 in level 6. See also the caption of figure 4.11.

The RPD of this state show that the two hydrogen atoms are localized in non-neighboring hcp sites. We have labeled this level $(0_B\ 0_B)_{II}$. This is the last level of non-excited states in what we call neighboring and non-neighboring configurations, as defined in section 3.2.2. There will be non-excited states in the "nearest-neighbor" AB_{NN} configuration. Their energy is considerably higher, though, to be of interest in the present study (see table 3.2).

We thus determined all non-excited vibrational states of the H_2/Pd(111) in a (3×3)-grid. The quasi-degeneracy of these levels corresponds to the configurational degeneracy obtained with the classical analysis based on the minima of the PES. The widths of these levels are rather small ($\leq$ 0.1 meV). They are even smaller than the nominal numerical accuracy of 0.2 meV. In this sense calculations of these levels are effectively more accurate than for more energetic levels. One reason for this is that the- SPF we use in each relaxation calculation block are automatically adapted by the MCTDH program to all vibrational states targeted on that block. This renders calculations of higher lying states more difficult and less accurate. Any degeneracy lifting of these levels by tunneling or any other coupling would in principle be smaller than 0.1 meV. This concludes the set of non-excited vibrational states calculated in this study.

We will now proceed to the analysis of the excited states. For the sake of clarity, we start with levels $\{L_{15}...L_{18}\}$.

4.4.2 Analysis of mode 2 excited states in the $(AB)_I$ configuration

Level 15

We refer to figure 4.17. The RPD of the first hydrogen atom have amplitudes at the fcc and hcp sites (figure 4.17a). These densities are node-less at the fcc sites and show a single nodal structure at the hcp sites. The RPD of the second hydrogen atom have similar characteristics. This indicates that this configuration corresponds to a situation in which one non-exited hydrogen atom is located at an fcc site, while

the second one is located at a hcp site and has one quantum of vibrational excitation in a mode parallel to the substrate.

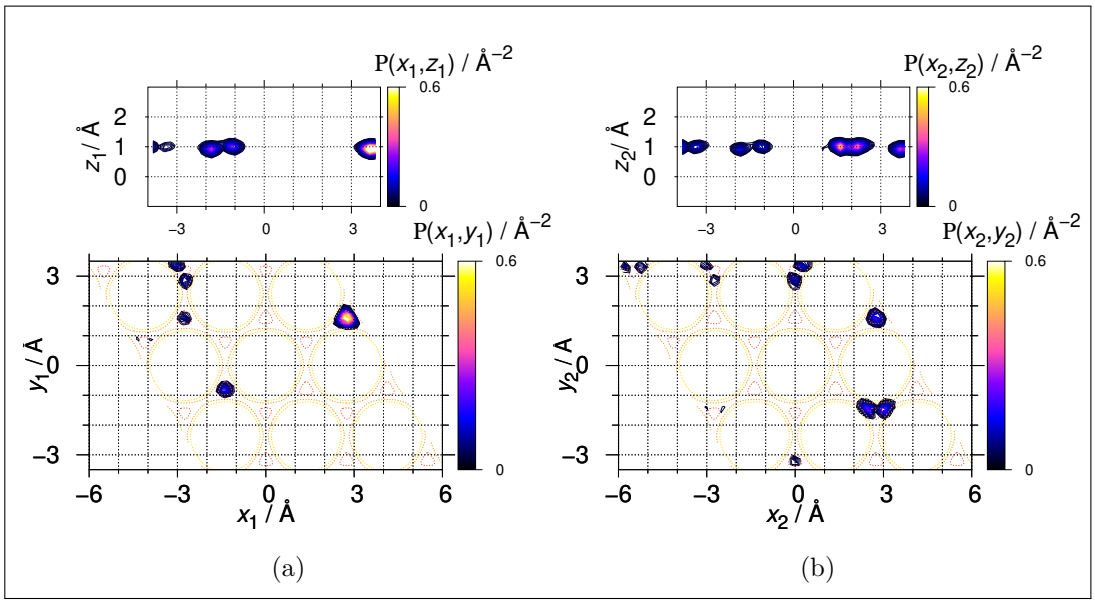

Figure 4.17: Two-dimensional representation of the RPD of eigenstate 690 in level 15. See also the caption of figure 4.11.

Typical for the states of this level is that the nodal planes found locally at the hcp sites in both x_1, y_1 and x_2, y_2-planes are aligned with the interatomic axis, suggesting that the hydrogen atoms at the hcp sites move in a direction that is perpendicular to the interatomic axis. Because the first atom is non-excited at the fcc site, this motion corresponds rather to a pendulum motion of the interatomic axis. If the hydrogen atom at the hcp site was singly desorbed, this motion would go over into a translational motion perpendicular to the interatomic axis.

The probability density distribution does not allow us to know with certainty whether these atoms are occupying neighboring sites or not. But given the energy difference between the $(AB)_I$ and $(AB)_{II}$ configurations (33 meV from table 3.2), we may firmly assert the $(AB)_I$-labeling.

Consequently, we have labeled this level $(0_A\ 2^1_B)^{\perp}_I$. The direction of the motion perpendicular to the interatomic axis is indicated by the symbol "$\perp$" on the label. In the following, we shall use the acronym "IAA" to refer to the interatomic axis.

The fact that the RPD of an individual atom show some probability for it to be found

simultaneously at both next-neighbor hcp and fcc sites does not necessarily indicate the possibility that it tunnels under the barrier that separates these potential wells. Consider as a possible state representative of the $(0_A\ 2^1_B)^{\perp}_I$ level the state given by the diatomic wave function of equation 4.8 with real MAF ϕ_{0_A} and $\phi_{2^1_B}$. The RPD of atom 1 would then be

$$P(1) \;=\; \cos^2(\alpha)\,\phi^2_{0_A}(1) \;+\; \sin^2(\alpha)\,\phi^2_{2^1_B}(1) \;+\; \sin(2\alpha)\,\phi_{2^1_B}(1)\,\phi_{0_A}(1) \qquad (4.9)$$

Clearly, such a RPD could yield figure 4.17. However, the same holds for the following function, in which the MAF represent delocalized tunneling states between two next-neighboring fcc and hcp sites:

$$\Phi(1,2) \;=\; \left[\cos(\alpha)\,\phi_{0_A}(1) + \sin(\alpha)\,\phi_{2^1_B}(1)\right]\ \left[\cos(\alpha)\,\phi_{0_A}(2) - \sin(\alpha)\,\phi_{2^1_B}(2)\right] \qquad (4.10)$$

Such a tunneling process occurs in the H/Pd(111) system. It might also occur in the H_2/Pd(111) system, and we shall discuss this possibility below.

Level 16

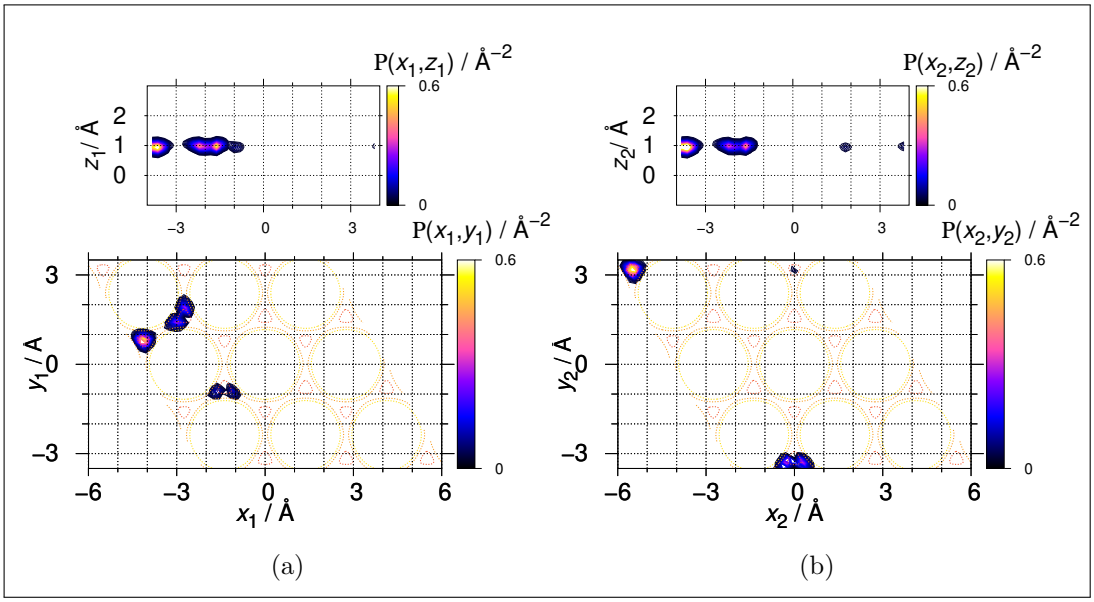

Figure 4.18: Two-dimensional representation of the RPD of eigenstate 741 in level 16. See also the caption of figure 4.11.

We refer now to figure 4.18. The RPD of this state show similar structures to the previous one, but this time the excitation is located on the hydrogen atom at

the fcc site. As for level 15, the orientation of the nodal planes at the fcc sites suggest that the hydrogen atoms vibrate at this site in a direction perpendicular to the interatomic axis in a $(AB)_I$ configuration. Following a similar approach to the previous one, we have labeled the states of this level by $(2^1_A\ 0_B)^{\perp}_I$.

Level 17

The structure of the RPD of a typical state in this level, given in figure 4.19, shows once again a configuration in which one non-exited hydrogen atom is located at an fcc site, while the second one is located at an hcp site and has one quantum of local vibrational excitation in a mode parallel to the substrate. The excitation-type of this level is similar to that of level 15, but the orientation of the nodal pattern suggests that the excited atom now moves along the IAA. We therefore denote this level by $(0_A\ 2^1_B)^{\parallel}_I$.

In the case of a single hydrogen atom, the two vibrations of the 2^1 mode are essentially degenerate, as we saw in section 4.2, due to the local $\boldsymbol{C}_{3v}$ symmetry of the potential. This symmetry is more strongly broken by the presence of the second hydrogen atom at an equivalent excitation energy, which lifts the degeneracy.

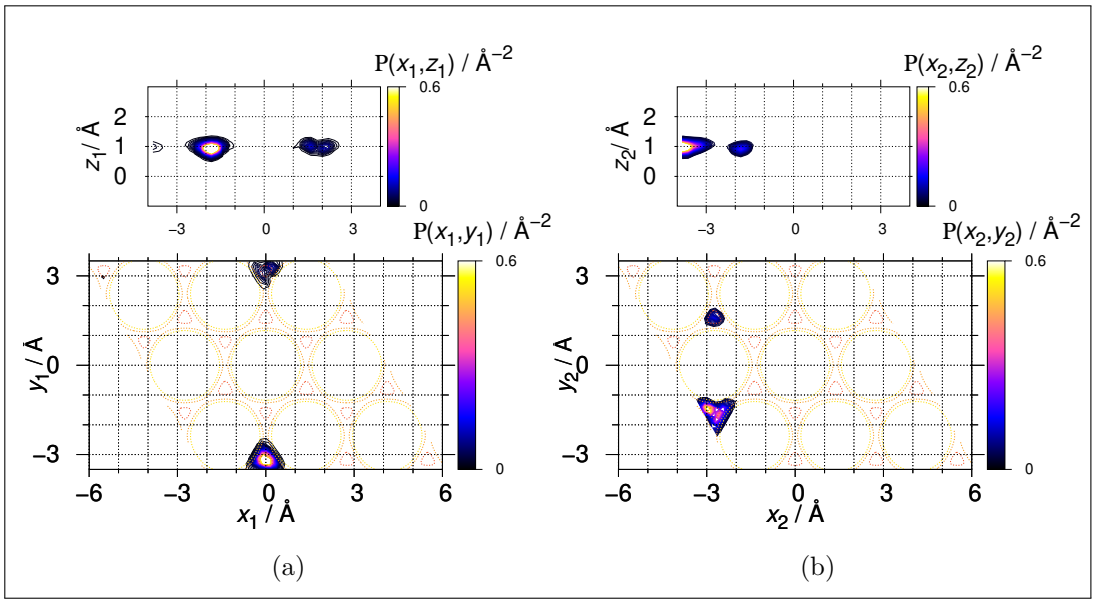

Figure 4.19: Two-dimensional representation of the RPD of eigenstate 795 in level 17. See also the caption of figure 4.11.

Level 18

A typical state of this level is represented in figure 4.20.

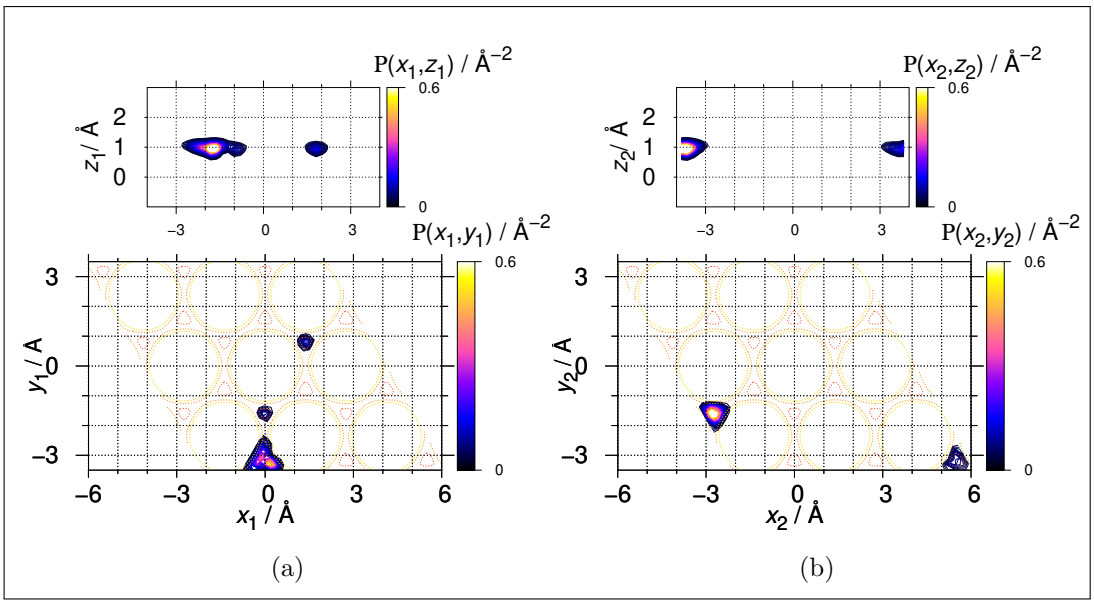

Figure 4.20: Two-dimensional representation of the RPD of eigenstate 849 in level 18. See also the caption of figure 4.11.

The RPD of this state show that the two hydrogen atoms are in the $(AB)_I$ configuration similar to the previous one, where this time the excited hydrogen atom is on the fcc site and moves along the IAA. We label this level $(2^1_A\ 0_B)^{\parallel}_I$. This is the last level completing the quadruplet of the first excited states corresponding to configurations of $(AB)_I$-type.

4.4.3 Tunneling of mode 2 states in the $(AB)_I$ configuration

The analysis of the vibrational states in the four levels discussed in the previous section has shown that, when the two hydrogen atoms occupy neighboring sites of different types, excitation in the local mode 2 parallel to the substrate leads to independent vibrations of the individual atoms. The question now arises regarding the possibility of tunneling of the excited atom.

In the H/Pd(111) system, the levels 3 and 4 have been identified as containing $2^1_A + 2^1_B$ AB-tunneling states (see table 4.3). Additionally, they give rise to 18 states

each, which split into three sub-levels because of tunneling of the ABA or BAB type, as discussed in section 4.2. The corresponding levels in the H_2/Pd(111) system compose the joint set of levels $\{L_{15}, L_{16}, L_{17}, L_{18}\}$ discussed in the present section. Here, however, we count 54 energetically equivalent states in the configuration $(AB)_I$ conforming to table 3.2. Each hydrogen atom has two vibrational components in mode 2 parallel to the substrate. Contrary to the H/Pd(111) system, these two components give rise to energetically different levels $(2^1_A\ 0_B)^{\perp}_I$ (level 16) and $(2^1_A\ 0_B)^{\parallel}_I$ (level 18), on one hand for the atom at the fcc site, and $(0_A\ 2^1_B)^{\perp}_I$ (level 15) and $(0_A\ 2^1_B)^{\parallel}_I$ (level 17) for the atom at the hcp site on the other hand, each 54-fold degenerate. The energy differences $E_{17} - E_{15} \approx 4\,\text{meV}$ and $E_{18} - E_{16} \approx 6\,\text{meV}$ are pieces of evidence that the local $\boldsymbol{C}_{3v}$ symmetry is more strongly broken in the H_2/Pd(111) system than in the H/Pd(111) system at comparable energies.

To identify the potentially corresponding tunneling doublets formed with these levels, we follow a different line of reasoning to that used in the case of the H/Pd(111) system, since inspection of the RPD does not allow us to identify as clearly the manifestation of tunneling. The case of two hydrogen atoms in the $(AB)_I$ configuration is illustrated in the two dimensional sections of the potential given in figures 3.9 and 3.10. We can see from these figures that, when one hydrogen atom is located at an fcc (A) site, the second hydrogen atom located at a corresponding neighboring hcp (B) site configuration will have three possibilities to move to a nearest-neighboring fcc site: for two of them, along directions perpendicular to the IAA (symbol $\perp$) the potential barriers to overcome are 231 meV(section along line 1 in figure 3.9), while in the third one, aligned with the IAA (symbol $\parallel$, section along line 3 in figure 3.9), the barrier is 267 meV. If tunneling is to be considered, it will be more favorable in the first case ($\perp$ vibration). The same observation can be made for the hydrogen atom located at the fcc site (see sections along line 8 and 6 in figure 3.10), with barriers 268 and 284 meV, respectively. These representations are based on the fact that one of the two atoms is fixed in space. The actual effective barriers perceived by the two atoms are different. But this analysis allows us to identify the potential barriers that are most favorable for tunneling. In any case, given the height of these barriers compared to those for the AB-tunneling in the H/Pd(111) system [8] , we

[8]The minimum potential energy at the hcp site is 40 meV. This has not been taken into account

might expect a significantly smaller tunneling effect in the H_2/Pd(111) system.

If tunneling affects only one of the two hydrogen atoms, then that atom would tunnel to a site of the different type, which would entail a change of configuration from $(AB)_I$ to $(AA)_I$ or $(BB)_I$. If tunneling affects both atoms simultaneously, then the configuration is unaltered. For example, if we consider the situation of a state in a level $(0_A\ 2^1_B)^\perp_I$, the corresponding tunnel doublet would be $(2^1_A\ 0_B)^\perp_I$. This second scenario seems to be much more probable than the first one. We therefore might tentatively assign the pair of levels $\{L_{15}, L_{16}\}$ as containing tunnel doublet states. Correspondingly, $\{L_{17}, L_{18}\}$ would be the other pair of tunneling doublet states. One has, $E_{16} - E_{15} \approx 1.7\,\text{meV}$, and $E_{18} - E_{17} \approx 3.9\,\text{meV}$. It therefore seems that in the $(AB)_I$ configuration, tunneling of one hydrogen atom to a next-neighboring site is likely to occur while conditioned by the simultaneous tunneling of the second hydrogen atom. We will refer to this as correlated tunneling.

The widths of the excited levels are larger than those of the non-excited levels. The numerical error introduced into the calculations increases with the energy of the system's states, as the latter require more SPF for an accurate evaluation of the wave functions. We re-optimized the bases used for these calculations by systematically increasing the size of the SPF bases, even after the achievement of a presumable convergence, in order to reduce the numerical error introduced in the calculations as much as possible. This slightly reduced the width of these levels, resulting in the optimum widths shown in table 4.4. One sees for instance that L_{16} has a maximum width of around 0.38 meV, which is not negligible. The broadening of these levels is still within the error bars of the numerical treatment. Yet, it could also be due to tunneling, very likely of the ABA or BAB type, such as calculated in the H/Pd(111) system. Given that the effective barriers for tunneling to the next-neighbor adsorption sites are much higher in the H_2/Pd(111) system than in the H/Pd(111) system, the corresponding tunneling band widths of the former may indeed be expected to be much smaller than in the latter.

Next, we move to the analysis of the vibrational states of levels $\{L_7, L_8, L_{10}, L_{13}\}$. We start with the levels L_8 and L_{10}, then L_7 and L_{13}.

---

in the relative barrier height for ease of reading.

4.4.4 Analysis of mode 2 excited states in the $(AA)_I$ configuration

Level 8

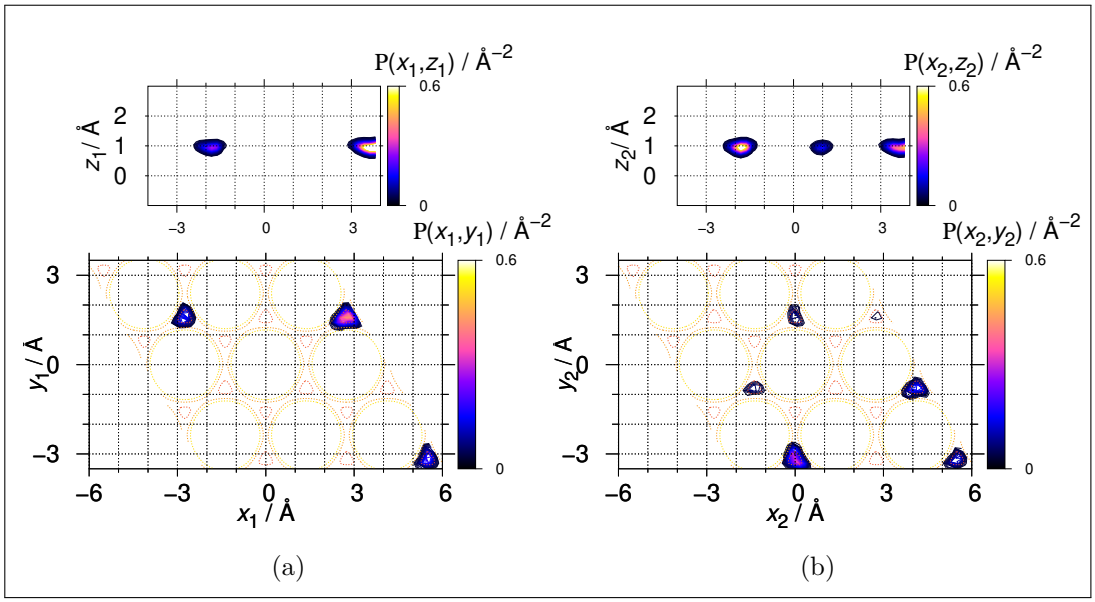

Figure 4.21: Two-dimensional representation of the RPD of eigenstate 313 in level 8. See also the caption of figure 4.11.

The RPD of a typical state are shown in figure 4.21. They have amplitudes only at the fcc potential wells, indicating a (AA)-type configuration. The representations of the latter have no clear nodal structure at the DOF of an individual hydrogen atom. Given that the RPDs are obtained by integrating the total probability density of the system over the remaining coordinates, nodal structures might appear more clearly in representations involving the DOF of different atoms. In the following, we analyze the structures of the RPD at corresponding DOF of the two atoms, i.e. $P(x_{t1}, x_{t2})$, $P(y_{t1}, y_{t2})$ and $P(z_{t1}, z_{t2})$. The twisted coordinates (x_t, y_t, z_t) of the two atoms will be used for the representation of those RPD.

The RPD shown in figure 4.22a has some nodal structures located along the diagonal of the $x_{t1}x_{t2}$-plane. This reflects that this state possesses vibrational excitation that simultaneously involves the x_t DOF of the two hydrogen atoms. The fact that the nodes occur only on the diagonal shows that the excited atoms share the same

equilibrium x_t-coordinate, i.e. $x_{t1}^{eq} = x_{t2}^{eq} \in \{-\frac{2d}{3}; \frac{4d}{3}\}$[9]. This situation is only possible if both atoms occupy fcc sites aligned along a direction parallel to the axis of the twisted coordinate y_t, as illustrated in figure 4.23a. A state with such an excitation therefore corresponds to a situation where the two atoms vibrate along a direction in the x_t, y_t-plane that makes an angle $\alpha = 60°$ (or 120°) with respect to the line joining the two fcc sites (dotted line in figure 4.23), i.e. the interatomic axis (IAA).

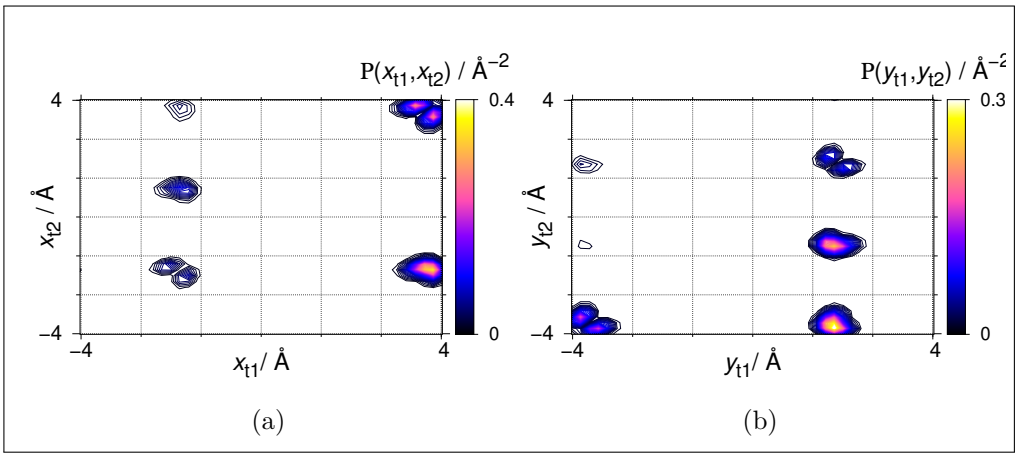

Figure 4.22: Two-dimensional representation of the RPD of the same selected eigenstate 313 as in figure 4.21, now in the x_{t1}, x_{t2} (panel a) and y_{t1}, y_{t2} (panel b) planes.

Figure 4.22b shows a similar structure at the DOF (y_1, y_2) where both excited atoms move around $y_{t1}^{eq} = y_{t2}^{eq} \in \{-\frac{4d}{3}; \frac{2d}{3}\}$. Using the same reasoning as above, this corresponds to the situation where the two atoms are placed in two neighboring potential wells in a line parallel to the twisted axis x_t from where they move along the twisted coordinates y_{t1} and y_{t2}. In this case, the vibrational motion of both atoms is also concerted along a line making an angle of 60° with the IAA, as illustrated in figure 4.23b.

We notice that the RPD in figure 4.22a have a node-less structure at the sites outside the diagonal. To understand this, consider the two situations sketched in figure 4.23[10]. In the first configuration (figure 4.23a), $P(x_{t1}, x_{t2})$ will have a node at a point on the diagonal given by $x_{t1} = x_{t2} = 4d/3$, while in the second case (figure

[9]These terms correspond to the coordinates of certain fcc sites in twisted coordinates (see table 3.1). With $d = 2.75$Å

[10]These two configurations correspond only schematically to the state given in figure 4.22.

4.23b), $P(x_{t1}, x_{t2})$ will present a node-less structure at the point with coordinates $x_{t1} = d/3$ and $x_{t2} = 4d/3$, because the vibrational excitation in this configuration is totally localized on the y_t modes. And conversely, the representation of $P(y_{t1}, y_{t2})$ will have a node at $y_{t1} = y_{t2} = 2d/3$ in the configuration shown in figure 4.23b and a node-less structure at $y_{t1} = -d/3$ and $y_{t2} = 2d/3$ in the configuration sketched in figure 4.23a.

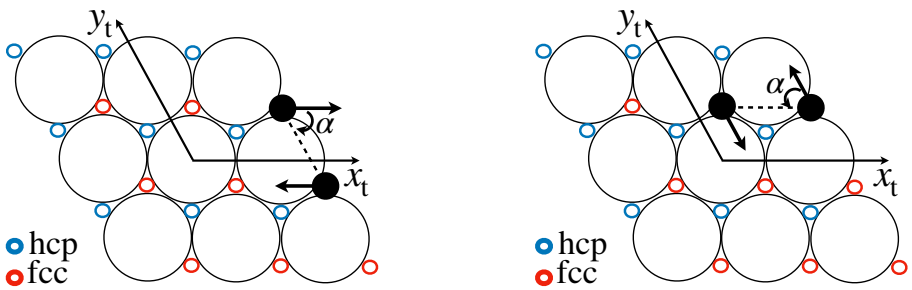

Figure 4.23: Schematic representation of two hydrogen atoms vibrating out-of-phase along a direction making an angle $\alpha = 60°$ with the IAA.

The sketches considered in figure 4.23 relate to spatially localized states, whereas the system's eigenstates are often delocalized in nature. The latter are given by linear combinations of these localized states. We then observe this multitude of possibilities simultaneously, which translates on RPD $P(x_{t1}, x_{t2})$ and $P(y_{t1}, y_{t2})$ having several nodal structures at the diagonal and node-less structures at off-diagonal sites simultaneously.

Looking at the nodal structure of $P(x_{t1}, x_{t2})$ (respectively $P(y_{t1}, y_{t2})$) along the diagonal, we see that the excitation between the two modes follows a direction in which x_1 decreases and x_2 increases (respectively y_1 decreases and y_2 increases), and vice versa. This results into a motion in which the two atoms vibrate out-of-phase. We illustrated this using arrows to indicate schematically the motion of each hydrogen atom in figure 4.23. If the molecule was desorbed, i.e. in the gas phase, this motion would resemble the rotational motion of the helices of a helicopter; the corresponding vibration is thus a frustrated rotation which may be dubbed "helicopter" mode.

The RPD in the z_1, z_2-plane (figure 4.24) shows a node-less structure. The latter is located around an equilibrium point given by $z_1 = z_2 = z_{\mathrm{eq}} \approx 0.91$Å. This leads to the conclusion that the excitation energy considered for this state is concentrated in the vibrational mode parallel to the substrate.

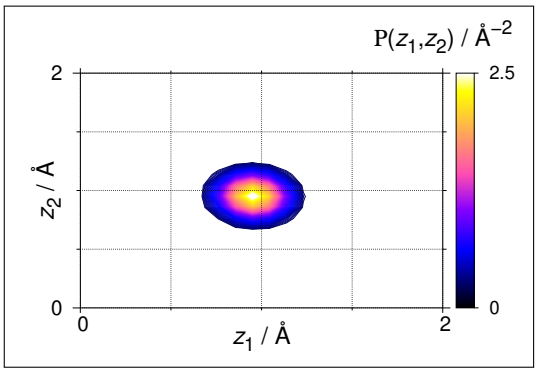

Figure 4.24: Two-dimensional representation of the RPD of the same selected eigenstate 313 as in figure 4.21, here in the z_1, z_2-plane.

Similar structural properties of the RPD result for all vibrational states of the level L_8 we could inspect in detail. This leads us to the following conclusion: the vibrational states of the L_8 level possess vibrational excitations distributed in a correlated way between the two hydrogen atoms; the latter vibrate out-of-phase (symbol "-") along a line making an angle of 60° with the IAA; atomic displacements are thus essentially perpendicular to the IAA, for which the symbol "⊥" is used. Consequently, we attribute the label $(0_{\mathrm{A}}\ 2^1_{\mathrm{B}})^{\perp -}_{\mathrm{I}}$ to level 8.

The "-" symbol is related to the out-of-phase concerted vibrational motion of the two hydrogen atoms. It does not relate to the anti-symmetric irreducible representation of the diatomic wave function under permutation of the two atoms. The symbol can indeed be understood as relating to a specific linear combination of products of monoatomic wave functions localized at two different sites A and A′, respectively, both of type A. Let these functions be $\phi_{\mathrm{A}0}, \phi_{\mathrm{A}1}, \phi_{\mathrm{A}'0}$ and $\phi_{\mathrm{A}'1}$, where 1 and 0 refer respectively to excited and non-excited, e.g. in local mode 2. A typical diatomic wave function in level 8 would then be given as

$$\Phi^{\mathrm{AA}'}_{-}(1,2) \;=\; \frac{1}{\sqrt{2}}\left(\phi_{\mathrm{A}1}(1)\,\phi_{\mathrm{A}'0}(2) - \phi_{\mathrm{A}0}(1)\,\phi_{\mathrm{A}'1}(2)\right) \qquad (4.11)$$

This function is not symmetrized with respect to the permutation of the two atoms,

as atom 1 always occupies site A and atom 2 site A′. Another typical function would be

$$\Phi_{-}^{\mathrm{A'A}}(1,2) \;=\; \frac{1}{\sqrt{2}}\left(\phi_{\mathrm{A'}1}(1)\,\phi_{\mathrm{A}0}(2) - \phi_{\mathrm{A'}0}(1)\,\phi_{\mathrm{A}1}(2)\right) \tag{4.12}$$

The linear combinations

$$\Phi_{\mathrm{s}}(1,2) \;=\; \frac{1}{\sqrt{2}}\left(\Phi_{-}^{\mathrm{AA'}}(1,2) + \Phi_{-}^{\mathrm{A'A}}(1,2)\right) \tag{4.13}$$

$$\Phi_{\mathrm{a}}(1,2) \;=\; \frac{1}{\sqrt{2}}\left(\Phi_{-}^{\mathrm{AA'}}(1,2) - \Phi_{-}^{\mathrm{A'A}}(1,2)\right) \tag{4.14}$$

yield, however, symmetric and anti-symmetric total wave functions with respect to permutation, respectively.

Level 10

Taking up the discussion for level 8 on the previous pages, we now assemble the different representations of the RPD of a typical state of level 10 in a single figure 4.25.

In this state atoms are likely to be found at fcc sites, only (figure 4.25a), indicating an (AA) configuration. RPD show nodal structures similar to the states of level 8, for which excitation is delocalized on both atoms.

Figure 4.25b shows the RPD $P(x_{\mathrm{t}1}, x_{\mathrm{t}2})$ and $P(y_{\mathrm{t}1}, y_{\mathrm{t}2})$ of this state. The nodal structures are again positioned on the diagonal of these representations, whereas the off-diagonal structures are node-less. We can apply the same reasoning used in the analysis of the previous level, from which we conclude that the two atoms vibrate along a direction making an angle $\alpha = 60°$ with the IAA. The difference with the previous level is that this time atomic displacements along $x_{\mathrm{t}1}$ and $x_{\mathrm{t}2}$ (respectively $y_{\mathrm{t}1}$ and $y_{\mathrm{t}2}$) have the same sense of variation. This indicates that the vibrations of the two atoms are in-phase. Figure 4.26 sketches schematically classical situations that correspond to the states of this level. In these diagrams, we have positioned arrows in the same direction to indicate in-phase displacements of the two atoms. If atoms were desorbed, i.e. at very large values of the z coordinates, the motion would be a translation of the diatomic in a direction essentially perpendicular to the IAA.

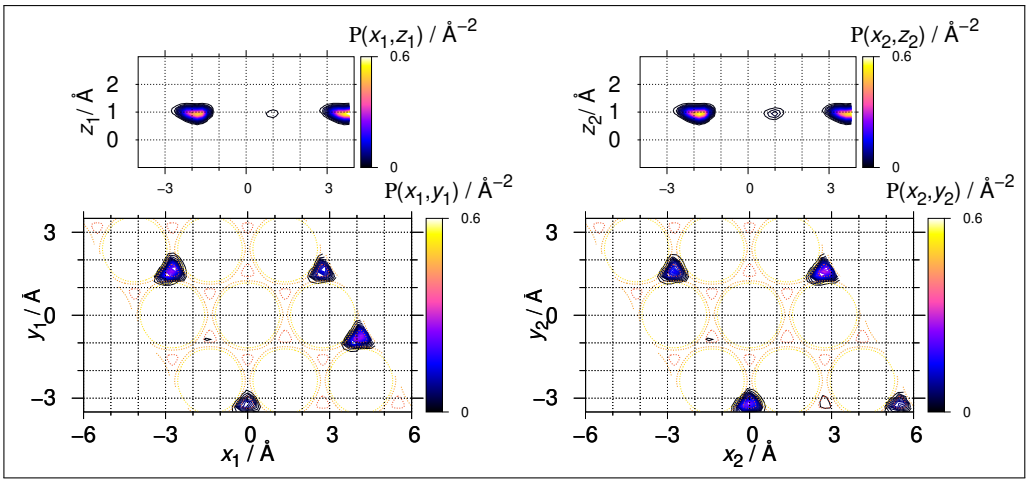

(a)

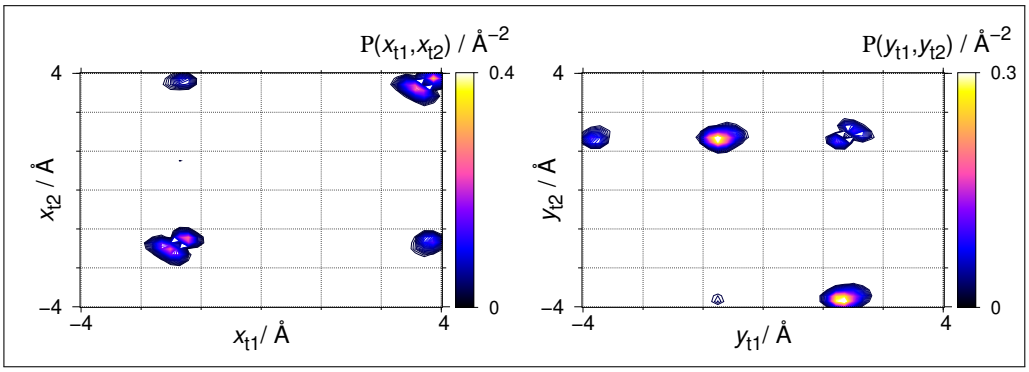

(b)

Figure 4.25: Two-dimensional representation of the RPD of an eigenstate 416 in level 10. For the upper panel (a) see also the caption of figure 4.11. For the lower panel (b) see the caption of figure 4.22.

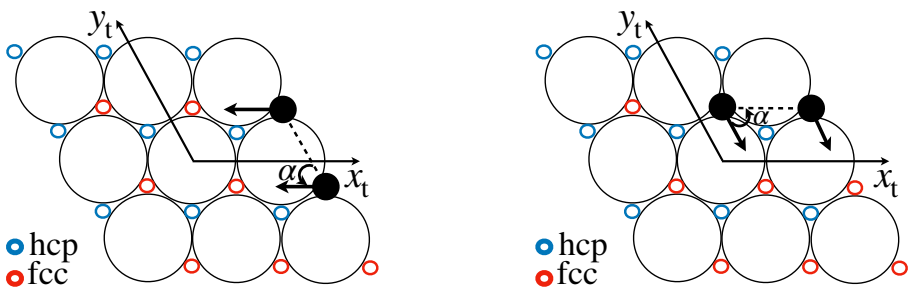

(a) (b)

Figure 4.26: Schematic representation of two hydrogen atoms vibrating in-phase along a direction making an angle $\alpha = 60°$ with the IAA.

All states we investigated in this level have the same characteristics regarding the

shape of their RPD, i.e. the nodes occur only along the diagonal, and the DOF of the two atoms have the same sense of variation. We have not represented the RPD in the z_1,z_2-plane, which is very similar to that shown in figure 4.24. We label this level $(0_A\ 2^1_A)^{\perp+}_I$, to refer to states with the same characteristics as those of the L_8 level, with exception of the relative phase, which is positive here (symbol "+").

Level 7

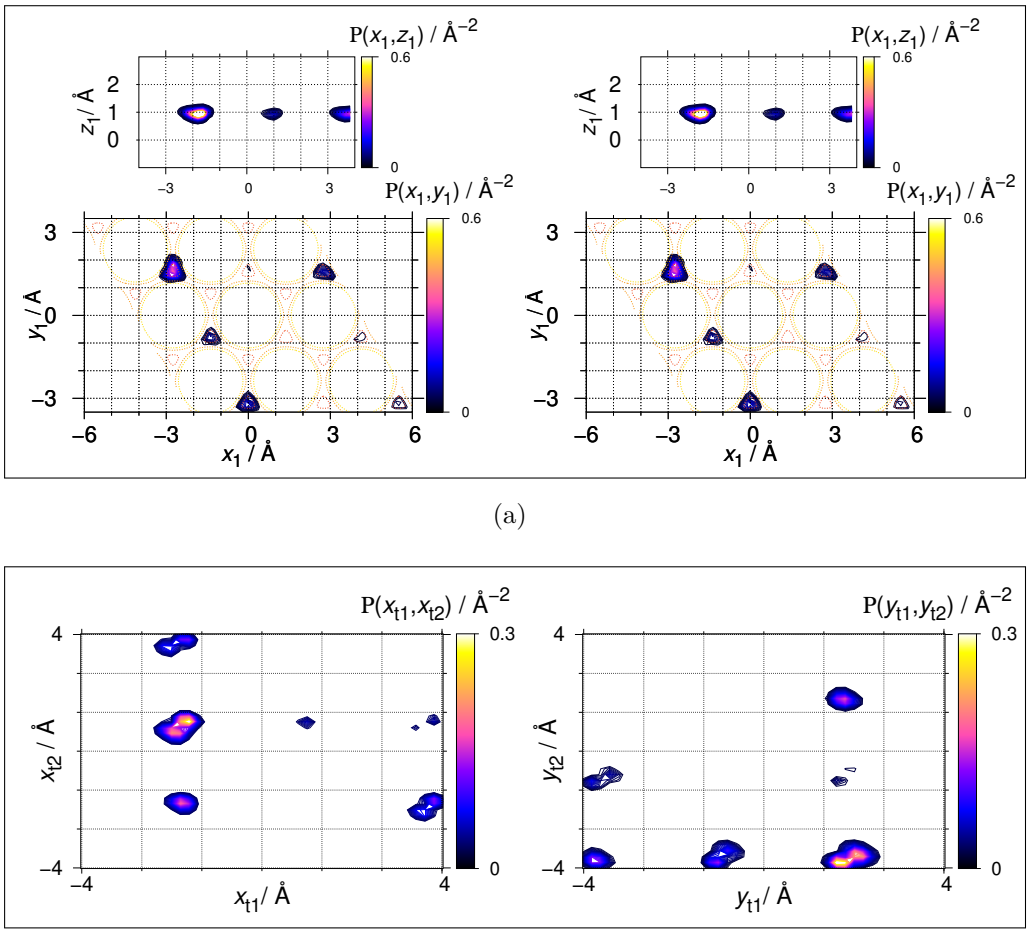

(a)

(b)

Figure 4.27: Two-dimensional representation of the RPD of eigenstate 253 in level 7. See also the captions of figures 4.11 and 4.22.

RPD shown in figure 4.27a have amplitudes only at the fcc sites, indicating an (AA) configuration. $P(x_{t1}, x_{t2})$ (figure 4.27b) shows nodal structures at off-diagonal sites; structures are node-less on the diagonal. This means that in situations where $x_{t1} = x_{t2}$, the vibrational excitation is entirely localized in the y_{t1} and y_{t2} DOF ($P(z_1, z_2)$ is node-less). Consequently, atoms move concertedly along the interatomic

axis, here parallel to the y_t axis. Figure 4.28a illustrates this situation.

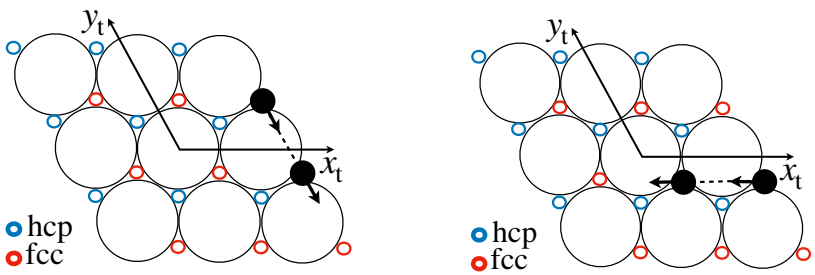

(a) (b)

Figure 4.28: Schematic representation of two hydrogen atoms vibrating in-phase along the interatomic axis IAA.

When $x_{t1} \neq x_{t2}$ nodal structures appear at $P(x_1, x_2)$. This means that vibrational excitation in the x_{t1} and x_{t2} DOF only occurs when the two hydrogen atoms occupy fcc sites with different x_t coordinates. A typical example is when the two hydrogen atoms occupy neighboring fcc sites aligned with the twisted coordinate x_t. For instance, the situation illustrated in figure 4.28b leads to a nodal structure in $P(x_{t1}, x_{t2})$ located around a point with coordinates $x_{t1} = d/3$ and $x_{t2} = 4d/3$. Here, too, one sees that each hydrogen atom moves along the IAA.

The RPD $P(y_{t1}, y_{t2})$ (figure 4.27b) show similar properties; when the two atoms are located at sites with the same value of y_t, excitation is delocalized between x_{t1} and $x_{t2} \neq x_{t1}$ (no nodal structure at the diagonal), whereas in the case where $y_1 \neq y_2$ excitation will appear at these DOF. This again indicates configurations where both atoms vibrate along the IAA.

Furthermore, the local nodal structure of the RPD around the fcc sites indicates that the two atoms are vibrating in-phase (following a reasoning analogous to that used in the analysis of level 10). Arrows were used in figure 4.28 to indicate the in-phase vibrations. If the diatomic was desorbed, this motion would correspond to its free translation along the IAA.

All inspected eigenstates of the L_7 level have the same properties. Which leads us to conclude that these states describe in-phase vibrational motion parallel to the interatomic axis. Accordingly, we label this level $(0_A\ 2^1_A)^{\parallel +}_I$.

Level 13

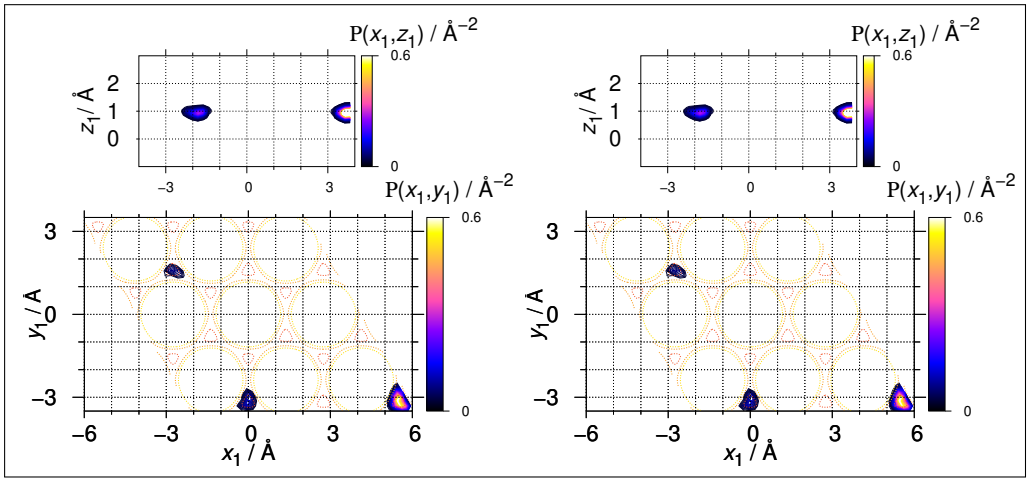

(a)

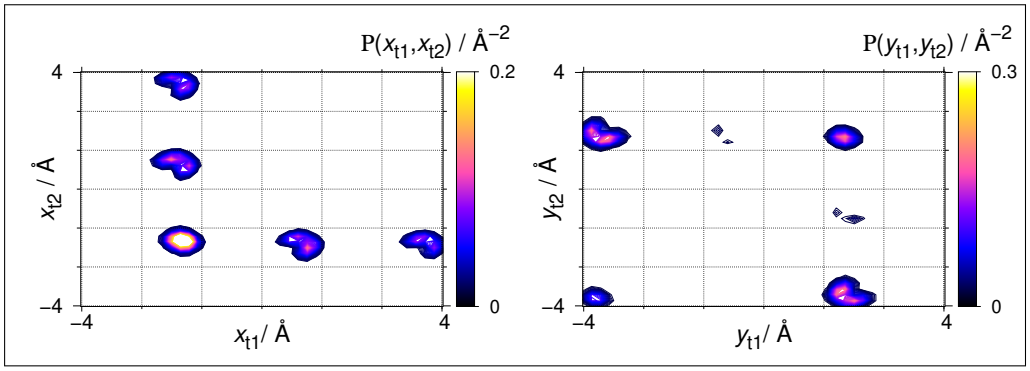

(b)

Figure 4.29: Two-dimensional representation of the RPD of eigenstate 578 in level 13. See also the captions of figures 4.11 and 4.22.

This state has presence probability only at fcc sites, indicating an $(\mathrm{AA})_\mathrm{I}$ configuration. The RPD $P(x_{\mathrm{t}1}, x_{\mathrm{t}2})$ and $P(y_{\mathrm{t}1}, y_{\mathrm{t}2})$ given in figure 4.29b show nodal structures similar to the L_7 level discussed above, except that the two atoms vibrate out-of-phase. We have labeled this level $(0_\mathrm{A}\ 2^1_\mathrm{A})^{\parallel-}_\mathrm{I}$, indicating states where the two hydrogen atoms vibrate out-of-phase along the IAA, as illustrated in figure 4.30. In the gas phase, the corresponding motion is the intramolecular stretching vibration.

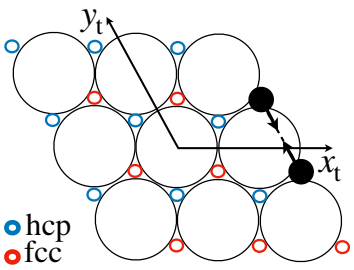

Figure 4.30: Schematic representation of two hydrogen atoms vibrating out-of-phase along the IAA.

Analysis of the vibrational state structure of these levels has shown that when two hydrogen atoms occupy neighboring fcc sites in the $(AA)_I$ configuration, vibrational excitation of the system in the local mode 2 results in their concerted vibrational motion parallel to the substrate, forming four levels with distinct vibrational energies. Levels 7 and 10 contain states that describe concerted and oriented in-phase vibrations of the atoms; in level 7 these are oriented along the IAA, in level 10 the orientation is essentially perpendicular to it; the former are labeled by the symbol "$\parallel$" and correspond to a frustrated translation along the IAA, the latter by "$\perp$", corresponding a frustrated translation in the perpendicular direction to the IAA; both translations are parallel to the substrate.

Levels 8 and 13 contain states that describe out-of-phase concerted vibrations with displacements oriented along the IAA (level 13, symbol "$\parallel$"), or essentially perpendicular to it (level 8, symbol "$\perp$"); level 13 states correspond to stretching vibrations of the diatomic in the gas phase, level 8 to hindered rotations of the helicopter type. It is difficult to correlate the energy differences in the parallel and perpendicular motions to the breakdown of the local $\boldsymbol{C}_{3v}$ symmetry, or to the (harmonic) coupling causing the atoms to move concertedly and, on the same token, to split the energy level of zeroth order local modes. They likely correlate to both. Quite obviously, the concerted motion is related to the resonance condition of zeroth order states, which is absent in the AB-type configurations discussed so far.

A direct consequence of the concerted motion is that the states describing a single excited hydrogen atom in the classical sense are not stationary states of the system. These types of states are in fact given by a superposition of states in which the

two atoms vibrate in phase with states where the two atoms vibrate out-of-phase in the same direction. We have illustrated this in the study carried out on a one-dimensional model given in appendix D. To illustrate this in the actual system, let us consider two typical states of the L_7 and L_{13} levels (figure 4.31). Like all the states of these levels, the RPD of the latter show no significant nodal structure in planes defined by the DOF of individual atoms. In both states hydrogen atoms move along the interatomic axis. In level 7 motion is in-phase, in level 13 it is out-of-phase. We will denote these two states by Φ_7 and Φ_{13}.

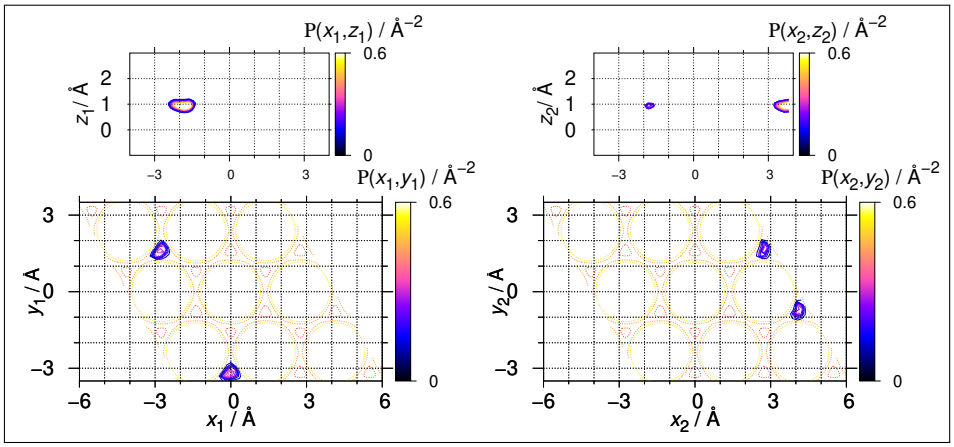

(a)

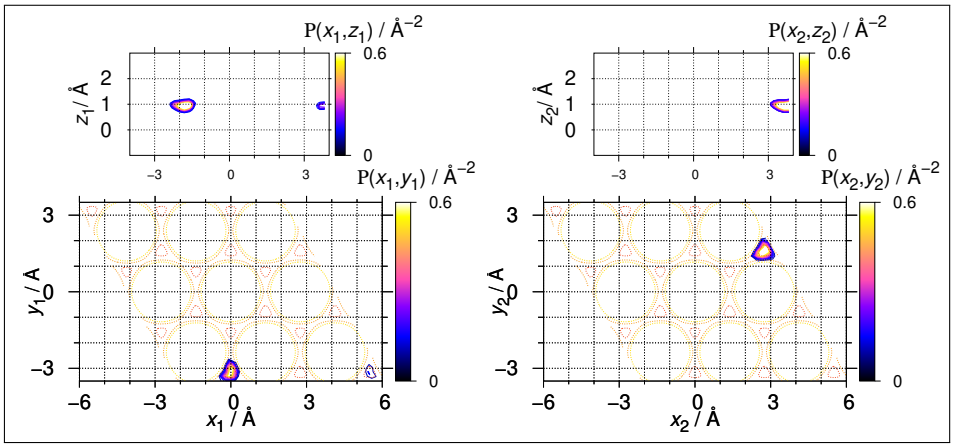

(b)

Figure 4.31: Two-dimensional representation of the RPD of two selected eigenstates in level 7 (panel (a), state 260) and level 13 (panel (b), state 601). See also the caption of figure 4.11.

Let us now consider two states Ψ_1 and Ψ_2 given by :

$$\begin{aligned} \Psi_1 &= \frac{\Phi_7 + \Phi_{13}}{\sqrt{2}} \\ \Psi_2 &= \frac{\Phi_7 - \Phi_{13}}{\sqrt{2}} \end{aligned} \tag{4.15}$$

Figure 4.32a shows the RPD of Ψ_1. It can be seen that the first hydrogen atom has a very clear nodal structure at an fcc site, while the second is totally node-less. This indicates a configuration in which only hydrogen atom 1 has vibrational excitation.

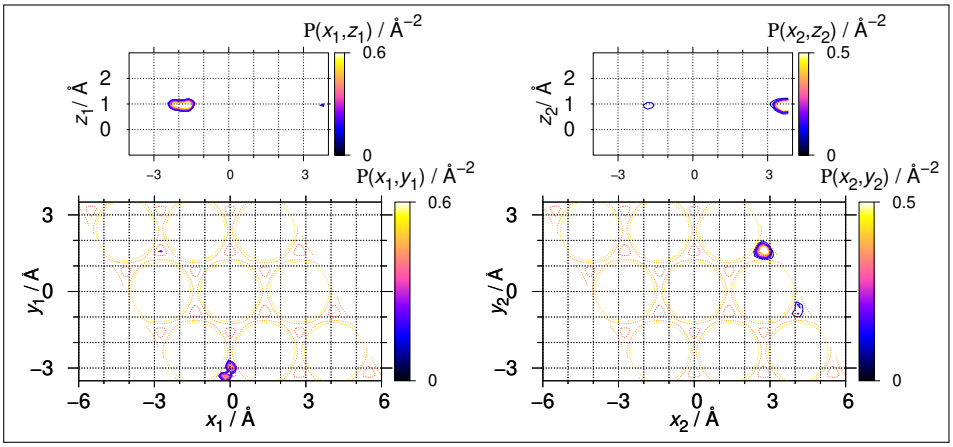

(a)

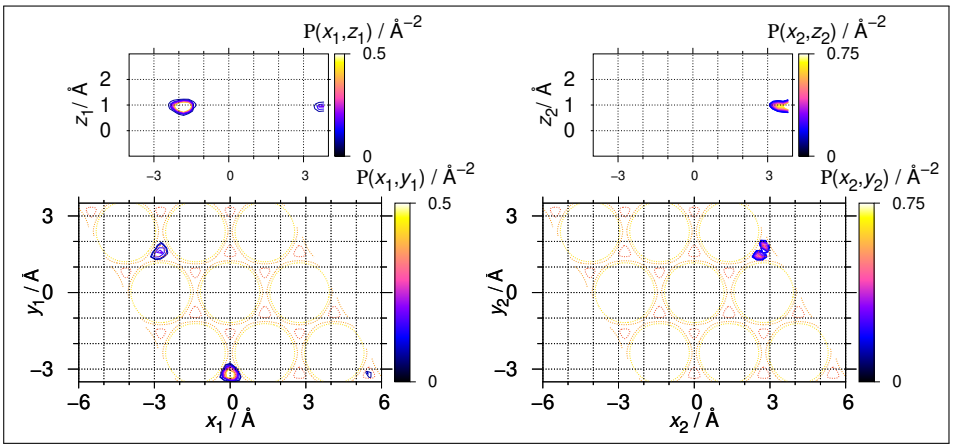

(b)

Figure 4.32: Two-dimensional representation of the RPD of Ψ_1 (a) and Ψ_2 (b). See equations 4.15 as well as the caption of figure 4.11.

The RPD of Ψ_2, given in figure 4.32b, show the opposite situation where excitation is entirely localized on hydrogen atom 2. Ψ_1 and Ψ_2 are henceforth non-stationary states of the system, and will evolve essentially periodically between these two states,

giving rise to an energy transfer mechanism between the two atoms. A study of the dynamical behavior of such states is presented in chapter 5.

4.4.5 Analysis of mode 2 excited states in the $(BB)_I$ configuration

Similar results hold for the configurations of the $(BB)_I$ type where the two hydrogen atoms occupy neighboring hcp sites. The corresponding levels are $\{L_6, L_9, L_{11}, L_{12}\}$. We have used the same nomenclature to label the latter (table 4.4). We will now conclude this analysis section with the remaining levels $\{L_{19}, L_{20}\}$ (and $\{L_{21}, L_{22}\}$).

4.4.6 Analysis of mode 1 excited states in the $(AA)_I$ and $(BB)_I$ configuration

Levels 19 and 20

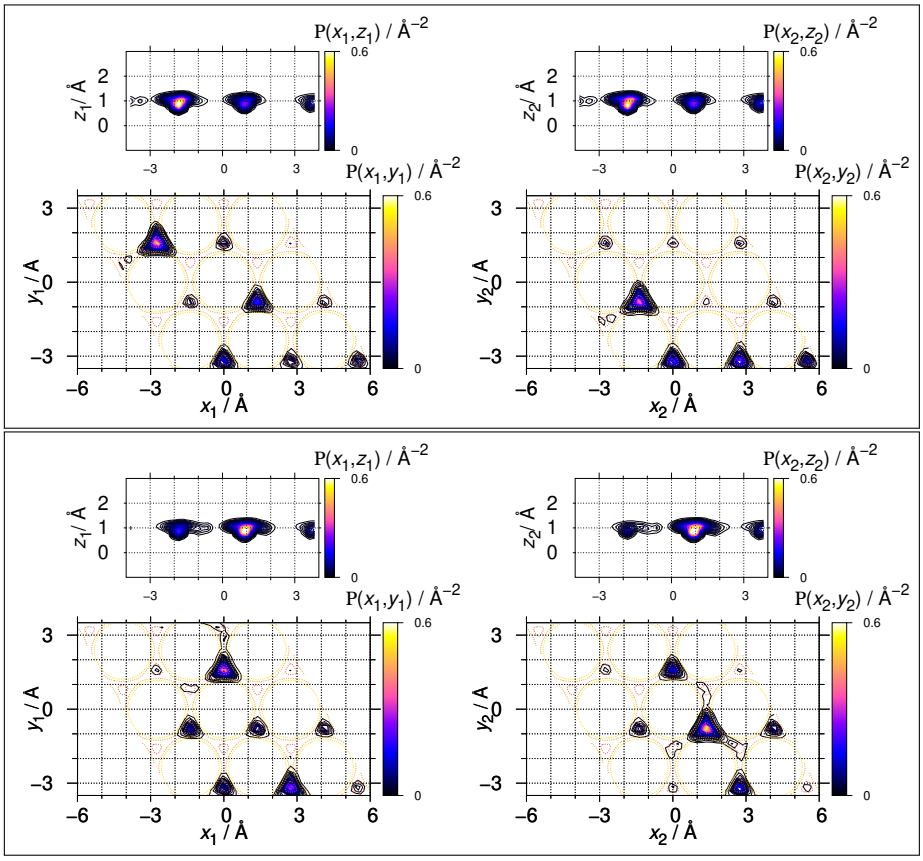

Figure 4.33: Two-dimensional representation of the RPD of eigenstates 940 in level 19 (a) and 960 in level 20 (b). See also the caption of figure 4.11.

Figure 4.33 show the RPD of two selected states from levels 19 and 20, respectively. Both of them possess presence probability of the two hydrogen atoms mainly at the fcc sites, indicating a predominantly (AA)-type configuration. There are no clear nodal structures visible on the DOF of individual atoms parallel to the substrate.

Figure 4.34 shows the representations of the RPD $P(x_1, x_2)$ and $P(y_1, y_2)$ of these two states. The latter have no particular nodal structure and do not allow us to deduce the nature of the vibrational excitation of this state.

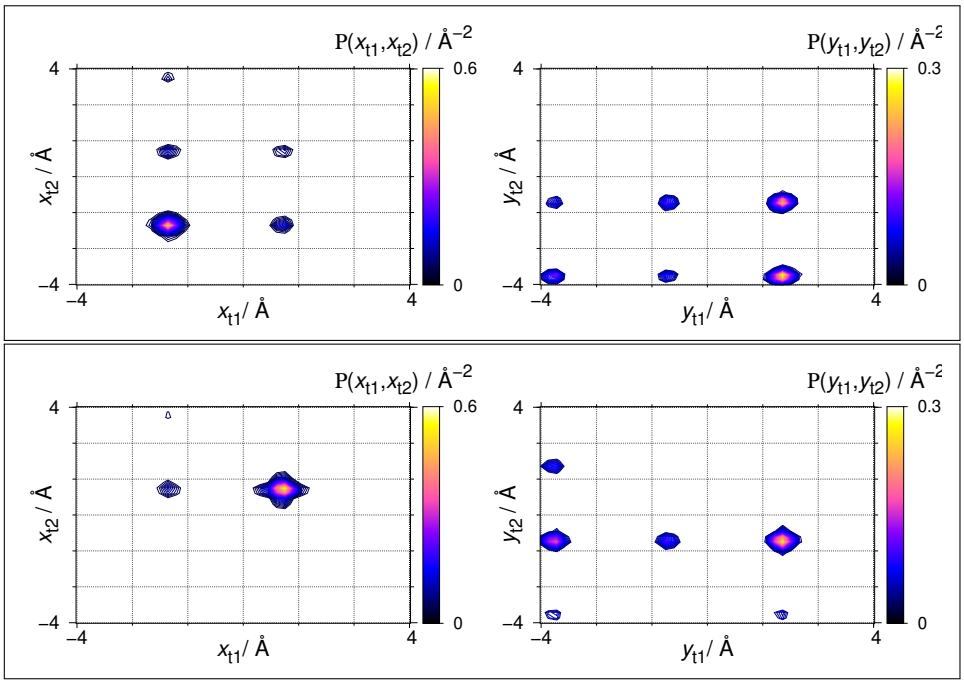

Figure 4.34: Two-dimensional representation of the RPD of the same two selected eigenstates as in figure 4.33, here in the x_{t1}, x_{t2} and y_{t1}, y_{t2}-planes on the left and right hand side, respectively.

Figure 4.35 shows the representation of the RPD in the $z_1 z_2$-plane. The latter shows the presence of a node localized at the diagonal around $z_1 = z_2 = z_{eq} \approx 90$ pm. This indicates the presence of a concerted vibrational excitation between the z_1 and z_2 DOF, shared by the two hydrogen atoms. Following a similar line of reasoning to that used in the analysis of excitation in mode 2 parallel to the substrate, we can deduce from the location of the nodal structure at the diagonal that both atoms vibrate concertedly in a direction perpendicular to the interatomic axis.

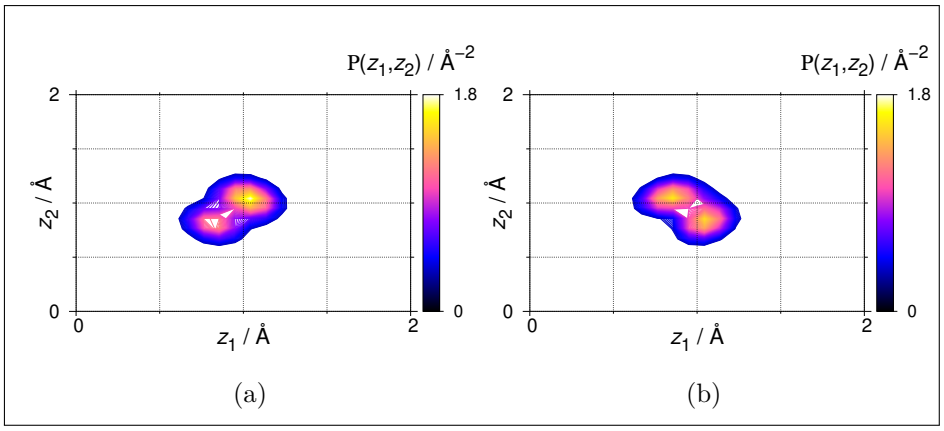

Figure 4.35: Two-dimensional representation of the RPD of eigenstates 940 (a) and 960 (b) as in figure 4.33, here in the z_1, z_1-plane.

Following the same reasoning to explain the mode 2 excited states in the $(AA)_I$ configuration, figure 4.35 suggests that state 940 of level 19 represents in-phase vibrations of the two hydrogen atoms, while in state 960 atoms vibrate out-of-phase. A schematic representation of the two vibrational modes is shown in figure 4.36.

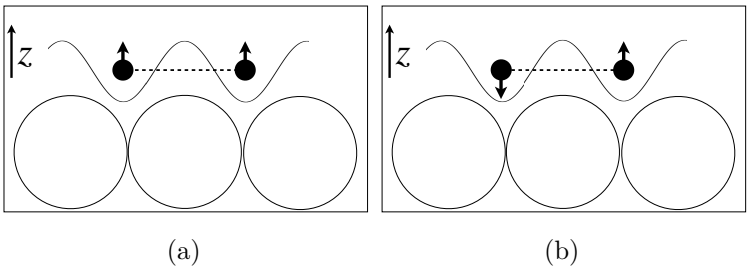

Figure 4.36: Schematic representation of two hydrogen atoms vibrating in-phase (a) and out-of-phase (b) along a direction perpendicular to the IAA.

Furthermore, the RPD of these states possess some small amplitudes at some hcp sites. This can be seen in particular at the $P(x_i, z_i)$ representation of the two atoms. This feature might be related to tunneling of the atoms to neighboring hcp sites.

Most importantly, the RPD reveal the existence of a local $1^1 + 2^2(A_1)$ Fermi resonance, as in the H/Pd(111) system. The resonance coupling is perhaps weakened here by the strong (harmonic) coupling between the two atoms. It might be stronger at the level of local states, i.e. by taking the superposition of two states similar to

those in equations 4.15. Figure 4.37 shows the RPD of a state resulting from such a superposition of states 940 and 960 in levels 19 and 20.

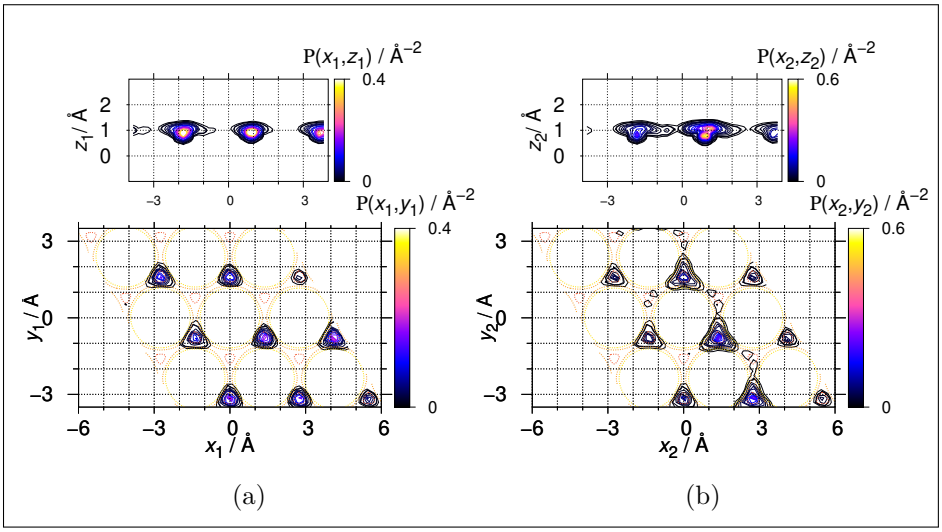

Figure 4.37: Two-dimensional representation of the RPD of the superposition $\Psi = (\Phi_{940} + \Phi_{960})/\sqrt{2}$ of the two selected states in levels 19 and 20. Panel (a) shows the RPD of atom 1, panel (b) that of atom 2. See also the caption of figure 4.11.

Excitation is clearly more important on the second atom. The latter shows the typical pattern of a 1:2 Fermi resonance between the local modes 1 and 2, similar to the case of a single hydrogen atomdiscussed in section 4.2.

Analysis of other states in these two levels show similar results. To summarize, in the case where the two hydrogen atoms are located at two neighboring fcc sites in the $(AA)_I$ configuration, the excitation in the local mode 1 perpendicular to the substrate results in a concerted vibrational motion of both atoms. The latter then vibrate in-phase or out-of-phase. The energies of these two global vibrational modes differ by 0.76 meV. This gives rise to two energetically almost overlapping levels 19 and 20, yet with distinct energies. Vibrations in level 19 are in-phase and correspond, in the gas phase, to a translational motion of the diatomic molecule perpendicular to the substrate; this mode also describes the direct adsorption or desorption process. Vibrations in level 20 are out-of-phase and can be related to a cartwheel rotation of the diatomic molecule in the gas phase.

The Fermi resonance between the locally perpendicular and parallel modes 1 and 2 of each hydrogen atom is still present. The correlation between the two hydrogen

atoms leads via the harmonic coupling somehow to a sharing of the Fermi resonance coupling between the two atoms. We will discuss these effects further in the quantum dynamics study of this system in chapter 5. This summary rationalizes the chosen labels $(0_{\mathrm{A}}\ [1^1+2^2]_{\mathrm{A}})_{\mathrm{I}}^{+}$ for level 19 and $(0_{\mathrm{A}}\ [1^1+2^2]_{\mathrm{A}})_{\mathrm{I}}^{-}$ for level 20.

Analysis of the levels 21 and 22 shows that these states are localized at hcp sites and possess the same properties as the levels 19 and 20. We have labeled these levels analogously. Some states of these levels have non-zero presence probabilities in the fcc sites, which might be indicative of tunneling. Level widths are 0.49 meV and 0.63 meV, respectively. We might attribute this broadening to possible AB-tunneling[11].

4.4.7 Discussion about Para and Ortho hydrogen

MCTDH makes it possible to (anti-)symmetrize the spatial wave function of a given system. In the following, we will explain the numerical procedure we followed to achieve this.

As the DOFs of each hydrogen atom are grouped into combined modes $Q_i = \{x_{\mathrm{t}i}, z_{\mathrm{t}i}, z_{\mathrm{t}i}\}$, the wave function of the system reads

$$\Psi(Q_1,Q_2,t)=\sum_{i_1=1}^{N_{Q_1}}\sum_{i_2=1}^{N_{Q_2}} A_{i_1,i_2}(t)\Phi_{i_1}^{(Q_1)}(Q_1,t)\Phi_{i_2}^{(Q_2)}(Q_2,t) \tag{4.16}$$

(Anti-)symmetrization is achieved by imposing the condition

$$A_{i_1,i_2}(t)=\pm A_{i_2,i_1}(t),\ \forall t \tag{4.17}$$

This is achieved by using the command "(a)symcoeff=persist, dav" when creating the initial wave function, which (anti-)symmetrizes the A-Vector initially and after each orbital relaxation. The "dav" argument additionally symmetrizes the Davidson vectors used in the calculation [21]. The set of SPF used to describe the modes of the two hydrogen atoms must be identical for equation 4.16 to be meaningful. The "id" command is used in the declaration of the SPF in order to instruct the program to use the same SPF to describe the Q_i modes[12]

[11] These states are not pure perpendicular modes because of the Fermi resonance. The latter have a non-zero lateral component. They can therefore also tunnel through lateral potential barriers.

[12] We found during the calculations that a large number of SPFs is required to achieve convergence. 150 identical SPF were used for each combined mode.

Since a combined mode is used to describe each hydrogen atom, the A-Vector symmetry reflects the permutation symmetry of the two atoms. Using the above parameters, symmetrization is then systematic at every time step, guaranteeing the conservation of permutation symmetry during the relaxation process.

Symmetric wave functions correspond to para-H_2 (with total nuclear spin 0), and antisymmetric wave functions to ortho-H_2 (with total nuclear spin 1).

Discussion

We evaluated symmetric and antisymmetric wave functions for all levels up to level 10. So far, no significant energy discrimination could be made between symmetric and antisymmetric states: they are all essentially degenerate. Table 4.5 below gives values obtained for level 8 of table 4.4 (the helicopter AA mode). Symmetrized calculations are naturally more stable than non-symmetrized ones, as the SPF bases are relatively larger with regard to the block size.

state	E/meV		
	non-sym	sym	asym
307	84.1	84.0	84.0
⋮	⋮	⋮	⋮
360	84.4	84.3	84.3

Table 4.5: Eigenvalues H_2/Pd(111); lowest and highest energy states in level 8; state numbers from non-symmetrized calculations (54 states); symmetrized calculations yield each 27 states that could be in principle attributed to individual states from the non-symmetrized calculations (see text).

In each level discussed so far, half of the states are symmetric, half of them are antisymmetric. In principle, if numerical accuracy is improved, one could use the results from the present work to calculate reaction rates for the ortho-para interconversion governed by the potentially very small hyperfine splitting of adsorbed dihydrogen.

At higher energies, symmetric and antisymmetric levels should split in energy. This

is expected to occur upon desorption, as gas phase dihydrogen has energetically well distinguished levels: para-H_2 correlates with even J rotational quantum numbers, ortho-H_2 with odd J values.

4.4.8 Concluding remarks on the eigenstates of the H_2/Pd(111) system

The spectrum of a single hydrogen atom is strongly affected by the presence of other atoms of the same species. When these atoms occupy neighboring sites of the same type, a strong correlation is established between them. Vibrational excitation of the system in such a configuration results in concerted motion of the two atoms. The latter then adopt correlated modes of vibration with distinct vibrational energies. When the two atoms are located at two neighboring sites of different type, this correlation is weaker. We then observe vibrational excitations that are essentially localized on only one atom. This difference in the behavior of hydrogen atoms is related to resonances which promote coupling and correlation between the local vibrational modes of the two atoms when they occupy sites of the same type. The correlation between the two atoms is weaker when they occupy sites of different types. Atoms then behave more independently.

The presence of tunneling is confirmed in the spectrum of the H_2/Pd(111) system. Tunneling likely takes place in a correlated way with the two hydrogen atoms tunneling simultaneously to next-neighboring sites. However, this tunneling processes are less important than in the spectrum of a single hydrogen atom. It manifests itself in level shifts (AB-tunneling) and eventually in the broadening of levels. Level shifts and widths remain relatively small, however, and no conclusive quantitative results on level widths can be drawn from the present calculations due to numerical error limitations.

Vibrational excitations in configurations where the two atoms occupy non-neighboring sites in the $(AB)_{II}$ and $(AA)_{II}$ or $(BB)_{II}$ configurations are more energetic. Although it would be possible to treat these cases here, too, the energy range in which we have optimized the PES representation with POTFIT is limited to 500 meV. Beyond this energy range, the potential representation becomes less accurate. The total energy

of the last level calculated in table 4.4 is already near to the limits of the optimal potential. Beyond this level we began to observe a very significant broadening of the bands, which did not correspond to any physical situation. A re-optimization of the potential representation over larger energy domains would enable to determine the behavior of the vibrational states of hydrogen atoms when they are further apart. It would be very interesting to see whether this correlation persists even at great distances. Such a study is, however, beyond the scope of the present thesis.

Chapter 5

Time-dependent study : Quantum dynamics of H/Pd(111) and H_2/Pd(111)

When hydrogen atoms adsorb on a palladium surface, they most often remain trapped on the surface level without penetrating into the bulk. They may, however, have a lateral motion along the surface, either spontaneously or as a result of energy gain through interaction with an external system. The resulting dynamics depends only on the nature of the interaction between the hydrogen and palladium atoms. In quantum mechanics, a system's dynamics is expressed in terms of the time evolution of its wave function. The squared modulus of the latter gives the probability density of the system under study. The quantum nature of atoms does not allow us to evaluate their trajectories in the classical sense, but the analysis of the probability density of their presence at given points in space gives us an indication of the type of dynamical behavior that atoms can or cannot adopt over time. The advantage of this approach is that it allows us to take into account all the quantum phenomena likely to influence the dynamics of atoms beyond the classical approach.

In the eigenstate basis $|\varphi_k\rangle$ of a time-independent, non-dissipative Hamiltonian, the time evolution of the state of the system $|\Psi(t)\rangle$ is given by:

$$|\Psi(t)\rangle = \sum_k c_k(0) e^{-\mathrm{i}E_k t/\hbar} |\varphi_k\rangle \tag{5.1}$$

With E_k the eigenenergy associated to $|\varphi_k\rangle$ and $c_k(0) = \langle\varphi_k|\Psi(0)\rangle$ are the coefficient of $|\Psi(0)\rangle$ in this basis. Since the eigenstates are stationary, each component of $|\Psi(t)\rangle$ will oscillate in time with a period given by $T_k = \frac{2\pi\hbar}{E_k}$. The dynamics of a system then appears in this picture as the consequence of the time evolution of the superposition of these individual states evolving with different phase velocities. On the other hand, we have highlighted in the previous chapter that quantum effects such as tunneling or Fermi resonance have a significant impact on both the spatial structure of the eigenstates and their energies. Consequently, these quantum effects will be visible in any state that includes in its spectral decomposition eigenstates impacted by them.

In the following, we present a study of the dynamics of hydrogen atoms following excitation in local modes 1 and 2 discussed in the previous chapter, which can be parallel or perpendicular to the substrate. This type of excitation can arise, for example, from interaction with neutrons or helium atoms in spin echo experiments [3], or directly from interaction of hydrogen atoms with external photons or just thermally. In particular, we will investigate situations in which a single quantum of vibrational excitation is transferred to the system.

The study carried out in this chapter is based on a non-dissipative, frictionless model in which the Pd atoms are all considered to be fixed at their equilibrium positions. We wish to highlight mainly the consequence of the quantum character of hydrogen atoms in their motion on the Pd(111) surface.

5.1 Technical details on the propagation calculations

All propagation calculations were performed using the MCTDH program. In each calculation, the initial wave function (IWF) used is defined as a sum of products of one-dimensional SPF. We work within the constant mean field (CMF) scheme described in section 4.1.2. Both the SPFs and the A-vector are propagated separately in time according to equation 2.40. Bulirsch-Stoer (BS) extrapolation scheme with polynomial extrapolation with variable order and stepsize was used for SPF propaga-

tion, and a short iterative Lanczos (SIL) algorithm with variable order and stepsize for the ntegration of the A-vector. The latter are more suitable for propagation calculations[21]. Table 5.1 summarizes the parameters used for each integrator.

Integrators (CMF)	
SPF	A-vector
BS { accuracy $=10^{-7}$; maximalorder$=$ 8 }	SIL { accuracy $=10^{-7}$; maximalorder$=$ 20 }

Table 5.1: Integrator parameters used to propagate SPF and A-vector.

For a given propagation time interval, the time required for each calculation depends mainly on the size of the grid, the size of the SPF basis and the accuracy of the calculation. The propagation calculations we have carried out require a considerable amount of numerical resources. The use of parallel shared memory hardware was essential in order to make the simulation times feasible. Information about the wall simulation time and the number of SPF used is given in table 5.2.

SPFs $[n_\kappa^{\min}, n_\kappa^{\max}]$				
H/Pd(111)			H_2/Pd(111)	
n_x	n_y	n_z	$n_{x_1y_1z_1}$	$n_{x_2y_2z_2}$
$[30, 40]$	$[30, 40]$	$[10, 15]$	$[15, 30]$	$[15, 30]$

Table 5.2: Number of SPFs used to describe the different system modes during propagation calculations. The average minimum and maximum wall time required for 1 ps of propagation calculation ranges from 2h to 250h on the HPC cluster at Strasbourg university.

5.2 Quantum dynamics of H/Pd(111)

In this section, we present two studies of the dynamics of a single hydrogen atom following a vibrational excitation on a parallel mode (study 1) and a perpendicular mode (study 2) to the substrate.

5.2.1 Propagation of a local state with one quantum of vibrational excitation in the parallel mode

The study on the H/Pd(111) spectrum showed that the levels including states with one quantum of vibrational excitation in the parallel modes are affected by tunneling splitting, leading to a change in their local vibrational behaviour. In this study, we aim to assess the impact of this splitting on the dynamics of the system initially excited in the local mode parallel to the substrate.

We will consider in the following the situation where the hydrogen atom is in a state initially localized at an fcc site and has a single quantum of vibrational excitation in one of the components parallel to the substrate. There are several ways of constructing such a state, the simplest of which is to consider a wave function defined by a harmonic oscillator and which has a node at the x or y DOF. This state involves uncorrelated DOF and can easily be put in the form of products of one-dimensional functions adapted to MCTDH. Several propagation tests have been carried out with states of this type, and we have found that their average energy is very high compared with the targeted energy interval. The drawback with pre-constructed states is that they are not necessarily well adapted to the local structure of the potential well and do not represent all characteristics of a locally excited state. A better alternative is to use the local PES eigenstates presented in appendix C. These states reflect the local $\boldsymbol{C}_{3v}$ symmetry of the potential and can represent to a better approximation the state of a hydrogen atom excited locally at an fcc site by an external interaction.

In this first study, we have used state number 3 of the local PES (see figure 5.1 at t=0 fs) as the initial state of the system[1]. Its total energy is 235.5 meV, or around 80 meV when the ZPE is subtracted[2]. As the system is non-dissipative, the total energy of this state must remain constant during propagation, if the choice of the SPF basis and integrators is optimal. We propagated this state over 4 ps. Figure 5.1 shows snapshots of the time evolution of the RPD over this time interval.

[1] This state is not stationary under the action of the system's global Hamiltonian.

[2] Here and in the remainder of this section, state energies are given with respect to the ZPE of the system.

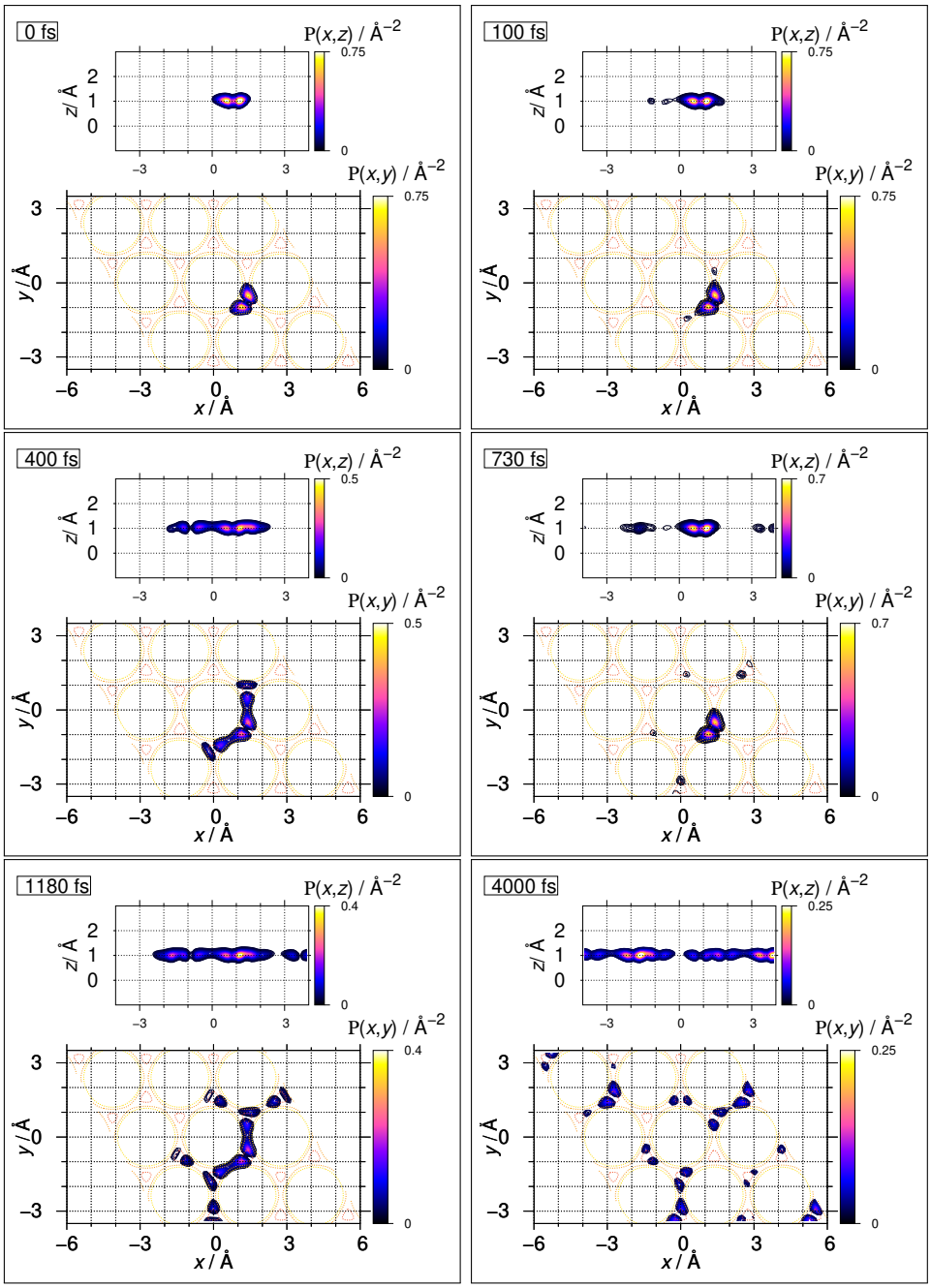

Figure 5.1: Snapshots of the time evolution of the RPD of a state with one quantum of vibrational excitation in a given component of the parallel mode. The latter is initially localized in an fcc site.

At the initial instant, the system's wavefunction is entirely localized around an fcc site. The structure of RPD shows a nodal structure corresponding to excitation in one of the two components parallel to the substrate. At 100 fs, presence probabilities at neighboring hcp sites appear, indicating that during this time the hydrogen atom is able to pass through the potential barrier separating it from these sites. At 400 fs,

the system's wavefunction has spread across the potential barriers and significant presence probabilities appear at next neighboring hcp sites. The nodal structure of the RPD at these sites shows that the hydrogen atom retains its vibrational excitation during this passage. Between 400 fs and 730 fs, a large part of the wave function returns to the initial fcc site, while a fraction of it appears at other nearby fcc sites. Further propagation shows a repetition of this process over time, leading the system's wave function to spread out over all the sites at the surface. Nevertheless, at 4 ps, the probability of the hydrogen atom being present at the initial fcc site is zero, indicating that it has left this site.

The presence probability of the hydrogen atom at the initial fcc site seems to be oscillatory. This is due to the wave nature of the state defining the hydrogen atom. A qualitative way of interpreting this behavior is to say that, as a result of excitation, the system gains energy, and its wave function spreads over the energetically accessible region. Part of the wave function is reflected at the potential barrier separating the fcc and hcp sites, as well as at the wall to the Pd atom, resulting in a reversed dynamics leading to the relocation of the wave function to the initial site. In order to understand the origin of these oscillatory dynamics in a more quantitative way, we evaluated the presence probability of the hydrogen atom at the initial fcc site. More specifically, we calculated the probability to find the hydrogen atom in a well defined volume V delimiting the initial fcc potential well. Its time evolution is then evaluated by integrating the time dependent probability density in the restricted space defined by V. Let

$$P(t) = \int_V |\Psi(x, y, z, t)|^2 \mathrm{d}x\mathrm{d}y\mathrm{d}z \tag{5.2}$$

The volume V can be chosen in any way as long as it initially contains the entire area around the fcc potential well. A simple choice is a parallelepiped box (in the twisted coordinates) with $x_\mathrm{t} \in [0; d/2]$, $y_\mathrm{t} \in [-d/2; 0]$ and $z_\mathrm{t} \in [0.2\ \text{Å}; 1.7\ \text{Å}]$. We evaluated this quantity in MCTDH using an operator defined by

$$\hat{P} = \prod_\kappa (\hat{1} - \hat{\Theta}_{\kappa_\mathrm{min}}) \hat{\Theta}_{\kappa_\mathrm{max}} \tag{5.3}$$

With $\hat{\Theta}_\kappa$ is the operator of the step function that acts only on the DOF $\kappa \in$

$\{x_t, y_t, z_t\}$ such that :

$$\hat{\Theta}_{\kappa_m} = \begin{cases} \hat{0} & \text{if } \kappa < \kappa_m \\ \hat{1} & \text{if } \kappa \geq \kappa_m \end{cases} \tag{5.4}$$

$\kappa_m \in \{\kappa_{min}; \kappa_{max}\}$ correspond to the values that delimit the box of volume V . In the following, we will refer to $\hat{P}$ as the box operator.

The probability $P(t)$ of finding the hydrogen atom in volume V is then given by the expectation value of this operator, i.e.

$$P(t) = \langle \Psi(t) | \hat{P} | \Psi(t) \rangle \tag{5.5}$$

Where $|\Psi(t)\rangle$ is the state defining the system. This approach finally allows us to numerically evaluate the integral given in equation 5.2 within the MCTDH program suite using the "expect" keyword.

In order to cover a wider time interval, we extended the propagation of the system wavefunction over 17 ps. Figure 5.2 shows the time evolution of this function.

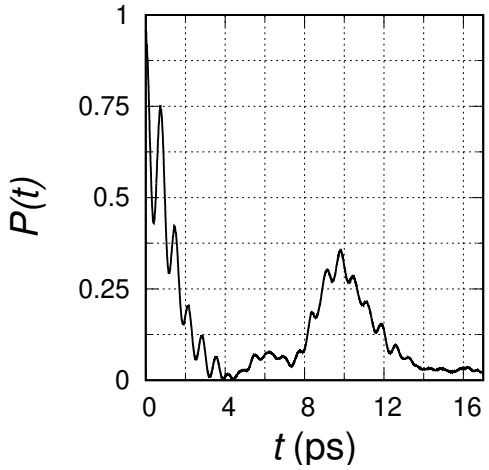

Figure 5.2: Presence probability at the initial fcc site.

The figure shows the presence of essentially two types of oscillations with quasi-periods $T_1 \approx 0.7$ ps and $T_2 \approx 9.8$ ps. The hydrogen atom is initially contained in volume V, resulting in $P(0) = 1$. The oscillation of period T_1 first causes this probability to drop below 0.5 at around 0.39 ps, corresponding approximately to the third snapshot in figure 5.1 Then it increases again, but only partially, to around 0.73 ps, corresponding to the fourth snapshot in figure 5.1, where the amplitude of the RPD is again significant at the initial fcc site. The function then continues to

oscillate with almost the same periodicity while being slowly damped to zero. At half the period of T_2, the probability has fallen to zero, i.e. at around 4 ps, corresponding to the last snapshot in figure 5.1 where the hydrogen atom has completely left the initial potential well.

As we pointed out in the introduction to this chapter, the dynamics of the system is governed by the way in which the stationary states composing the system's wave function interfere with each other over time. To identify this composition, we determined the spectral decomposition of the system's wave function over the set of eigenstates calculated in section 4.2. To this and, an auxiliary analysis program of the MCTDH program suite called "crosscorr" was used which projects the system's state on a reference state.

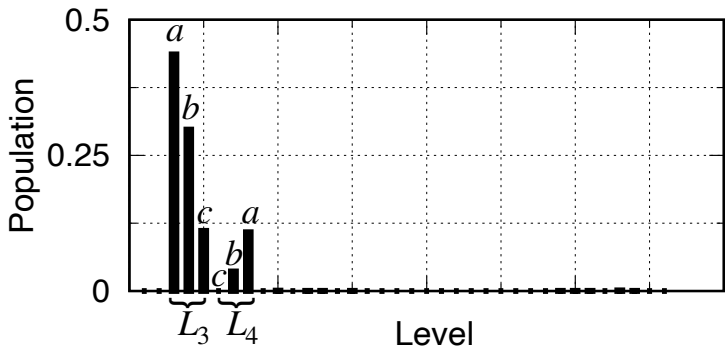

Figure 5.3: Populations of sub-levels. The latter are obtained by summing the populations of all the (quasi-)degenerate states belonging to each sub-level.

Figure 5.3 shows the population of each sub-level given in table 4.3[3]. We can see that this state contains mainly components in levels 3 and 4. Given that the IWF is an eigenfunction of the local PES including a single quantum of vibrational excitation in the parallel mode, its decomposition in the total eigenbasis of the system mainly involves the state of the corresponding level L_3 of the global PES as well as the states forming tunnel doublets with the latter (L_4). The populations of the other

[3]The population p_k of an eigenstate component $|\varphi_k\rangle$ is given by $p_k = |c_k|^2 = |\langle\varphi_k|\Psi(0)\rangle|^2$. The population of each sub-level L_i is then obtained by summing the populations of all the (quasi-)degenerate states belonging to it, i.e. $p_{L_i} = \sum_{k\in\{L_i\}} p_k$.

levels are considered negligible in the following. We therefore consider the eigenstate decomposition of the system's wave function given by :

$$|\Psi(t)\rangle = \sum_{k\in\{L_3,L_4\}} c_k(0)e^{-iE_kt/\hbar}\,|\varphi_k\rangle \tag{5.6}$$

To identify the contribution of these states to the presence probability in figure 5.2, we will evaluate the analytical formulation of $P(t)$ in this basis using equation 5.6.

$$\begin{aligned} P(t) &= \langle\Psi|\hat{P}|\Psi\rangle = \langle\Psi|\Psi\rangle_V \\ &= \sum_{k\in\{L_3,L_4\}} c_k(0)^2\,\langle\varphi_k|\varphi_k\rangle_V \\ &+ 2\sum_{\substack{k,k'\in\{L_3,L_4\}\\ k\neq k'}} c_k(0)c_{k'}(0)\,\langle\varphi_{k'}|\varphi_k\rangle_V\cos((E_{k'}-E_k)t/\hbar) \end{aligned} \tag{5.7}$$

With[4]

$$\langle f|g\rangle_V = \int_V f^* g\mathrm{d}V \tag{5.8}$$

The second term of equation 5.7 shows that the amplitude of the oscillation of the presence probability of the hydrogen atom in the fcc site comes from the eigenstates of different energies that have a non-zero local overlap in the volume V, i.e. $\langle\varphi_{k'}|\varphi_k\rangle_V \neq 0$ and $E_k \neq E_{k'}$[5]. The period of each oscillation is given by $T = 2\pi\hbar/(E_k - E_{k'})$. Several properties can be deduced from equation 5.7:

- Since states of L_3 have a large local overlap in V and close energies, the second term of equation 5.7 yields slow oscillations with large amplitudes[6].
- The states of L_4 have a relatively small local overlap in V and close energies. In the second term of equation 5.7, this translates into slow oscillations with small amplitudes.
- The states belonging to these two different levels have a non negligible overlap, their energy difference is large. This results in fast oscillations and small amplitudes.

[4] $|\varphi_k\rangle$ and $c_k(0)$ are real.

[5] This term naturally cancels out if integrated over the total space, given the orthogonality between the system's eigenstates.

[6] Provided that the c_k are not very small

The periods of oscillation T_1 and T_2 observed in figure 5.2 correspond to energy differences of $\Delta E_1 = 2\pi\hbar/T_1 \approx 5.8$ meV and $\Delta E_2 = 2\pi\hbar/T_2 \approx 0.4$ meV, which can be related to the average energy difference between the states of levels L_3 and L_4 (T_1) and between the sub-levels of the latter (T_2). We can therefore deduce that the breathing motion initially observed for the RPD is due to the superposition of states of levels L_3 and L_4, which form tunneling doublets within the system which we termed AB-tunneling. A slower tunneling process is superimposed on this motion, leading the hydrogen atom's wave function to progressively leave the initial fcc site, we related this to a ABA-tunneling process.

We conclude this study with a discussion of the contribution of the tunneling effect to the dynamics of the system. Following excitation of the hydrogen atom in a parallel mode to the substrate, the latter does not acquire sufficiently high energy to 'classically' overcome the potential barrier separating the fcc and hcp sites. We have seen in this study that the driving force behind this dynamic is the energy gap between the eigenstates of levels (and sub-levels) 3 and 4. This gap is due in part to the difference in potential structure in the fcc and hcp wells, but also to the tunneling splitting that has affected the spectrum of the system. The dynamics of the hydrogen atom is therefore governed by tunneling to two different types : first a tunneling to the nearest neighbor site (AB-tunneling), then a subsequent tunneling to sites of the same type further away (ABA-tunneling).

5.2.2 Propagation of a local state with one quantum of vibrational excitation in the perpendicular mode

In the following, a propagation study will be presented of the hydrogen atom prepared in a state with one quantum of vibrational excitation in the perpendicular mode. The latter is considered to be initially localizd at an fcc site. The aim of this study is to highlight the impact of the Fermi resonance coupling between the perpendicular and parallel modes on the overall dynamics of the system.

To construct such a state, we have modified the local PES given in appendix C so as to suppress the coupling between the parallel and perpendicular modes in equation C.1. Removing this term from the potential results in eigenstates where the pure

states 1^1 and $2^2(A_1)$ are decoupled. Figure 5.4 shows the RPD of these two states.

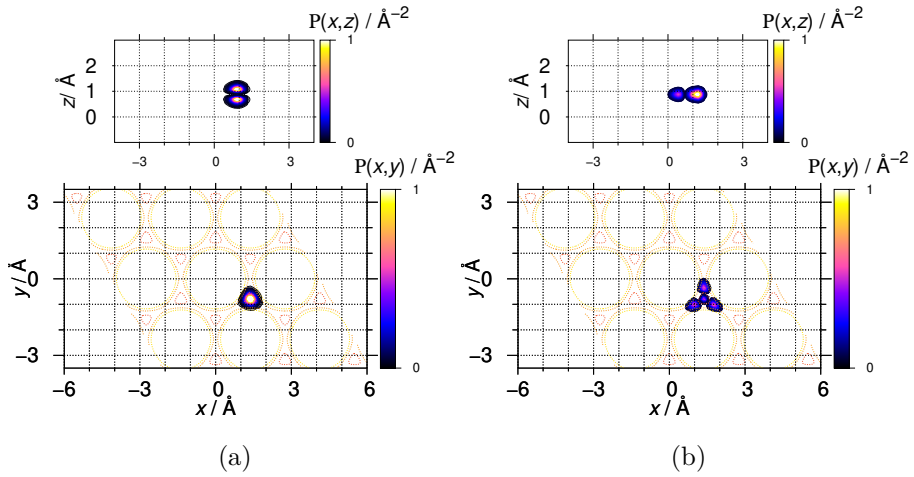

Figure 5.4: Two-dimensional representation of the RPD of the pure states 1^1 (a) and $2^2(A_1)(b)$.

We can see from figure 5.4a a presence of a node in the z DOF and a node-less structure in the xy-plane, indicating a 1^1 pure state, while the state given in 5.4b has a nodal structure in the xy-plane corresponding to a doubly excited state, its structure in the xz-plane is node-less, indicating a pure state of type $2^2(A_1)$.

The state shown in figure 5.4a has been used as the IWF in this simulation. It has the advantage of being better adapted to the local structure of the potential and allows us to represent the situation we wish to study here. The total energy of this state is 155 meV. Figure 5.5 shows snapshots of the time evolution of the RPD over 2 ps.

Time evolution of the RPD shows that after 44 fs, the system's wavefunction presents an important component in the pure state $2^2(A_1)$. It also begins to spread symmetrically across the three potential barriers around the fcc site. This process continues until 68 fs, at which point the system has lost the shape of the initial 1^1 pure state component, and significant presence probabilities appear at nearby hcp sites. At 124 fs, nodal structures appear at the hcp sites, indicating the presence of non-zero components belonging to the 1^1 and $2^2(A_1)$ states. At 160 fs, the amplitudes of the RPD at the initial fcc site are once again significant, while a fraction of these remain localized at nearby hcp sites. Part of the system's wave function seems to have re-

turned to a configuration close to its initial state. Further propagation shows that this breathing motion repeats over time, in parallel with a progressive spreading of the wave function over the other sites. At 2 ps, presence probabilities appear at all sites on the surface.

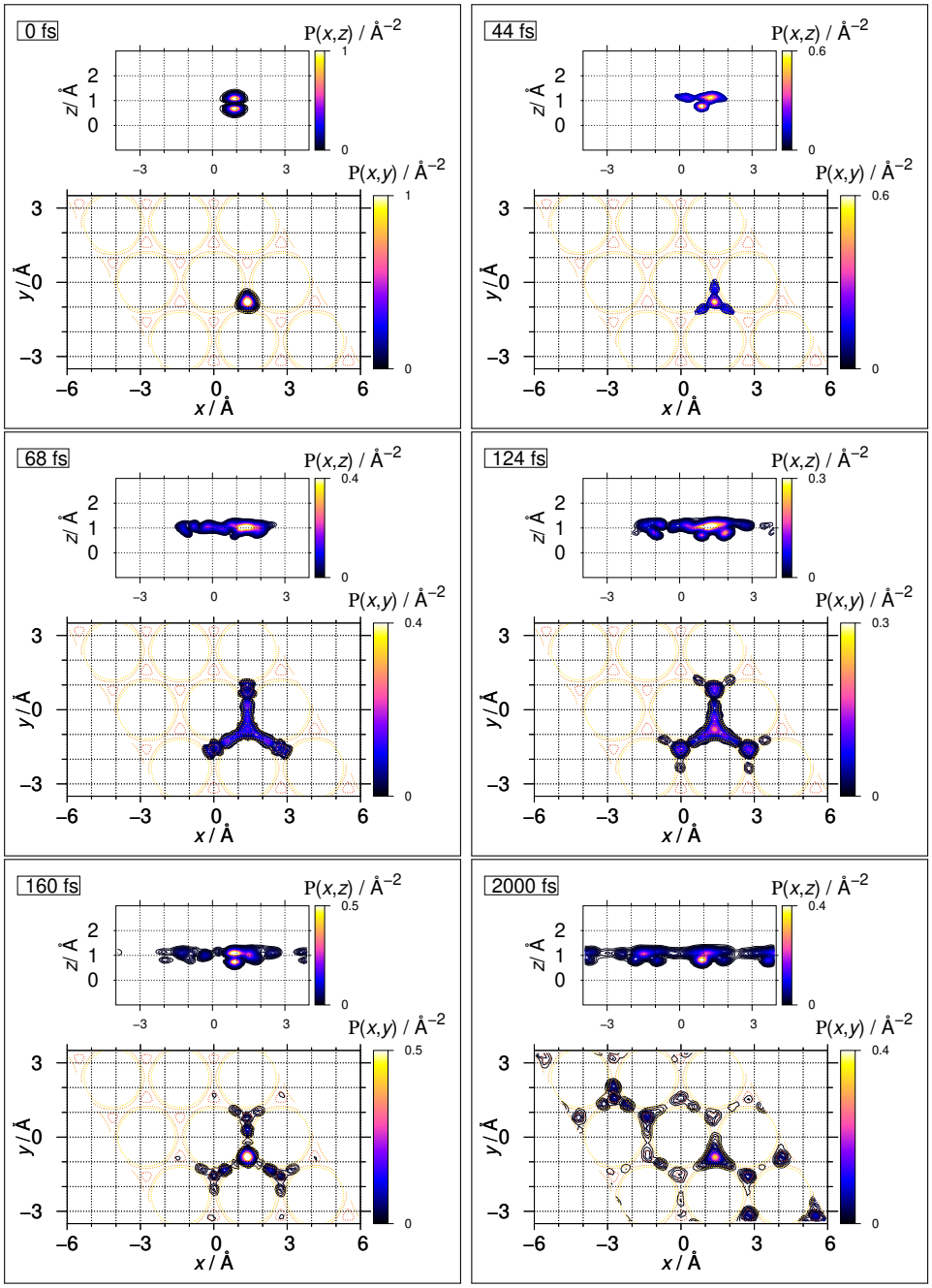

Figure 5.5: Snapshots of the time evolution of the RPD of a state with initially one quantum of vibrational excitation in the pure perpendicular mode, localized in an fcc site.

Analysis of the time evolution of the RPD shows that, following excitation of the

hydrogen atom mode 1, a periodic population transfer between the latter and the $2^2(A_1)$ pure state takes place, which directly manifests the Fermi resonance coupling between these modes.

As mentioned in the previous study, the origin of the oscillations observed in the wave function is due to the superposition of certain spectral components over time. The resulting quasi-periods are directly linked to the energy difference between them. Initially, the 1^1 mode population appears to oscillate with a period of around 160 fs. This oscillation is due to a superposition of states that differ by $\Delta E \approx 25$ meV. To determine the set of eigenstates contributing to the system dynamics, we calculated the spectral decomposition of this state on the eigenbasis. Figure 5.6 shows the population of each (sub)level.

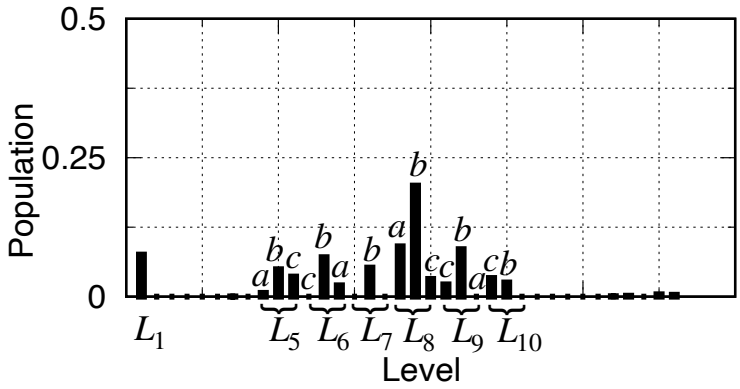

Figure 5.6: Populations of sub-levels. The latter are obtained by summing the populations of all the (quasi-)degenerate states belonging to each sub-level.

The eigenstate decomposition of this state is relatively broad, involving almost all the levels in which the 1_A mode appears (table 4.3). On one hand, the periodicity observed in the population transfer time between the perpendicular and parallel modes could be due to the superposition of several components at the same time, since several levels here have an energy difference of approximately 25 meV.

On the other hand, analysis of the RPD shows that this breathing motion is accompanied by a spreading of the wave function at the surface, which is itself periodic. This periodicity can be seen directly by inspecting of the time evolution of the pres-

ence probability $P(t)$ at the initial fcc site[7]. Figure 5.7 shows the representation of this function over 2 ps.

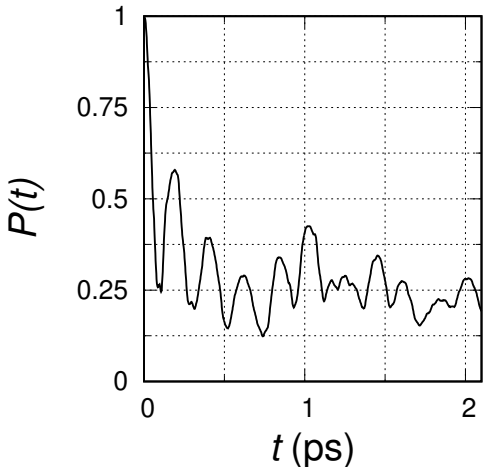

Figure 5.7: Presence probability at the initial fcc site.

The figure shows a damped oscillation of $P(t)$ with a quasi-period of around 200 fs. A superposition between states with an energy difference of around 20 meV could cause this type of oscillation. But given the large spectral decomposition of this state, we cannot identify which components of this state in the eigenbasis directly contribute to this behavior. Damping leads P to steadily while converging towards an asymptotic value of around 0.25, indicating a high probability that the hydrogen atom quits definitively the initial fcc site during this period. This significant drop in overall amplitude of $P(t)$ is due to the superposition of a large number of states in the same level with large overlap, resulting in many oscillations with non-commensurate periods which tend to mutually cancel out. The number of periods involved in the superposition is large. Nevertheless, it is finite. By Liouvilles's recurrence theorem for finite dynamical systems, we can expect that for a longer propagation time, the probability of finding the hydrogen atom at the initial fcc site could again increase, although the theorem does not asset when the recurrence time will be.

From figure 5.6 one could suppose that states in sublevels 6.b and 8.b are more prominently involved in the dynamics than others. Their energy difference from table 4.3 is about 20 meV. States in sublevel 8.b are upper components of the Fermi

[7]The presence probability was defined in equation 5.3

resonance pair, the lower components of which are in level 5. States in sublevel 6.b are upper components of AB tunneling doublets, the lower component of which are level 5, too.

The dynamics investigated in this example seem to involve both tunneling and intramolecular vibrational redistribution (IVR) via common intermediate states, in level 5, specifically. While IVR would be at the origin of the (quasi-)periodic behaviour of the probability density, tunneling to nearby lying hcp sites would effectively lead to the damping of $P(t)$ toward a remaining occupation probability of the initially occupied fcc site of about 25 %. This is still much larger than the statistical value at thermal equilibrium ($\approx$ 10%, in the 3×3-grid, if only fcc sites are considered, or 5%, H atoms occupy all fcc and hcp sites). Yet, probability density is broadly distributed over the entire configuration space. subsequent evolution might eventually show a recurrent particle concentration at the initial fcc site, but we cannot say when this happens. The dynamics shown here is totally coherent and reversible; yet it resembles a statistical and effectively irreversible diffusion of particles.

5.3 Quantum dynamics of H_2/Pd(111)

In this section, we present three studies on the dynamics of two hydrogen atoms following the excitation of a single atom. In the first and second study, the two atoms are initially localized at neighboring fcc sites. One of the two atoms is then excited in a parallel mode (study 1) or a perpendicular mode (2). In the third study, we consider a situation similar to that of the first study, where this time the two atoms occupy neighbouring fcc and hcp sites.

5.3.1 Propagation of a local AA-state with one quantum of vibrational excitation in the parallel mode

In this section, we present a study of the dynamics of the two hydrogen atoms following the excitation of one of them in a parallel mode to the substrate. The study we have carried out on the stationary states of H_2/Pd(111) has shown the presence of a strong coupling between the hydrogen atoms when they are located at neigh-

boring sites of the same type. The aim of this study is to assess the effect of this coupling on the individual dynamics of each hydrogen atom. In particular, we wish to investigate two properties: firstly, the time evolution of the vibrational excitation carried by the first atom, in particular if there is an excitation transfer between the two atoms; secondly, if the excitation of one hydrogen atom is likely to cause one or two atoms to leave their initial sites.

The IWF is given by a six-dimensional function depending on the DOFs of each atom. The latter are initially located at two neighbouring fcc sites. A quantum of vibrational excitation is then introduced on only one hydrogen atom, while the second remains in its ground state. There are several ways of constructing such a state. In the following, we present the approach we have taken to achieve this.
The state ψ_1 shown in figure 4.32 is given by a superposition of two eigenstates, one in level 7, the other in level 13. In this state, one quantum of vibrational excitation is entirely localized on the first atom. We used a state similar to the latter, where all the presence probabilities of each atom are initially localized at a single site. To do this, we used the box operator defined by :

$$\hat{P} = \hat{P}_1 \otimes \hat{P}_2 \tag{5.9}$$

$\hat{P}_i$ is the box operator acting only on the atom $i \in \{1; 2\}$. The latter has been defined in equation 5.3. In MCTDH, this definition can be expressed by the entries given in table 5.3.

	x_{t1}	y_{t1}	z_{t1}	x_{t2}	y_{t2}	z_{t2}
$\hat{P}_1$	$(\hat{I} - \hat{\Theta}_0)\hat{\Theta}_{-d}$	$(\hat{I} - \hat{\Theta}_{-d})\hat{\Theta}_{\frac{-3d}{2}}$	$\hat{I}$	$\hat{I}$	$\hat{I}$	$\hat{I}$
$\hat{P}_2$	$\hat{I}$	$\hat{I}$	$\hat{I}$	$(\hat{I} - \hat{\Theta}_{\frac{3d}{2}})\hat{\Theta}_d$	$(\hat{I} - \hat{\Theta}_d)\hat{\Theta}_{\frac{d}{2}}$	$\hat{I}$

Table 5.3: MCTDH definition of the box operator in equation 5.9.

$\hat{I}$ is the identity operator acting on a single DOF. These parameters have been chosen so as to build a box around each potential well in which we wish the hydrogen atom to remain localized. By applying this operator to the $|\psi_1\rangle$ state, the amplitudes of its wave function outside these regions are all reduced to zero. The resulting

normalized state $|\Psi_0\rangle$ has presence probability of both hydrogen atoms only in the targeted fcc sites. The latter is given by:

$$|\Psi_0\rangle = \frac{1}{\langle\psi_1|\,\hat{P}^*\hat{P}\,|\psi_1\rangle}\hat{P}\,|\psi_1\rangle \tag{5.10}$$

This state is now given by the superposition of several states of levels 7 and 13. Its total energy is 94 meV. We have therefore used $|\Psi_0\rangle$ as the initial wave function for a propagation study over 400 fs. Figure 5.8 shows snapshots of the time evolution of these RPD over this period.

Initially, the first hydrogen atom is located at an fcc site and possesses a single quantum of vibrational excitation in a parallel mode to the substrate. The second atom is in its ground state. At 100 fs, the nodal structure of the RPD on the first hydrogen atom disappears, and a local spreading of the wave function of the second atom is observed. At 200 fs, the nodal structure at the second hydrogen atom indicates that the latter has a quantum of vibrational excitation in a parallel mode to the substrate, while the first atom is in its ground state. At 400 fs, vibrational excitation reappears on the first atom, while the second returns to its ground state.

The analysis of the RPD shows that a quantum of vibrational excitation has been transferred between the two hydrogen atoms. The latter appears to oscillate between them with a period of less than 400 fs. The auto-correlation function given by $f(t) = |\,\langle\psi(0)|\Psi(t)\rangle\,|$ allows us to determine this period more precisely. Indeed, the time required for a double transfer of excitation corresponds to the time during which the system returns to a state close to its initial state. The periodicity observed in the auto-correlation function reflects this characteristic time. We have calculated this function over the 400 fs of propagation. Figure 5.9 shows a graphical representation of the obtained function.

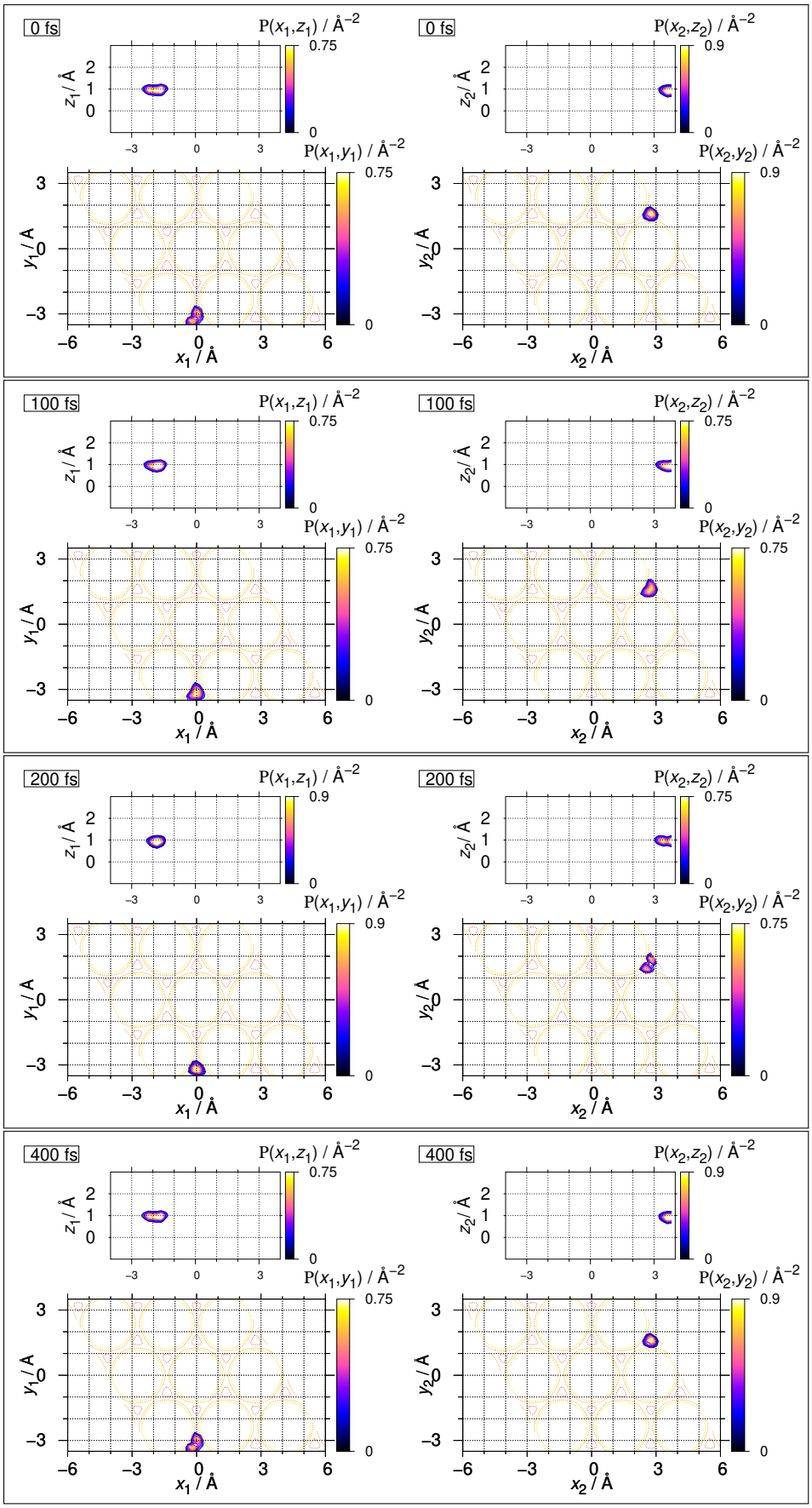

Figure 5.8: Snapshots of the time evolution of the RPD of a state with one quantum of vibrational excitation in the parallel mode. The two hydrogen atoms are initially localized in neighbouring fcc sites.

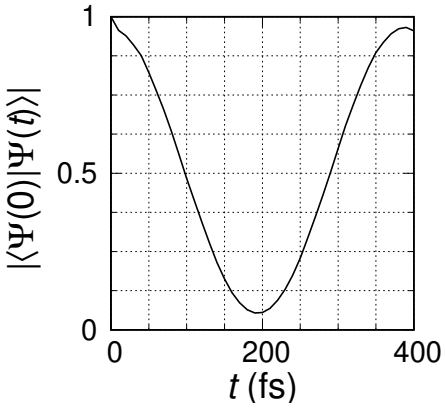

Figure 5.9: Autocorrelation function.

The auto-correlation function[8] has a quasi-period $T \approx 390$ fs. In the system's eigenstate basis, this periodic character is due to the time evolution of the superposition of two (or more) eigenstates with different vibrational energies. In fact, if we first consider that the initial state is given solely by the superposition of two states from levels 7 and 13, which we denote respectively by $|\varphi_{L_7}\rangle$ and $|\varphi_{L_7}\rangle$, i.e.

$$|\Psi(0)\rangle = c_{L_7}\,|\varphi_{L_7}\rangle + c_{L_{13}}\,|\varphi_{L_{13}}\rangle \tag{5.11}$$

The evaluation of $f(t)$ in this case is immediate:

$$f(t) = \Big(|c_{L_2}|^4 + |c_{L_{13}}|^4 + 2|c_{L_7}|^2|c_{L_{13}}|^2\cos\Big((E_{13} - E_7)t/\hbar\Big)\Big)^{1/2} \tag{5.12}$$

This function will then oscillate with a periodic $T = \dfrac{2\pi\hbar}{\Delta E}$, where ΔE is the energy difference between levels 7 and 13. The "quasi-"period of 390 fs given in figure 5.9 corresponds to an energy difference $\Delta E \approx 10.5$ meV. This corresponds to the energy difference between levels 7 and 13 (table 4.4) and shows that the excitation transfer time between the two hydrogen atoms mirrors the energy gap between these levels. However, the minimum of this function does not coincide perfectly with zero. This minimum is reached when the excitation is entirely localized on the second hydrogen atom. This means that the two states are not perfectly orthogonal. In a two-level system, this orthogonality is preserved and the excitation evolves coherently between the two hydrogen atoms. In the problem treated here, the decomposition of the initial state in the eigenbasis involves several states of the same level. The latter are

[8]The latter is initially equal to unity, given that the IWF is normalized.

not perfectly degenerate and may possess a non-negligible energy gap, as we pointed out in section 4.4. A rewriting of the initial state is therefore given by:

$$|\Psi(0)\rangle = \sum_{k\in L_7} c^k_{L_7} |\varphi^k_{L_7}\rangle + \sum_{k'\in L_{13}} c^{k'}_{L_{13}} |\varphi^{k'}_{L_{13}}\rangle \tag{5.13}$$

Some of the components of the same level will therefore vary with very close lying periods, causing them to interfere and create a beating phenomenon. This perturbs otherwise the periodic evolution of vibrational excitation between the two atoms, as in the case of a two-level system[9], which explains the term "quasi-"period used above.

The multiple beating between states of the same level also leads to the gradual delocalization of the system's wave function onto the other potential wells of the surface, supposedly inducing a tunneling process, under the hypothesis that the energy difference between these states comes from a tunneling splitting. The larger the width of a level, the faster the process. This is 0.13 and 0.25 meV for levels 7 and 13 respectively. These quantities are still relatively small and, strictly within the numerical accuracy of the calculations, leading to a very slow tunneling process compared to our propagation time scale. Calculation of the presence probability of the two hydrogen atoms at their initial site showed a drop of around 3% after 400fs. We can speculate that, after about ten picoseconds, non-negligible presence probabilities may appear at other fcc sites on the surface[10].

This study allows us to conclude that when the two hydrogen atoms are localized at neighboring fcc sites, the excitation of one of the two atoms in a mode parallel to the substrate is accompanied by an energy transfer mechanism between the two atoms, this leads to a complete transport of a quantum of vibrational excitation from one atom to the other. The characteristic time of this transfer is about 195 fs. The latter depends directly on the energy difference between the levels of states vibrating in phase and in out-of-phase (table 4.4)[11]. Additional tunneling processes

[9] This can also be observed on the value of this function after one period. This is less than 1.

[10] Tunneling to hcp sites remains negligible in this example. In fact, the spectral decomposition of the system state involves exclusively level 7 and 13 states, which have no amplitude at hcp sites.

[11] We can deduce by analogy from this study that in the case of excitation in the second parallel

toward other fcc sites might occur, but only on a longer time scale, and were not resolved by the present calculation.

5.3.2 Propagation of a local AA-state with one quantum of vibrational excitation in the perpendicular mode

This study will focus on the dynamics of two hydrogen atoms following excitation of one of them in a pure perpendicular mode to the substrate. The two atoms are assumed to be initially located at two neighboring fcc sites. The vibrational excitation is carried entirely by the second hydrogen atom, the first one being in its ground state. The aim of this study is to investigate three aspects of the system's dynamics: the consequence of the Fermi resonance coupling between perpendicular and parallel modes on the motion of the excited hydrogen atom in the presence of a second hydrogen atom in a neighboring fcc site; the dynamical correlation between the two atoms; the impact of tunneling.

Our approach to constructe the initial state is similar to that used for a single hydrogen atom. We used the local PES given in appendix C, cancelling out the coupling term between the pure modes parallel and perpendicular to the substrate. The eigenstates obtained are three-dimensional states of a single hydrogen atom. To construct a six-dimensional state in the configuration we wish to study in this example, we built a new local six-dimensional PES using a local three-dimensional PES for each hydrogen atom separately. Each of these then evolves in a potential well surrounding the fcc site in which it is located. No interaction between the two atoms is taken into account in this PES, so the eigenstates obtained are completely decoupled. The total wave function is therefore given by the tensor product of the individual states. Among the obtained eigenstates, we have selected the one in which the first atom is in its ground state, and the second possesses a quantum of vibrational excitation in the pure mode perpendicular to the substrate. Using the

---

mode, the characteristic time of the excitation transfer is given by the energy difference between levels 8 and 10, i.e. $T/2 \approx 1500$ fs.

same notation as in section 4.2, the initial state writes:

$$|\Psi_0\rangle = N_0 \, |0_{\mathrm{A}}\rangle \otimes |1^1_{\mathrm{A}}\rangle \tag{5.14}$$

Such a state is not stationary under the action of the system's Hamiltonian. Its total energy is 152 meV. It represents a typical state in which the system may exists following excitation of one of the two hydrogen atoms in a mode perpendicular to the substrate.
We propagated this state over 400 fs. Figure 5.10 shows snapshots of the time evolution of these RPD during this time interval.

Initially, the presence probabilities of both atoms are entirely localized at the two fcc potential wells. The RPD of the second hydrogen atom has a node in the DOF z indicating a single quantum of vibrational excitation in the pure perpendicular mode. During this propagation, the first hydrogen atom remains in a quasi-stationary state at the fcc site. In the following, we first discuss only the time evolution of the RPD of the second hydrogen atom, a discussion about the dynamics of the first atom will be given later. At 40 fs, nodal structures appear in the xy-plane indicating a double excitation in the parallel mode. The local state representing the system at this moment seems to be given by the superposition of the two pure states 1^1 and $2^2(\mathrm{A}_1)$. At 80 fs, presence probabilities appear at two neighbouring hcp sites. We note that the amplitudes of the RPD at the two sites are not equivalent, being slightly larger on the hcp site neighbouring to first hydrogen atom[12]. At the same time, the component in the pure state $2^2(\mathrm{A}_1)$ increases, while that on 1^1 decreases. At 140 fs, the RPD are again localized mainly around the initial fcc site showing a nodal structure in the direction perpendicular to the substrate. Nevertheless, presence probabilities are still noticeable at the neighboring hcp site. The structure of the RPD at this site is somewhat spread out in the z direction. A more detailed analysis of this structure (not visible on the figure) shows the presence of a node in the direction perpendicular to the substrate. Between 140 and 280 fs, the same mechanism seems to repeat, but with a higher presence probability at next neighboring sites. At 280 fs, nodal structures in the parallel mode appear at hcp sites that are opposite to the first atom.

[12]These two potential barriers are not equivalent (figure 3.10).

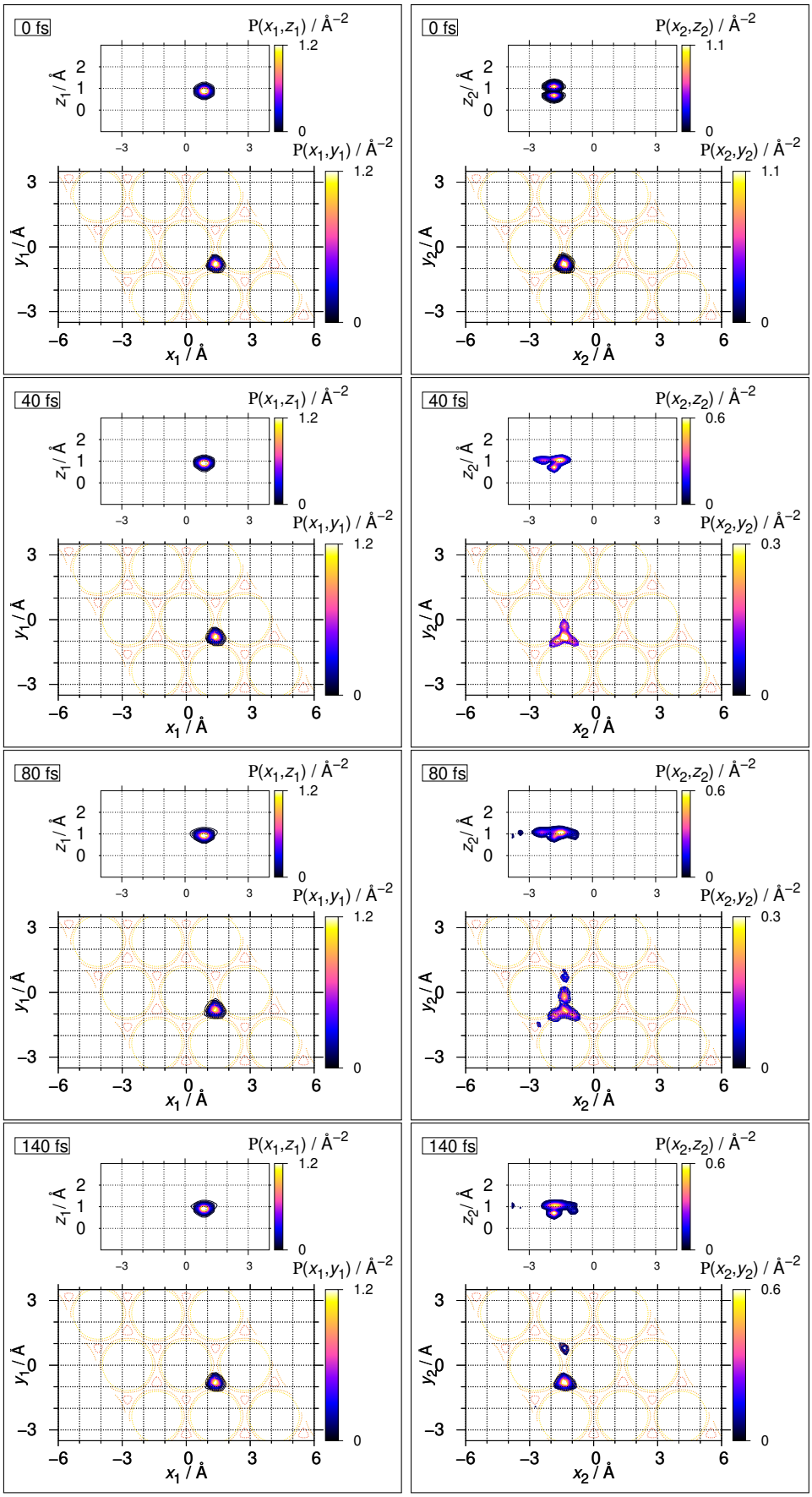
0 fs
P(x_1,z_1) / Å^{-2}
P(x_1,y_1) / Å^{-2}
P(x_2,z_2) / Å^{-2}
P(x_2,y_2) / Å^{-2}
40 fs
80 fs
140 fs
z_1 / Å
y_1 / Å
x_1 / Å
z_2 / Å
y_2 / Å
x_2 / Å

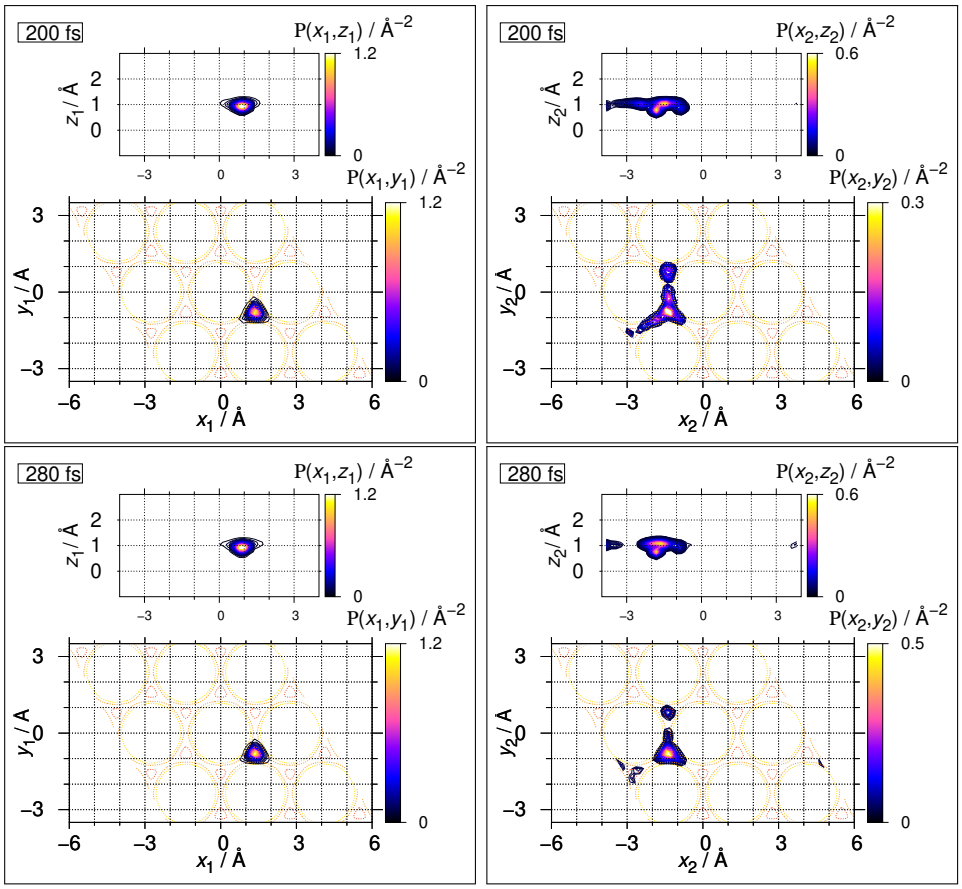

Figure 5.10: Snapshots of the time evolution of the RPD of a state with one quantum of vibrational excitation in the perpendicular mode. The two hydrogen atoms are initially localized in neighbouring fcc sites.

From the analysis of the time evolution of the system's RPD, it appears that following excitation of the second hydrogen atom in the pure perpendicular mode, a population transfer process between the pure states 1^1 and $2^2(A_1)$ is rapidly taking place. This is a direct manifestation of the Fermi resonance coupling between the latter. To quantify this process more precisely, we calculated the populations of these two pure modes during propagation. The population of the $2^2(A_1)$ mode is obtained by evaluating the square modulus of the projection of the system wave function onto this mode. This state has been constructed in a similar way to the initial wave function. The 1^1 mode population is obtained directly by calculating the autocorrelation function. Figure 5.11 shows the obtained results.

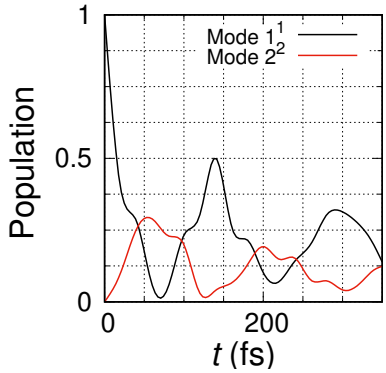

Figure 5.11: Time evolution of the pure states 1^1 and $2^2(A_1)$ populations.

At t=0, the population of state $2^2(A_1)$ is zero, since the latter is orthogonal to the pure state 1^1. The variation in the populations of the two states over time appears to be complementary (with a slight shift). This demonstrates the process of population transfer between the two pure states. The fact that the latter do not vary perfectly in phase opposition shows that population transfer to other modes also takes place during propagation. Both populations have a quasi-oscillatory character, with a quasi-period of 140 fs. This corresponds to the breathing motion observed on the system's RPD in figure 5.10. The origin of these oscillations, as we pointed out in section 5.2, potentially comes from the time evolution of the superposition of two (or more) eigenstates of the system. The latter must possess an energy gap given by $\Delta E = 2\pi\hbar/T \approx 29.3$ meV. A spectral decomposition is required to identify the set of eigenstates involved in the system dynamics. To this end, we have evaluated the projection of this state onto the set of eigenstates we have calculated in this study. Figure 5.12 shows the population corresponding to each level, the latter is obtained by summing over the populations of the 54 states in each level.

This decomposition shows that the system's wave function contains mainly components on the eigenstates of levels 19 $(0_A\ [1^1 + 2^2]_A)_I^+$ and 20 $(0_A\ [1^1 + 2^2]_A)_I^-$. The latter correspond to states located mainly at fcc sites and possessing a quantum of vibrational excitation in the perpendicular mode. The energy difference between the levels of all non vanishing components in the spectral decomposition of this state do not correspond to the energy gap causing the oscillation observed during the propagation. Furthermore, the sum of all populations calculated is 0.47, which represents 47% of the total population. This shows that the eigenstate basis we have

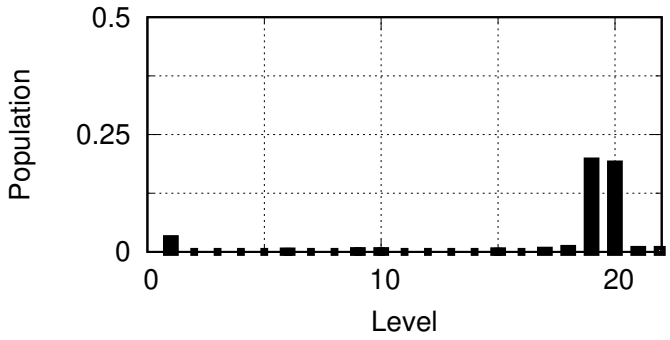

Figure 5.12: Populations of sub-levels. The latter are obtained by summing the populations of all the (quasi-)degenerate states belonging to each sub-level.

calculated is not complete for the description of this state. The latter has probably non-zero components on higher-energy eigenstates.

The Fourier transform of the autocorrelation function gives the spectral energy density of the system [51] , which has peaks around the eigenstate energies that contribute most to the system's dynamics during propagation. Figure 5.13 shows the result obtained by calculating the latter over an energy range between 400 and 500 meV[13].

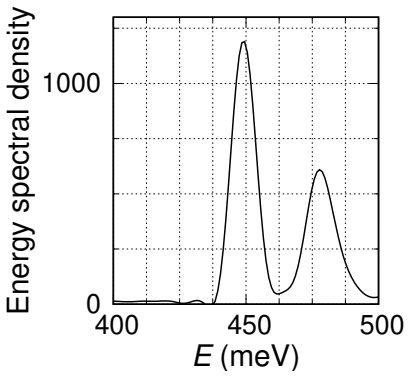

Figure 5.13: Energy spectral density (arbitrary units) obtained by the Fourier transform of the autocorrelation function.

The function obtained has two significant signals located around 448 meV and 477 meV[14]. After subtracting the ZPE, the energy of the first band is around 116 meV

[13]The aim is to cover the complementary part of the spectrum up to the optimum value for potential representation, i.e. 500 meV.

[14]The Fourier transform of the autocorrelation function gives spectral densities that are all the

and that of the second is around 145 meV. The first value corresponds to the average energy of levels 19 and 20[15], which is in agreement with the spectral decomposition shown in figure 5.12. The second value is above the energy range covered by our calculations of eigenstates. In particular, the energy difference between the two bands is 29 meV. This corresponds roughly to the energy gap between the two presumably oscillation-inducing states in the system's wave function. This energy might correspond to the energy gap of the states forming the Fermi resonance diad, of which levels 19 and 20 are the lowest components. As highlighted in the study of a single hydrogen atom, the dynamics of the latter following excitation in a perpendicular mode will be governed primarily by an oscillatory behavior with period related to the energy gap between states forming Fermi resonance pairs.

The damping of the oscillation amplitude in the system's autocorrelation function implicitly reflects a tunneling process whereby part of the wave function is transferred to neighboring hcp sites via tunneling each time it hits a potential barrier. This leads to the progressive delocalization of the probability density on the other adsoption sites of the substrate as function of time.

To conclude, the excitation of one of the two hydrogen atoms in a mode perpendicular to the substrate is accompanied by the dynamics similar to that of an isolated hydrogen atom in short propagation times. This is mainly governed by a Fermi resonance coupling mechanism, linking the in-plane breathing motion to the motion of the hydrogen atom along the z DOF perpendicular to the substrate. This motion is simultaneously accompanied by a tunneling process leading to the progressive spreading of the wave function on other nearby sites. The unexcited hydrogen atom remains in a quasi-stationary state during this time interval. We have not observed any significant correlation between the two atoms involving energy transfer similar to that described in the previous study. These correlations might actually still be present, but on a longer time scale compared to the propagation done in this study. Indeed, in the previous study, we showed that the energy gap between levels

---

more precise the longer the integration domain, i.e. the longer the propagation. Integration over several ps transforms broadband signals into peaks centered around discrete energies.

[15] A more accurate representation should reveal two distinct peaks

7 and 13 is directly related to the time required to transfer a quantum of vibrational excitation from one atom to another. The larger the gap, the shorter the energy exchange time. In the system studied here, we estimate that the time required to transfer a quantum of vibrational excitation in the perpendicular mode is linked to the energy difference between levels 19 and 20, which is around 0.66 meV. A characteristic time related to this energy difference is around 6.2 ps[16]. We estimate that beyond 3 ps, a vibrational excitation transfer mechanism could take place between the perpendicular modes of two hydrogen atoms.

5.3.3 Propagation of a local AB-state with one quantum of vibrational excitation in the parallel mode

In this last section, we present a study on the dynamics of two hydrogen atoms following excitation of one of them in a mode parallel to the substrate. Initially, the two atoms are considered to be located at neighboring fcc and hcp sites, and the vibrational excitation is carried by the atom located at the fcc site. We saw in section 4.4 that when the two atoms occupy neighboring fcc and hcp sites (AB configuration), on one hand they are less strongly coupled than in the case of the AA (or BB) configuration. On the other hand, we saw that tunneling could potentially affect both atoms, leading to a double tunneling process. The aim of this study is to investigate the dynamics of the two atoms in this type of configuration. In particular, we wish to investigate the possibility of excitation transfer between the two atoms, as well as the concerted tunneling process.

The initial wave function was constructed from the individual eigenfunctions of an isolated hydrogen atom. The approach used for its construction is similar to that described in the previous study. Using the same labels as in section 4.2, the initial state is defined as

$$|\Psi_0\rangle = \mathrm{N}_0 \, |2^1_{\mathrm{A}}\rangle \otimes |0_{\mathrm{B}}\rangle \tag{5.15}$$

With N_0 a normalization constant.

The total energy of this state is 124 meV. It is propagated over 700 fs. Figure 5.14

[16]Propagation of this system took around 100h of computation time on relatively powerful machines. A 4 ps propagation, for example, will require at least 1000h of computation time.

shows snapshots of the evolution of the RPD of the two hydrogen atoms during propagation.

At t=0, the RPD in the xy-plane of the first atom has a nodal structure corresponding to a single quantum of vibrational excitation in the parallel mode to the substrate. The RPD of the second atom have a node-less structure corresponding to a non-excited state. After 80 fs, the RPD of the first atom begin to exhibit non-zero amplitudes at the two next neighboring hcp potential wells. This indicates a probabilities for the hydrogen atom to move towards the two hcp sites next neighbouring the first atom. During this time, the second atom remains localized at its initial site. At 160 fs, the RPD of the first atom show higher presence probabilities at the two next neighbouring hcp sites, and a nodal structure appears in the z mode, indicating that this hydrogen atom is likely to be excited in the mode perpendicular to the substrate at these sites. The wave function of the second hydrogen atom begins to delocalize towards the fcc sites neighbouring the initial site in which the first atom is initially localized. At 300 fs, the RPD of the first atom seem to stagnate, but there is an increase of presence probability at both hcp sites. The RPD of the second hydrogen atom show non-zero amplitudes at the two fcc sites adjacent to the first atom. There is also a small presence probability at the potential barrier leading to a non-neighboring fcc site. At 520 fs, the amplitudes of the RPD of the first atom begin to decrease again at the hcp sites, indicating the start of reverse dynamics returning the first atom wave function to its initial site. Meanwhile, the probability of the second hydrogen atom continues to increase at its initial site. It can be seen that the structures of the RPD at neighboring fcc sites all have nodal structures. This indicates that the passage of this atom to neighboring sites is accompanied by a gain of a quantum of vibrational excitation in a mode parallel to the substrate. At 700 fs, the RPD of the first atom again show presence probabilities concentrated exclusively around the initial fcc site. However, the initial nodal structure is less present.

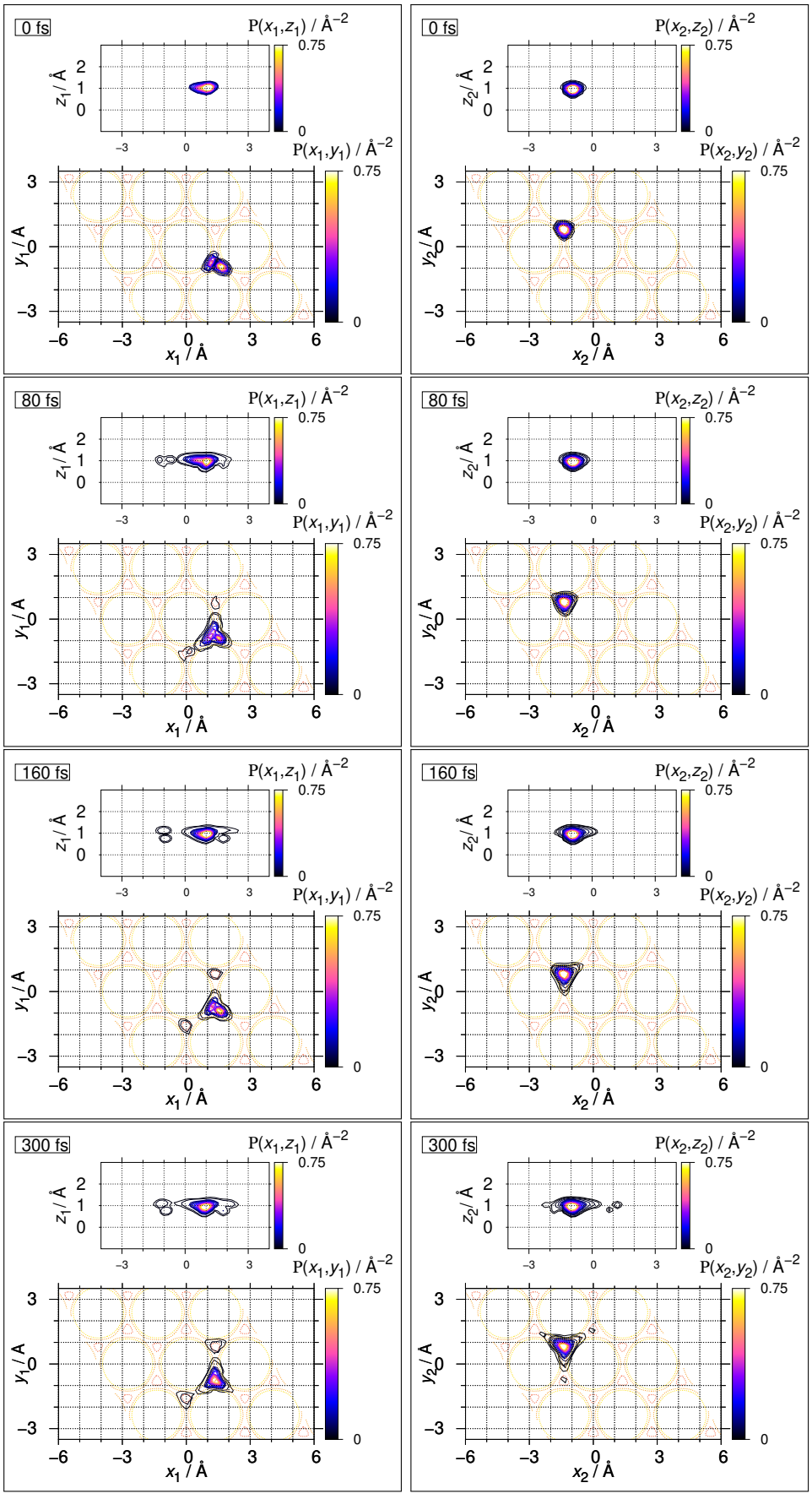
0 fs
P(x1,z1) / Å−2
z1 / Å
P(x1,y1) / Å−2
y1 / Å
x1 / Å
P(x2,z2) / Å−2
z2 / Å
P(x2,y2) / Å−2
y2 / Å
x2 / Å
80 fs
160 fs
300 fs
0.75
0

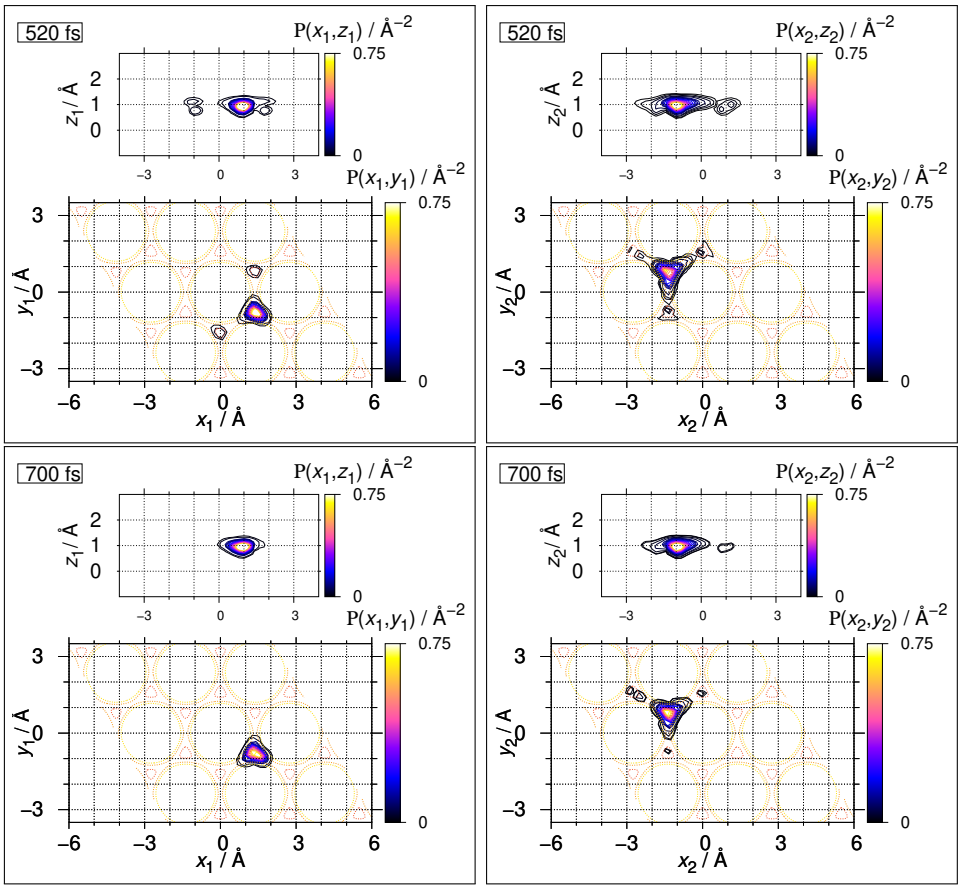

Figure 5.14: Snapshots of the time evolution of the RPD of a state with one quantum of vibrational excitation in the parallel mode 2. The two hydrogen atoms are initially localized in neighbouring fcc and hcp sites.

Analysis of the time evolution of the RPD shows that, following excitation of the hydrogen atom located at the fcc site, the latter can initiate a dynamic towards one of the fcc sites neighbouring the second atom in less than 100 fs. The probability of the second atom leaving its initial site seems to vary more slowly than that of the first. To assess these quantities more accurately, we calculated the probability that each atom occupies the two neighbouring sites over time. To do this, we constructed two box operators in a similar way to that given in equation 5.3. In the first case, we positioned two boxes around the two neighbouring hcp sites of the first atom, as shown in figure 5.15a.

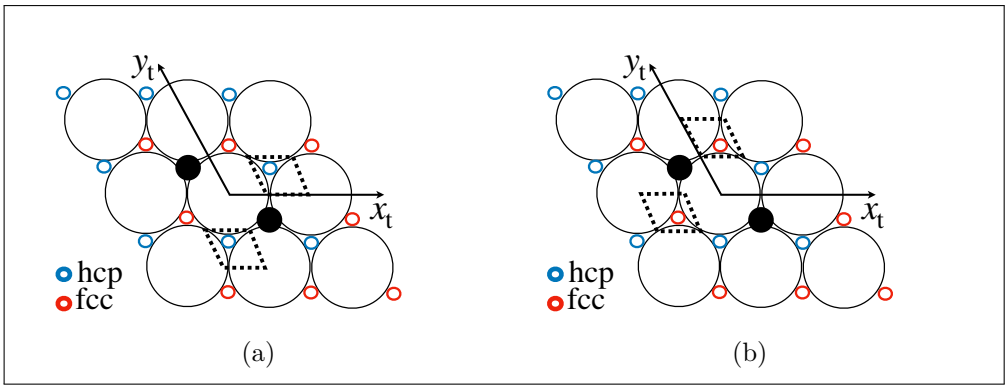

Figure 5.15: Schematic representations of the box of volume V in which presence probabilities are evaluated.

The average value of this operator therefore gives us the probability of occupation of the two hcp sites by the first hydrogen atom. In the second case, we positioned the latter around the other two fcc sites (figure 5.15b). The average value of this operator gives the probability of occupation of the two fcc sites by the second atom. Figure 5.16 shows the results obtained for both operators.

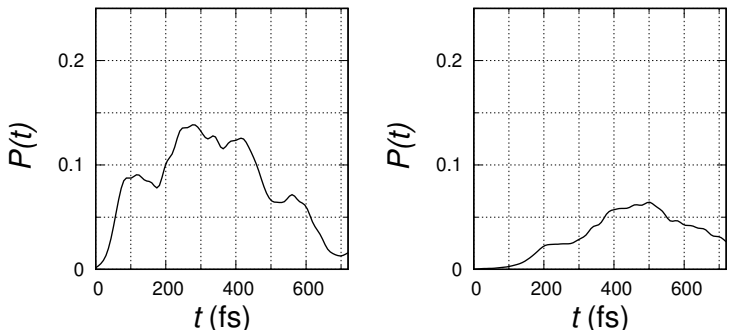

Figure 5.16: Time evolution of the presence probability at the hcp (a) and fcc (b) sites indicated in figures 5.15a and 5.15b respectively.

The figure 5.16a shows that for the first hydrogen atom, the occupancy probability of the two neighboring hcp sites peaks at around 280 fs, while that of the second atom reaches its maximum around 500 fs (figure 5.16b). This indicates that, in terms of probabilities, the dynamics is first triggered by the hydrogen atom initially excited at an fcc site, and is then accompanied by the dynamics of the second atom towards neighbouring fcc sites. If we restrict ourselves to the structures of RPD

only at the two next neighbouring sites, we can see that, for each atom, the probability of moving to any one of these two sites is totally equivalent over this period of time. This simply reflects the local symmetry of the potential, which means that the two potential barriers are initially equivalent, as illustrated in figure 3.10 in section 3.2.2. The quantum nature of these atoms does not allow us to determine the trajectory they may follow over time. The structure of RPD suggests a multitude of possibilities for the simultaneous motion of the two hydrogen atoms. The information we can extract by analyzing these functions can help us to construct certain classical dynamical scenarios. One possible scenario is that the first hydrogen atom initially leaves an fcc site for a next neighboring hcp site. This is accompanied by the passage of the second atom either to an fcc site diametrically opposite the new hcp site occupied by the first atom which we termed neighbouring fcc site, or to the other non-neighbouring fcc site. The delay observed between the dynamics of the two atoms is the time needed for energy transfer to occur : the first one is transferring energy to the second one after moving to the neighbouring fcc site. Indeed, the passage of the second hydrogen atom from one site to the other is accompanied by a gain of a quantum of vibrational excitation in a mode parallel to the substrate, which is a vibrational excitation transfer between the two atoms.

This study gives an insight into the dynamics that hydrogen atoms can exhibit following excitation in this type of configuration. As the spectral decomposition of this state is relatively broad, we cannot directly deduce the contribution of the individual eigenstates in each level in the system's dynamical behavior. However, we can conclude that the excitation of the hydrogen atom located at the fcc site generates via tunneling of the AB-type a high probability of dynamics for both atoms, leading them to leave their initial sites and diffuse along the surface.

Chapter 6

Diffusion of hydrogen atoms on the Pd(111) surface : The Intermediate Scattering Function

The diffusion of adsorbed particles on solid surfaces is an important kinematic process occurring at the gas/solid interface. It is relevant for technological applications of current interest such as molecular storage [4] and machines working at the scale of nanometers [52]. In particular, its importance to heterogeneous catalysis has been evoked for decades [53, 54]. The main and obvious reason is that when adsorbed reactants first meet the solid interface catalyst, they do not necessarily attach on the most favourable coordination sites and have hence to move there before the actual catalytic reaction step takes place. Unless this motion is controlled or guided by an external means, it is governed by diffusion.

Surface diffusion is a two dimensional stochastic motion of particles, whose mean square displacement, is in Brownian regime, a linearly increasing function of time t: $\langle r^2 \rangle (t) = 4Dt$ [55]. In this equation, D is the diffusion coefficient. The diffusion coefficient of an adsorbate is a material property that is essentially governed by the stochastic interaction of particle with its environment; one aspect of this interaction is dictated by the topography of the potential energy surfaces (PES) underlying the dynamics of the adsorbates. The other aspect is friction. In the present study, we shall neglect friction. This is an approximation of the real situation which is

expected to hold well for times much shorter than typical collision times rendering friction. For hydrogen on palladium, these times are on the order of the picosecond or beyond [25, 56].

The experimental determination of diffusion coefficients is not easy. The perhaps most accurate method currently applied to assess experimentally diffusion coefficients are helium-3 spin-echo experiments (^{3}HeSE) [3]. However, to extract them from the measured data, and beyond that to deduce from data on the topography of the PES of catalytic surfaces, many intermediate modeling steps have to be carried out. The experimental results from the ^{3}HeSE experiments rely on the evaluation of the dynamical structure factor (DSF), first introduced by van Hove [8], or on its Fourier-transform, the intermediate scattering function (ISF). Rather than focusing on the diffusion coefficient directly, research is now concentrated on the evaluation and interpretation of the directly observable DSF and ISF, as clearly described in ref. [3].

In this chapter, we present a method for calculating the ISF function using a fully quantum mechanical approach. The latter will be discussed mainly for the case of a single scattering particle suitable for the treatment of the H/Pd(111) system. The generalization of the approach can be established without difficulty. We will first present the theoretical approach used, then give the results of a preliminary study carried out in this project for the H/Pd(111) system.

6.1 Quantum mechanical expression for the ISF from stochastic thermal wave packets

6.1.1 Theoretical model

The ISF $I(\boldsymbol{q}, t)$ measured in ^{3}HeSE experiments is the temporal Fourier transform of the DSF $S(\boldsymbol{q}, E)$, where $\boldsymbol{q}$ stands for the momentum transferred from the scattered ^{3}He atoms to the hydrogen atom moving on the surface, E and t are energy and time respectively. For the latter, van Hove [8] derived the following formula

$$S(\boldsymbol{q}, E) = \sum_n P_n \sum_m \left| \langle m | e^{\mathrm{i}\boldsymbol{q}\boldsymbol{r}} | n \rangle \right|^2 \delta(E - (E_m - E_n)) \tag{6.1}$$

In this equation, $|n\rangle$ and $|m\rangle$ are eigenstates of the scattering center at energies E_n and E_m; P_n is the Boltzmann population distribution at temperature T; $\boldsymbol{r}$ is the coordinate of the scattering center, in our case the hydrogen atom.

Hence, we write for the ISF:

$$I(\boldsymbol{q},t) = \frac{1}{2\pi}\sum_n P_n \sum_m \left| \langle m|e^{\mathrm{i}\boldsymbol{qr}}|n\rangle \right|^2 e^{\mathrm{i}(E_m-E_n)t/\hbar} \tag{6.2}$$

Following van Hove we interpret

$$|n(t)\rangle = e^{-\mathrm{i}E_n t/\hbar}\,|n\rangle = e^{-\mathrm{i}\hat{H}t/\hbar}\,|n(0)\rangle \tag{6.3}$$

where $|n(0)\rangle \equiv |n\rangle$, and $\hat{H}$ is the Hamiltonian of the scattering center. Equation 6.3 is true, as long as $|n\rangle$ are eigenstates and E_n the corresponding eigenvalues of $\hat{H}$.

Still following van Hove we then write

$$\begin{aligned} I(\boldsymbol{q},t) &= \sum_n P_n \sum_m \langle n|\, e^{-\mathrm{i}\boldsymbol{qr}}\,|m\rangle\,\langle m|\, e^{\mathrm{i}\hat{H}t/\hbar}e^{\mathrm{i}\boldsymbol{qr}}e^{-\mathrm{i}\hat{H}t/\hbar}\,|n\rangle \\ &= \sum_n P_n\ \langle n|\, e^{-\mathrm{i}\boldsymbol{qr}}e^{\mathrm{i}\hat{H}t/\hbar}e^{\mathrm{i}\boldsymbol{qr}}e^{-\mathrm{i}\hat{H}t/\hbar}\,|n\rangle \\ &= \mathrm{tr}\,\left\{\hat{\rho}(T)e^{-\mathrm{i}\boldsymbol{q}\hat{\boldsymbol{r}}}e^{\mathrm{i}\hat{H}t/\hbar}e^{\mathrm{i}\boldsymbol{q}\hat{\boldsymbol{r}}}e^{-\mathrm{i}\hat{H}t/\hbar}\right\} \end{aligned} \tag{6.4}$$

where $\hat{\rho}(T) = \sum_n P_n\ |n\rangle\langle n|$ is the density operator of a thermal state.

Equation 6.4 can be evaluated by averaging over an ensemble of *stochastic thermal wave packets*. This idea was suggested by Tolman [57] and has been used in the past, for instance in refs. [58, 59]. We consider wave functions Ψ_k $(k = 1,\ldots,K)$ defined as linear combinations of the eigenstates of the Hamiltonian, where the coefficients are given by the square root of the Boltzmann distribution with random phases $\theta_k^{(\mathrm{r})}(n)$:

$$|\psi_k^{(T)}\rangle = \sum_n e^{\mathrm{i}\theta_k(n)}\,\sqrt{\frac{1}{Q(T)}e^{-(E_n-E_1)/k_\mathrm{B}T}}\ |n\rangle\ , \tag{6.5}$$

where $Q(T)$ is the partition function, k_B is the Boltzmann constant and T is the temperature. For a given k, $\theta_k(n)$ is one realization of random phases. Thermal expectation values of observables are then evaluated as average values of the quantum expectation value of the given hermitian operator $\hat{A}$ in the given random thermal

wave packet, which is denoted as $\left\langle \hat{A} \right\rangle_{\underline{k}}$, where $\underline{k}$ is the set of random realizations:

$$\begin{aligned} \mathrm{tr}\left\{\hat{\rho}(T)\ \hat{A}\right\} &= \left\langle \hat{A} \right\rangle_{\underline{k}}(T) && (6.6) \\ &= \frac{1}{K}\sum_{k=1}^{K} \langle \psi_k^{(T)}|\, \hat{A}\, |\psi_k^{(T)}\rangle && (6.7) \end{aligned}$$

In this approach, equation 6.4 becomes

$$\begin{aligned} I(\boldsymbol{q},t) &= \mathrm{tr}\left\{\hat{\rho}(T)\ e^{-\mathrm{i}\boldsymbol{q}\hat{\boldsymbol{r}}}\ e^{\mathrm{i}\hat{H}t/\hbar}e^{\mathrm{i}\boldsymbol{q}\hat{\boldsymbol{r}}}e^{-\mathrm{i}\hat{H}t/\hbar}\right\} \\ &= \left\langle e^{-\mathrm{i}\boldsymbol{q}\hat{\boldsymbol{r}}}\ e^{\mathrm{i}\hat{H}t/\hbar}e^{\mathrm{i}\boldsymbol{q}\hat{\boldsymbol{r}}}e^{-\mathrm{i}\hat{H}t/\hbar}\right\rangle_{\underline{k}} \\ &= \boxed{\frac{1}{K}\sum_{k} I_k(\boldsymbol{q},t)} \qquad (6.8) \end{aligned}$$

where

$$\boxed{I_k(\boldsymbol{q},t) = \langle \psi_k^{(T)}|\, e^{-\mathrm{i}\boldsymbol{q}\hat{\boldsymbol{r}}}e^{\mathrm{i}\hat{H}t/\hbar}e^{\mathrm{i}\boldsymbol{q}\hat{\boldsymbol{r}}}e^{-\mathrm{i}\hat{H}t/\hbar}\, |\psi_k^{(T)}\rangle} \qquad (6.9)$$

$|\psi_k^{(T)}\rangle$ is a stochastic thermal wave packet at temperature T, and k is one realization of random phases[1].

The evaluation of equation 6.9 relies on the determination of a set of stochastic thermal wave packets. The procedure for constructing these states is described below.

6.1.2 Construction of a stochastic thermal wave packet

The higher the temperature of a state, the larger the decomposition given in equation 6.5. For states with relatively high temperatures, the use of the eigenstate basis we calculated for the H/Pd(111) system may be insufficient for a good description of the state under consideration. We followed a more general method for constructing such states. This will be briefly discussed in this section.

Gelman and Kosloff have proposed a method for constructing such states without going through the determination of an eigenstates basis in the first place [59]. This is a stochastic approach based on the idea that relaxation of an infinite temperature state $|\psi_k^{(\infty)}\rangle$ over a period of time $\tau = \hbar/(2k_bT)$ leads to a thermal state at temperature T.

[1] In practice, the expectation value might already converge for a few $K \approx 3 \sim 8$ realizations of random phases.

To better understand this approach. We will present a brief analytical demonstration of this method in the eigenstates basis set. Consider the spectral decomposition of a stochastic infinite temperature state[2] in the eigenstates basis $\{|\varphi_1\rangle, \ldots, |\varphi_N\rangle\}$

$$|\psi_k^{(\infty)}\rangle = \frac{1}{\sqrt{N}} \sum_n e^{\mathrm{i}\theta_k(n)} \ |\varphi_n\rangle \ , \tag{6.10}$$

Relaxation is achieved by propagating the wave function with the Schrödinger equation in negative imaginary time $t = -i\tau$. The time evolution of this state in the eigenstates basis is given by :

$$\frac{1}{\sqrt{\langle\Psi(\tau)|\Psi(\tau)\rangle}} |\Psi(\tau)\rangle = \frac{1}{(\sum_{k'} e^{-2E_{k'}\tau/\hbar})^{1/2}} \sum_k e^{\mathrm{i}\theta_k(n)} e^{-E_k\tau/\hbar} |\varphi_k\rangle \tag{6.11}$$

By multiplying the numerator and denominator by $e^{2E_1\tau/\hbar}$ and propagating to $\tau = \hbar/(2k_bT)$ we arrive at the expression for a stochastic thermal state

$$|\Psi^{(T)}\rangle = \sum_k e^{\mathrm{i}\theta_k(n)} \sqrt{\frac{1}{Q(T)} e^{-(E_k - E_1)/k_bT)}} |\varphi_k\rangle \tag{6.12}$$

With $Q(T) = \sum_k e^{-(E_k - E_1)/k_bT)}$ the partition function and k_b the Boltzmann constant. We thus obtain the Boltzmann distribution corresponding to a stochastic thermal state of temperature T.

For the construction of an infinite temperature state in the general case, it is irrelevant whether the thermal density operator is expanded in a basis of eigenstates or in any other complete basis set. In such a state, all basis states will have the same weight:

$$|\tilde{\psi}_k^{(\infty)}\rangle = \frac{1}{\sqrt{N}} \sum_n e_k^{\mathrm{i}\theta}(n) \ |\chi_n\rangle \ , \tag{6.13}$$

where $\{|\chi_1\rangle, \ldots, |\chi_N\rangle\}$ is a complete set of basis states in a finite subspace of dimension N. The approach is numerical and convergence must be secured by increasing the value of N.

Gelman and Kosloff showed that with propagation in the negative imaginary time $-\mathrm{i}\hbar/(2k_\mathrm{B}T)$,

$$|\tilde{\psi}_k^{(T)}\rangle = e^{-\mathrm{i}\hat{H}/(\mathrm{i}2k_\mathrm{B}T)} \ |\tilde{\psi}_k^{(\infty)}\rangle \rightarrow |\psi_k^{(T)}\rangle \ , \tag{6.14}$$

for $K \rightarrow \infty$, while the error decreases with $1/\sqrt{K}$.

[2] An infinite temperature state is defined by homogeneous populations over all eigenstates.

6.2 Numerical implementation

In this section, we present the details of the calculations we followed to evaluate equation 6.8.

All these calculations were performed on MCTDH. The primitive basis and other parameters used for these calculations are the same as those used for the time (in)dependent study of the H/Pd(111) system (section 4.2).

The first step is to construct $|\psi_k^{(\infty)}\rangle$ in the primitive basis. The latter must be given in the form of a Hartree product involving functions depending on the three DOFs separately. For each realization k, we construct a unique set of random phases associated with the grid of each DOF. We then use a similar procedure to that presented in section 4.1.1 (equation 4.5) to construct the total wave function.

The resulting state is then propagated in negative imagine time given by $t = -\mathrm{i}\tau = -\mathrm{i}\hbar/(2k_bT)$, allowing the system to relax until reaching the temperature T. The resulting state will serve as the initial state for propagation in real time, and will be denoted in the following by $|\psi_k^{(T)}(0)\rangle$.
To evaluate equation 6.8, we proceed as follows:

- A first propagation is done on $|\psi_k^{(T)}(0)\rangle$ with the Hamiltonian of the system, the obtained state is given by $|\psi_k^{(T)}(t)\rangle = e^{-\mathrm{i}\hat{H}t/\hbar}\,|\psi_k^{(T)}(0)\rangle$.
- We initially apply the operator $e^{\mathrm{i}\boldsymbol{q}\hat{\boldsymbol{r}}}$ to $|\psi_k^{(T)}(0)\rangle$, then propagate the resulting state a with the Hamiltonian of the system. The latter is then given by[3] $|\psi_k(t)\rangle = e^{-\mathrm{i}\hat{H}t/\hbar}e^{\mathrm{i}\boldsymbol{q}\hat{\boldsymbol{r}}}\,|\psi_k^{(T)}(0)\rangle$.
- For each realization k, we evaluate the ISF by calculating the cross integral given by :

$$I_k(\boldsymbol{q},t) = \overbrace{\langle\psi_k^{(T)}(0)|\,e^{-\mathrm{i}\boldsymbol{q}\hat{\boldsymbol{r}}}e^{\mathrm{i}\hat{H}t/\hbar}}^{\langle\psi_k(t)|}\,e^{\mathrm{i}\boldsymbol{q}\hat{\boldsymbol{r}}}\,\underbrace{e^{-\mathrm{i}\hat{H}t/\hbar}\,|\psi_k^{(T)}(0)\rangle}_{|\psi_k^{(T)}(t)\rangle} \tag{6.15}$$

$$= \langle\psi_k(t)|e^{\mathrm{i}\boldsymbol{q}\hat{\boldsymbol{r}}}|\psi_k^{(T)}(t)\rangle \tag{6.16}$$

[3]The resulting state by application of the operator $e^{\mathrm{i}\boldsymbol{q}\hat{\boldsymbol{r}}}$ is no longer thermal, it may be "kicked" thermal state, as it results from a thermal state that received a momentum transfer $\boldsymbol{q}$.

- The final ISF result is then obtained by averaging over all realizations K, i.e.

$$I(\boldsymbol{q},t) \;=\; \frac{1}{K}\sum_{k} I_k(\boldsymbol{q},t) \tag{6.17}$$

The evaluation of the ISF given by equation 6.8 has been proposed in the context of the project QDDA [14] of which this thesis is a part. This formulation from a fully quantum mechanical approach, provides a method to calculate the ISF directly without any preliminary knowledge of the system's eigenbasis. The main ingredient of this method is the set of stochastic thermal states. The latter present no particular difficulty for their construction. However, if we wish to evaluate the ISF for several values of the momentum transfer $\boldsymbol{q}$, a new calculation of the bra propagation given in equation 6.16 must be made for each value of $\boldsymbol{q}$. This can be time-consuming if an individual propagation requires a lot of numerical resources.

An alternative formulation of the ISF was proposed as part of this project [14], with the intention to reduce computation time. Here, we briefly discuss a few important points about this alternative formula. Keeping the same notation as before, the ISF can be written as

$$I(\boldsymbol{q},t) \approx N \left\langle \left\langle J^{*}_{k',k}(\boldsymbol{q},0)\; J_{k,k'}(\boldsymbol{q},t) \right\rangle_{\underline{k}} \right\rangle_{\underline{k'}} \tag{6.18}$$

Where N is the number of realizations and

$$J_{k,k'}(\boldsymbol{q},t) \;=\; \langle \psi_k^{(\infty)}(0)|\, e^{\mathrm{i}\hat{H}t/\hbar} e^{\mathrm{i}\boldsymbol{q}\hat{\boldsymbol{r}}} e^{-\mathrm{i}\hat{H}t/\hbar}\, |\psi_{k'}^{(T)}(0)\rangle \tag{6.19}$$

$$\;=\; \langle \psi_k^{(\infty)}(t)|\, e^{\mathrm{i}\boldsymbol{q}\hat{\boldsymbol{r}}}\, |\psi_{k'}^{(T)}(t)\rangle \tag{6.20}$$

The determination of the ISF with this formula relies mainly on the evaluation of the cross integral $J_{k,k'}(\boldsymbol{q},t)$. The advantage of this formulation is that for a single set of thermal stochastic state realizations, we can evaluate the ISF for any amount of momentum transfer $\boldsymbol{q}$ between helium atoms and hydrogen atoms. Evaluation of the bra of equation 6.16, on one hand, requires the propagation of a wave packet at infinite temperature. These states are energetic, and their propagation generally takes a long time. On the other hand, this formulation remains more practical for systems defined on non-large computing grids, where we wish to evaluate the ISF for a wide range of $\boldsymbol{q}$. Also equation 6.18 is expected to yield approximate results

only, that rely on a large number of stochastic realisations. The conditions under which this equation is valid could not be conclusively verified during this thesis.

The ISF study we carried out on the H/Pd(111) system in this work is based exclusively on equation 6.8. This approach remains the most suitable for this system, given the size of the grid we use.

6.3 Results & discussion

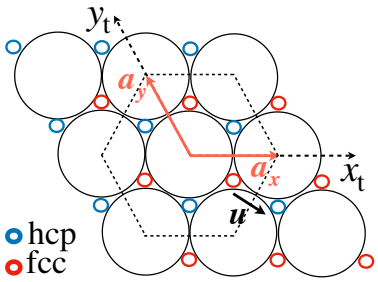

Figure 6.1: Representation of the two Bravais lattice vectors vectors $\boldsymbol{a}_x$ and $\boldsymbol{a}_y$ in the hexagonal lattice.$\boldsymbol{u}$ is a unitary direction vector of the momentum transfer $\boldsymbol{q} = q\boldsymbol{u}$.

In this study, we will consider the situation in which the interaction of the helium atom with the hydrogen atom induces a momentum transfer in a direction parallel to a straight line connecting a neighboring fcc and hcp site. Given the local $\boldsymbol{C}_{3v}$ symmetry of the potential, there are three directions compatible with this type of interaction. We consider the situation given by $\boldsymbol{q} = q\boldsymbol{u}$ where $\boldsymbol{u}$ is a unitary direction vector defined in the Cartesian basis by $\boldsymbol{u} = (\sqrt{3}/2, -1/2, 0)$. The latter is illustrated in figure 6.1. The lattice vectors $\boldsymbol{a}_x$ and $\boldsymbol{a}_y$ are defined along the twisted axes in the hexagonal lattice of the Bravais representation [60], the crystallographic direction of the momentum transfer is given by $\langle 1\bar{1}00 \rangle$. We considered the modulus $q \approx 0.77\text{Å}^{-1}$ in this study as representative value of experimental data [61].

Additionally, we considered the situation where the system is thermalized at $T = 300$ K. As we mentioned in the previous section, the evaluation of the thermal average of the ISF requires several realizations, each of which involves the propagation of a non-interacting thermal state with the external system and the propagation of the thermal state following interaction with the helium atom (the "kicked" thermal

state). 5 realizations were made in total, for each realization two states were propagated over 30 ps. Each propagation took 80h wall time on 30 nodes in parallelized mode.

In the following, we will show the dynamics of two typical states used in the set of realizations. In the last section, we discuss the results obtained for the evaluation of the ISF of this system.

6.3.1 Quantum dynamics of the stochastic thermal states

Relaxation of an infinite temperature state over a time $\tau = \hbar/(2k_bT) \approx 12.73$ fs leads to a state at temperature $T \approx 300$ K. Figure 6.2 shows the two-dimensional representation of the RPD of a typical stochastic thermal state we used.

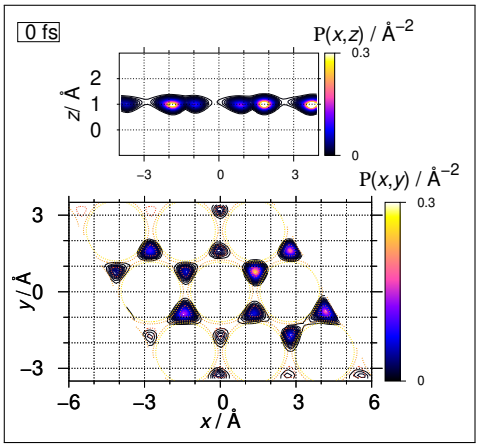

Figure 6.2: Two-dimensional representation of the RPD of a typical stochastic thermal state at temperature T=300 K.

The energy of this state is 18 meV. It has a rather homogeneous distribution probability density occupying similarly well almost all adsoption sites on the surface[4]. This reflects the thermal character of this state.

To verify the thermal distribution of this state, the eigenstates populations were evaluated by projecting the thermal wave packet from equation 6.14 on the eigenbasis already calculated in this work. The populations for each sub-level containing a

[4]We note that the RPD at some sites are quite small. This is due to the level degeneracy, which eventually leads the program to localize certain eigenstates of the system, as highlighted in section 4.2.

set of quasi-degenerate eigenstates was evaluated. These must follow a Boltzmann distribution for a temperature $T = 300$ K. Thus:

$$p_k = p_1 e^{-(E_k - E_1)/k_b T} \tag{6.21}$$

Or

$$\ln\left(\frac{p_k}{p_1}\right) = -\frac{1}{k_b T}(E_k - E_1) \tag{6.22}$$

In the second formulation, the logarithm of the population varies linearly with the energies relative to the ground state, so the slope gives access to the system temperature. This formulation is more suitable for graphical representation. Figure 6.3 shows the results obtained for the state under consideration.

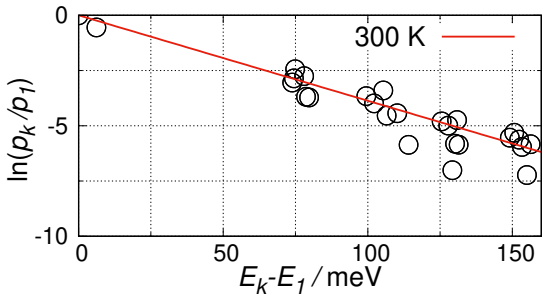

Figure 6.3: Populations of the stochastic thermal state in the basis of eigenstates of the H/Pd(111) potential. Circles give level energies and populations, degeneracy included. The line gives the expected slope at 300 K.

The red line in figure 6.3 shows the population distribution of a perfectly thermal state at temperature $T = 300$ K. The populations of the stochastic thermal state are mainly distributed around the straight line. The relative difference represents the error in each realization. The latter is stochastic and disappears as soon as it is averaged over several realizations. The populations of non-excited states (the first two circles from the origin) and the populations of states with one quantum of vibrational excitation in the parallel mode (circles around 75 meV) represent around 97% of the total populations of this state (87%+10% respectively). This proportion is nearly the same for all the stochastic thermal states used in this study. A state at temperature $T = 300$ K is still populated mainly in its lowest levels. Stochastic errors at higher-energy states negligibly affect the description of the system wave function

over time. We found in this study that after three realizations, the thermal average of the ISF quickly stabilizes. Five realizations were sufficient to reach convergence.

Evaluating the ISF for each realization requires calculating the time evolution of the stochastic thermal states with and without interaction with the helium atom. In the following, an overview of the dynamics of these two states will be given.

Time evolution of the non-interacting stochastic thermal state

Figure 6.4 shows the time evolution of the RPD of the stochastic thermal state presented in the previous section over the first two picoseconds.

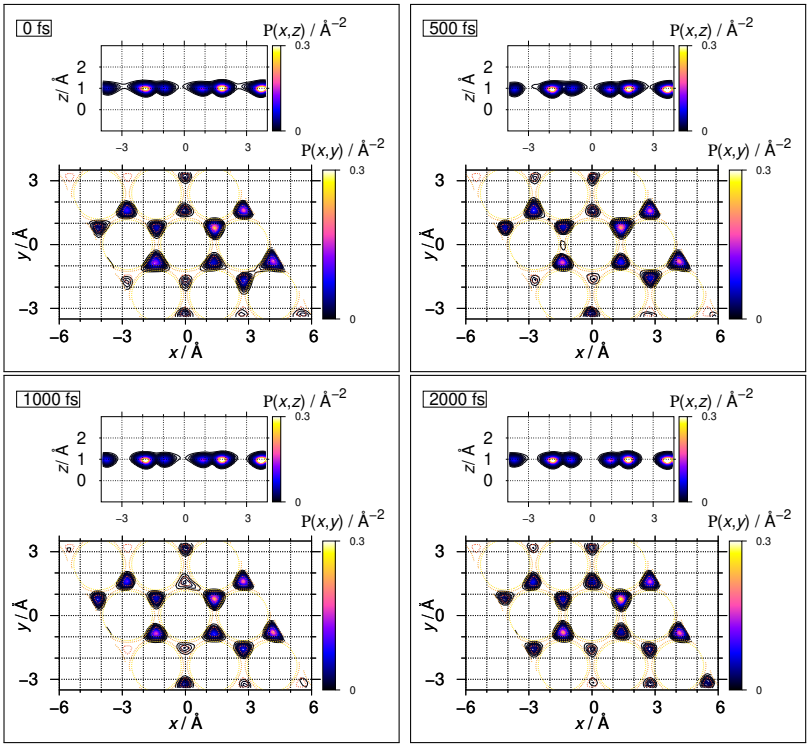

Figure 6.4: Snapshots of the time evolution of the RPD of a stochastic thermal state at temperature T=300 K.

During propagation, the RPD remain delocalized at almost all adsoption sites on the surface. However, the presence probability at each site varies over time, reflecting the non-stationary nature of this state. We also note that all RPD structures are nodeless, indicating that at this temperature the hydrogen atom remains predominantly on non-excited levels. Yet, a detailed population analysis of this state shows that it has non-negligible components in the eigenstates of levels 3 and 4. The latter are

split into several sub-levels due to tunneling. The dynamics of the hydrogen atom at this temperature will therefore be partially governed by tunneling.

Time evolution of the interacting stochastic thermal state

As a result of the interaction of the thermal hydrogen atom with the helium atom, a momentum transfer takes place between the latter, which also modifies the energy of the system. This leads to a different dynamics than the one presented above. In the example considered here, the energy of the system after interaction is 37 meV, representing an energy gain of around 19 meV for the system.

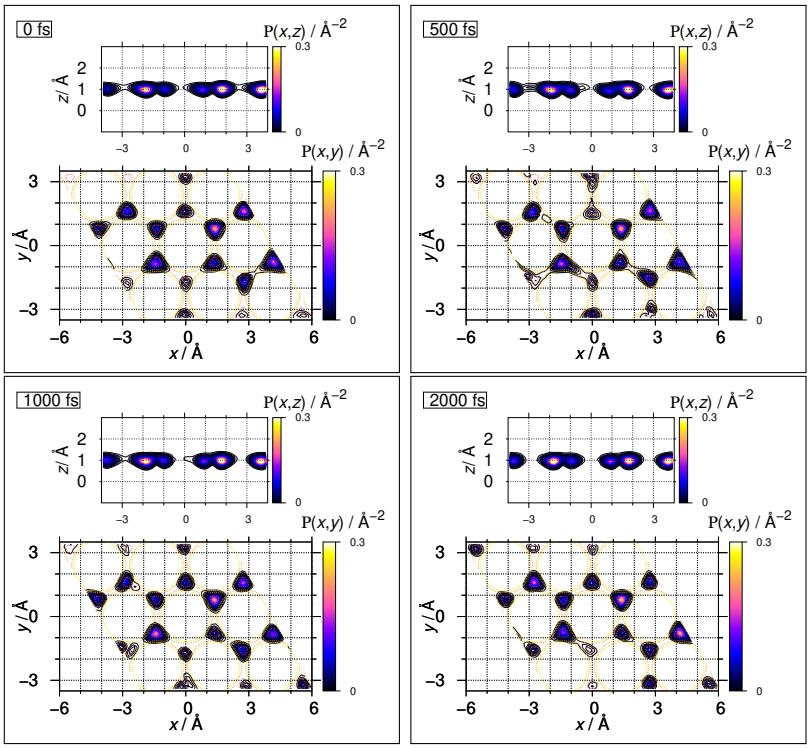

Figure 6.5: Snapshots of the time evolution of the RPD of a stochastic thermal state following interaction with a helium atom. The latter is initially prepared at temperature T=300 K.

The state given in figure 6.2 is used as an IWF to which we apply the operator $e^{i\boldsymbol{q}\hat{\boldsymbol{r}}}$ with the parameter defined above. This state is then propagated in time with the system's Hamiltonian. Figure 6.5 shows the time evolution of the RPD during the first two picoseconds.

The RPD of this state have larger amplitudes in the more energetic regions of the

surface. In particular, there is a non-negligible probability to find hydrogen atoms at potential barriers over time. At 1 ps, nodal structures appear at certain fcc sites, indicating the probability of excitation of the hydrogen atom in a parallel mode to the substrate.

We can thus see that the interaction of the hydrogen atom with the helium atom leads to a different dynamics from the one it would have adopted in this time frame in the absence of external perturbation (the "kick"). This difference in this behaviour of the hydrogen atom is the key element in the evaluation of the ISF, which implicitly infers correlations between the "kicked" and "unkicked" state evolution.

6.3.2 Results for the ISF

The ISF is calculated by averaging over all realisations. We are particularly interested in the real part of the normalized ISF

$$P_x(\boldsymbol{q}, t) = \mathrm{Re}\left[\frac{I(\boldsymbol{q}, t)}{I(\boldsymbol{q}, 0)}\right] \tag{6.23}$$

This function is related to the loss of polarization at helium atoms scattered at the surface, that can be measured directly in spin echo experiments. Detailed explanations of this relation and a thorough description of this method are given in [3]. In the following, we will only recall some key points concerning the meaning of this quantity.

In spin echo experiments, the nuclear spins of helium atoms are initially polarized in a given direction. The two spin components are then separated by a magnetic field so that the wave packet representing each atom is given by a coherent superposition of spin components parallel and anti-parallel to the applied field. As they have different energies, the two components move at different speeds and reach the surface with a relative delay. If the surface does not change during this time, the two components of the wave packet will scatter identically and recombine to regenerate their original spin orientation, so there will be no loss of polarization. Otherwise, the two spin components will be scattered differently and the recombined wave packet will not have the same final state, so a loss of polarization is observed. In these experiments, measurements are made on many helium atoms belonging to the same beam. By

averaging the results obtained, a component of the polarization is evaluated over this time, corresponding to $P_x(\boldsymbol{q}, t)$, which we evaluate with equation 6.23.

The polarization $P_x(\boldsymbol{q}, t)$ is evaluated in this study over 30 ps. The obtained result is shown in figure 6.6.

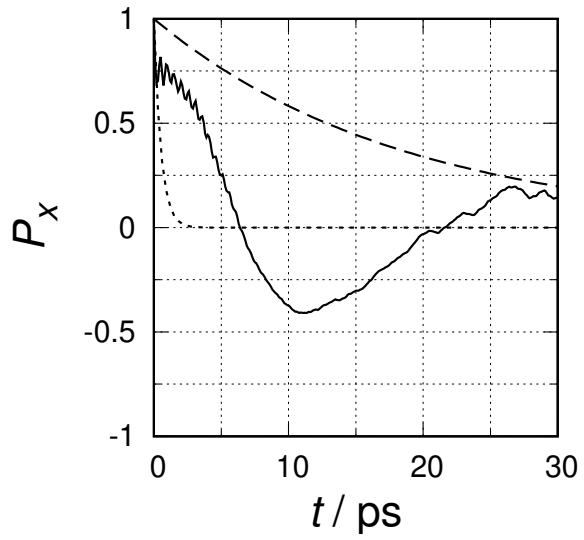

Figure 6.6: Polarization decays $P_x(\boldsymbol{q}, t)$ for H/Pd(111) along $\langle 1\bar{1}00 \rangle$ ($q = |\boldsymbol{q}| = 0.77\text{Å}^{-1}$). Theoretical results from Eq. 6.8 using K = 5 random initial states (continuous line). T = 300 K. Broken lines are exponential decaying functions used to rationalize the data (see text): the long dashed line is for a decay constant $k_{\text{env}} \approx 0.05\,\text{ps}^{-1}$, the short dashed line is for a decay constant $k_{\text{diss}} = 1.9\,\text{ps}^{-1}$.

The variations in $P_x(\boldsymbol{q}, t)$ show short-term oscillations, which decrease relatively rapidly; they generally correspond to vibrational modes of the hydrogen atom [3]. Negative values of the polarization are observed between 6 ps and 20 ps. The general shape of the function is aperiodic and decreasing with time, probably tending towards a zero value at longer times. This reflects aperiodic loss of surface correlation with time which can generally be related to diffusion.

The speed rate at which this function decreases with time depends on the diffusion mechanism. In the situation where the decay of this function is exponential, diffusion coefficients D can be extracted from these simulations. The example we have taken in this study is a first attempt to determine the ISF in the formulation proposed in this project. Further tests on longer timescales and different values of $\boldsymbol{q}$ and T need

to be carried out to compare the results of this model fully with the experimental data.

However, some very preliminary comparison can be carried out at this stage of the investigation. First of all, it is conceivable that the two maximal values of the ISF shown in the time interval of figure 6.6 lie on an exponential decay function. Indeed, in the analysis of the experimental data, mono- or multi-exponential decay functions are adjusted to the decay of the ISF in order to determine the so-called dephasing rate α. That rate is in fact a rather complex function of several factors, including friction coefficients. The rate determined from adapting a single exponential decay to the envelope function from figure 6.6 yields $k_{\mathrm{env}} \approx 0.05\,\mathrm{ps}^{-1}$.

Peter Townsend investigated the hydrogen on palladium system in his thesis [62]. In figure 6.30 of his thesis manuscript he reports on values for the dephasing rate as a function of $\boldsymbol{q}$ at a surface temperature of 350 K. For the direction corresponding to the $\langle 1\bar{1}00\rangle$ direction investigated here (the $\langle 11\rangle$ azimuth in Townsend's thesis), one finds at the value $q \approx 0.8\text{Å}^{-1}$ the value $\alpha \approx 0.05\,\mathrm{ps}^{-1}$. Indeed, the source data for this value are reproduced in figure 6.27a of Townsend's thesis in the form of a decaying ISF function. The experimental function misses the negative values calculated in figure 6.6 above, but is otherwise rather consistent with theory in respect to the time scales and also the initial oscillatory behavior.

In the present theory friction is neglected. It is highly reasonable to say that friction will lead to an additional damping of the ISF. The short dashed exponential decay function plotted in superposition to the numerical function in figure 6.6 represents one possibility of such an additional decay with a friction rate of about 2 ps^{-1}, which was calculated to hold for hydrogen on palladium [56]. This friction rate might be unrealistically large, yet it shows that additional damping can lead to a more monotonous decay of the ISF.

The exact matching of the decay rate of the ISF enveloping function and the experimental dephasing rate is very likely fortuitous. Further investigation is needed in any case at this point to elucidate the behavior disclosed by the present calculations and to compare them with experimental data. The essential aspect of the present findings is, however, that the ISF decays, despite the absence of friction, in a time

scale that is comparable with experimental findings. And that this decay is entirely due to the quantum mechanical evolution of thermal wave packets.

Chapter 7

Conclusion

The theoretical study of the vibrational spectroscopy carried out in this thesis has provided a powerful means to understand on one hand, the structure of the vibrational eigenstates of one and two hydrogen atoms adsorbed on the palladium Pd(111) surface, on the other hand, this understanding allows us to rationalize the intricate quantum dynamical behaviour of these atoms on the surface. the following points summarize the key findings and implications of this research:

- The theoretical study of the vibrational spectroscopy of a single hydrogen atom adsorbed on the palladium surface revealed the presence of tunneling affecting all excited vibrational states. The latter manifested itself in a variety of ways across different potential barriers, leading to multiple splittings of several energy levels into sub-levels with relative gaps ranging from 1 meV to 8 meV.

  The study also confirmed the existence of Fermi resonance between local vibrational mode of single hydrogen atoms where a state with a single quantum of vibrational excitation perpendicular to the substrate strongly couples with a state carrying two quanta of vibrational excitation parallel to the substrate. The interaction between these two vibrational states results in the formation of Fermi pairs of stationary states possessing vibrational excitations perpendicular and parallel to the substrate simultaneously.

- The theoretical study of the vibrational spectroscopy of H_2/Pd(111) has shown

that in situations where the two hydrogen atoms occupy neighboring adsorption sites of the same type, excitation of the system systematically manifests itself on both atoms. The latter then adopt concerted modes of vibration in phase and out-of-phase, thus demonstrating the presence of a strong correlation between the two atoms. In cases where the latter occupy sites of different types, the vibrational excitations were observed only on one of the two atoms, indicating a weaker correlation in this type of configuration.

In both cases, the presence of a second hydrogen atom in the vicinity significantly changes the spectrum of the system. In particular, we found that the potential barriers separating the different sites are significant, leading to a much less pronounced tunneling effect than that observed on the isolated hydrogen atom.

The Fermi resonance, as observed on an isolated hydrogen atom remains locally present on each atom despite the strong interactions between them when they occupy neighboring sites of the same type. This also shows the persistence of the intensity of local interactions between the internal vibrational modes of each hydrogen atom.

- The integration of quantum dynamics in this study has enabled us to gain a deeper understanding of the quantum processes underlying the vibrational eigenstate structure of the systems. We considered several numerical simulations highlighting the manifestation of tunneling and Fermi resonance in the dynamical behavior of hydrogen atoms on the palladium surface. Three major findings emerged from these studies:
  - The dynamics of hydrogen atoms involving a translational motion parallel to the substrate toward other adsorption sites on the surface following excitation is governed mainly by tunneling through potential barriers. This is much more important in the case of an isolated hydrogen atom.
  - Fermi resonance as predicted in this study, couples the perpendicular and in-plane breathing motion. When a hydrogen atom is excited in a mode perpendicular to the substrate, the vibrational excitation alternates in time between parallel and perpendicular modes. The quasi-periodicity

of these purely quantum motions is directly related to the energy gap between the Fermi pair states within the system.

  - The excitation of a hydrogen atom leads to a systematic transfer of energy to the neighboring hydrogen atom on the time scale of a few hundredths of femtoseconds, if the latter occupies a neighboring site of the same type. The transfer time of this energy is directly related to the energies of the vibrational states corresponding to the same type of excitation.

- The method for the calculation of the intermediate scattering function (ISF) used in this thesis enables to directly link experimental observations in spin-echo experiments to the quantum mechanical view of diffusion. The preliminary study we have carried out in this project represents a first step towards understanding these mechanisms. Further work is planned to extract scattering coefficients from numerical simulations, while accurately describing all the mechanisms taking place on the femtosecond scale.

The calculation of the vibrational eigenstate and quantum dynamics carried out in this study presented a real challenge for numerical computation, indeed. The interatomic interactions between hydrogen atoms and the substrate atoms are of a very complex nature. The duality between the strong correlation involving the internal and external degrees of freedom of each hydrogen atom renders the calculation of the time dependent and time independent dynamics very costly. The choice of 'good' basis vectors with mode combinations suitable for this type of interaction was essential for accomplishment of the calculations. The long-range interactions between the hydrogen atoms mean that large periodic calculation cells are required to model the system correctly, necessitating very large primitive bases. This makes the study of the dynamics of these systems on the picosecond time scale extremely costly numerically, given the time step needed to guarantee accurate calculations.

The knowledge gained from this thesis opens up new opportunities for future research. To name but a few:

- the evaluation of the impact of dissipation and friction; three main sources can be targeted, in this respect, namely the interaction between more than two adsorbed hydrogen atoms, the interaction with moving palladium atoms

(phonon-couplings), and the interactions with the surrounding electrons from the break-down of the Born-Oppenheimer approximation (couplings to electron-hole pairs);

- a precise theoretical assessment of the complicated HREELS spectrum of hydrogen on palladium; ideas have been explored in this thesis, results are promising but absent in this manuscript, as they need further investigation;
- the study of the para and ortho modifications of adsorbed H_2, and the subtle mechanism of their interconversion adsoption upon adsorption via inclusion of the weak hyperfine coupling; to this end, however, the numerical accuracy will need to be increased by at least two orders of magnitude.

Ultimately, this research highlights the profound interconnection between vibrational spectroscopy and quantum dynamics, two fields that mutually enrich each other to provide a deeper understanding of molecular phenomena at the interface between solid materials and their environment.

Appendix A

Details on construction of the H_2/Pd(111) PES

The strategy adopted in many quantum molecular dynamical studies is to build first a potential energy surface (PES) from a database obtained from DFT calculations then carry out quantum dynamics calculations with it. In its most general form, the PES of the H_2/Pd(111) system is a six-dimensional hypersurface. It was developed by W. Dong et al. [22]. The construction of this PES was done in two steps. First, the generation of the database which consists in calculating the system energy along several well-chosen pathways of the dissociative adsorption of H_2 on Pd(111) by using the density functional theory (DFT). Then fitting the obtained database on an adequate interatomic potential. The type of interatomic potential they have chosen is based on the Reactive Force Fields (RFFs) approach developed by Brenner [38], which confers to the potential a fully analytical formula.

In the following, we will give some important details about the construction of this PES. A more detailed description is given in [22, 23]

A.1 Energy calculations and database

The calculation of the system energies used for fitting was carried out using an approach based on DFT calculations with the generalized gradient approximation (GGA) of Perdew and Wang (PW91) [63]. Plane waves basis were used for expand-

ing the wave functions and the electron-ion interaction is described by ultrasoft pseudopotentials proposed by Vanderbilt [64]. The calculations were made on a slab of five Pd layers with a (3×3) Pd(111) surface cell and a vacuum space corresponding to five Pd layers used to avoid the interaction between the slab and its periodic images. The displacements of the Palladium atoms were taken into account in these calculations, more particularly the displacement outward (to the gas phase) of either one Pd atom or all the Pd atoms in the topmost layer by 0.1 Å from their equilibrium positions. The set of the computed energies constitute the database used for the fit.

A.2 Analytical representation of the PES

An approach based on the reactive bond order (REBO) force field was used by the authors to the parametrization of the PES. In the following, the analytical formula including the parameters used to describe the PES will be exposed.

In its most general form, the potential energy of a system can be written as

$$E = E_{nr} + E_r \tag{A.1}$$

E_r if the RFF contribution and E_{nr} correponds to a non-bonding potential. The RFF term is also given by the sum of two terms

$$E_r = E_{rep} + E_{bond} \tag{A.2}$$

E_{rep} and E_{bond} are the repulsive part and the bond energy respectively. The bond energy, E_{bond}, describes the bonding between atoms and is the crucial part of a RFF. Dong showed that the use of the REBO force field approach leads to a significantly better description of reaction dynamics for the H_2/Pd(111) system compared to other approaches like the Second Moment Approximation (SMA) [65, 66]. In this case, the RFF term of the potential can be expressed in terms of bond order using Brenner's REBO potential

$$E_r = \sum_{\alpha=1}^{n} \sum_{\substack{\beta=\alpha \\ (j>i,\, if\ \alpha=\beta)}}^{n} \sum_{i=1}^{N_\alpha} \sum_{j=1}^{N_\beta} \left[V_{\alpha\beta}^{R}(r_{ij}^{\alpha\beta}) - \bar{b}_{ij}^{\alpha\beta} h_{\alpha\beta}(r_{ij}^{\alpha\beta}) \right] \tag{A.3}$$

$V^R_{\alpha\beta}(r^{\alpha\beta}_{ij})$ and $h_{\alpha\beta}(r^{\alpha\beta}_{ij})$ represent respectively the repulsive potential and hopping integral. They are given by the following

$$V^R_{\alpha\beta}(r^{\alpha\beta}_{ij}) = A_{\alpha\beta} f_{\alpha\beta}(r^{\alpha\beta}_{ij}) \left(1 + \frac{B_{\alpha\beta}}{r^{\alpha\beta}_{ij}}\right) e^{-\sigma_{\alpha\beta} r^{\alpha\beta}_{ij}} \tag{A.4}$$

$$h_{\alpha\beta}(r^{\alpha\beta}_{ij}) = C_{\alpha\beta} f_{\alpha\beta}(r^{\alpha\beta}_{ij}) e^{-\omega_{\alpha\beta} r^{\alpha\beta}_{ij}} \tag{A.5}$$

$A_{\alpha\beta}$, $B_{\alpha\beta}$, $C_{\alpha\beta}$, $\sigma_{\alpha\beta}$ and $\omega_{\alpha\beta}$ are constant parameters to be calculated by fitting. $f_{\alpha\beta}(r^{\alpha\beta}_{ij})$ are the cutoff functions defined by

$$f_{\alpha\beta}(r^{\alpha\beta}_{ij}) = \begin{cases} 1, & r^{\alpha\beta}_{ij} \leq r^{\alpha\beta}_{s1} \\ \frac{1}{2}\left(1 + \cos[\pi(r^{\alpha\beta}_{ij} - r^{\alpha\beta}_{s1})/(r^{\alpha\beta}_{s2} - r^{\alpha\beta}_{s1})]\right), & r^{\alpha\beta}_{s1} < r^{\alpha\beta}_{ij} \leq r^{\alpha\beta}_{s2} \\ 0, & r^{\alpha\beta}_{ij} > r^{\alpha\beta}_{s2} \end{cases} \tag{A.6}$$

$r^{\alpha\beta}_{s1}$ is the starting cutoff distance from which the potential is attenuated gradually and $r^{\alpha\beta}_{s2}$ if the cutoff distance beyond which there is no interaction.

$\overline{b}^{\alpha\beta}_{ij}$ is the symmetrized bond order term that describes the effect of chemical environment on the bonding strength between the ith atoms of species α and the jth atom of species β. This term is defined by

$$\overline{b}^{\alpha\beta}_{ij} = \frac{1}{2}(b^{\alpha\beta}_{ij} - b^{\beta\alpha}_{ji}) \tag{A.7}$$

where

$$b^{\alpha\beta}_{ij} = \left(1 + \sum_{\gamma=1}^{n} \sum_{\substack{k=1 \\ (k\neq i,\, if\ \gamma=\alpha) \\ (k\neq j,\, if\ \gamma=\beta)}}^{N_\gamma} f_{\alpha\beta}(r^{\alpha\gamma}_{ik}) g_{\alpha\beta\gamma}(\cos\theta_{ijk}) e^{-\lambda_{\alpha\beta\gamma}(r^{\alpha\gamma}_{ik} - r^{\alpha\beta}_{ij})}\right)^{-\frac{1}{2}} \tag{A.8}$$

θ_{ijk} is the bond angle between the bonds ij and ik and $g_{\alpha\beta\gamma}(\cos\theta_{ijk})$ is defined by a third-degree polynomial given by

$$g_{\alpha\beta\gamma}(y) = a^{\alpha\beta\gamma}_0 + a^{\alpha\beta\gamma}_1(1+y) + a^{\alpha\beta\gamma}_2(1+y)^2 + a^{\alpha\beta\gamma}_3(1+y)^3 \tag{A.9}$$

The set of the total parameters used for the REBO potentials are given in table A.1. One sees that fifteen parameters are needed for the two-body interactions : Pd-Pd, Pd-H and H-H needed for Eqs. A.4 and A.5 , twenty parameters for the three-body

Interaction	A (eV)	B (Å)	C (eV)	σ (Å^{-1})	ω (Å^{-1})	r_{s1} (Å)	r_{s2} (Å)
Pd–Pd	127.968	33.893	88.164	2.937	1.108	3.2	3.3
Pd–H	38.030	13.360	62.288	3.479	2.421	3.5	3.9
H–H	6.848	13.051	13.212	6.732	0.814	1.9	2.2

(a) Two-body terms.

Interaction	a_0	a_1	a_2	a_3	λ (Å^{-1})
Pd–Pd-Pd	0.186	0.406	0.157	0.000	1.073
Pd–Pd-H	0.285	0.641	-0.547	0.272	2.421
H–Pd-H	0.538	2.181	-2.872	1.215	2.421
H-H-Pd	0.906	-0.0808	-0.608	0.362	2.421
Pd-H-Pd	0.661	0.755	-1.406	0.437	2.421

(b) Three-body terms.

Table A.1: REBO force field parameters.

terms : Pd-Pd-Pd, Pd-Pd-H, Pd-H-Pd, H-Pd-H and H-H-Pd needed for Eq. A.9 and two parameters for $\lambda_{\alpha\beta\gamma}$. That makes a total of a set of 37 parameters.

The long range adsorbate-surface interaction (beyond a distance of 4.0 Å to the surface) are included in the nonbonding term of the potential E_{nr} (Eq). This term can be described by a simple potential as a function of only the distance Z between the adsorbate's center of mass and the surface[1]

$$E_{nr} = f_L(Z)\left(c_0 - \frac{c_1}{Z^2}\right) \tag{A.10}$$

c_0 and c_1 are the two parameters to be determined by fitting and $f_L(Z)$ is a window function given by

$$f_L(Z) = \begin{cases} 0, & Z \leq Z_1 \\ \frac{1}{2}\left(1 - \cos[\pi(Z - Z_1/(Z_2 - Z_1)]\right), & Z_1 < Z \leq Z_2 \\ 1, & Z > Z_2 \end{cases} \tag{A.11}$$

[1]This is justified by the fact that the surface corrugation effect is negligible when the adsorbate is far from the surface.

with $Z_1 = 3.5$ Å and $Z_2 = 4.5$ Å. The energy of H_2 at a point far from the surface ($Z = 7.0$ Å) is taken as the zero of the potential energy of the system.

E_z	c_0 (eV)	c_1 (eV-Å^2)
	0.0188	0.291

Table A.2: Long range interaction parameters.

Appendix B

Study of some simple analytical models

The study of the spectrum of hydrogen atoms adsorbed on the Pd(111) surface revealed that the vibrational stationary states of these systems are strongly impacted by tunneling across the potential barriers and also by the local coupling between the DOFs of the system inducing, in particular, a Fermi resonance between the zeroth order perpendicular mode and modes parallel to the substrate. These two effects manifested in the structure of the vibrational states of the system and in their energies, leading in particular to the degeneracy lifting of several energy levels. These two quantum phenomena are well described in the literature [7, 67, 44, 43, 24, 68], but there is few documentation on systems including both effects simultaneously. We investigated a simple three-dimensional model of an asymmetric double-well potential, integrating the tunneling effect and a Fermi resonance coupling between certain modes of the system. In the model, both zeroth order states and coupling strengths can be explicitly defined, which allows us to understand the nature and intensity of the coupling between the DOFs when it is affected by these two quantum effects simultaneously. Three examples are presented below. In the first example, we consider a system affected only by the tunneling effect, then in the second and third examples we include a Fermi resonance coupling between the modes of the system.

B.1 Asymmetric double-well potential (uncoupled)

In this example, we consider a three-dimensional system in Cartesian coordinates $\kappa \equiv \{x, y, z\}$ defined by an asymmetric double-well potential. In this model, no correlations have been integrated, so the DOFs of the system are considered completely decoupled. The potential V is given by :

$$V(x, y, z) = ax^4 + bx^3 + cx^2 + \frac{1}{2}m\omega_y^2 y^2 + \frac{1}{2}m\omega_z^2 z^2 + d \tag{B.1}$$

m is the mass of the system, ω_κ represents the proper pulsation along the $\kappa = y, z$ coordinates, the potentials of which are considered to be harmonic. The parameters a, b and c are real numbers ($c \leq 0$) chosen numerically to adjust the potential curvature and the energy difference between the minima of the two wells along x. d is a constant chosen to make the potential V positive. All the parameters used are given in table C.1.

Parameters	Values
a (meV/Å^4)	2.72
b (meV/Å^3)	0.54
c (meV/Å^2)	-21.76
m (u)	1.00
$\omega_y/\hbar$ (meV)	31.2
$\omega_z/\hbar$ (meV)	62.4
d (meV)	48.14

Table B.1: Parameters used for the potential.

The double-well potential is defined along the x coordinate by a fourth-degree polynomial. Figure B.1 shows a one-dimensional section of the potential along this coordinate ($y = z = 0$).

We will note in the following the potential well around the global minimum by A and the other by B. The potential barrier with a height of about 50 meV and the energy difference between the two wells is around 10 meV. The potential is chosen to be harmonic along the y and z coordinates, with proper pulsation verifying $\omega_z = 2\omega_y$. The nomenclature used to label the eigenstates is of the form[1] $N^\kappa_{\mathrm{A/B}}$ where

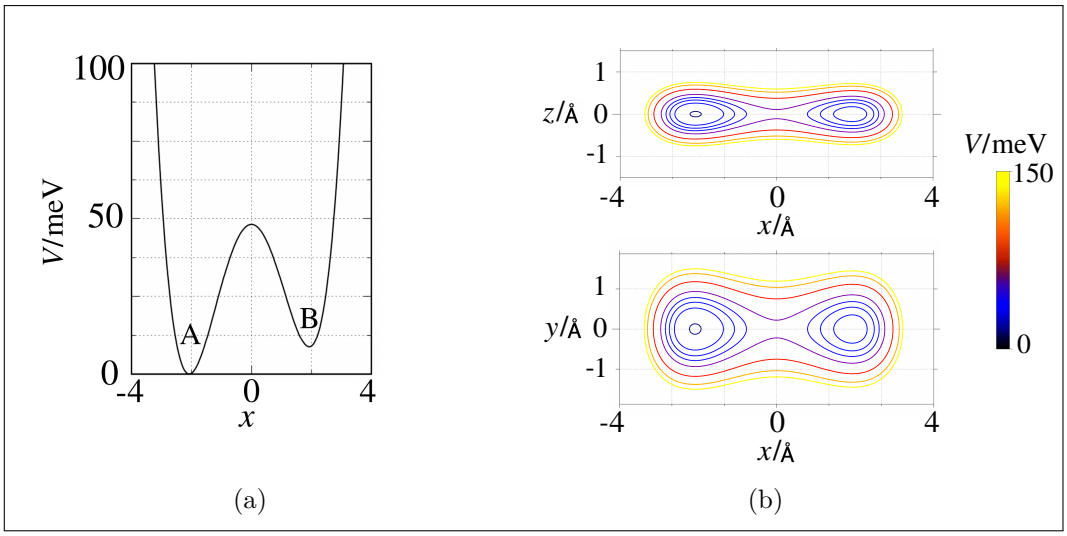

Figure B.1: (a) One-dimensional sections of the potential along the line joining A and B sites with z and y fixed at 0 Å. (b) Two-dimensional section of the PES in the xy-plane ($z = 0$) and xy-plane ($y = 0$).

N represents the number of quantum excitation along the κ coordinate. The indices A and B refer to the well at which the eigenstate is located. For example, the state 1^x_{B} represents an eigenstate localized on well A with a quantum excitation in the x mode. If this state is delocalized over both wells, then we add the two labels corresponding to each well. For example, $1^x_{\mathrm{B}} + 1^x_{\mathrm{A}}$ represents a state similar to the previous one, but present on both potential wells simultaneously. Finally, when an eigenstate has two or more excitations in different modes separately, we multiply the two labels. For example, $1^x_{\mathrm{A}} 1^y_{\mathrm{A}}$ is a state located only in well A and having one quantum excitation in mode x and one quantum excitation in mode y. The combination of these terms allows us to label the various eigenstates of the system. The type of excitations can be deduced by looking at the spatial and nodal structure of the wave function. The presence of a node along a κ mode represents a quantum excitation at the latter. Eigenstates are calculated as explained in the main part using the improved relaxation method (section 2.3.3). Details are omitted, here. Results for eigenenergies are converged and given in table B.2.

[1]We've used a different nomenclature from that used in other systems. The numbers 1 and 2 represent the excitation numbers and no longer refer to the perpendicular and parallel modes. This way of labeling states is more appropriate to the problem addressed in this appendix.

State number	State label	E_n/meV
1	0_{A}	0.0
2	0_{B}	7.9
3	1^x_{A}	28.0
4	1^y_{A}	31.2
5	$1^x_{\mathrm{B}}(+1^x_{\mathrm{A}})$	36.7
6	1^y_{B}	39.1
7	$2^x_{\mathrm{A}} + 2^x_{\mathrm{B}}$	53.4
8	$1^x_{\mathrm{A}}1^y_{\mathrm{A}}$	59.2
9	1^z_{A}	62.4
10	2^y_{A}	62.4
11	$1^x_{\mathrm{B}}1^y_{\mathrm{B}}(+1^x_{\mathrm{A}}1^y_{\mathrm{A}})$	67.9
12	1^z_{B}	70.3
13	2^y_{B}	70.3
14	$2^x_{\mathrm{B}} + 2^x_{\mathrm{A}}$	71.3

Table B.2: Eigenenergies of the uncoupled double-well potential.

To visualize the structure of the eigenstates, figure B.2 shows the 2D reduced probability densities (RPD) P_k of the eigenstates $|\varphi_k\rangle$ associated to the eigenergies E_k given in table B.2. The RPD are obtained by integrating the system's total probability density of presence on the third one of the three coordinates. For example, $P_k(x,y) = \int_{z_{\min}}^{z_{\max}} |\varphi_k(x,y,z)|^2 \mathrm{d}z$. By representing the different RPD, we can visualize the spatial structure of the state under consideration.

Analysis of these results shows that the y and z modes defined by a quadratic term give energies corresponding to those of the harmonic oscillator. These are all spaced by $\Delta E_\kappa = \hbar\omega_\kappa$ for $\kappa = \{y, z\}$. Given that $\omega_z = 2\omega_y$, at each potential well, the transition energy between the ground state and an excited state in the z mode coincides with that of a doubly excited state in y. This choice has been made to optimize coupling in the next example. Excited states in the x mode are affected by the tunneling that occurs across the potential barrier separating the two wells. By looking at the structure of state pairs $\{3, 5\}$ or $\{7, 14\}$, we can see that they have been coupled in such a way as to form two states with a tendency towards a (quasi)symmetrical or (quasi)antisymmetrical spatial representation with respect to

the plane perpendicular to the potential barrier[2]. These two coupled modes form two eigenstates called tunnel doublets.

The symmetry of these states manifests itself at the amplitude of their wave function around the potential barrier. In the first case, the amplitude of the wave function is large in this region, while in the second case it is almost zero, since the wave function cancels out to preserve antisymmetry at this plane. This criterion is very useful for identifying tunneling doublets within the system.

The tunneling effect tends to shift the energies of the modes concerned, so that if the zeroth order states localized on either well have the same energy, we speak of tunneling splitting. But here the two wells are not symmetrical, and the energy difference between these states is partly due to this difference and partly to tunneling[3]. In the following, we refer to this potential as the zeroth order, uncoupled system, with energies and eigenstates denoted by $E_k^{(0)}$ and $|\varphi_k^{(0)}\rangle$.

[2]This observation is clearly more visible for states 7 and 14.

[3]As with many systems affected by tunneling, the anti-symmetrical eigenstates tend to have higher kinetic energies than the symmetrical ones. The symmetric state usually has a higher potential energy than the antisymmetric one.

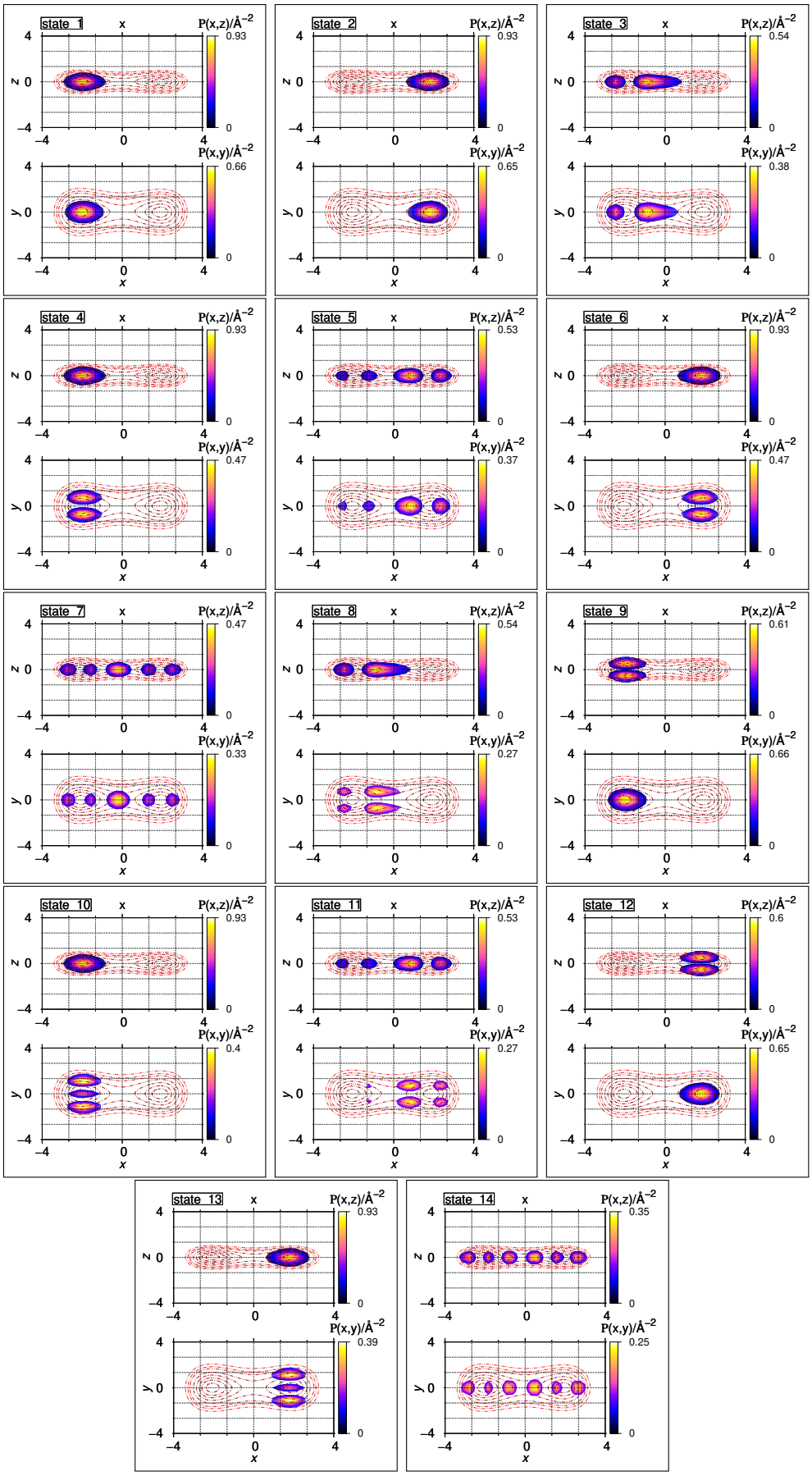

Figure B.2: Two-dimensional representation of the reduced probability densities (RPD) of the eigenstates of the uncoupled double-well potential. The latter are superimposed on equipotentials represented by dashed red lines.

B.2 Asymmetric double-well potential (coupled)

Coupling between y and z modes

We will now add a coupling term to the potential of the form $\hat{W}_1 = \epsilon y^2 z$ with ϵ a real number chosen to be small (≈ 2.7) to remain within the limit of perturbative treatment. The potential is now given by :

$$V(x,y,z) = ax^4 + bx^3 + cx^2 + \frac{1}{2}m\omega_y^2 y^2 + \frac{1}{2}m\omega_z^2 z^2 + \epsilon y^2 z + d \tag{B.2}$$

The $\hat{W}_1$ term induces a coupling only between y and z modes, and more specifically between modes with at least two quanta of excitation in y and modes with at least one quantum of excitation in z. This can be identified to be a Fermi resonance coupling term. We calculated the eigenenergies of this perturbed system, denoted by $E_k^{(1)}$, using an approach similar to that employed in section B.1. The results are shown in table B.3.

State number	State label	$E_n^{(1)}$/meV
1	0_{A}	0.0
2	0_{B}	7.9
3	1^x_{A}	28.0
4	1^y_{A}	31.2
5	$1^x_{\mathrm{B}}(+1^x_{\mathrm{A}})$	36.7
6	1^y_{B}	39.1
7	$2^x_{\mathrm{A}} + 2^x_{\mathrm{B}}$	53.4
8	$1^x_{\mathrm{A}}1^y_{\mathrm{A}}$	59.2
9	$2^{yz}_{\mathrm{A}-}$	62.1
10	$2^{yz}_{\mathrm{A}+}$	62.7
11	$1^x_{\mathrm{B}}1^y_{\mathrm{B}}(+1^x_{\mathrm{A}}1^y_{\mathrm{A}})$	67.9
12	$2^{yz}_{\mathrm{B}-}$	70.0
13	$2^{yz}_{\mathrm{B}+}$	70.6
14	$2^x_{\mathrm{B}} + 2^x_{\mathrm{A}}$	71.3

Table B.3: Eigenenergies of the yz-coupled modes double-well potential.

The nomenclature used for these states is based on the structure of their wave functions. Figure B.3 shows the reduced probability densities in the (x,y) and (y,z)

planes. We can see that all eigenstates were only slightly affected by the coupling, except for states $\{9, 10\}$ and $\{12, 13\}$. The wavefunction structure of the latter shows that there are no nodes proper to the y and z modes separately. The excitiation is now somehow shared between the two modes. We have therefore labeled these states by grouping the indices of both coordinates in the same term. For example, states 9 and 10 are labeled by $2^{yz}_{\mathrm{A}-}$ and $2^{yz}_{\mathrm{A}+}$ to indicate two states with excitation distributed between modes y and z and located at potential well A, the symbol $\pm$ is used to distinguish between them. States $\{9, 10\}$ and $\{12, 13\}$ form conjugate pairs called Fermi pairs.

In a perturbative approach, first order eigenstates are very little affected by the perturbation, except for those included in Fermi pairs. These are given by the linear combination of the two parent modes 1^z and 2^y of the zeroth order system that constitutes them[4].

Diagonalization of the zeroth order Hamiltonian matrix in the vector sub-space composed of the two parent modes involved in the coupling gives the corresponding first order eigenstates and their energies. If we consider, the sub-pace restricted to the zeroth order modes 2^y_{A} and 1^z_{A}, this matrix is given by :

$$\begin{pmatrix} E_9^{(0)} & C \\ C & E_{10}^{(0)} \end{pmatrix} \tag{B.3}$$

With $E_9^{(0)}$ and $E_{10}^{(0)}$ are the zeroth order energies of these modes given in table B.2 and $C = \langle 2^y_{\mathrm{A}}|\hat{W}_1|1^z_{\mathrm{A}}\rangle$ which represents a real coupling constant in this example. By diagonalizing this matrix, we arrive at the first order energies given by :

$$\begin{cases} E_9^{(1)} = E_9^{(0)} - |C| \\ E_{10}^{(1)} = E_{10}^{(0)} + |C| \end{cases} \tag{B.4}$$

[4]When the coupling is strong, the first order states may have a spectral decomposition in the larger zeroth order basis, and other parent modes may appear in the coupled states

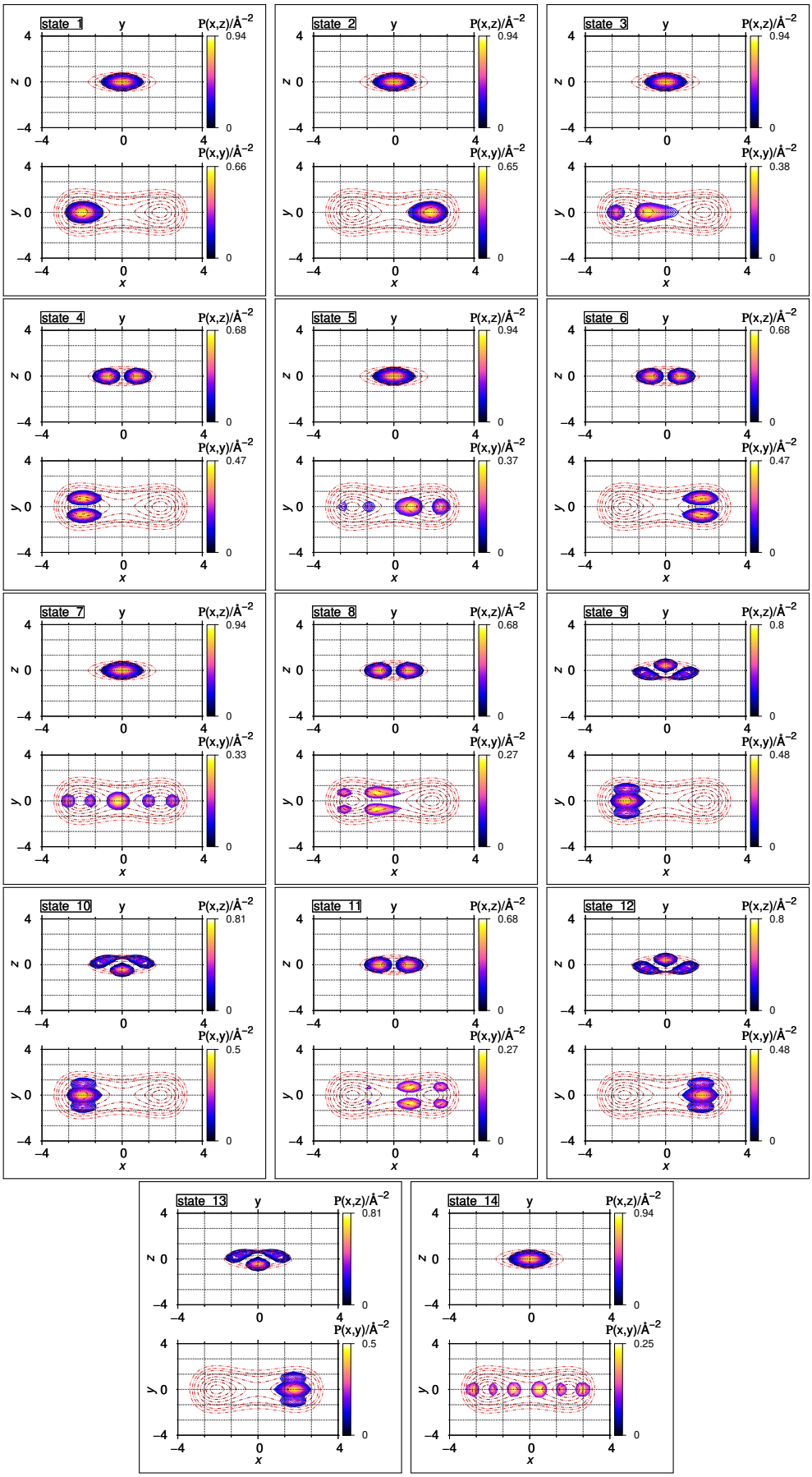

Figure B.3: Two-dimensional representation of the reduced probability densities of the eigenstates of the yz-coupled modes double-well potential. The latter are superimposed on equipotentials represented by dashed red lines.

The Fermi resonance shifts the energies of these two states, and the coupling constant is identified as half the energy difference between them. It is therefore a quantity that can be measured experimentally. It is often referred to as the 'Fermi resonance coupling constant'. It directly expresses the strength of the Fermi resonance coupling between the system's zeroth order modes. Subtracting the two equations, we can deduce that the smaller the energy difference $E_{10}^{(0)} - E_9^{(0)}$, the greater is C. In this example, both modes are initially degenerate, the coupling is therefore optimal. The energy difference between states 9 and 10 is 0.6 meV, corresponding to $C = 0.3$ meV. Since coupling is introduced identically at both potential wells, the same energy difference is observed between states 12 and 13. When the system is affected by tunneling, the local structure of certain modes and their energies can change, as highlighted in the previous example. If these are also involved in Fermi resonance, then this can impact on the value of the Fermi resonance coupling constant. We then observe couplings with different intensities, as illustrated in the next example.

Coupling between x and z modes

In this last example, we'll introduce a term into the potential similar to the previous one, but this time coupling the x and z modes. The system potential is given by:

$$V(x, y, z) = ax^4 + bx^3 + cx^2 + \frac{1}{2}m\omega_y^2 y^2 + \frac{1}{2}m\omega_z^2 z^2 + \epsilon x^2 z + d \tag{B.5}$$

We have taken $\omega_z/\hbar \approx 53.4$ meV and all other parameters remain unchanged. The value of ω_z has been lowered so as to bring the energy of zeroth order eigenstates with one quantum of excitation in the z mode closer to the energy of the state with two quanta of excitation in the x mode localized (mainly) at the potential well A. The eigenenergies and eigenstates of the new system (also those of the non-perturbed system) are given in table B.4 and figure B.4.

We now see that coupling has induced an energy gap between states $\{7, 8\}$ of 1.2 meV, and that the two energy levels $\{10, 14\}$ have moved closer by 0.4 meV. States $\{7, 8\}$ were strongly affected by the coupling and formed a Fermi pair, whereas states $\{10, 14\}$ were only slightly affected and do not show the characteristics associated with Fermi resonance[5]. The difference in coupling intensity between the two pairs is

[5]Fermi resonance increases the energy gap between the coupled zeroth order states (see equa-

State number	State label$^{(1)}$	$E_n^{(1)}$/meV	State label$^{(0)}$	$E_n^{(0)}$/meV
1	0_{A}	0.0	0_{A}	0.0
2	0_{B}	7.9	0_{B}	7.9
3	1^x_{A}	28.1	1^x_{A}	28.0
4	1^y_{A}	31.2	1^y_{A}	31.2
5	$1^x_{\mathrm{B}}(+1^x_{\mathrm{A}})$	36.7	$1^x_{\mathrm{B}}(+1^x_{\mathrm{A}})$	36.7
6	1^y_{B}	39.2	1^y_{B}	39.1
7	$1^z_{\mathrm{A}} + 2^x_{\mathrm{A}} + 2^x_{\mathrm{B}}$	52.8	$2^x_{\mathrm{A}} + 2^x_{\mathrm{B}}$	53.4
8	$1^z_{\mathrm{A}} + 2^x_{\mathrm{A}}$	54.0	1^z_{A}	53.4
9	$1^x_{\mathrm{A}}1^y_{\mathrm{A}}$	59.3	$1^x_{\mathrm{A}}1^y_{\mathrm{A}}$	59.2
10	1^z_{B}	61.5	1^z_{B}	61.3
11	2^y_{A}	62.4	2^y_{A}	62.4
12	$1^x_{\mathrm{B}}1^y_{\mathrm{B}}(+1^x_{\mathrm{A}}1^y_{\mathrm{A}})$	67.9	$1^x_{\mathrm{B}}1^y_{\mathrm{B}}(+1^x_{\mathrm{A}}1^y_{\mathrm{A}})$	67.9
13	2^y_{B}	70.4	2^y_{B}	70.3
14	$2^x_{\mathrm{B}} + 2^x_{\mathrm{A}}$	71.1	$2^x_{\mathrm{B}} + 2^x_{\mathrm{A}}$	71.3

Table B.4: Eigenenergies of the xz-coupled modes double-well potential.

due to the initial energy difference of the zeroth order states. This can be identified as being around 10 meV for states $\{10, 14\}$, whereas it is zero for states $\{7, 8\}$.

This difference in coupling intensity is not only due to the tunneling effect in this example, but also in part to the difference in local structure between the two wells at the x mode. If we considered a perfectly symmetrical double-well potential with optimal coupling in both wells, the introduction of tunneling through the barrier would have created tunneling doublets and shifted their energy in opposite directions. This energy shift will then reduce or increase the energy gap with the modes to which they are coupled by the Fermi resonance. We would then have observed here a variation in coupling intensity similar to the previous one, but this time due to the tunneling only.

---

tion B.4).

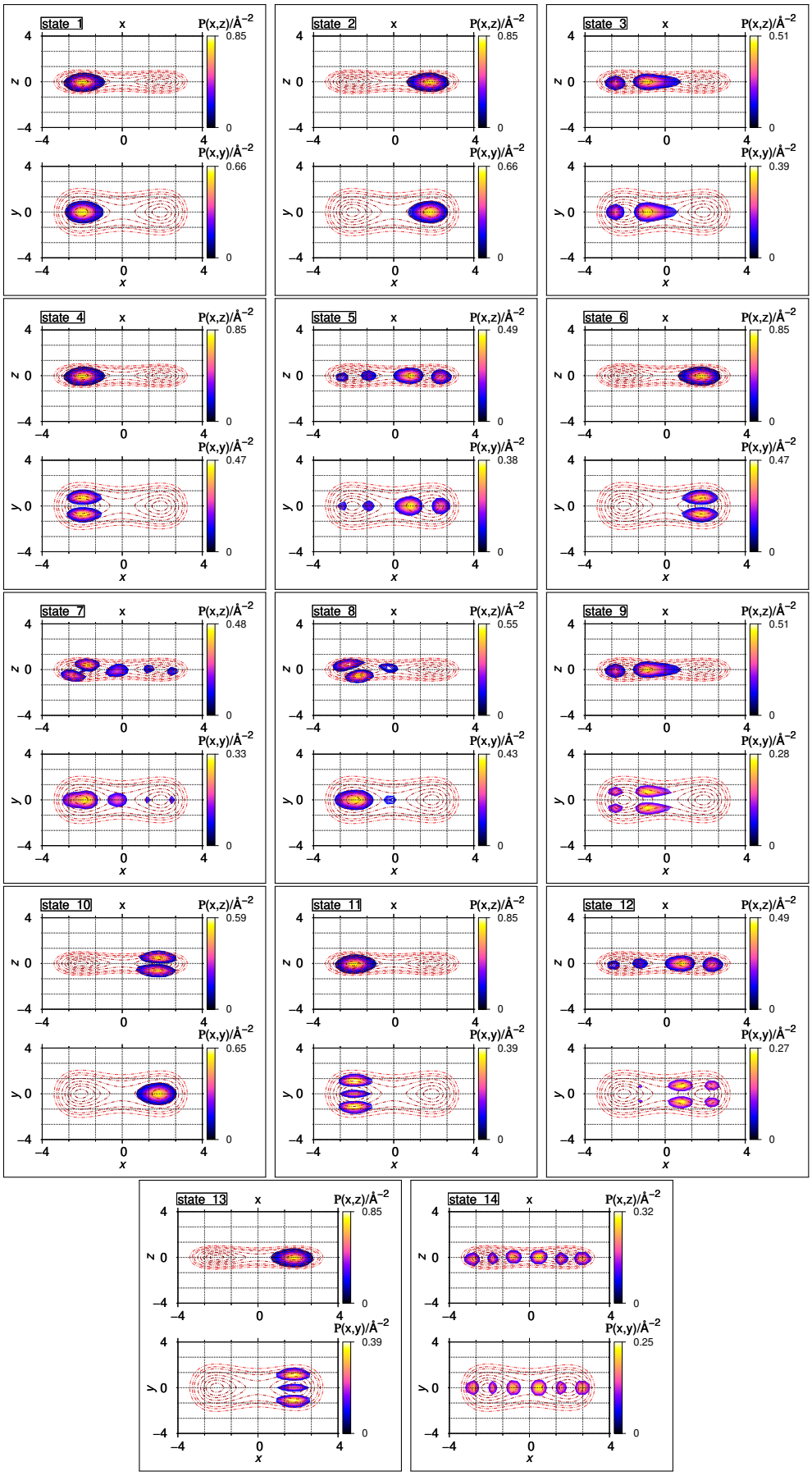

Figure B.4: Two-dimensional representation of the reduced probability densities of the eigenstates of the xz-coupled modes double-well potential. The latter are superimposed on equipotentials represented by dashed red lines.

In the case of interatomic potentials, there are different types of anharmonic coupling between the system modes. This simple model cannot report on all the phenomena that can occur within the system. But it does provide a basis on which to rationalize and describe the structure of the spectrum and stationary states of certain systems affected by these two types of coupling. We see in particular in the study of the spectra of the H/Pd(111) and H_2/Pd(111) systems that these phenomena have a strong impact on the vibrational states of the system. The simultaneous presence of these two effects leads to the creation of both tunnel doublets and Fermi pairs of different kinds between some modes.

Appendix C

Local potential study of the H/Pd(111) system

The time (in)-dependent calculations we have carried out on the H/Pd(111) system are based on a periodic approach with an elementary cell containing 18 potential wells, 9 of which are of the fcc type and 9 of the hcp type (figure 3.6). The latter are separated by a potential barrier of finite size, allowing the possibility of tunneling through it. The presence of tunneling has an impact not only on the surface dynamics of the adsorbates, but also on the structure of their vibrational stationary states. It is interesting to study the local properties of the vibrational states of the hydrogen atom in the vicinity of a single potential well in the absence of tunneling. To this end, an analytical three-dimensional potential was constructed by collaborators within the framework of the ANR project of which this thesis is a part, to reproduce locally the shape of the global potential from ref. [23] at an fcc site. We will refer to these two potentials as the local PES and global PES in the following.

The local PES is designed to fit the global PES at low energies around the fcc potential well. As energy increases, the global PES tends to fall off in certain directions to form a potential barrier, while the local PES continues to increase. The common vibrational states of the two systems will then begin to show differences as they approach the potential barrier. All the local properties of the global PES have been integrated into this potential to preserve the local $\boldsymbol{C}_{3v}$ symmetry of the vibrational states, as well as the different correlations between the DOFs of the

system.

In the following, we first give the technical details of the construction of this local PES and its implementation in MCTDH, then discuss the results from calculations of the obtained local vibrational hydrogen states at the fcc site.

C.1 Details about the construction of the local PES

C.1.1 Model

The analytical expression of the function used to reproduce the PES contains elements chosen to match the shape of the potential and its symmetry. In the following, we will work in the Cartesian coordinate system (x, y, z) to locate the position of the hydrogen atom. The potential model used is of the form :

$$V(x,y,z) = V_{\perp}(z) + V_{\parallel}(x,y) f_{\mathrm{damp}}(z) \tag{C.1}$$

Where

$$V_{\perp}(z) = \frac{1}{2} f_{\perp} y_{\perp}^2(z) \tag{C.2}$$

$$\begin{aligned} V_{\parallel}(x,y) = \frac{1}{2} f_{\parallel} R^2(x,y) & \\ \times \exp[-\mathrm{a}_{\parallel 2}\mathrm{R}^2(\mathrm{x},\mathrm{y}) - \mathrm{a}_{\parallel 3}\mathrm{R}^3(\mathrm{x},\mathrm{y})\sin(3\varphi(\mathrm{x},\mathrm{y})) & \\ + a_{\parallel 6a} R^6(x,y)\sin^2(3\varphi(x,y)) + a_{\parallel 6b} R^6(x,y)\sin^2(3\varphi(x,y))] & \end{aligned} \tag{C.3}$$

With

$$\begin{cases} y_{\perp}(z) = & \dfrac{\mathrm{e}^{-a_{\perp}(z - z_{\mathrm{eq}})}}{a_{\perp}} \\ R^2(x,y) = & (x - x_{\mathrm{eq}})^2 + (y - y_{\mathrm{eq}})^2 \\ \varphi(x,y) = & \arctan\left(\dfrac{y - y_{\mathrm{eq}}}{x - x_{\mathrm{eq}}}\right) \end{cases} \tag{C.4}$$

x_{eq}, y_{eq} and z_{eq} are the equilibrium coordinates of a fcc site. The function f_{damp} is given by

$$f_{\mathrm{damp}}(z) = \mathrm{e}^{a_{\mathrm{damp}}(\mathrm{e}^{b_{\mathrm{damp}}(z - z_{\mathrm{eq}})} - 1))} \tag{C.5}$$

and has a double role: first, in the case that the parameters a_{damp} and b_{damp} are positive, it leads to a damping of the parallel potential $V_{\parallel}$ for large distances from

the substrate, i.e. the parallel potential becomes a flat potential for large values of z. Secondly, because of the low order expansion :

$$V(x,y,z) \approx \frac{1}{2}f_{\perp}\Delta z^2 + \frac{1}{2}f_{\parallel}(\Delta x^2 + \Delta y^2) + \frac{1}{2}f_{\parallel}a_{\text{damp}}b_{\text{damp}}(\Delta x^2 + \Delta y^2)\Delta z^2 \quad \text{(C.6)}$$

where $\Delta\kappa = \kappa - \kappa_{\text{eq}}$ for $\kappa = \{x, y, z\}$. The term $\propto f_{\parallel}a_{\text{damp}}b_{\text{damp}}$ is potentially generating a Fermi resonance coupling between the first overtone of the parallel and the fundamental of the perpendicular mode.

By judiciously setting $f_{\parallel} = \mathrm{e}^{l_{f_{\parallel}}}$, $f_{\perp} = \mathrm{e}^{l_{f_{\perp}}}$, $a_{\text{damp}} = \mathrm{e}^{l_{a_{\text{damp}}}}$ and $b_{\text{damp}} = \mathrm{e}^{l_{b_{\text{damp}}}}$, and letting the logarithmic parameters $l_{f_{\parallel}}$, $l_{f_{\perp}}$, $l_{a_{\text{damp}}}$ and $l_{b_{\text{damp}}}$ be actual fitting parameters, one naturally ensures positive definiteness of the potential and the said damping behavior.

The terms

$$\begin{aligned} R^3\sin(3\varphi) &= y^3 - 3xy^2 \\ R^3\cos(3\varphi) &= x^3 - 3yx^2 \end{aligned} \quad \text{(C.7)}$$

are respectively A_1 and A_2 labeled cubic terms of $\boldsymbol{C}_{3\text{v}}$-symmetry [41]. The factor $\exp\left(-a_{\parallel 2}R^2...\right)$ in equation C.1 is hence a lowest order $\boldsymbol{C}_{3\text{v}}$-symmetric modulation of the otherwise cylindrical potential. By setting $a_{\parallel 2} = \mathrm{e}^{l_{\parallel 2}}$, one additional enforces a damping of the modulation with larger displacements from the stable equilibrium site, avoiding in this way side minima. The various parameters given in this model are obtained by adjustment to the global PES around one of the fcc wells on the surface. We have taken the region of space defined by:

$$\begin{aligned} 0.9756\ \text{Å} &\leq x \leq 1.8756\ \text{Å} \\ -1.3756\ \text{Å} &\leq y \leq 0.0\ \text{Å} \\ 0.6\ \text{Å} &\leq z \leq 1.5\ \text{Å} \end{aligned} \quad \text{(C.8)}$$

The model is fitted to the 600 data points with the simple version of the Marquardt-Levenberg algorithm [69] by which the optimum set of parameters is obtained and given in Table B.4.

The root mean square deviation of this fit is 277 $hc\,\text{cm}^{-1}$ over all points. The total energy reached in the spatial volume used for the fit is 50,000 $hc\,\text{cm}^{-1}$. The energy interval in which the energy difference between the two potentials must be minimal

Parameters	Values
$f_{\perp} \times \text{Å}^2/hc\,\text{cm}^{-1}$	23 412
$f_{\parallel} \times \text{Å}^2/hc\,\text{cm}^{-1}$	23 790
$a_{\parallel 2} \times \text{Å}^2/hc\,\text{cm}^{-1}$	2.22
$a_{\parallel 3} \times \text{Å}^3$	9.5
$a_{\parallel 6a} \times \text{Å}^6$	-4.2
$a_{\parallel 6b} \times \text{Å}^6$	4.0
a_{damp}	3.56
$b_{\text{damp}} \times \text{Å}^{-1}$	1.34

Table C.1: Optimal parameter values for the model potential equation C.1.

is below that of the potential barrier, i.e. around 1 500 $hc\,\text{cm}^{-1}$ (majoring). The vast majority of points showing significant deviation are all above this value. A two-dimensional representation of the local PES (solid line) superimposed on the global PES (dashed line) is given in figure C.1. The various parameters were calculated in units of corresponding wave numbers, i.e. $hc\,\text{cm}^{-1}$. We use however meV units in the following calculations.

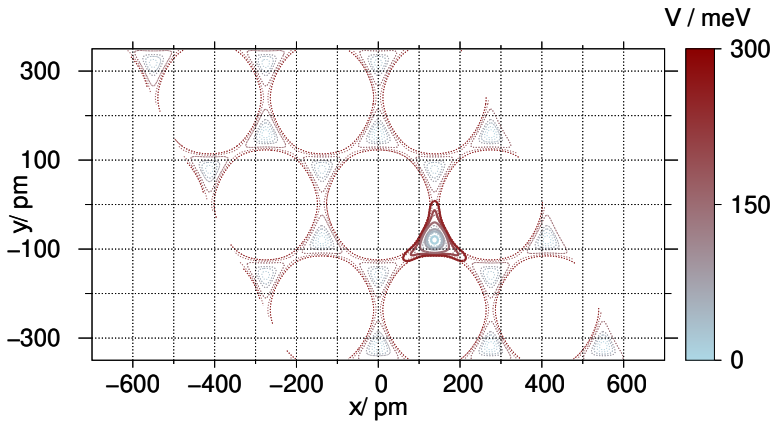

Figure C.1: Two dimensional section of the PES along the substrate coordinates ($z = 90$Å). The local PES (solid line) is superimposed on the global PES (dashed line).

C.2 Results and discussion

The vibrational stationary states of this system are calculated with MCTDH using the block improved relaxation program. The analytical model of the local PES does not allow decomposition as a sum of product a one-dimensional operator. We therefore used POTFIT to represent the potential in a form suitable for MCTDH calculations. The same primitive basis used for the global potential (section 4.2) is used for these calculations. The rms error on the fit is totally negligible for this system.

We are only interested in the vibrational states corresponding to those calculated in the global potential in section 4.2. That is ground state, the levels of excited states with a single excitation, then part of the levels of doubly-excited states. This corresponds to a total of 7 vibrational states. Table C.2 and figure C.2 show the vibrational eigenenergies and two-dimensional representations of the reduced probability densities of the local vibrational states.

Level	State number	State label	E_n/meV	Degeneracy g
1	1	0	0.0	1
2	2, 3	2^1	80.0	2
3	4	$2^2(A_1)+1^1$	102.7	1
4	5	$2^2(A_1)+1^1$	129.6	1
5	6, 7	$2^2(E)$	132.4	2

Table C.2: Vibrational eigenenergies of H/Pd(111) in the local PES.

To label the vibrational states of the system, we have adopted a nomenclature given by N^i. Where $N = \{0; 1; 2\}$ refers to the direction of vibrational excitation: vibrations perpendicular and parallel to the substrate are denoted by 1 and 2 respectively. The ground state is denoted by 0. The integer i refers to the number of vibrational excitations of the considered state. For example, 2^1 refers to a state with a single vibrational excitation parallel to the surface. In this nomenclature, no distinction is made between vibrational modes parallel to the substrate separately. These two modes are degenerate because of the local C_{3v} symmetry of the potential, so we speak only of excitation parallel or perpendicular to the substrate.

The structure of the reduced probability density of state 1 is node-less, indicating a non-excited state. This state is considered to be the ground state of the system. Its energy is around 155 meV (with respect to the potential minimum), and is taken as a reference in table C.2.

The first level of excited states contains two vibrational states excited in the parallel modes. Figure C.2 shows that the wave function of these two states has a node localized at the center of the potential well, with two anti-node structures (states 2 and 3). Given the $\boldsymbol{C}_{3v}$ symmetry of the potential, partial or total degeneracy results in excited modes parallel to the substrate. Here, states 2 and 3 are perfectly degenerate, with an energy of 80 meV.

This degeneracy appears partially in the doubly excited state level 2^2, which contains two degenerate states and a third one with a slightly lower energy[1]. These three states differ in their $\boldsymbol{C}_{3v}$ symmetry labels. The two degenerate states have E label and are denoted by $2^2(\mathrm{E})$ (states 6 and 7), while the third one has an A_1 label denoted by $2^2(\mathrm{A}_1)$.

The latter appears, together with state 1^1, in states 4 and 5. The reduced probability density of these states in the xz-plane also shows the presence of a node at this plane. These states therefore simultaneously have one quantum of vibrational excitation in mode 1 and two quanta of vibrational excitation in mode 2. In a harmonic approximation, this would correspond to the coupling between the fundamental of the perpendicular mode and and the first overtone of parallel mode. This is akin to a Fermi resonance between these two modes. The latter belong to the same symmetry representation group (A_1) and may thus couple. Given that the potential is more contracted in the perpendicular mode, a state with one quantum of excitation in mode 1 could have an energy close to that with two quanta of excitation in mode 2. They are therefore susceptible to couple resonantly. The resulting vibrational states, known as Fermi pairs, are given by the combination of these two modes. We use this image here for the nomenclature of these states. States 4 and 5 are therefore both labeled by $2^2(\mathrm{A}_1)+1^1$.

[1]The A_1 component is not necessarily always the lowest energy component of the triplet formed by an $\mathrm{E} \otimes \mathrm{E}$ reduction.

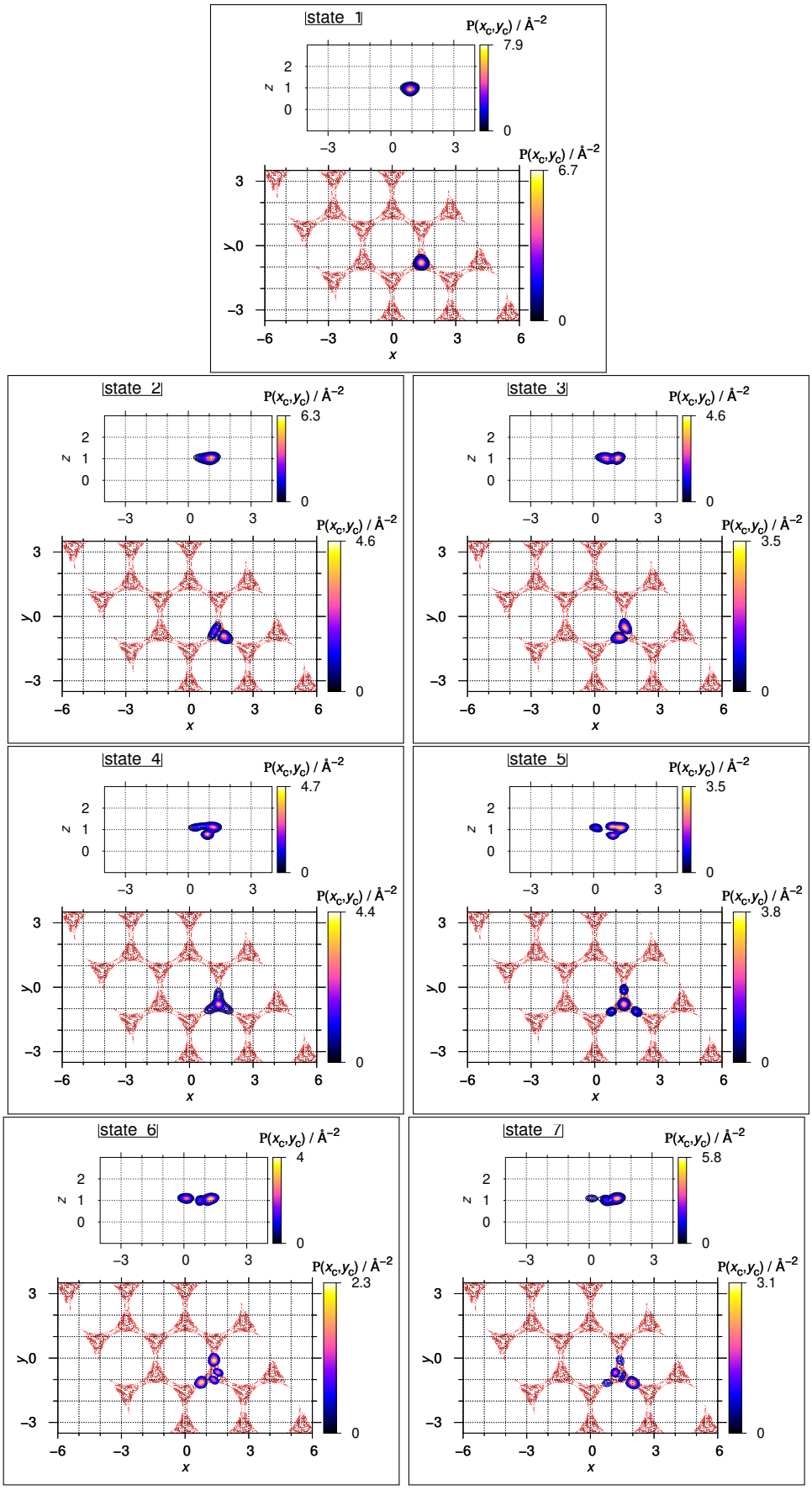

Figure C.2: Two-dimensional representation of the reduced probability densities of the vibrational eigenstates of the lcoal PES. The latter are superimposed on equipotentials represented by dashed red lines.

If we now consider a second neighboring potential well located at the hcp site with vibrational states that possess the same local properties as those of the fcc well, then the presence of the finite-size potential barrier between the two wells can lead certain vibrational states at the fcc site to couple with those located at the hcp site and form tunnel doublets. If states 4 and 5 are also affected by tunneling, then each of them will form a tunnel doublet with a corresponding state in the hcp well. We thus have 4 vibrational states forming two Fermi pairs and two tunnel doublets simultaneously. To illustrate this in a similar spirit to the approach used in appendix B, figure C.3 shows schematically the impact of successively introducing the tunneling effect between the two potential wells, then Fermi resonance between the $2^2(A_1)$ and 1 modes localized at each well. In the following, we refer to the fcc and hcp potential wells as A and B respectively, and the 2 mode symmetry label will be omitted for the sake of simplicity.

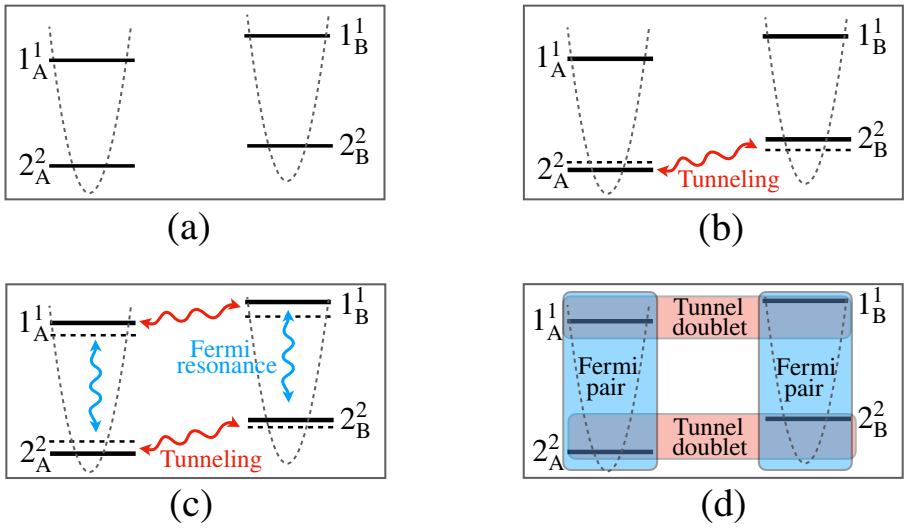

Figure C.3: Schematic representation showing the tunnel doublets and Fermi pairs that can be formed between a quadruplet of states.

Figure C.3.a shows a system where the vibrational states at each well are assumed to be fully decoupled. Introducing tunneling between the parallel modes located at A and B shifts their energies and leads to the formation of a first tunnel doublet. If we also introduce a local coupling that induces Fermi resonance between modes 1 and 2^2 (figure C.3.c), this will lead to the formation of two Fermi pairs localized at each well. The 1^1_A and 1^1_B modes are now also impacted by tunneling indirectly through

coupling with the 2^2 modes, forming a second tunnel doublet. The four vibrational states thus obtained contain two Fermi pairs (blue) and two tunnel doublets (red), as illustrated in figure C.3.d. If the system contains 9 equivalent potential wells of each type, then each of these states will be 'in principle' 9 fold times degenerate. Coupling will take place between 4 levels, each containing 9 vibrational states. We refer to these levels as tunnel doublet and Fermi pair levels.

Tunneling is generally followed by a change in the wavefunction of the involved state, as well as its energy. If this state is part of a Fermi pair, tunneling can weaken or strengthen the intensity of the local resonance. Inversely, the Fermi resonance can modify considerably the local structure of the wavefunction, leading thus to a weakening or enhancement of the tunneling effect. Depending on the relative strength of the tunneling and Fermi resonance coupling, the resulting vibrational state will be dominated by the 'parent' mode that constitutes it, and by looking at the structure of the reduced probability densities of these states, we can trace them back to the 'parent' mode of the vibrational state under consideration, as illustrated in appendix B. When both the tunneling and Fermi resonance coupling are strong, i.e. at close to optimal resonance conditions, it becomes difficult to extract the dominant character of one coupling scheme, given that the nodes are perfectly shared between the two coupled modes.

This desire to distinguish between these coupled states is of no particular interest when studying the spectrum of this local PES, as it contains only one easily identifiable Fermi pair. But in the case of the global PES, where the latter are mixed with tunneling doublets, it becomes complicated to find the different conjugate pairs formed within the spectrum of the system. The structure of vibrational states that have been less affected by the Fermi resonance informs us about the primary nature of the levels to which they belong, and this makes it easier to identify the different tunneling doublets and Fermi pairs in the spectrum.

Finally, by making the comparison with the vibrational states of the global PES given in chapter 4.2 (table 4.3), we identify the following correspondence between the local and global PES levels (the first number refers to the local, the second to the global PES): $1 \leftrightarrow 1$, $2 \leftrightarrow 3$, $3 \leftrightarrow 5$, and $4 \leftrightarrow 8$. Energies are not exactly comparable

due to the approximate character of the local PES, which departs from the global PES at higher energies, and tunneling, which is absent in the local PES model. It is therefore difficult to extract the exact contribution of tunneling to the energy gap between the two levels based on these elements only.

In addition to providing information on the local aspect of the vibrational states of the hydrogen atom in fcc potential wells, the local PES has been useful in several dynamical simulations to initialize the hydrogen wavefunction at an fcc site as reported in chapter 5.

Appendix D

One-dimensional adsoption model for a diatomic molecule

The procedure we have followed to determine the nature of the stationary states of hydrogen atoms adsorbed on the palladium Pd(111) surface is based mainly on the analysis of the structure of their reduced probability densities (RPDs). In the study of the H_2/Pd(111) system, we found that when the two hydrogen atoms are located on neighboring sites of the same type, the stationary states having one quantum of excitation are given by four vibrational modes adopted by the two hydrogen atoms. The latter oscillate simultaneously in certain directions and with varying phases. These findings were made by looking at the structure of RPDs involving DOFs of the same type from both atoms, i.e., $P(x_{t1}, x_{t2})$, $P(y_{t1}, y_{t2})$ and $P(z_{t1}, z_{t2})$. In particular, our analysis was based on the nodal structures of diagonal (and off-diagonal) RPDs in these representations to deduce the nature of the vibrational states of the corresponding levels. In this appendix, we present a simple one-dimensional problem to illustrate the links between the type of vibrational excitation adopted by two atoms and the structure of their RPDs involving DOFs of the same type. Despite the simplicity of this model, it allows us to deduce certain general properties that can be applied to the situation of the two hydrogen tomes adsorbed on the palladium surface.

D.1 1D model

We'll consider a one-dimensional problem where two identical atoms are adsorbed onto a periodic metal surface. Figure D.1 illustrates the potential created by the substrate atoms by a simple periodic function, in which two atoms are placed at neighboring potential wells.

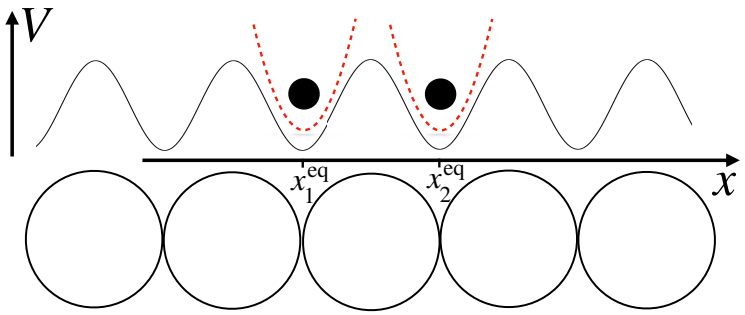

Figure D.1: Schematic representation of adsoprtion of two atoms in a one-dimensional potential.

In the following, we'll use the harmonic approximation to simplify the calculations. The total potential is two-dimensional and depends on the x_1 and x_2 coordinates of the two atoms. Rather than working on these coordinates, we'll consider the (x_d, y_d) modes defined in equation D.1.

$$\begin{cases} x_d = x_2 - x_1 \\ x_c = \dfrac{x_1 + x_2}{2} \end{cases} \tag{D.1}$$

These coordinates represent the distance between the center of the two atoms and the center-of-mass coordinate respectively. They are adapted to a molecular description of the system, in particular to a situation where the two atoms maintain a strong interaction even after adsoption.

In a harmonic approximation in which the two modes x_d and x_c are decoupled. The Hamiltonian of the system can be written as:

$$\hat{H}(x_d, x_c) = \frac{1}{2} m\omega_d^2 (x_d - x_d^{\text{eq}})^2 + \frac{1}{2} m\omega_c^2 (x_c - x_c^{\text{eq}})^2 \tag{D.2}$$

With

$$\begin{cases} x_d^{\text{eq}} = x_2^{\text{eq}} - x_1^{\text{eq}} \\ x_c^{\text{eq}} = \dfrac{x_1^{\text{eq}} + x_2^{\text{eq}}}{2} \end{cases} \tag{D.3}$$

Where ω_d and ω_c are the eigenpulsations of each mode. m is the mass of each atom. x_i^{eq} is the equilibrium position of each atom.

The eigenstates of such a system are given by the product of the general harmonic oscillator solutions for each mode:

$$\{\psi_k(x_d, x_c)\}_{k\in\mathcal{N}} = \{\varphi_d^m(x_d)\varphi_c^n(x_c)\}_{m,n\in\mathcal{N}} \tag{D.4}$$

Where φ^n is the nth excited state of a one-dimensional harmonic oscillator. The ground state and the first two excited states of the total system are given by:

$$\begin{cases} \psi_0(x_d, x_c) = C_0 G_d(x_d) G_c(x_c) \\ \psi_1(x_d, x_c) = C_1\Big(x_d - x_d^{\text{eq}}\Big) G_d(x_d) G_c(x_c) \\ \psi_2(x_d, x_c) = C_2\Big(x_c - x_c^{\text{eq}}\Big) G_d(x_d) G_c(x_c) \end{cases} \tag{D.5}$$

With C_k normalization constants, and G Gaussian functions given by :

$$G_l(X) = e^{\frac{-m\omega_l}{2\hbar}(X - X^{\text{eq}})^2} \tag{D.6}$$

Returning now to the (x_1, x_2) representation, D.5 becomes:

$$\begin{cases} \psi_0(x_1, x_1) = C_0 G_d(x_2 - x_1) G_c(\frac{x_2 + x_1}{2}) \\ \psi_1(x_1, x_2) = C_1\Big(\Big(x_2 - x_2^{\text{eq}}\Big) - \Big(x_1 - x_1^{\text{eq}}\Big)\Big) G_d(x_2 - x_1) G_c(\frac{x_2 + x_1}{2}) \\ \psi_2(x_1, x_2) = C_2/2\Big(\Big(x_2 - x_2^{\text{eq}}\Big) + \Big(x_1 - x_1^{\text{eq}}\Big)\Big) G_d(x_2 - x_1) G_c(\frac{x_2 + x_1}{2}) \end{cases} \tag{D.7}$$

Let us now look at the spatial representation of the first two excited states ψ_1 and ψ_2 in the x_1x_2-plane. Figure D.2 shows a two-dimensional representation of the latter where the parameters x_1^{eq} and x_2^{eq} have been arbitrarily chosen such that $x_1^{\text{eq}} \neq x_2^{\text{eq}}$.

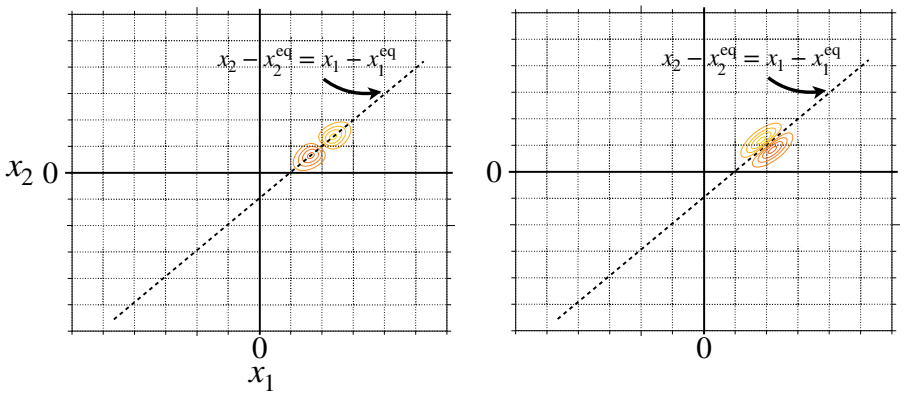

(a) ψ_2 (b) ψ_1

Figure D.2: Two-dimensional representation in the x_1x_2-plane of the first two excited states.

The two eigenstates have two symmetry axes given by equation D.8[1].

$$(x_2 - x_2^{eq}) = \pm(x_1 - x_1^{eq}) \tag{D.8}$$

In what follows, we'll consider only the symmetry axis with a positive slope. The same reasoning given below could be applied to the second symmetry axis.
ψ_1 and ψ_2 have one quantum of excitation in the x_d and x_c modes respectively. When excitation is localized on the x_c mode, this results in concerted motion of both atoms, i.e. in-phase vibration. When the excitation is localized on the x_d mode, this results in a stretching motion leading to an out-of-phase vibration between the two atoms. This can be seen directly in the structure of these states. In figure D.2a the antinodes and node of the wave function are aligned along a line of equation $(x_2 - x_2^{eq}) = (x_1 - x_1^{eq})$. This indicates that this excitation is constraining the x_1 and x_2 modes to have the same variation. Whereas in figure D.2b, the antinodes and node of the wave function are aligned along a line of equation $(x_2 - x_2^{eq}) = -(x_1 - x_1^{eq})$. This indicates that this excitation constrains the x_1 and x_2 modes to evolve in opposite variation. These two types of excitation implicitly induce both in-phase

[1]This can also be deduced directly from equations D.9.

and out-of-phase motion. These two vibration modes are illustrated schematically in the figure. D.3. The (R)PDs of these states have the same nodal structure as their wave functions. By looking at the structure of the latter along this line, we can deduce the relative motion between the two atoms.

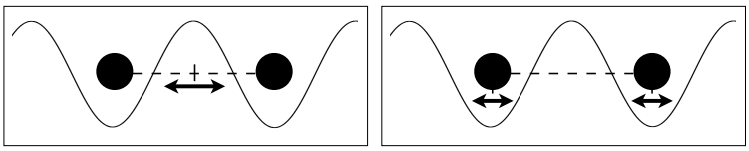

(a) (b)

Figure D.3: Scheme showing the resulting vibration motion following excitation at x_c mode (a), and at x_d mode (b).

On the other hand, when $x_1^{\text{eq}} = x_2^{\text{eq}}$, the axis of symmetry coincides with the diagonal. This situation is not possible in the one-dimensional case, as the two atoms cannot be superimposed in the same potential well. But if we consider a two-dimensional situation in Cartesian coordinates (x, y), the above situation becomes possible. Figure D.1 shows schematically a typical example of this configuration.

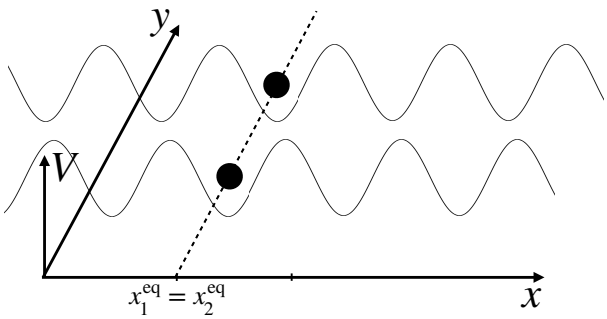

Figure D.4: Schematic representation of the configuration where $x_1^{\text{eq}} = x_2^{\text{eq}}$

In this example, we've considered the situation where the two hydrogen atoms occupy sites aligned along the y direction. Given that the latter have the same equilibrium position with respect to the x axis, the RPDs in the (x_1, x_2) representation of a state having a quantum of excitation in the x_d and x_c modes will now have

nodal structures located on the diagonal (since x_1^{eq} and x_2^{eq} simplify)[2]. In contrast to the previous situation, each atom will vibrate systematically in a direction perpendicular to the equilibrium system axis[3]. Figure D.1 shows an illustration of this situation.

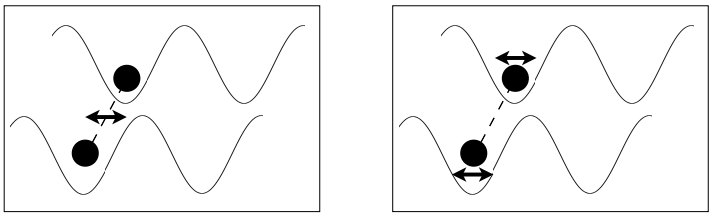

Figure D.5: Scheme showing the resulting vibration motion following excitation at x_c mode, and at x_d mode when $x_1^{\text{eq}} = x_2^{\text{eq}}$.

Finally, by combining these various remarks, we arrive at the following conclusions:

- When both atoms vibrate perpendicular to the equilibrium system axis, the nodal structures of their RPDs involving the same DOFs are located on the diagonal. When both atoms vibrate parallel to the equilibrium system axis, the nodal structures of the RPDs are located around a straight line different from the diagonal.

- When the two atoms vibrate in phase, the nodes and antinodes of the RPDs are located on the diagonal. When they vibrate out-of-phase, the latter are located on a line perpendicular to the latter.

Note

In this type of problem, configurations where the excitation is carried separately by a single atom (the second remains in its ground state) are given by the linear combination of states vibrating in phase and out-of-phase. For example, the superposition

[2] while the RPDs of states with excitations in the y_d and y_c will exhibit nodal structures localized around the line defined by $(y_2 - y_2^{\text{eq}}) = (y_1 - y_1^{\text{eq}})$ different from the diagonal.

[3] The equilibrium system axis is defined as the straight line joining the two atoms when the latter are located at the center of the potential wells.

of ψ_1 and ψ_2 in equation D.9 gives:

$$\begin{cases} a\psi_1(x_1,x_2)+b\psi_2(x_1,x_2)\equiv(x_2-x_2^{\text{eq}})G_d(x_2-x_1)G_c(\frac{x_2+x_1}{2}) \\ a\psi_1(x_1,x_2)-b\psi_2(x_1,x_2)\equiv(x_1-x_1^{\text{eq}})G_d(x_2-x_1)G_c(\frac{x_2+x_1}{2}) \end{cases} \tag{D.9}$$

In the first equation, we observe a nodal structure localized only on the second atom, while in the second case, the nodal structure is localized on the first atom. Such a state is not an eigenstate of the system; it evolves over time, oscillating between these two modes of vibration.

Appendix E

Some calculation files

E.1 Example of input files used in MCTDH calculations

E.1.1 Typical input file used for a block improved relaxation calculation

```
RUN-SECTION
usepthreads=16
name=block-75states-3x3-1
relaxation=0,olsen precon=2000
rlxunit=cm-1 , 1284.912567671
split-rst
tfinal=60 tout=all tpsi=10.00
title=Test
gridpop steps orben
end-run-section
OPERATOR-SECTION
opname = HPd111
end-operator-section
SPF-BASIS-SECTION
          packet=75,single-set
```

```
        x = 30
        y = 30
        z = 4
end-spf-basis-section
PRIMITIVE-BASIS-SECTION
   x        exp   61   -4.12671,Angst    4.12671,Angst     s-periodic
   y        exp   61   -4.12671,Angst    4.12671,Angst     s-periodic
   z        sin   31    0.2,Angst        1.7,Angst         long
end-primitive-basis-section
INTEGRATOR-SECTION
CMF = 1.0, 3.0d-3
RK8/spf = 1.0d-8, 0.1
RRDAV/A =4000, 1.0d-9
energyorb eps_inv=1.d-9
end-integrator-section
INIT_WF-SECTION
build
    x     readspf    Gauss-fcc-hcp-x-61
    y     readspf    Gauss-fcc-hcp-y-61
    z     gauss      0.9000,Angst        0.0d0      0.50d0
end-build
autoblock
end-init_wf-section
end-input
```

E.1.2 Typical input file used for a propagation calculation

```
RUN-SECTION
propagation
output
usepthreads=30
name=HO-pop2-x-fcc
tfinal=1000 tout= 2.00 tpsi=2.00
```

```
title=Test
psi #= double
gridpop steps
end-run-section
OPERATOR-SECTION
opname = HPd111
end-operator-section
SPF-BASIS-SECTION
        x = 42
        y = 42
        z = 14
end-spf-basis-section
PRIMITIVE-BASIS-SECTION
    x       exp  61  -4.12671,Angst   4.12671,Angst    s-periodic
    y       exp  61  -4.12671,Angst   4.12671,Angst    s-periodic
    z       sin  31   0.2,Angst       1.7,Angst        long
end-primitive-basis-section
INTEGRATOR-SECTION
CMF/varphi = 0.5, 1.0d-6
 BS/spf  =   8   , 1.0d-7
 SIL/A   =  20   , 1.0d-6
end-integrator-section
INIT_WF-SECTION
build
x    HO     0.91704,Angst    0.0d0    0.1,eV  1.007825,AMU  pop=2
y    HO    -0.91704,Angst    0.0d0    0.1,eV  1.007825,AMU
z    HO     0.9000,Angst     0.0d0    0.1,eV  1.007825,AMU
end-build
end-init_wf-section
ALLOC-SECTION
   maxkoe=15000
   maxhtm=15000
```

```
    maxhop=15000
    maxsub=400
end-alloc-section
end-input
```

E.2 Example of input files used for the ISF calculations

E.2.1 Generation of the ensemble of stochastic thermal wavepackets

Script file

```
#!/bin/bash
# command file for running fortran code
if test $# -eq 0
 then
  echo "Usage: generate-mctdh-ISF-evaluation-files.com T iseed"
 exit 1
fi

export CurrDir=$(pwd)

export WorkDir=$1K

if [ ! -d $WorkDir ]; then
  mkdir $WorkDir
fi

cd $WorkDir

T=$1
```

```
let nxstate=61  #$ncell*$nstpc
let nystate=61
let nzstate=31
iseed=$2
#let jseed=$iseed+1000

cp ../rlx-Therm.f .
cp ../HPd111.op .
  gfortran rlx-Therm.f -o rlx-Therm.exe -fno-automatic

#  if [ ! -e OPERATOR.op ]; then
#      ln -s operators-without-CAP.op OPERATOR.op
#  fi

  echo "T:     " > INPUT
  echo $T       >> INPUT
  echo "Iseed:">> INPUT
  echo $iseed  >> INPUT
  echo "Nx:"     >> INPUT
  echo $nxstate >> INPUT
  echo "Ny:"     >> INPUT
  echo $nystate >> INPUT
  echo "Nz:"     >> INPUT
  echo $nzstate >> INPUT
#  echo "Ncell" >> INPUT
#  echo $ncell  >> INPUT

  ./rlx-Therm.exe < INPUT
  echo "rlx-Therm done"
  rm INPUT
  rm -f rlx-Therm.f rlx-Therm.exe
```

```
if [ ! -d KG-THERMALISATION ]; then
    mkdir KG-THERMALISATION
fi

cd KG-THERMALISATION
if test -d iseed$iseed-KG-relaxation; then
    echo "iseed$iseed-KG-relaxation exists."
    rm -f ../iseed$iseed-KG-relaxation.inp

else
    mv ../iseed$iseed-KG-relaxation.inp .
    mv ../RANDOMVECTOR*$iseed .
    mv ../Therm-$iseed .
    sbatch Therm-$iseed
fi
cd ../

watch squeue -u obindech


exit
```

FORTRAN file

```
      program grv
c generates a normalized vector of length N with random phases
c as well as mctdh input files for relaxation following Kosloff-Gelman
c and propagation files at finite and infinite temperatures
c 190528 non-exact propagation
c 190529      exact propagation tested and then discarded,
c             as crosscorr needs MCTDH type WF, not exact WF
```

```
      implicit real*8 (a-h,o-z)
      parameter (nstate=8049)
      parameter (iseed0=1729)
      parameter (fsK=3819.116289)
      parameter(a0=0.5291772107)
      parameter(ac=1.278)
      dimension br(nstate),bi(nstate)
      character*80 com,iof,rlx,RANDx,RANDy,RANDz,filename
      character*50 zeile
      character*20 str

      tpi=acos(-1.d0)*2.

      read(5,*) com
      read(5,*) T
      read(5,*) com
      read(5,*) iseed
      read(5,*) com
      read(5,*) nxmax
      read(5,*) com
      read(5,*) nymax
      read(5,*) com
      read(5,*) nzmax
C      if(nxmax.gt.nstate) stop 'n out of range.'
C      read(5,*) com
C      read(5,*) ncell

      p=1./sqrt(nxmax*1.0)

      if (iseed .lt. 10) then
        write(RANDx,"(A13,I1)") 'RANDOMVECTORx',iseed
        write(RANDy,"(A13,I1)") 'RANDOMVECTORy',iseed
```

```
      write(RANDz,"(A13,I1)") 'RANDOMVECTORz',iseed
    endif

    if (iseed .gt. 9 .and. iseed .lt. 100) then
      write(RANDx,"(A13,I2)") 'RANDOMVECTORx',iseed
      write(RANDy,"(A13,I2)") 'RANDOMVECTORy',iseed
      write(RANDz,"(A13,I2)") 'RANDOMVECTORz',iseed
    endif

    if (iseed .gt. 90) then
     stop 'Max of realisations reached. See Iq.f file'
    endif

    open(2,FILE=trim(RANDx),
   &form='formatted',status='unknown')

    call srand(iseed)

    do n=1,nxmax
       phi=tpi*rand()
       br(n)=p*cos(phi)
       bi(n)=p*sin(phi)
       write(2,*) br(n),bi(n)
    enddo

    close(2)


C RandVecy

    p=1./sqrt(nymax*1.0)
```

```
  open(2,FILE=trim(RANDy),
 &form='formatted',status='unknown')


  jseed=iseed+1000
  call srand(jseed)

  do n=1,nymax
     phi=tpi*rand()
     br(n)=p*cos(phi)
     bi(n)=p*sin(phi)
     write(2,*) br(n),bi(n)
  enddo

  close(2)


  jseed=jseed+1000
  p=1./sqrt(nzmax*1.0)

  open(2,FILE=trim(RANDz),
 &form='formatted',status='unknown')

  call srand(jseed)

  do n=1,nzmax
     phi=tpi*rand()
     br(n)=p*cos(phi)
     bi(n)=p*sin(phi)
     write(2,*) br(n),bi(n)
  enddo
```

```
      close(2)


c     generation of MCTDH input files
c     relaxation

      tf=fsK/T
      itape=11
      com='iseed'//trim(str(iseed))//'-KG-relaxation'
      iof=trim(com)//'.inp'
      rlx=com

      open(itape,file=iof,form='formatted',status='unknown')

      write(itape,*) 'RUN-SECTION'
      write(itape,*) ' name = '//com
      write(itape,*) ' relaxation'
      write(itape,*) ' usepthreads=16'
      write(itape,*) ' tfinal=',tf,'tout=',tf/20,'tpsi=',tf/20
      write(itape,*) ' steps auto psi gridpop'
      write(itape,*) ' end-run-section'

      write(itape,*) 'PRIMITIVE-BASIS-SECTION'
      write(itape,*) ' x exp ',nxmax,'  -4.12671,Angst  4.12671,Angst',
     1 '   s-periodic'
      write(itape,*) ' y exp ',nymax,'  -4.12671,Angst  4.12671,Angst',
     1 '   s-periodic'
      write(itape,*) ' z sin ',nzmax,'  0.2,Angst  1.7,Angst',
     1 '   long'
      write(itape,*) 'end-primitive-basis-section'

      write(itape,*) 'SPF-BASIS-SECTION'
```

```
      write(itape,*) ' x=25'
      write(itape,*) ' y=25'
      write(itape,*) ' z=15'
      write(itape,*) 'end-spf-basis-section'

      write(itape,*) 'OPERATOR-SECTION'
      write(itape,*) ' opname=HPd111'
      write(itape,*) ' oppath=../'
C     1     /EIGENSTATES'
      write(itape,*) 'end-operator-section'

      write(itape,*) 'INIT_WF-SECTION'
      write(itape,*) ' build'
      write(itape,*) '  x readspf  ', RANDx
      write(itape,*) '  y readspf  ', RANDy
      write(itape,*) '  z readspf  ', RANDz
      write(itape,*) ' end-build'
      write(itape,*) 'end-init_wf-section'

      write(itape,*) 'INTEGRATOR-SECTION'
      write(itape,*) ' VMF'
      write(itape,*) ' RK8 = 1.0d-7, 1.0d-7'
      write(itape,*) ' proj-h'
      write(itape,*) 'end-integrator-section'

      write(itape,*) 'ALLOC-SECTION'
      write(itape,*) '   maxkoe=15000'
      write(itape,*) '   maxhtm=15000'
      write(itape,*) '   maxhop=15000'
      write(itape,*) '   maxsub=780'
      write(itape,*) '   maxham=1000'
      write(itape,*) 'end-alloc-section'
```

```
      write(itape,*) ' '
      write(itape,'(A)') 'end-input'
      close(itape)




C********************Generate scripts for HPC calculation*************
C*****Thermalisation
      itape=14
      iof='Therm-'//trim(str(iseed))
      open(itape,file=iof,form='formatted',status='unknown')


      write(itape,'(A)') '#! /bin/bash'

      write(itape,'(A)') '#SBATCH -p grant    '
      write(itape,'(A)') '#SBATCH -A **********'
      write(itape,'(A)') '#SBATCH --exclusive'
      write(itape,'(A)') '#SBATCH -N 1'
      write(itape,'(A)') '#SBATCH --mem=20G '
      write(itape,'(A)') '#SBATCH --mail-type=END  '
      write(itape,'(A)') 'source ~/.bashrc'

      write(itape,'(A)') 'hostname '

!       write(filename,"(A13,I2)")'RANDOMVECTORx',iseed
      com='filename=iseed'//trim(str(iseed))//'-KG-relaxation.inp'
      write(itape,'(A)') com
```

```
      write(itape,*) 'sed -i "s/usepthreads=.*/usepthreads=','$','SLURM'
     1 ,'_CPUS_ON_NODE/"','  $filename '
      write(itape,'(A)') 'mctdh86 -mnd $filename'

      close(itape)



c
      stop 'Normal conclusion.'
      end
C-----------------------------------------------------------------------
      character(20) function str(k)
!   "Convert an integer to string."
!       integer, intent(in) :: k
      write (str, *) k
      str = adjustl(str)
      end
C-----------------------------------------------------------------------
```

E.2.2 Propagation of the non-interacting stochastic thermal wave-packets

Script file

```
#!/bin/bash
# command file for running fortran code
if test $# -eq 0
        then
            echo "Usage: prop-Ket.com T iseed"
        exit 1
fi
```

```
export CurrDir=$(pwd)


export WorkDir=$1K

if [ ! -d $WorkDir ]; then
  mkdir $WorkDir
fi

cd $WorkDir
#ln -s ../HPd111.op HPd111.op
T=$1
#ncell=24
#nstpc=24
tf=10000.
let nxstate=61  #$ncell*$nstpc
let nystate=61
let nzstate=31
iseed=$2

cp ../prop-Ket.f .
#cp ../HPd111.op .
  gfortran prop-Ket.f -o prop-Ket.exe -fno-automatic

#  if [ ! -e OPERATOR.op ]; then
#       ln -s operators-without-CAP.op OPERATOR.op
#  fi

  echo "T:     " > INPUT
  echo $T       >> INPUT
  echo "Iseed:">> INPUT
  echo $iseed  >> INPUT
```

```
   echo "Nx:"     >> INPUT
   echo $nxstate >> INPUT
   echo "Ny:"     >> INPUT
   echo $nystate >> INPUT
   echo "Nz:"     >> INPUT
   echo $nzstate >> INPUT
#  echo "Ncell" >> INPUT
#  echo $ncell  >> INPUT
   echo "tfinal">> INPUT
   echo $tf      >> INPUT

   ./prop-Ket.exe < INPUT
   echo "prop-Ket done"
   rm INPUT
   rm -f prop-Ket.f prop-Ket.exe

#export oper=Ek6th

#if [ ! -d $oper ]; then
#  mkdir $oper
#fi
#cd $oper



   if [ ! -d PROPAGATION ]; then
       mkdir PROPAGATION
   fi
   cd PROPAGATION
   ln -s ../HPd111.op HPd111.op

   if [ ! -d prop-Ket ]; then
       mkdir prop-Ket
```

```
  fi
  cd prop-Ket

  if test -d iseed$iseed-KG-propagation-Ket; then
      echo "iseed$iseed-KG-propagation-Ket exists."

  else
      mv ../../iseed$iseed-KG-propagation-Ket.inp .
      mv ../../Ket-$iseed .
      sbatch Ket-$iseed
  fi
   watch squeue -u obindech


exit
```

FORTRAN file

```
      program grv
c generates a normalized vector of length N with random phases
c as well as mctdh input files for relaxation following Kosloff-Gelman
c and propagation files at finite and infinite temperatures
c 190528 non-exact propagation
c 190529      exact propagation tested and then discarded,
c             as crosscorr needs MCTDH type WF, not exact WF
      implicit real*8 (a-h,o-z)
      parameter (nstate=8049)
      parameter (iseed0=1729)
      parameter (fsK=3819.116289)
      parameter(a0=0.5291772107)
      parameter(ac=1.278)
      dimension br(nstate),bi(nstate)
      character*80 com,iof,rlx,RANDx,RANDy,RANDz,filename
```

```
      character*50 zeile
      character*20 str

      tpi=acos(-1.d0)*2.

      read(5,*) com
      read(5,*) T
      read(5,*) com
      read(5,*) iseed
      read(5,*) com
      read(5,*) nxmax
      read(5,*) com
      read(5,*) nymax
      read(5,*) com
      read(5,*) nzmax
C      if(nxmax.gt.nstate) stop 'n out of range.'
C      read(5,*) com
C      read(5,*) ncell
      read(5,*) com
      read(5,*) tfinal

      rlx='iseed'//trim(str(iseed))//'-KG-relaxation'


c     propagation

      tf=tfinal
      dt=tf/100
      itape=12
      com='iseed'//trim(str(iseed))//'-KG-propagation-Ket'
      iof=trim(com)//'.inp'
```

```
      open(itape,file=iof,form='formatted',status='unknown')

      write(itape,*) 'RUN-SECTION'
      write(itape,*) 'name = '//com
      write(itape,*) 'propagation'
      write(itape,*) 'usepthreads=16'
      write(itape,*) 'tinit=0.0 tfinal=',tf,
     &'tout=',   dt,'tpsi=',   dt
      write(itape,*) 'no-timing no-speed no-update psi gridpop'
      write(itape,*) 'end-run-section'

      write(itape,*) 'PRIMITIVE-BASIS-SECTION'
      write(itape,*) ' x exp ',nxmax,'  -4.12671,Angst  4.12671,Angst',
     1 '   s-periodic'
      write(itape,*) ' y exp ',nymax,'  -4.12671,Angst  4.12671,Angst',
     1 '   s-periodic'
      write(itape,*) ' z sin ',nzmax,'  0.2,Angst  1.7,Angst',
     1 '   long'
      write(itape,*) 'end-primitive-basis-section'

      write(itape,*) 'SPF-BASIS-SECTION'
      write(itape,*) ' x=25'
      write(itape,*) ' y=25'
      write(itape,*) ' z=15'
      write(itape,*) 'end-spf-basis-section'

      write(itape,*) 'OPERATOR-SECTION'
      write(itape,*) ' opname=HPd111'
      write(itape,*) ' oppath=../'
C     1    /EIGENSTATES'
      write(itape,*) 'end-operator-section'
```

```
      write(itape,*) 'INIT_WF-SECTION'
      write(itape,*) 'file=../../KG-THERMALISATION/'//rlx
      write(itape,*) 'end-init_wf-section'

      write(itape,*) 'INTEGRATOR-SECTION'
      write(itape,*) 'CMF/varphi = 0.5, 1.0d-6'
      write(itape,*) 'BS/spf   =   8   , 1.0d-7'
      write(itape,*) 'SIL/A    =  20   , 1.0d-6'
      write(itape,*) 'end-integrator-section'

      write(itape,*) 'ALLOC-SECTION'
      write(itape,*) '    maxkoe=15000'
      write(itape,*) '    maxhtm=15000'
      write(itape,*) '    maxhop=15000'
      write(itape,*) '    maxsub=780'
      write(itape,*) '    maxham=1000'
      write(itape,*) 'end-alloc-section'

      write(itape,*) ' '
      write(itape,'(A)') 'end-input'
      close(itape)
```

```
C*********************Generate scripts for HPC calculation*************
```

```
C*****Propagation Ket
      itape=14
      iof='Ket-'//trim(str(iseed))
```

```
      open(itape,file=iof,form='formatted',status='unknown')


      write(itape,'(A)') '#! /bin/bash'

      write(itape,'(A)') '#SBATCH -p grant    '
      write(itape,'(A)') '#SBATCH -A **********'
      write(itape,'(A)') '#SBATCH --exclusive'
      write(itape,'(A)') '#SBATCH -N 1'
      write(itape,'(A)') '#SBATCH --mem=20G '
      write(itape,'(A)') '#SBATCH --mail-type=END  '
      write(itape,'(A)') 'source ~/.bashrc'

      write(itape,'(A)') 'hostname '

      com='filename=iseed'//trim(str(iseed))//'-KG-propagation-Ket.inp'
      write(itape,'(A)') com



      write(itape,*) 'sed -i "s/usepthreads=.*/usepthreads=','$','SLURM'
     1 ,'_CPUS_ON_NODE/"','  $filename '
      write(itape,'(A)') 'mctdh86 -mnd $filename'

      close(itape)

c
      stop 'Normal conclusion.'
      end
C-----------------------------------------------------------------------
      character(20) function str(k)
!   "Convert an integer to string."
```

```
!       integer, intent(in) :: k
        write (str, *) k
        str = adjustl(str)
        end
C-----------------------------------------------------------------------
```

E.2.3 Propagation of the interacting stochastic thermal wave-packets

Script file

```
#!/bin/bash
# command file for running fortran code
if test $# -eq 0
        then
            echo "Usage: prop-Bra.com T iseed    Ekth-Number"
        exit 1
fi

export CurrDir=$(pwd)



export WorkDir=$1K

if [ ! -d $WorkDir ]; then
  mkdir $WorkDir
fi

cd $WorkDir
#ln -s ../HPd111.op HPd111.op
T=$1
#ncell=24
#nstpc=24
```

```
tf=10000.
let nxstate=61  #$ncell*$nstpc
let nystate=61
let nzstate=31
iseed=$2
op=Ek$3th

cp ../prop-Bra.f .
#cp ../HPd111.op .
  gfortran prop-Bra.f -o prop-Bra.exe -fno-automatic

#  if [ ! -e OPERATOR.op ]; then
#      ln -s operators-without-CAP.op OPERATOR.op
#  fi

  echo "T:     " > INPUT
  echo $T       >> INPUT
  echo "Iseed:">> INPUT
  echo $iseed  >> INPUT
  echo "Nx:"     >> INPUT
  echo $nxstate >> INPUT
  echo "Ny:"     >> INPUT
  echo $nystate >> INPUT
  echo "Nz:"     >> INPUT
  echo $nzstate >> INPUT
#  echo "Ncell" >> INPUT
#  echo $ncell  >> INPUT
  echo "tfinal">> INPUT
  echo $tf     >> INPUT
  echo "Ekth"  >> INPUT
  echo $op     >> INPUT
```

```
  ./prop-Bra.exe < INPUT
  echo "prop-Bra done"
  rm INPUT
  rm -f prop-Bra.f prop-Bra.exe

#export oper=Ek6th

#if [ ! -d $oper ]; then
#  mkdir $oper
#fi
#cd $oper

  if [ ! -d PROPAGATION ]; then
      mkdir PROPAGATION
  fi
  cd PROPAGATION


  if [ ! -d prop-Bra ]; then
      mkdir prop-Bra
  fi
  cd prop-Bra
#  ln -s ../HPd111.op HPd111.op

if [ ! -d $op ]; then
      mkdir $op
  fi
  cd $op

  if test -d iseed$iseed-KG-propagation-Bra; then
      echo "iseed$iseed-KG-propagation-Bra exists."
```

```
  else
      mv ../../../iseed$iseed-KG-propagation-Bra.inp .
      mv ../../../Bra-$iseed .
      sbatch Bra-$iseed
  fi
   watch squeue -u obindech


exit


  if test -d iseed$iseed-KG-propagation-Bra; then
      echo "iseed$iseed-KG-propagation-Bra exists."
      rm -f ../iseed$iseed-KG-propagation-Bra.inp


  if test -d iseed$iseed-KG-propagation-Bra; then
      echo "iseed$iseed-KG-propagation-Bra exists."

  else
      mv ../../iseed$iseed-KG-propagation-Bra.inp .
      mv ../../Bra-$iseed .
      sbatch Bra-$iseed   fi
#


  cd ../../




exit
```

FORTRAN file

```
      program grv
c generates a normalized vector of length N with random phases
c as well as mctdh input files for relaxation following Kosloff-Gelman
c and propagation files at finite and infinite temperatures
c 190528 non-exact propagation
c 190529      exact propagation tested and then discarded,
c             as crosscorr needs MCTDH type WF, not exact WF
      implicit real*8 (a-h,o-z)
      parameter (nstate=8049)
      parameter (iseed0=1729)
      parameter (fsK=3819.116289)
      parameter(a0=0.5291772107)
      parameter(ac=1.278)
      dimension br(nstate),bi(nstate)
      character*80 com,iof,rlx,RANDx,RANDy,RANDz,filename,op
      character*50 zeile
      character*20 str
      integer tt

      read(5,*) com
      read(5,*) T
      read(5,*) com
      read(5,*) iseed
      read(5,*) com
      read(5,*) nxmax
      read(5,*) com
      read(5,*) nymax
      read(5,*) com
      read(5,*) nzmax
C      if(nxmax.gt.nstate) stop 'n out of range.'
C      read(5,*) com
```

```
C       read(5,*) ncell
        read(5,*) com
        read(5,*) tfinal
        read(5,*) com
        read(5,*) tinitial

        rlx='iseed'//trim(str(iseed))//'-KG-propagation-Bra'

c       propagation

        ti=tinitial
        tf=tfinal
        dt=(tf-ti)/100
        tt=tf/1000


        itape=13

        com=trim(rlx)//'-cont-'//trim(str(tt))//'ps'
        iof=trim(com)//'.inp'
        open(itape,file=iof,form='formatted',status='unknown')

        write(itape,*) 'RUN-SECTION'
        write(itape,*) 'name = '//com
        write(itape,*) 'propagation'
        write(itape,*) 'usepthreads=16'
        write(itape,*) 'tinit=',ti, 'tfinal=',tf,
       &'tout=',   dt,'tpsi=',   dt
        write(itape,*) 'no-timing no-speed no-update psi gridpop'
        write(itape,*) 'end-run-section'

        write(itape,*) 'PRIMITIVE-BASIS-SECTION'
```

```
      write(itape,*) ' x exp ',nxmax,'  -4.12671,Angst  4.12671,Angst',
     1 '   s-periodic'
      write(itape,*) ' y exp ',nymax,'  -4.12671,Angst  4.12671,Angst',
     1 '   s-periodic'
      write(itape,*) ' z sin ',nzmax,'  0.2,Angst  1.7,Angst',
     1 '   long'
      write(itape,*) 'end-primitive-basis-section'

      write(itape,*) 'SPF-BASIS-SECTION'
      write(itape,*) ' x=35'
      write(itape,*) ' y=35'
      write(itape,*) ' z=20'
      write(itape,*) 'end-spf-basis-section'

      write(itape,*) 'OPERATOR-SECTION'
      write(itape,*) ' opname=HPd111'
      write(itape,*) ' oppath=../../'
C     1     /EIGENSTATES'
      write(itape,*) 'end-operator-section'

      write(itape,*) 'INIT_WF-SECTION'
      write(itape,*) 'file=',rlx
!      write(itape,*) 'operate =', op
      write(itape,*) 'end-init_wf-section'

      write(itape,*) 'INTEGRATOR-SECTION'
      write(itape,*) 'CMF/varphi = 0.5, 1.0d-6'
      write(itape,*) 'BS/spf  =   8   , 1.0d-7'
      write(itape,*) 'SIL/A   =  20   , 1.0d-6'
      write(itape,*) 'end-integrator-section'

      write(itape,*) 'ALLOC-SECTION'
```

```
      write(itape,*) '    maxkoe=15000'
      write(itape,*) '    maxhtm=15000'
      write(itape,*) '    maxhop=15000'
      write(itape,*) '    maxsub=780'
      write(itape,*) '    maxham=1000'
      write(itape,*) 'end-alloc-section'



      write(itape,*) ' '
      write(itape,'(A)') 'end-input'
      close(itape)



C*********************Generate scripts for HPC calculation*************

C*****Propagation Bra
      itape=14
      iof='Bra-'//trim(str(iseed))
      open(itape,file=iof,form='formatted',status='unknown')


      write(itape,'(A)') '#! /bin/bash'

      write(itape,'(A)') '#SBATCH -p grant    '
      write(itape,'(A)') '#SBATCH -A **********'
      write(itape,'(A)') '#SBATCH --exclusive'
      write(itape,'(A)') '#SBATCH -N 1'
      write(itape,'(A)') '#SBATCH --mem=20G '
      write(itape,'(A)') '#SBATCH --mail-type=END  '
      write(itape,'(A)') 'source ~/.bashrc'
```

```
      write(itape,'(A)') 'hostname '

!      com='filename=iseed'//trim(str(iseed))//'-KG-propagation-Bra-cont.i
      write(itape,'(A)') 'filename='//trim(com)//'.inp'



      write(itape,*) 'sed -i "s/usepthreads=.*/usepthreads=','$','SLURM'
     1 ,'_CPUS_ON_NODE/"','  $filename '
      write(itape,'(A)') 'mctdh86 -mnd $filename'

      close(itape)


c
      stop 'Normal conclusion.'
      end
C-----------------------------------------------------------------------
      character(20) function str(k)
!   "Convert an integer to string."
!      integer, intent(in) :: k
      write (str, *) k
      str = adjustl(str)
      end
C-----------------------------------------------------------------------
```

E.2.4 Averaging over all realisations

Script file

```
#!/bin/bash
# command file for running fortran code
```

```
if [ $# -eq 0 ]
        then
            echo "Usage: calculate-ISF.com <k> iseed_min iseed_max
T  Nt(fs)"
            exit 1
fi
OPER=Ek$1th
#Nseed=$2+1
iseed_min=$2
iseed_max=$3
Nt=$5
#Nseed=$iseed_min+$iseed_max
export CurrDir=$(pwd)



export WorkDir=$4K
export ADir=$CurrDir"/"$WorkDir

if [ ! -d $WorkDir ]; then
  mkdir $WorkDir
fi

cd $WorkDir

# create cross correlation files with MCTDH (formula 11 report Roberto)
    if [ ! -d CC-FILES ]; then
      mkdir CC-FILES
    fi
    if [ ! -d CC-FILES/$OPER ]; then
      mkdir CC-FILES/$OPER
```

```
    cd $ADir/PROPAGATION
    for ((it=1;Nt-it+1; it++))
     do
     for ((ic=$iseed_min ; iseed_max-ic + 1  ; ic++))
      do
        i="prop-Bra/"$OPER"/iseed"$ic"-KG-propagation-Bra-"$it"0ps"
        echo $i

        cd $i
#         for ((jc=$iseed_min ; iseed_max -jc + 1 ; jc++))
#          do
            j="../../../prop-Ket/iseed"$ic"-KG-propagation-Ket-"$it"0ps"
            echo $j
            if [ ! -e $ADir"/CC-FILES/"$OPER/$ic-$ic-$it"0ps" ]; then

                crosscorr86  -f $j/ -o CC -M -O $OPER psi
#                rm -f $j/chi
                mv CC $ADir/CC-FILES/$OPER/$ic-$ic-$it"0ps"
            fi
#          done

       cd $ADir/PROPAGATION
       done


     done
     fi

cd $ADir/

# calculate average
 if [ ! -d ISF-FILES ]; then
```

```
 mkdir ISF-FILES
fi

if [ ! -d ISF-FILES/$OPER ]; then
 mkdir ISF-FILES/$OPER
fi

  cp ../averg-Iq.f CC-FILES/$OPER/.
  cd CC-FILES/$OPER
  gfortran averg-Iq.f -o averg-Iq.exe -fno-automatic


 echo $Nt           >> INPUT
 echo $iseed_min    >> INPUT
 echo $iseed_max    >> INPUT

 ./averg-Iq.exe < INPUT
 echo "average Iq done"
 rm INPUT
 rm -f averg-Iq.f    averg-Iq.exe

  plgen -u 1:2 ISF-FINAL.pld
  mv ISF-FINAL.pld  ../../ISF-FILES/$OPER/.
  rm -f averg-Iq.*


exit
```

FORTRAN file

```
      program CISF

      integer i,j,k,tt,Ntstep,ii
```

```
      real*8 x(100,1000),y(100,1000) !,x(Nseed,Nt)
      real*8 t,dt,a,b,tmax,ax0,ay0,ax,ay,Px
      character*50 com,zeile


      read(5,*) Nt        !Nt in fs
      read(5,*) iseedMin
      read(5,*) iseedMax


      Nseed=iseedMax-iseedMin+1

C      write(*,*) iseedMin,iseedMax


     OPEN(12,FILE='ISF-FINAL.pld', action = 'write')


      do tt=1,Nt
       do k=iseedMin,iseedMax

        if (k .lt. 10) then
         write(com,"(I1,A1,I1,A1,I1,A3)") k,'-',k,'-',tt,'0ps'
        endif

        if (k .gt. 9 .and. k.lt.100) then
         write(com,"(I2,A1,I2,A1,I1,A3)") k,'-',k,'-',tt,'0ps'
        endif

        if (k .gt. 99) then
          write(*,*) 'Error: iseedmax=99. See averg-Iq.f'
          goto 1700
```

```
   endif


   OPEN(10,FILE=trim(com), action = 'read')

   do i=1,12
    read(10,*) zeile
   enddo


   Ntstep=100
   do i=(tt-1)*100+1,tt*100
    read(10,*) t ,a ,b ,dummy,dummy
    x(k,i)=a
    y(k,i)=b
   enddo


   close(10)

  enddo
enddo


Nstep=Nt*100
tmax=t
t=0.
dt=tmax/(Ntstep-1)

ax0=0.
ay0=0.
```

```
      do i=1,Ntstep

       ax=0.
       ay=0.
       do k=1,Nseed
        if (i .eq. 1) then
         ax0= ax0+x(k,i)
         ay0= ay0+y(k,i)
        endif
        ax= ax+x(k,i)
        ay= ay+y(k,i)
       enddo


      Px=(ax*ax0+ay*ay0)/(ax0**2+ay0**2)
      write (12,*) t,Px
      t=t+dt
      enddo



 1700 continue

      end




c          com='new-'//com
c          OPEN(11,FILE=trim(com), action = 'write')

c          do i=1,12
```

```
c          write(11,*) zeile
c         enddo

c         do i=1,Nt
c          write(11,*) t  ,x(k,i)  ,y(k,i)  ,dummy,dummy
c         enddo

c         close(11)
c         close(10)
```

Bibliography

[1] April D Jewell, Guowen Peng, Michael FG Mattera, Emily A Lewis, Colin J Murphy, Georgios Kyriakou, Manos Mavrikakis, and E Charles H Sykes. Quantum tunneling enabled self-assembly of hydrogen atoms on Cu (111). *ACS nano*, 6(11):10115–10121, 2012.

[2] H Conrad, ME Kordesch, R Scala, and W Stenzel. Surface resonances on H/Pd(111) observed with HREELS. In *Studies in Surface Science and Catalysis*, volume 26, pages 289–298. Elsevier, 1986.

[3] AP Jardine, H Hedgeland, G Alexandrowicz, W Allison, and J Ellis. Helium-3 spin-echo: Principles and application to dynamics at surfaces. *Progress in Surface Science*, 84(11-12):323–379, 2009.

[4] JJ Reilly. Metal hydrides as hydrogen storage media and their applications. *Hydrogen: Its Technology and Implications*, 1:13–48, 2018.

[5] Souvik Mandal, Fabien Gatti, Oussama Bindech, Roberto Marquardt, and Jean-Christophe Tremblay. Multidimensional stochastic dissipative quantum dynamics using a Lindblad operator. *The Journal of Chemical Physics*, 156(9), 2022.

[6] Souvik Mandal, Fabien Gatti, Oussama Bindech, Roberto Marquardt, and Jean Christophe Tremblay. Stochastic multi-configuration time-dependent Hartree for dissipative quantum dynamics with strong intramolecular coupling. *The Journal of Chemical Physics*, 157(14), 2022.

[7] Enrico Fermi. Über den ramaneffekt des kohlendioxyds. *Zeitschrift für Physik*, 71(3-4):250–259, 1931.

[8] Léon Van Hove. Correlations in space and time and Born approximation scattering in systems of interacting particles. *Physical Review*, 95(1):249, 1954.

[9] Oussama Bindech and Roberto Marquardt. Mean square displacement of a free quantum particle on the basis of thermal Gaussian wave packets. *The European Physical Journal Special Topics*, 232(12):1885–1895, 2023.

[10] Thiago Firmino, Roberto Marquardt, Fabien Gatti, and Wei Dong. Diffusion rates for hydrogen on Pd (111) from molecular quantum dynamics calculations. *The Journal of Physical Chemistry Letters*, 5(24):4270–4274, 2014.

[11] Roberto Marquardt. Mean square displacement of a free quantum particle in a thermal state. *Molecular Physics*, 119(17-18):e1971315, 2021.

[12] Roberto Marquardt. The quantum mean square displacement of thermalized CO on Cu(100) in the short time approximation. *Phys. Chem. Chem. Phys.*, 24:26519, 2022.

[13] David Zanuttini, Fabien Gatti, and Roberto Marquardt. CO quantum diffusion dynamics on Cu(100). *Chem. Phys.*, 509:3–12, 2018.

[14] R. Marquardt. Quantum Dynamics of the Diffusion of Adsorbates. Project proposal, Agence National de la Recherche, Paris, France., 2019.

[15] Michael H Beck, Andreas Jäckle, Graham A Worth, and H-D Meyer. The multiconfiguration time-dependent Hartree (MCTDH) method: a highly efficient algorithm for propagating wavepackets. *Physics reports*, 324(1):1–105, 2000.

[16] Hans-Dieter Meyer, Fabien Gatti, and Graham A Worth. *Multidimensional quantum dynamics: MCTDH theory and applications*. John Wiley & Sons, 2009.

[17] Paul AM Dirac. Note on exchange phenomena in the Thomas atom. In *Mathematical proceedings of the Cambridge philosophical society*, volume 26, pages 376–385. Cambridge University Press, 1930.

[18] J Frenkel. Wave Mechanics, Clarendon, 1934.

[19] Loïc Joubert Doriol, Fabien Gatti, Christophe Iung, and Hans-Dieter Meyer. Computation of vibrational energy levels and eigenstates of fluoroform using the

multiconfiguration time-dependent Hartree method. *The Journal of chemical physics*, 129(22), 2008.

[20] Fabien Gatti, Benjamin Lasorne, Hans-Dieter Meyer, and André Nauts. *Applications of quantum dynamics in chemistry*, volume 98. Springer, 2017.

[21] GA Worth, MH Beck, A Jäckle, HD Meyer, F Otto, M Brill, and O Vendrell. The Heidelberg MCTDH Package: A set of programs for multi-dimensional quantum dynamics. *User's Guide, Version*, 8, 2000.

[22] W Dong, G Kresse, and J Hafner. Dissociative adsorption of H2 on the Pd (111) surface. *Journal of Molecular Catalysis A: Chemical*, 119(1-3):69–76, 1997.

[23] Y Xiao, W Dong, and HF Busnengo. Reactive force fields for surface chemical reactions: A case study with hydrogen dissociation on Pd surfaces. *The Journal of chemical physics*, 132(1), 2010.

[24] M. Quack and G. Seyfang. Atomic and Molecular Tunneling Processes in Chemistry. In R. Marquardt and M. Quack, editors, *Molecular Spectroscopy and Quantum Dynamics*, chapter 7. Elsevier, St. Louis (Missouri), USA, 2020.

[25] Thiago Diamond Reis Firmino. *The quantum dynamics of the diffusion of dissociatively adsorbed diatomic molecules*. PhD thesis, Université de Strasbourg, 2014.

[26] Brian T Sutcliffe. The idea of a potential energy surface. *Journal of Molecular Structure: THEOCHEM*, 341(1-3):217–235, 1995.

[27] Charles Cerjan. *Numerical grid methods and their application to Schrödinger's equation*. Number 412. Springer Science & Business Media, 1993.

[28] Albert Messiah. *Albert Messiah: Mécanique quantique. Tome 2*. Walter de Gruyter GmbH & Co KG, 2020.

[29] D Kosloff and R Kosloff. A Fourier method solution for the time dependent Schrödinger equation as a tool in molecular dynamics. *Journal of Computational Physics*, 52(1):35–53, 1983.

[30] John C Light and Tucker Carrington Jr. Discrete-variable representations and their utilization. *Advances in Chemical Physics*, 114:263–310, 2000.

[31] RB Gerber, MA Ratner, and V Buch. Simplified time-dependent self-consistent field approximation for intramolecular dynamics. *Chemical Physics Letters*, 91(3):173–177, 1982.

[32] Tae Jun Park and JC Light. Unitary quantum time evolution by iterative Lanczos reduction. *The Journal of chemical physics*, 85(10):5870–5876, 1986.

[33] Christopher W Murray, Stephen C Racine, and Ernest R Davidson. Improved algorithms for the lowest few eigenvalues and associated eigenvectors of large matrices. *Journal of Computational Physics*, 103(2):382–389, 1992.

[34] Ronnie Kosloff and H Tal-Ezer. A direct relaxation method for calculating eigenfunctions and eigenvalues of the Schrödinger equation on a grid. *Chemical Physics Letters*, 127(3):223–230, 1986.

[35] A Jäckle and H-D Meyer. Product representation of potential energy surfaces. II. *The Journal of chemical physics*, 109(10):3772–3779, 1998.

[36] A Jäckle and H-D Meyer. Product representation of potential energy surfaces. *The Journal of chemical physics*, 104(20):7974–7984, 1996.

[37] Jean-Luc Bonnardet and Gérard Papin. *L'indispensable en état solide*. Bréal, 2003.

[38] Donald W Brenner. Relationship between the embedded-atom method and Tersoff potentials. *Physical review letters*, 63(9):1022, 1989.

[39] Jean Christophe Tremblay and Peter Saalfrank. Selective Subsurface Absorption of Hydrogen in Palladium using Laser Distillation. 131(8):084716, 2009.

[40] R. S. Mulliken. Report on Notation for the Spectra of Polyatomic Molecules. 23(11):1997–2011, 1955. Joint Commission for Spectroscopy from IUPAC and IUPAP.

[41] Peter F Bernath. *Spectra of atoms and molecules*. Oxford University Press, 2005.

[42] N. D. Mermin and N. W. Ashcroft. *Solid State Physics*. Holt-Saunders International Editions, New York, 1976.

[43] R. Marquardt, M. Sanrey, F. Gatti, and F. Le Quéré. Full-Dimensional Quantum Dynamics of Vibrationally highly excited NHD_2. 133:174302, 2010.

[44] B. Fehrensen, D. Luckhaus, and M. Quack. Mode selective stereomutation tunneling in hydrogen peroxide isotopomers. 300:312–320, 1999.

[45] Thiago Firmino, Roberto Marquardt, Fabien Gatti, and Wei Dong. Diffusion Rates for Hydrogen on Pd(111) from Molecular Quantum Dynamics Calculations. *J. Phys. Chem. Lett.*, 5(24):4270–4274, 2014.

[46] T. D. R. Firmino. The quantum dynamics of the diffusion of dissociatively adsorbed diatomic molecules. Dissertation, Université de Strasbourg, F-67081 Strasbourg CEDEX, 2014.

[47] Nobuki Ozawa, Tanglaw A. Roman, Hiroshi Nakanishi, Hideaki Kasai, Jr. Nelson B. Arboleda, and Wilson Agerico Dino. Potential energy of hydrogen atom motion on Pd(111) surface and in subsurface: A first principles calculation. *Journal of Applied Physics*, 101(12):123530, 2007.

[48] J. C. Tremblay, 2023. Private communication.

[49] H. Conrad, M.E. Kordesch, W. Stenzel, M. Sunjić, and B. Trninic-Radja. Surface resonances in vibrational spectroscopy of hydrogen on transition metal surfaces: Pd(100) and Pd(111). *Surface Science*, 178(1):578–588, 1986.

[50] A. M. Bradshaw and N. V. Richardson. Symmetry, selection rules and nomenclature in surface spectroscopies. *Pure Appl. Chem.*, 68:457–467, 1996.

[51] Ron Bracewell and Peter B Kahn. The Fourier transform and its applications. *American Journal of Physics*, 34(8):712–712, 1966.

[52] Bala Krishna Pathem, Shelley A Claridge, Yue Bing Zheng, and Paul S Weiss. Molecular switches and motors on surfaces. *Annual review of physical chemistry*, 64:605–630, 2013.

[53] Gerhard Ertl. Reactions at surfaces: from atoms to complexity (Nobel lecture). *Angewandte Chemie International Edition*, 47(19):3524–3535, 2008.

[54] GA Somorjai. Catalysis on the atomic scale (Emmett Award Lecture of 1977). *Catalysis Reviews Science and Engineering*, 18(2):173–197, 1978.

[55] Rep Gomer. Diffusion of adsorbates on metal surfaces. *Reports on progress in Physics*, 53(7):917, 1990.

[56] Jean Christophe Tremblay. A Unifying Model for Non-Adiabatic Coupling at Metallic Surfaces beyond the Local Harmonic Approximation: from Vibrational Relaxation to Scanning Tunneling Microscopy. 138(24):244106, 2013.

[57] R. C. Tolman. *The principles of statistical mechanics*. Oxford University Press, Oxford (UK), 1938.

[58] JE Baggott, Mei-Chen Chuang, Richard N Zare, HR Dübal, and M Quack. Structure and dynamics of the excited CH–chromophore in (CF3) 3CH. *The Journal of chemical physics*, 82(3):1186–1194, 1985.

[59] David Gelman and Ronnie Kosloff. Simulating dissipative phenomena with a random phase thermal wavefunctions, high temperature application of the Surrogate Hamiltonian approach. *Chemical physics letters*, 381(1-2):129–138, 2003.

[60] Neil W Ashcroft and N David Mermin. *Solid state physics*. Cengage Learning, 2022.

[61] Peter Stephen Morris Townsend. *Diffusion of light adsorbates on transition metal surfaces*. PhD thesis, University of Cambridge, 2018.

[62] Peter S. M. Townsend. Diffusion of light adsorbates on transition metal surfaces. Dissertation, Cambridge University, Cavendish Laboratory, Cambridge, UK, 2018.

[63] John P Perdew, John A Chevary, Sy H Vosko, Koblar A Jackson, Mark R Pederson, Dig J Singh, and Carlos Fiolhais. Atoms, molecules, solids, and surfaces: Applications of the generalized gradient approximation for exchange and correlation. *Physical review B*, 46(11):6671, 1992.

[64] David Vanderbilt. Soft self-consistent pseudopotentials in a generalized eigenvalue formalism. *Physical review B*, 41(11):7892, 1990.

[65] Fabrizio Cleri and Vittorio Rosato. Tight-binding potentials for transition metals and alloys. *Physical Review B*, 48(1):22, 1993.

[66] Vittorio Rosato, M Guillope, and B Legrand. Thermodynamical and structural properties of fcc transition metals using a simple tight-binding model. *Philosophical Magazine A*, 59(2):321–336, 1989.

[67] Mohsen Razavy. *Quantum theory of tunneling*. World Scientific, 2013.

[68] R. Marquardt and M. Quack. Energy Redistribution in Reacting Systems. In Moore, J. and Spencer, N., editor, *Encyclopedia of Chemical Physics and Physical Chemistry*, volume I, chapter A3.13, pages 897–936. IOP Publishing, Bristol, 2001.

[69] Roberto Marquardt. Non linear adjustments with external conditions. *Journal of Mathematical Chemistry*, 50(3):577–587, 2012.

Université de Strasbourg

Oussama Bindech
Quantum dynamics of the diffusion of adsorbates.

EDSC École Doctorale des Sciences Chimiques

Résumé

Cette thèse a pour but d'étudier la dynamique des adsorbats avec une approche théorique entièrement quantique. Nous nous intéressons particulièrement aux systèmes H/Pd(111) et H_2/Pd(111). Une grande partie de ce travail est liée à l'étude des états vibrationnels et des énergies propres des atomes d'hydrogène sur la surface de palladium. Cette étude a montré la présence d'un couplage par effet tunnel et résonance de Fermi des modes vibrationnels localisés du système. Des simulations numériques mettant en évidence la manifestation de ces deux effets quantiques dans le comportement dynamique des atomes d'hydrogène à la surface du palladium sont présentées. Nous proposons enfin une nouvelle méthode de calcul de la fonction de diffusion intermédiaire qui repose sur une approche stochastique quantique. Un résultat préliminaire est comparé à des expériences de spin écho.

Mots-clés : Adsorption dissociative, spectroscopie vibrationnelle, diffusion quantique, Multi-Configuration Time-Dependent Hartree (MCTDH), résonance de Fermi, fonction de diffusion intermédiaire (ISF).

Abstract

The present thesis aims at studying the dynamics of adsorbates following a fully quantum theoretical approach. We are particularly interested in the H/Pd(111) and H_2/Pd(111) systems. A large part of this work is related to the study of the vibrational states and eigenenergies of the hydrogen atoms on the palladium surface. This study showed the presence of tunneling and Fermi resonance coupling of localized vibrational modes of the system. Numerical simulations highlighting the manifestation of these two quantum effects in the dynamical behavior of hydrogen atoms on the palladium surface are presented. We finally propose a new method to calculate the intermediate scattering function (ISF) which relies on a quantum stochastic approach. A preliminary result is confronted with spin echo experiments.

Keywords : Dissociative adsorption, vibrational spectroscopy, quantum diffusion, Multi-Configuration Time-Dependent Hartree (MCTDH), Fermi resonance, the intermediate scattering function (ISF).